THEORY OF THREE-DIMENSIONAL INTERCHANGE RECONNECTION AND THE DYNAMIC EVOLUTION OF THE GLOBAL SOLAR CORONAL MAGNETIC FIELD STRUCTURE: A MECHANISM FOR THE ORIGIN AND GENERATION OF THE SLOW SOLAR WIND

by

Justin K. Edmondson

A dissertation submitted in partial fulfillment
of the requirements for the degree of
Doctor of Philosophy
(Applied Physics)
in The University of Michigan
2009

Doctoral Committee:

Adjunct Professor Spiro K. Antiochos, Co-Chair
Professor Thomas H. Zurbuchen, Co-Chair
Professor Lennard A. Fisk
Professor Alec D. Gallimore
Professor Greg Tarlé

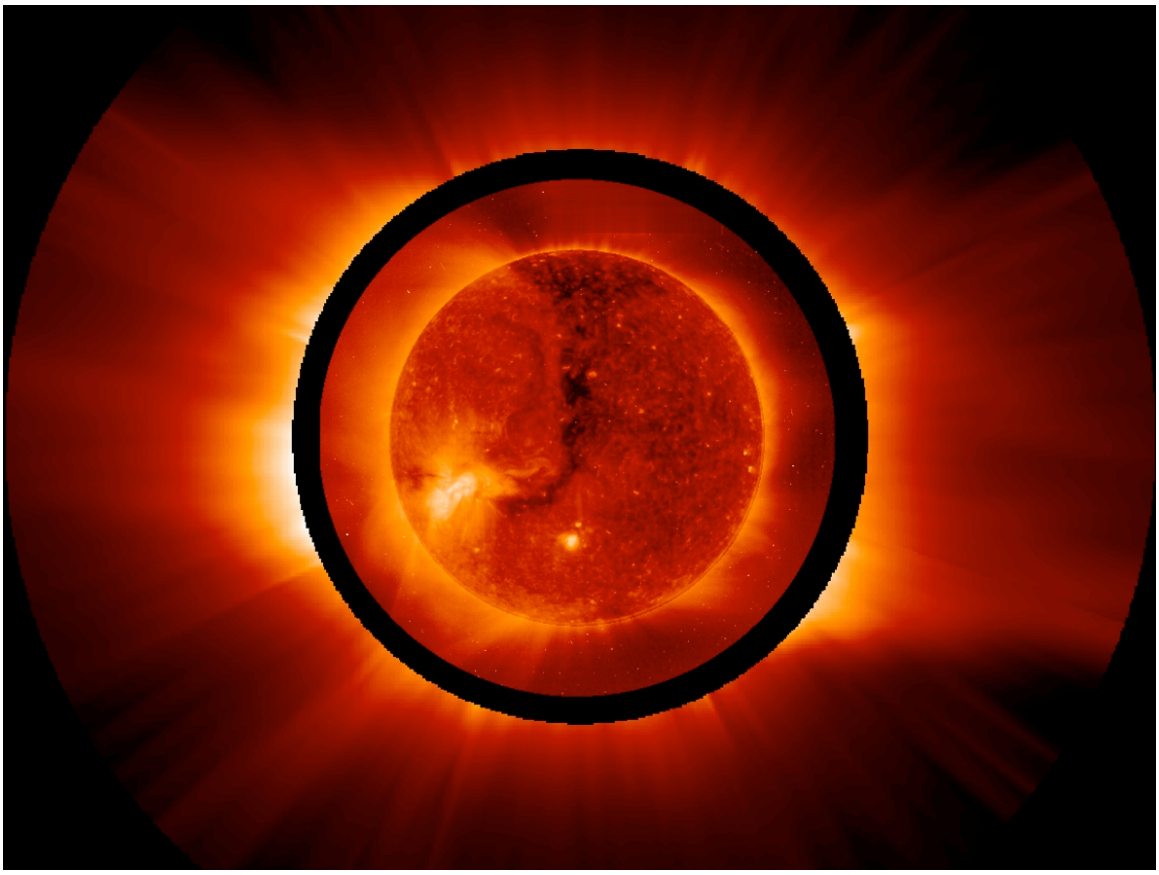

UVCS/EIT composite image. SOHO

To Dr. Jean Krisch

. . . who is, above all else, a teacher.

ACKNOWLEDGEMENTS

Thank you to all of the people who made this dissertation possible. First and foremost, to my advisors: Dr. Spiro K. Antiochos, who is a true mentor in both science and life; Dr. Thomas H. Zurbuchen, who introduced me to the field, and in doing so, gave me enough rope to hang myself; Dr. Lennard A. Fisk, who taught me to question everything, and then formulate the answers for myself. To my parents for supporting me no matter the choices I made along this long, and at times, arduous journey. Especially my mother who gave up her couch for me to sleep on for four years while I built the proper foundations. To my colleagues for all your advice, thoughts, and general conversations that deepened my understanding of this material. To my friends for teaching me that nothing worth doing comes easy. Finally, I want to gratefully acknowledge support for this work from the NASA HTP, TR&T, SR&T, and GSRP Programs, as well as the high-performance computing capabilities provided by the DoD HPCMP.

TABLE OF CONTENTS

LIST OF FIGURES

Figure

LIST OF APPENDICES

Appendix

LIST OF ABBREVIATIONS

1D one-dimensional

2D two-dimensional

3D three-dimensional

ACE Advanced Composition Explorer

AMR adaptive mesh refinement

ARMS Adaptively Refined Magnetohydrodynamic Solver

CME coronal mass ejection

EUV extreme ultraviolet

HCS heliospheric current sheet

IMF inter-planetary magnetic field

MDI Michelson Doppler Imager

MHD magnetohydrodynamic

PFSS potential field source surface

RHS right hand side

SOHO Solar and Heliospheric Observatory

TRACE Transition Region and Coronal Explorer

PIL polarity inversion line

ABSTRACT

THEORY OF THREE-DIMENSIONAL INTERCHANGE RECONNECTION AND THE DYNAMIC EVOLUTION OF THE GLOBAL SOLAR CORONAL MAGNETIC FIELD STRUCTURE: A MECHANISM FOR THE ORIGIN AND GENERATION OF THE SLOW SOLAR WIND

by

Justin K. Edmondson

CoChairs: Spiro K. Antiochos and Thomas H. Zurbuchen

To understand the evolution of the solar corona and the generation of the solar wind, it is necessary to understand the structure and dynamics of the coronal magnetic field. Phenomenologically-based "quasi-steady" models have been developed under the assumption that the corona evolves as a time series of force-free equilibrium states determined by the normal-flux distribution at the photosphere. These models are successful at predicting the overall field polarity, global magnetic structures, and position of the heliospheric current sheet. However, the quasi-steady models cannot account for the observed bi-modal flow structure of the solar wind, nor several heliospheric observations with implications for the dynamics of the magnetic field. Motivated by these limitations, several researchers have proposed a fundamentally different paradigm for the evolution of the corona, the so-called interchange model. Based on the interchange reconnection (IR) process, this model predicts a structure for the coronal magnetic field which substantially differs from the quasi-steady view.

Strictly speaking, IR describes three-dimensional (3D) null point reconnection, in

which closed bipolar flux reconnects with coronal hole flux opening into the heliosphere. More generally, the 3D null point reconnection mechanism is a direct consequence of the nested multi-polar field structure which occurs ubiquitously throughout the entire corona. This dissertation aims to rigorously investigate the 3D null point reconnection mechanism and the consequences thereof on the coronal environment. To that end, we present several related simulations that examine current sheet formation and stability, as well as the consequences of this type of reconnection on the structure and dynamics of the global magnetic field. We show the field topology remains smooth during the evolutions, incompatible with predictions of the initially proposed interchange model. In addition, we demonstrate dynamic effects of IR incompatible with the quasi-steady models. Therefore, we prove the necessity of a coronal description which includes fully-dynamic 3D magnetohydrodynamic effects. For sufficiently complex magnetic field structures and evolutions, the predicted dynamics of the quasi-steady and interchange models converge at the coronal hole boundaries. In the end, we offer the consequences of IR on the global coronal magnetic field as a generation mechanism for the slow solar wind.

CHAPTER I

Introduction

The heating of the solar corona and the origin and acceleration of the solar wind continue to be two of the most important unresolved problems in all of solar and heliospheric physics, and even within stellar astrophysics. The magnetic field is the most important property of the solar corona, as it is the principal conduit for coupling the energy of the Sun's convective envelope to the corona and, subsequently, to the solar wind, and therefore is the primary driver of solar activity. Fundamentally then, in order to understand the heating of the corona and the generation of the solar wind, it is necessary to resolve the evolution, energy transport, and dissipation processes of the evolving magnetic field structure. Therefore, the motivation underlying this dissertation research is to investigate the structure and dynamic processes of the coronal magnetic field central to all solar activity.

Observationally, the solar corona is known to be a magnetically dominated, highly-conductive, inhomogeneous environment. The average large-scale solar magnetic field exhibits a dipolar structure separated by an equatorial polarity inversion line (PIL), that reverses direction approximately every 11 years. Heliospheric measurements of the global inter-planetary magnetic field (IMF) structure are consistent with a single, warped heliospheric current sheet (HCS) marking the boundary between the inward/outward directed field polarity throughout the solar activity cycle. Coronal

magnetic field phenomenology is characterized by two basic structures: open coronal holes in which the field maps from the photospheric boundary out into the heliosphere making up the IMF, and closed-loop regions in which the magnetic connections map back to the photospheric surface within an altitude of 2.5 - 3 solar radii. Coronal hole regions display quasi-rigid rotations with the Sun, despite the differential rotation profile of the photospheric surface, implying an opening/closing of the largest-loops at the HCS. Heliospheric plasma observations reveal a bi-modal solar wind structure consisting of fast wind plasma correlated with coronal hole regions, and a slow wind regime compositionally associated with the closed-loop regions of the corona. In addition, the slow wind is highly variable, and confined to a relatively thick envelope about the HCS. As such, the theoretical models built in the attempt to understand the structure and dynamics of the solar magnetic field, as well as the origin and generation of the solar wind, must necessarily include these observational effects.

The standard quasi-steady coronal field models are fundamentally phenomenological because they are entirely determined by the observed photospheric normal flux distribution. Based upon the assumption that the coronal magnetic field evolves smoothly as a series of force-free equilibrium states, they are very robust in capturing the large-scale properties of the coronal magnetic field structure, such as the overall magnetic field polarity, coronal hole pattern, and the position of the HCS. Within the quasi-steady framework, coronal dynamics are only inferred from changes in the photospheric flux distribution. As a consequence, the quasi-steady models cannot describe transient activity on timescales faster than the photospheric observation time cadence. More importantly though, the quasi-steady models cannot explain the bi-modal nature of the solar wind in that their evolutions account for only the flows emanating from coronal holes, since the theory cannot explicitly put closed-loop plasma onto open field lines. Quasi-steady model evolutions only implicitly suggest a slow wind confined to a very thin envelope about the HCS by continuous open-

ing/closing of streamer flux and plasmoid release through reconnection at the HCS; supplemental dynamics outside the scope of the theoretical framework.

Motivated by the inability of the quasi-steady models to correctly describe the detailed observed bi-modal wind structure, as well as heliospheric flux measurements that suggest a constant minimum level of open flux throughout the solar activity cycle, and several heliospheric observations with implications regarding the large-scale dynamics of the IMF, a fundamentally different coronal field evolution paradigm has been proposed. Over the last decade, the so-called "interchange model" has been developed in which the global field evolves based on interchange reconnection, an elementary reconnection interaction between open and closed field. Presently, interchange-type reconnection and consequences thereof on coronal magnetic field dynamics have not been rigorously investigated with fully three-dimensional (3D) magnetohydrodynamic (MHD) calculations. But the statistical average of many field lines of the different open/closed topologies interchanging their identities through reconnection events, is modeled by a media-diffusion equation that predicts large-scale dynamics of the coronal field, such as a coherent reversal of a single HCS, and a rationalization for a minimum level of open flux maintained in the heliosphere. As a consequence of the exchange of field line identities, the interchange reconnection mechanism provides a venue to release closed-loop plasma onto the open field of coronal holes, and therefore into the slow wind expansion of the solar atmosphere. In addition, the interchange model provides a self-consistent explanation for open flux coalescence to form the large, well-defined polar coronal holes as the solar cycle approaches minimum activity phase; in some sense, the interchange model offers a self-constient justification for how a particular coronal hole pattern developed. The interchange reconnection mechanism, however, generates a highly complex, highly discontinuous coronal field structure that includes many disconnected coronal holes, seemingly incompatible with the observed dynamic timescales.

Strictly speaking, interchange reconnection refers to closed loop field interacting with open field (i.e., a bipole embedded within a coronal hole). More generally though, interchange reconnection is a specific case of the more general 3D null point reconnection process. In the highly-conductive, magnetically dominated plasma environment of the solar corona, the global field structure consists of complex arrangement of nested multi-polar field geometry which cannot sustain long-lived singular current systems. As this geometric structure is stressed in various ways (i.e., by flux injection, and/or driving flow fields at the photospheric boundary), highly dissipative singular current systems are generated along the nested flux domain boundaries, which are then dissipated through reconnection. Therefore, as a direct consequence of the stressing of nested bipolar field structure throughout the solar corona, the general process of 3D null point reconnection is likely a highly ubiquitous magnetic energy release process that arises throughout the entire solar corona. In addition, the evolution is highly dependent on the plasma dissipation mechanism that governs current sheet formation and subsequent reconnection dynamics.

In this dissertation, I show these dynamics, which neither the quasi-steady or the interchange model frameworks calculate explicitly, necessarily play a very important role in solar activity. In both model paradigms, the evolution of the coronal field structure is only implicitly captured. In this work, I characterize in detail the elementary 3D null point reconnection process within the context of low-beta magnetized plasma evolution, and the resulting dynamics of the large-scale coronal magnetic field structure. The evolution dynamics are calculated using fully analytic initial magnetic field structures, in fully-dynamic 3D MHD. I show that the dynamics are highly dependent on the dissipation mechanism that governs singular current sheet formation and therefore the reconnection dynamics. The results imply only fully-dynamic MHD calculations may even attempt to predict the proper large-scale dynamics of the coronal magnetic field. In addition, the ramifications of the full 3D MHD calculations

constrain the differences, similarities, limitations, and relationships between the two theoretical frameworks, which for sufficiently complex coronal field structure lead to a kind of convergence of the two competing paradigms. I argue, interchange reconnection is a self-consistent coronal plasma release mechanism generating the slow solar wind along coronal hole boundaries, in good agreement with observational evidence.

I attempt to arrange the presentation into two basic divisions: the theoretical framework (chapters II and III), and the dissertation research (chapters IV - VII). The two theory chapters review the relevant coronal environment, as well as magnetic field structure evolution within the MHD framework. Three separate, yet related, calculations of current sheet formation and reconnection are presented in the next three research chapters. The last chapter places the research and consequences thereof within the larger context, and summarize the overall impact of this dissertation on solar and heliospheric physics.

Chapter II is an overview of the current theoretical and observational understanding of solar and heliospheric astrophysics in order to build the proper environmental context. In section 2.1, I briefly review the solar interior from the thermonuclear energy generation process, through the energy transport regimes that define the various internal layers, as well as the rotational and magnetic structure. In section 2.2, I describe the phenomenological solar atmosphere, consisting of the photosphere, chromosphere, transition region, corona, and interplanetary medium. I derive Parker's solar wind solution under some simplifying assumptions, and augment this solution with the observational bi-modal wind structure and IMF. Finally, in section 2.3, I discuss the framework of the quasi-steady and interchange models that describe the large-scale coronal magnetic field evolution, noting the differences and consequences in the global field structure in each case.

In chapter III, I build the theory of geometric and topological magnetic domains within the strong-field, MHD-continuum approximation. This framework is, in gen-

eral, the correct description of multi-polar magnetic field structures interacting with a large-scale background coronal field, and is the most common geometry throughout the solar corona. Section 3.1 reviews the construction of the magnetic stress tensor, and describes how the individual magnetic domains are defined by the internal stress distribution which are fundamentally based on the global boundary conditions. In section 3.2, I examine the geometric and topological structure of the 3D magnetic null point, arguing the separation into nested magnetic domains requires this structure. Section 3.3 covers the theory of current sheet formation and stability in two-dimensional (2D). I discuss how the reconnection mechanism arises from the resistive tearing mode instability. Finally, the reconnection process is described in section 3.4, covering both Sweet-Parker and Petschek mechanisms. I end the chapter showing how helicity constraints, preserved by the reconnection process, lead to global force-free equilibrium of the global coronal magnetic field.

In chapter IV, I present a rigorous calculation of a high-resolution, fully-3D MHD, self-consistent current sheet formation and stability starting from an X-Line topology - with the intent to generalize the dynamics to 3D null point structure current sheet formation reconnection mechanism. I show this current sheet, though subject to plasmoid generation and expulsion by the resistive tearing mode, is stable under steady-driving conditions.

In Chapters V and VI, the 3D null point current sheet formation, stability, and reconnection process is placed within the larger context of coronal hole pattern and streamer belt dynamics. Chapter V gives a topologically rigorous definition of the interchange reconnection process; noting that only when the bipole flux system is embedded within a coronal hole, is the 3D null point reconnection process, in the strict sense, interchange reconnection. In chapters V and VI, several related numerical calculations of the interaction between bipolar flux systems and the global coronal magnetic field are analyzed. Each simulation offers compelling evidence of smooth,

continuous magnetic field topology throughout the evolutions incompatible with the original formulation of the interchange model, as well as demonstrating large-scale dynamics inconsistent with the quasi-steady framework. Finally, Chapter VII closes this dissertation with a discussion of the consequences of 3D null point reconnection and embedded flux systems on the global coronal magnetic field structure and dynamics.

CHAPTER II

Theoretical and Observational Solar Astrophysics

To build the foundations necessary for understanding the dynamic global solar magnetic field, it is necessary to place the solar magnetic structure properly within the context of the solar astrophysical environment. Section 2.1 is a brief overview the Sun as a star, discussing the standard solar model from the thermonuclear energy generation process, through the energy transport mechanisms that characterize the internal stratum, to the rotational and magnetic activity structures. Section 2.2 continues with a definition and description of the entire solar atmosphere above the visible disk, including coronal phenomenology, and the fundamental structure of the solar wind expansion. Finally, section 2.3 closes the chapter with an account of the current representations of the global plasma and magnetic environment, building the standard working-models that are the quasi-steady equilibrium models, contrasting them against the interchange model, and discussing the physical implications of each.

2.1 The Solar Internal Structure

Set in the context of stellar astrophysics, the Sun is a typical main-sequence star of spectral class G2V. The solar mass is approximately 1.989 $\times 10^{33}$ g, and contains of roughly 99.8% of the total material in the solar system. Though heavy elements such as C, O, Ca, Na, Si, Fe, etc. dominate the observed photospheric spectra, at the

present epoch the Sun is composed of about 70% hydrogen, 28% helium, and only 2% other metals by mass (Carroll & Ostlie (1996)). The thermonuclear energy generation process in the solar core is via the proton-proton chain, inferred from the observed luminosity, radius, and the effective surface blackbody temperature on the visible disk, 3.85 $\times 10^{33}$ erg s^{-1}, 6.96 $\times 10^{10}$ cm, and nearly 5770 K respectively (Bahcall et al. (2003)). The Sun's current age is approximately 4.5 billion years, and is estimated to continue burning predominantly hydrogen for another 5 billion years. At that stage, the Sun will begin to chiefly burn helium, heat up, and swell into a red giant. Once the helium fuel is exhausted, the thermonuclear burning will continue through the heavier elements up to iron, while gently shedding its outer layers at each principal reaction transition. Since the solar mass is below the Chandrasekhar limit, our Sun's final state will be a white dwarf about the size of the Earth, supported against gravitational collapse by electron degeneracy pressure (Carroll & Ostlie (1996)).

To the lowest order of approximation, the internal structure of the Sun can be estimated using the Vogt-Russell Theorem (Carroll & Ostlie (1996)). According to this Theorem, the mass and composition of a star uniquely determine its radius, luminosity, and internal structure. The effects of an internal rotational profile, magnetic fields, material accretion/loss, and local spacetime curvature (i.e., gravitational tidal forces) on the Sun's structure are to a first approximation neglected - simply because these properties likely did not play a principal role during the Star's formation stage. Using only the equations of hydrostatic force balance, energy conservation, as well as a material equation of state (Rose (1998)), the standard model for the solar internal structure consists of three major regimes: the thermonuclear core, the radiative zone, and the convection zone (see Figure 2.1).

The thermonuclear engine, at a density and temperature (depending on the details of the particular model) of around 150 g cm^{-3} and 15 MK respectively, converts roughly 4.5 billion metric tons of hydrogen into helium every second. The core's size

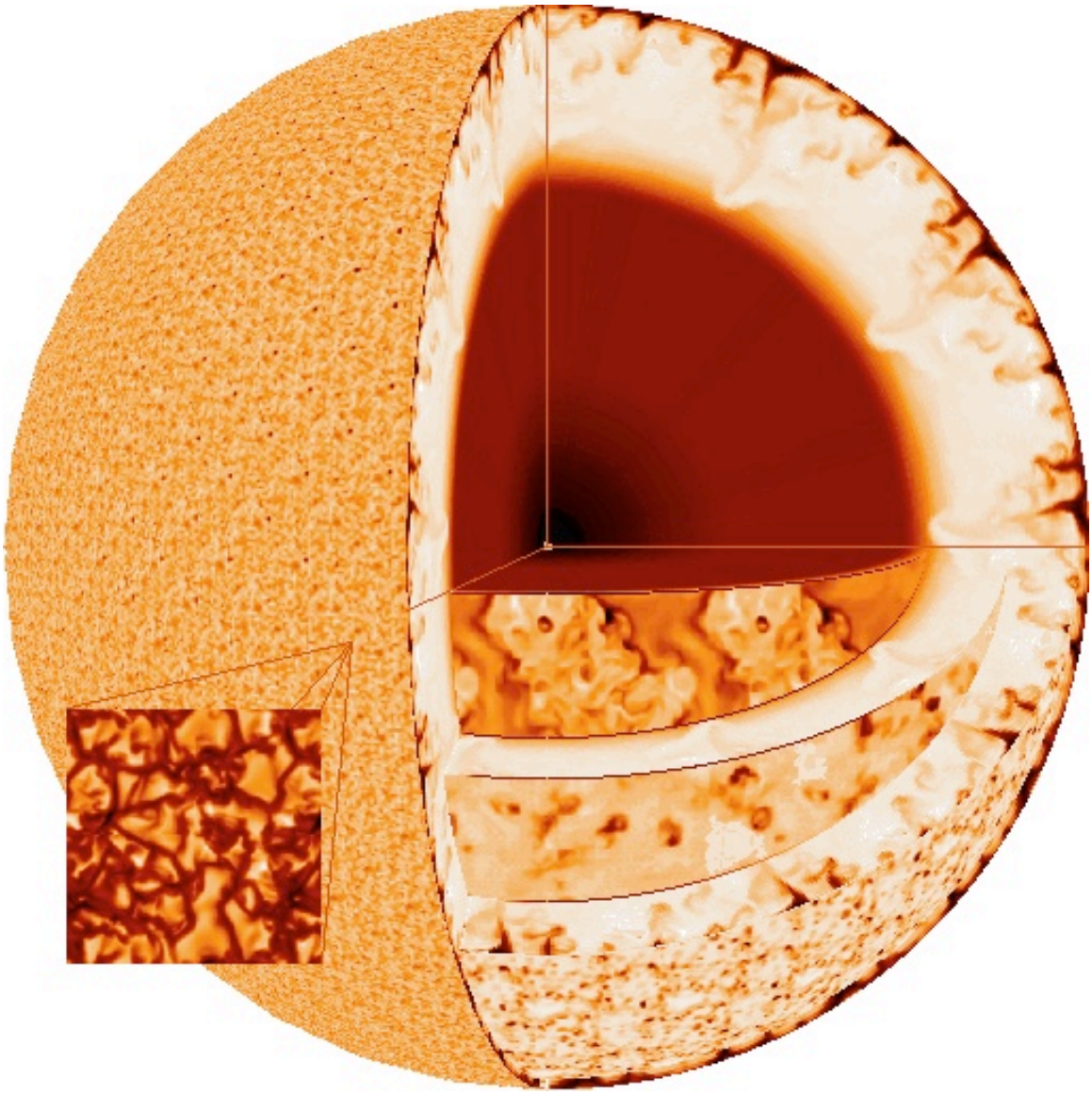

Figure 2.1: Solar Interior Structure: thermonuclear core, radiation zone, convection envelope, and photospheric granulation pattern on the visible surface. Figure from http://www.astro.ku.dk/∼aake/talks/NAP98/cover-tr.gif

is limited to roughly the innermost 20% - 30% of the star by radius. Deep within the solar interior the gas and radiation field are in local thermodynamic equilibrium, and therefore the energy generated in the core must be transported to the surface by the diffusive processes of radiation or convection. Radiative transport dominates roughly the inner-2/3 of the solar interior. In the outer third, the temperature gradient becomes superadiabatic, and thus the gas becomes unstable to convection (Rose (1998)). Physically, the opacity within the convection envelope has become large enough to inhibit efficient radiative transport. As a consequence of the different energy transport mechanisms, the temperature of the solar interior falls off non-linearly from 15 MK at the core to 6500 K at the top of the convection zone.

At the next level of approximation, rotation and magnetic field effects become important to the internal structure, and therefore to the coronal and heliospheric environment. Observations of the motions of surface features reveal a differential rotation in which the equator rotates much faster than the polar regions, approximately 26 days and 37 days respectively. Helioseismic analysis reveals this rotational flow profile persists throughout the convection envelope, implying convection gives rise to differential rotation. Between the convective and radiative zones is a thin transition region over which the rotational variation with latitude disappears, the so-called tachocline. Below the tachocline, the radiation zone (and likely the thermonuclear core as well) exhibits solid body rotation with a period about the same as the equatorial regions at the surface (Christensen-Dalsgaard & Thompson (2003)).

The Sun's large-scale magnetic field exhibits an approximate 22 year cyclic polarity cycle. In the course of each $\sim$11-year magnetic activity phase, characterized by a consistent overall polarity, sunspots (regions of highly concentrated, dipolar magnetic flux) initially appear in belts at high latitudes, and the emergence slowly progresses toward lower and lower latitudes (see Figure 2.2). Sunspot patterns in both hemispheres have a leading polarity opposite that of the average background hemispheric

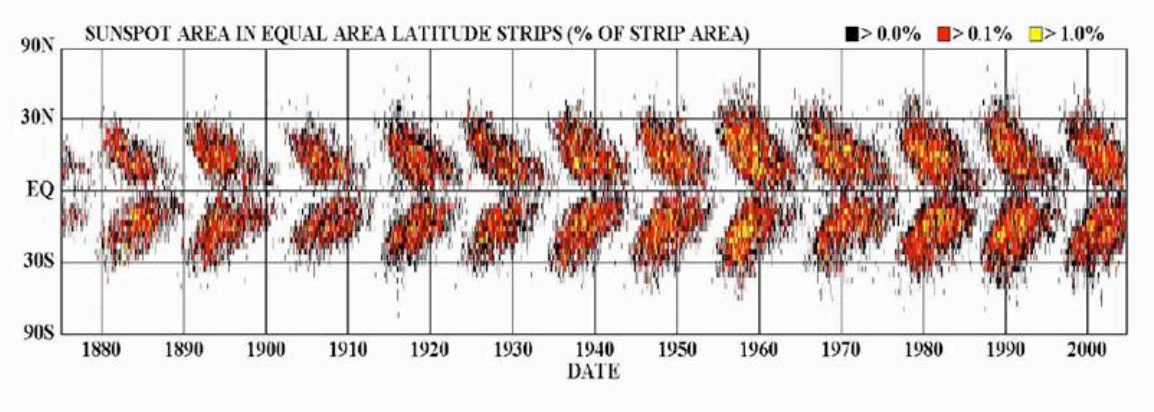

Figure 2.2: Sunspot activity cycle butterfly diagram showing the equatorward migration of emergence latitudes throughout the solar cycle (D. Hathaway)

polarity, known as Hale's Polarity Law (Carroll & Ostlie (1996)). Also, these bipolar active regions emerge tilted with a latitudinal tilt of roughly 35°, in which the leading polarity spot is closer to the equator. This cyclic activity suggests an internal dynamo mechanism that involves the interaction between the rotation and convective motions. Though the details of such dynamo action are not yet understood, current theories suggest the tachocline plays a very important role in the solar activity cycle.

The phenomenological nature of sunspots suggests that the interior magnetic field is concentrated into discrete flux tubes (i.e., localized bundles of field lines). Though hydromagnetic stability theory states continuous magnetic fields inhibit convective overturning, a simple energy argument demonstrates the total energy of the convection zone is decreased by magnetic fields concentrated into fibril states (Parker (1984)). From total pressure balance and thermal equilibrium, the material density inside the flux tube is less than that of the surrounding plasma giving rise to a buoyancy force on the flux tubes within the convection zone. In addition, these flux tubes must have magnetic energy densities at least of order the turbulent kinetic energy density of the plasma to overcome deformations due to turbulent convection throughout its rise and emergence at the surface. Finally, the flux intensity of the sunspots

tends to get amplified by the strong downdrafts of the convection cell boundaries at the solar surface.

2.2 The Solar Atmosphere

The solar atmosphere may be broadly defined as the optically thin region beyond the convection zone in which the solar energy flux escapes as radiation ($\sim$ 1367 W m^2, Carroll & Ostlie (1996)) and particles ($\sim 1.3 \times 10^{36}$ particles s^{-1}, Kallenrode (2004)). This tenuous environment engulfs the entire solar system, extending to the solar wind termination shock at roughly 100 AU from the Sun, where the interstellar medium becomes dominant. The solar atmosphere can be organized into two separate regimes based on the principal energy partition of the plasma: the magnetically dominated ($\beta < 1$) solar corona, and the thermally dominated ($\beta \geq 1$) supersonic, superalfvenic solar wind. Traditionally, coronal physics has further divided the magnetically dominated portion into four regions: the photosphere, the chromosphere, a very thin transition region, and the corona. Heliospheric physics beyond the low-beta corona, also referred to as the interplanetary medium, is concerned with the solar atmospheric plasma expansion that comprises the solar wind. This research concerns the coupling dynamics between the corona and heliosphere, and therefore necessarily takes the entire system point of view.

The boundary between the solar interior and the solar atmosphere is the photosphere. The visible solar disk has a sharp edge due to the fact that at this point the plasmas optical depth at a wavelength of 5000 $\mathring{A}$ (i.e., the absorption coefficient over path length for white light) transitions to unity over a very thin layer, approximately 500 km (equivalently 0.07% of a solar radius). Above the photosphere, electromagnetic radiation escapes the Sun relatively unimpeded into space. The plasma density within the photospheric layer is of order 10^{-7} g cm^{-3}, and the temperature decreases to a global minimum of roughly 6000 K . In sunspots, the local photospheric temper-

ature is even further reduced to approximately 2/3 of the surrounding value, since the strong field greatly inhibits convective overturning. White light observations of the photosphere show a highly compressible, granulation pattern driven by internal convection (see Figure 2.3). Typical length and turnover time scales of the granulation pattern are of order 1 - 2 Mm and 5 - 10 minutes respectively. Larger-scale supergranulation patters have also been observed at respective spatial and temporal scales of $\gtrsim$ 20 Mm and roughly 24 hours. Doppler shifted images reveal typical plasma flow velocities around 1 - 3 km s^{-1} or less.

The chromosphere and transition regions are in some sense a thin collar that couples the relatively cool, thermally-dominated solar surface, to the hot, tenuous, magnetically-dominated corona. Across approximately 10,000 km in altitude, the plasma density drops by nearly 8 orders of magnitude. The chromosphere, named for the Hα (Balmer series $3 \rightarrow 2$ line) dominated emission spectrum, is the layer extending about 2000 km above the photosphere. Within this region, the plasma temperature increases from 4500 K to nearly 25,000 K. Though the intensity in the chromosphere is nearly 10^{-4} of the photospheric value, a great deal of structure is seen in the He II, Fe II, Si II, Cr II, and in particular Hα, Ca II H, and K spectra. Among a rich array of phenomena observed within the chromosphere, supergranulation on length scales of order 30,000 km with convective velocities similar to photospheric values become evident. Abundant supersonic plasma jets known as spicules, driven by sound waves, burst forth on 5 minute timescales carrying material from the photosphere into the chromosphere and low corona. The transition region is defined as the extremely thin layer, only several hundred kilometers, above the chromosphere over which the temperature rises to order 10^6 K. As a result of such large temperature and density gradients, the transition region may only be selectively observed at various altitudes with ultraviolet and extreme ultraviolet (EUV) wavelengths of the 1216 $\mathring{A}$ Lyman α at 2 $\times 10^4$ K, the 977 $\mathring{A}$ C III at 9 $\times 10^4$ K, and the 1032 $\mathring{A}$ O VI at 3 $\times 10^5$ K.

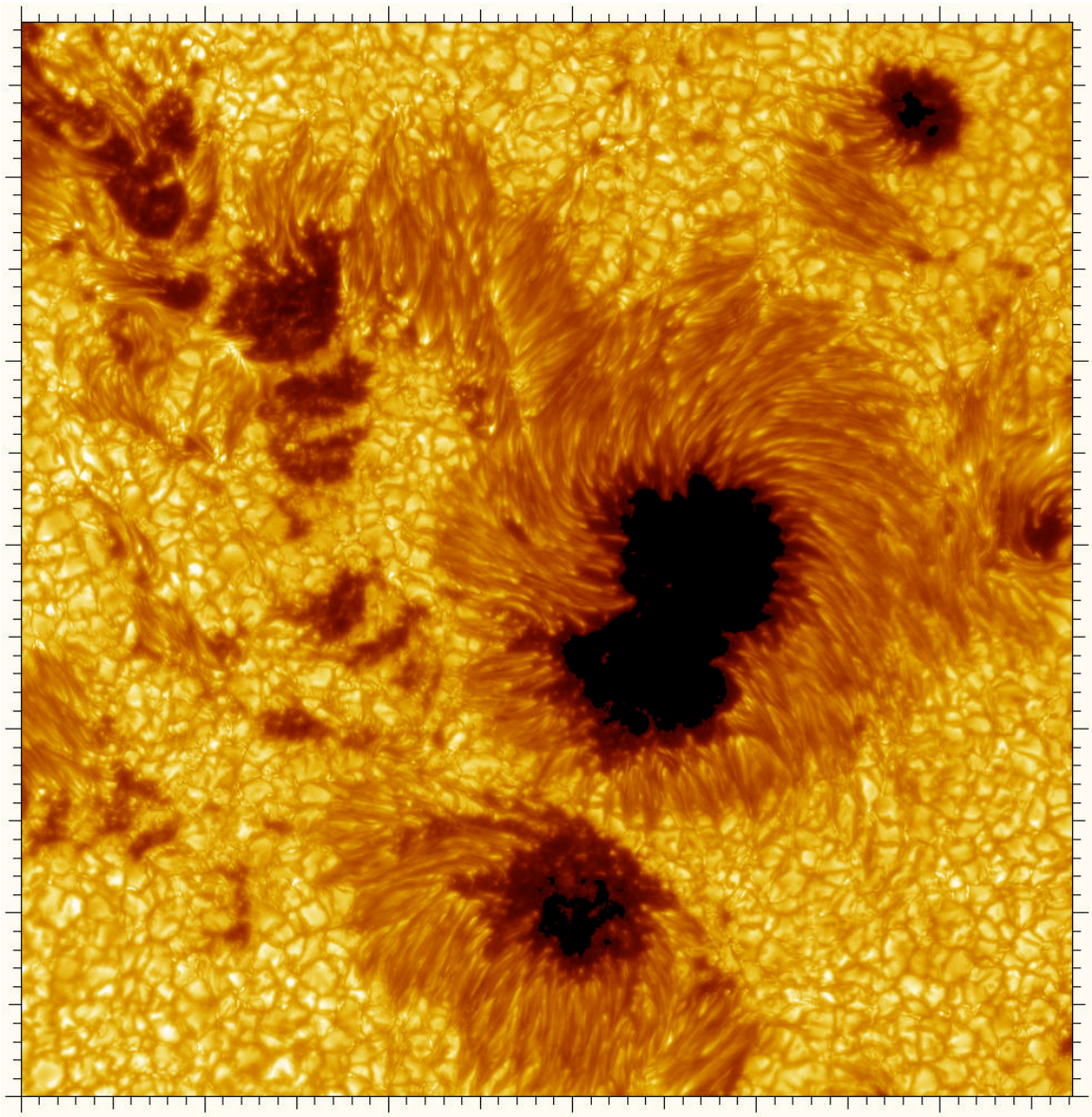

Figure 2.3: Photospheric granulation and sunspots in Active Region 10030, 15 July 2002 (G. Schamer, et al., Swedish 1-meter Solar Telescope (SST), Royal Swedish Academy of Sciences)

The magnetic field emerging from the solar interior is expelled to the inter-granular network lanes at the photosphere, and undergoes tremendous expansion across the chromospheric layer owing to the large decrease in plasma density. Missions such as the Solar and Heliospheric Observatory (SOHO), Transition Region and Coronal Explorer (TRACE) have revealed much about this dynamic expansion. The lowest concetration field strength of flux that reaches into the chromosphere and low corona is the so-called magnetic carpet. This ubiquitous, rapidly-varying, emergence, fragmentation, and cancellation structure has field strengths on the order of only a few G. Structure on the carpet scale is continuously replenished on timescales of order 40 hours (Title & Schrijver (1998)). This field is mainly observed with SOHO's Michelson Doppler Imager (MDI) experiment (also sometimes referred to as the salt and pepper field since MDI measurements represent the radial field polarity in black and white; see Figure 2.4), and is shown to occur across the entire solar surface. With typical field strengths at such a low level, it is unlikely the flux of the magnetic carpet can rise very far above the photospheric/chromospheric layers. Since the magnetic carpet field strength is so small and turnover timescale so fast, this component is normally neglected in the standard coronal magnetic field models.

Above the transition layer is the magnetically dominated plasma of the solar corona, so tenuous that it is essentially completely transparent to radiation (with the exception of radio). To altitudes less than roughly 1.5 - 2 solar radii above the visible disk, the magnetic energy exceeds the plasma thermal energy (with localized exceptions such as in the vicinity of a magnetic null-point or magnetic cusp). Gary (2001) built an observational picture constraining the coronal plasma beta using various physical parameters (see Figure 2.5). This comprehensive study finds a $\beta < 1$, across the majority of the solar corona. As a consequence of the low-beta condition, plasma flows are confined parallel to the field lines, and any cross field transport is greatly inhibited (at least over typical coronal dynamics timescales), resulting in

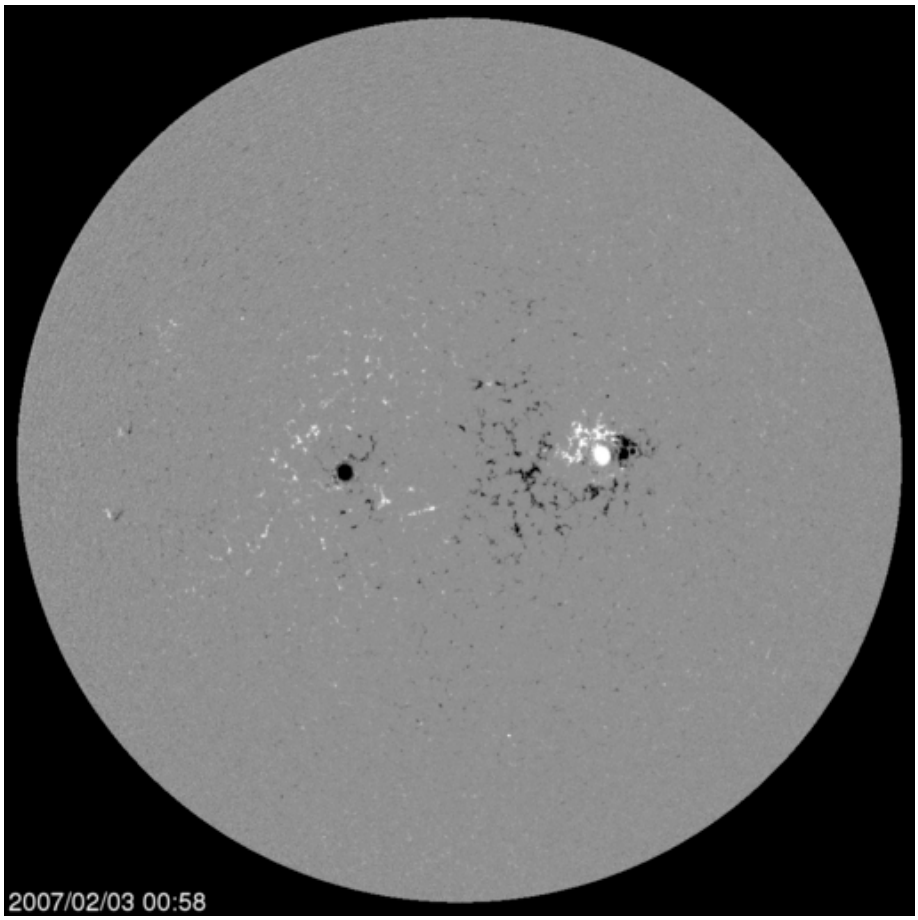

Figure 2.4: The magnetic carpet is the weak bipolar flux ubiquitous throughout the background (Full disk SOHO MDI image, 3 Feb, 2007)

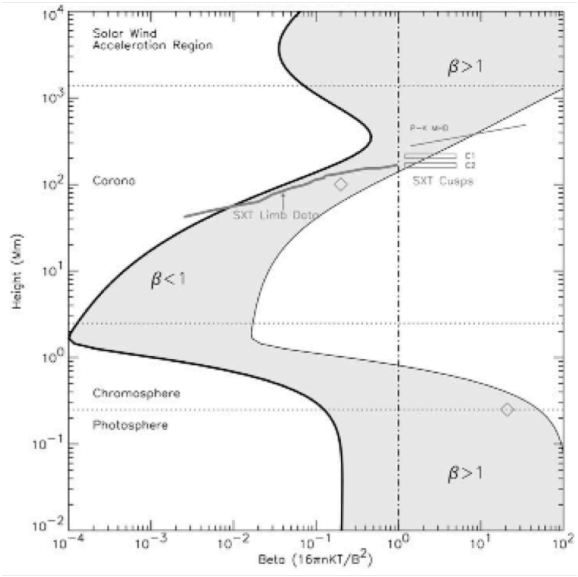

Figure 2.5: Solar coronal plasma beta profile (Gary (2001))

a thermodynamic structure in the corona not gravitationally stratified, but rather consisting of highly inhomogeneous, thermally isolated flux tube systems.

As a low-beta system, the energy of the corona is mainly stored, transported, and dissipated by the magnetic field, making the magnetic field and it's evolution the most important piece of the puzzle required to understand coronal dynamics. Unfortunately, even with all the advances in observational and measurement techniques in both space and ground-based observatories, the coronal magnetic field remains possibly the least well-defined physical property in the solar atmosphere. Of the existing measurement techniques, very few directly determine the magnetic field structure, and none measure the full field at high altitudes. For the most part, the geometric configuration is built from indirect measurements of the field strength and extrapolation methods. Table 2.1 lists the various solar magnetic field measurement techniques, both direct and indirect methods.

The radiative energy output over much of the corona is nearly 6 orders of magnitude less than the photosphere, making it only visible during a total solar eclipse where the glare from the solar disk has been blocked (Carroll & Ostlie (1996)). Typ-

Direct Methods
Faraday rotation
Polarization of free-free emission
Hanle effect
Zeeman splitting of spectral lines
Stokes polarimetry in infrared lines

Indirect Methods
In-situ vector field measurements by spacecraft at $\gtrsim 0.5$ AU
Microwave radio bursts with gyro-resonance emission
Decimetric bursts involving frequency drifts related to the Alfvén speed
Metric type II radio bursts (shock speeds related to the Alfvénic Mach number)
Circularly polarized Type III bursts (dependent upon the refractive index of the local magnetic field)
Potential Field and Force-Free field extrapolations from magnetograms

Table 2.1: Direct and Indirect solar magnetic field measurement methods

ical plasma densities in the corona are of order 10^5 - 10^9 particles cm^{-3}. Under these conditions, the gas and radiation field are not in local thermodynamic equilibrium, so a unique temperature is not strictly definable. Fortunately, a reasonably consistent temperature range of order 1 - 3 MK may be inferred from consideration of line widths produced by thermal Doppler broadening, ionization state, and radio emissions. Emission lines at these temperatures, seen in the EUV and soft X-ray regimes of the solar spectrum, are mostly produced by free-free emission of electrons scattering off highly ionized atoms such as Fe X and Fe XIV (Carroll & Ostlie (1996)). At these temperatures and densities, the mean-free path of a particle is approximately 3×10^6 cm, orders of magnitude smaller than any typical structure length-scales (10^9 - 10^{10} cm). Finally, the dimensionless Lundquist number R_m is a measure of the resistive effects within a conductive, magnetized plasma; a Lunquist number $R_m >> 1$ implies a highly conductive medium with negligible dissipation. For typical coronal parameters, the Lundquist number $R_m > 10^{10}$, save regions like singular current sheets with thicknesses small enough to reduce $R_m \lesssim 1$. Therefore, in the solar corona the ideal (frozen-in) MHD approximation is a valid plasma description.

Driven by the convective gas motions in the high-beta photosphere, the coronal magnetic field can develop extremely complex and dynamic structures. In general though, the minimum energy state of the magnetic field external to an isolated, static, magnetized astrophysical body is the dipole. A hot, expanding atmosphere, however, has the effect of dragging field lines away with the escaping gas. With the advent of EUV/X-ray imaging from space missions, it became possible to observe this coronal magnetic field structure directly. Even the low-resolution images from the early SKYLAB mission showed clearly that the large-scale corona is composed of two physically distinct regions: closed-field regions, consisting primarily of bright X-ray loops, and coronal holes that are dark in X-rays (Zirker (1977)). The photospheric flux below coronal loops is observed to be bipolar implying a closed field topology with both foot points anchored in the photosphere, and field line connections remaining entirely within the low-beta corona. On the other hand, the photospheric flux below coronal holes is unipolar, on average, implying the field topology there is open, in which the field lines have only one foot point fixed in the photosphere, and the field line connections pass into and are carried away with the solar wind, out of the low-beta corona extending into the heliosphere[1]. Coronal holes, therefore, are a source region for solar wind, which also explains why these regions are dark in X-rays. The plasma density there is low due to the large mass and energy flux required to power the solar wind.

On the whole, the coronal magnetic field structure resembles a dipolar configuration with a combination of separate open field coronal-holes, and large-scale, closed field helmet-streamer regions (see Figure 2.6). This global geometry is the consequence of the interplay between the magnetic energy and the thermal energy of the expanding gas. Once the thermal pressure exceeds the magnetic pressure, the gas

[1]Physically, as there are of yet no magnetic monopoles, the divergence free condition for the magnetic field is always satisfied requiring all field line mappings to be continuous everywhere. The open field lines in actuality either return to the sun, closing hundreds of astronomical units away, or connect to the inter-stellar galactic magnetic field.

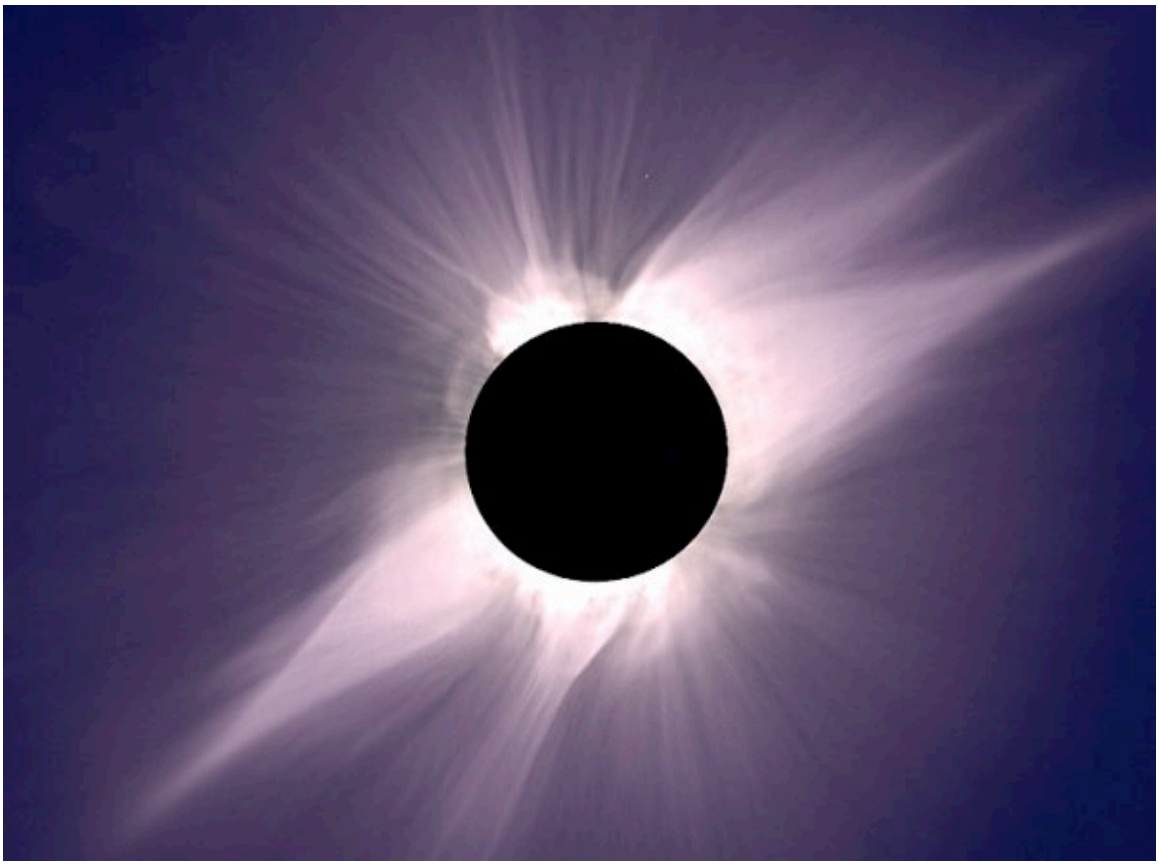

Figure 2.6: The topological structure of the coronal magnetic field configuration is a combination of open and closed flux topologies (S. Albers, High Altitude Observatory, July 11, 1991).

expansion drags the field radially outward. The open and closed flux characterization is a topological distinction, defined by the magnetic field line connections only within the low-beta solar atmosphere. This large-scale solar coronal expansion process is highly dependent on the particulars of the magnetic field strength distribution and the coronal heating mechanism. Traditionally solar researchers have distinguished the corona from the entire solar atmosphere based on this open-closed topological characterization. In other words, for modeling and calculation purposes the solar corona is nicely defined as the low-beta spherical annulus above the photosphere r $\equiv R_{\odot}$, extending out to a solar wind source surface r $\equiv R_{ss}$, where the field becomes effectively radial.

Of the rich variety of coronal field phenomenology, the simplest identifiable features are the low-level, closed loop-like flux of the quiet-sun background, and the open field coronal holes. The solar corona exhibits some semblance of these characteristics consistently throughout the entire magnetic activity cycle; steadily evolving between well-ordered at minimum activity to highly complex at maximum activity. Both the quiet sun and coronal holes have typical field strengths on the order of 10 - 50 G and are, in some sense, the average level of field strength continuously maintained across the entire solar surface, suggesting a lower bound field strength threshold required of the flux emerging from the convection envelope to expand the through the chromosphere into the corona. Both open and closed topologies are inferred from EUV and soft X-ray observations (Figure 2.7). Close examination reveals the quiet-sun background is by no means homogeneous, but rather seems to be filled with small-scale magnetic structures. On the other hand, coronal holes are not directly observed, rather inferred from the dark regions (in X-ray) on the solar disk, indicating lower density and temperature in the plasma. The open field topology provides efficient plasma transport into the solar wind.

Coronal loop characteristics cover a wide range of sizes and field strengths. Larger-scale "active region" loops occur over photospheric sunspots, and are typically filled with relatively hot plasma, bright in both EUV and soft X-ray spectral ranges (Figure 2.7). The thermodynamic conditions of these loops are determined by the coronal heating mechanism, apparently independent of what is happening at the photospheric/chromospheric levels. Typical field strengths are several hundred G. Quiescent active regions have a typical lifetime on the order of several days, perhaps up to a solar rotation period, following the lifetime of the photospheric sunspots below. The energy that powers solar flares and coronal mass ejection (CME) is stored in strong magnetic fields of active regions. A typical solar flare can release energies on the order of 10^{32} ergs in about 10 minutes.

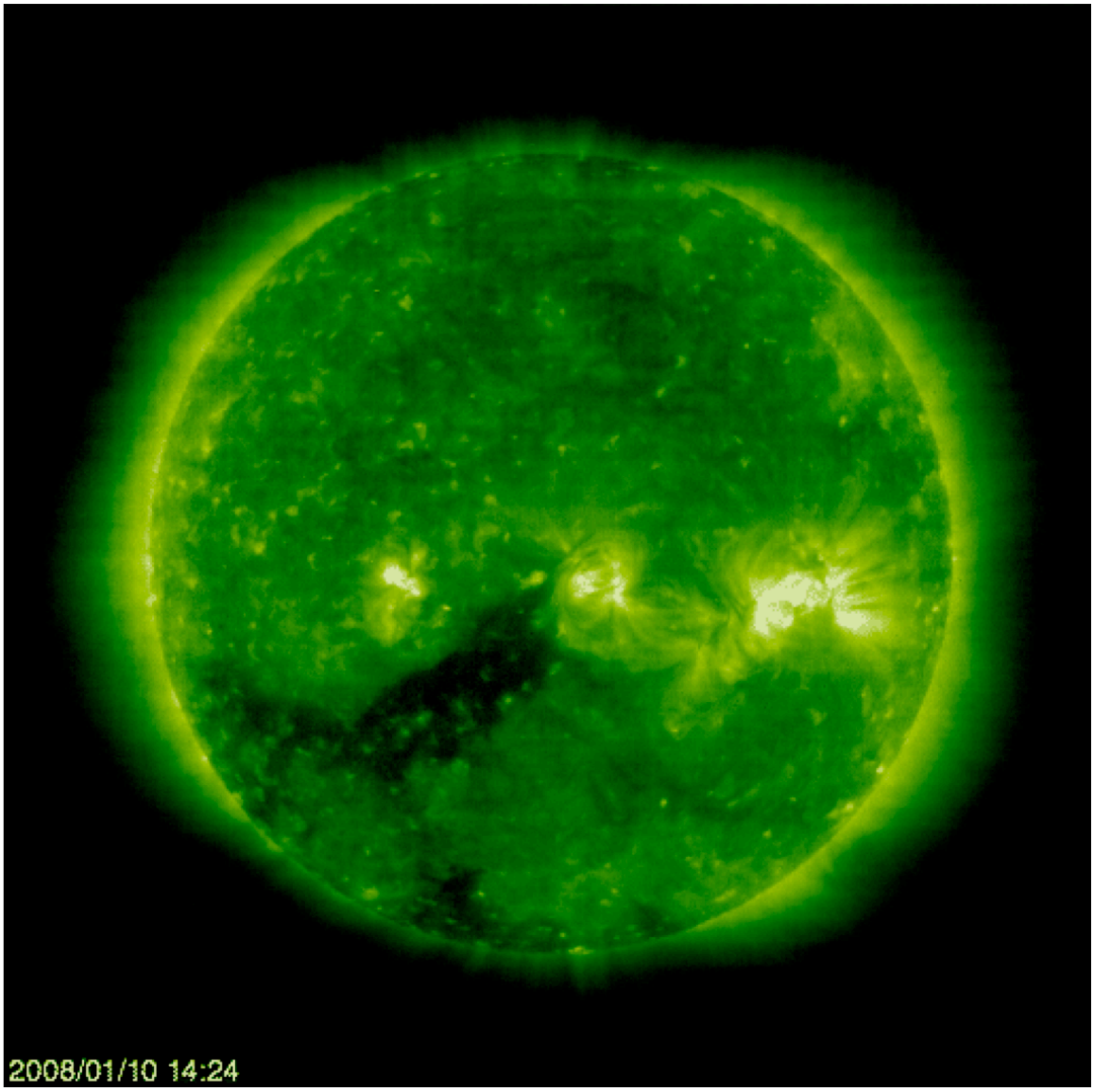

Figure 2.7: Coronal magnetic field phenomenology characterization. "Quiet-Sun" background, bright "Active Region" loops, and dark "Coronal Holes" open flux (SOHO EIT 195 $\mathring{A}$, Jan 10, 2008).

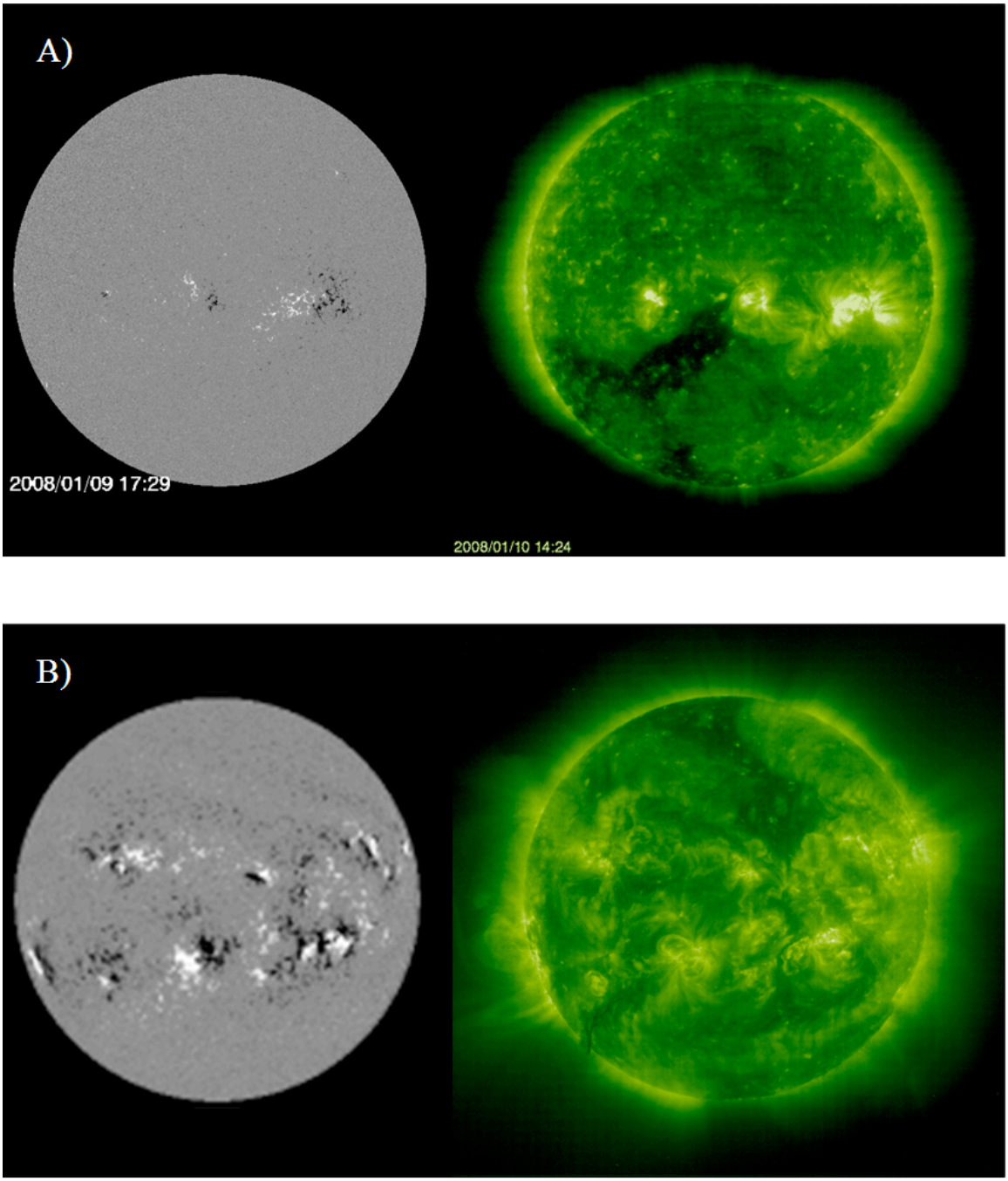

Figure 2.8: The coronal-hole pattern is governed by the photospheric flux distribution following the solar magnetic activity cycle. SOHO; MDI & EIT 195 Å comparison: A) 09-10 Jan 2008, B) 09 Nov 2002

The large-scale coronal magnetic field complexity follows the solar activity cycle, and in general, it is the photospheric flux distribution that governs the coronal hole pattern (see Figure 2.8). To illustrate, during solar minimum coronal holes tend to coalesce at the poles. As the activity cycle progresses, coronal active regions form and dissipate with photospheric sunspots. The strong magnetic fields of active regions distort the coronal hole boundaries, allowing open field corridors to dip into the lower latitudes. With the increased number of sunspots, and by extension active regions, during maximum activity, the coronal field develops an extremely complex, highly dynamic geometric structure.

In a series of seminal papers, Parker predicted the existence of a supersonic solar wind (Parker (1958), Parker (1963)b, Parker (1964)a, Parker (1964)b, Parker (1965), Parker (1966)). The outward flow profile follows from consideration of the radial component of the hydrodynamic equation of motion, continuity, and (for simplicity) an isothermal energy equation (Velli (1994)). The solution to this system can be put into a non-dimensionalized form for the flow Mach number as a function of radial distance from the coronal base at r = R_0,

$$\frac{1}{2}M(r)^2 - \ln P(r) - \frac{gR_0}{r} = \frac{1}{2}M_0^2 - \ln P_0 - g \tag{2.1}$$

Where M_0 and P_0 are the Mach number and pressure at the base of the corona, respectively; g = $\frac{GM_\odot}{R_0 c^2}$ is a non-dimensionalized gravitational constant, and c is the thermodynamic speed of sound. Equation 2.1 is valid for both stellar atmospheric expansion and accretion dynamics (Velli (1994))

The general solutions to this non-linear equation are illustrated by contours in the well known (M, r) phase plane (Figure 2.9). Physical solutions for stellar coronae expansion-flows correspond to single-valued contours initially subsonic ($M_0 < 1$) at the coronal base, and expanding into an inter-stellar medium with a low pressure.

The solution manifold for steady-state outflow subject to these boundary conditions is therefore, the transonic stellar wind curve, and the totally subsonic stellar breeze. Of the separate expansion solutions, only the shocked supersonic stellar wind solution is stable (e.g., Parker (1966), Velli (1994)). Finite inter-stellar pressure requires a termination shock to shift the flow subsonic; only if the inter-stellar pressure is truly zero will the wind remain supersonic to infinity. For a fixed pressure ratio and up-stream (supersonic) Mach number, the Rankine-Hugonoit shock equations determine the down-stream (subsonic) Mach number (shown as the dashed line in Figure 2.9). The position of the termination shock is uniquely determined by the strength of the back pressure and is given by the intersection of the dashed curve with the double-valued region II solutions in Figure 2.9; the separation between the shock and the transonic point decreases with increasing back pressure. Of course, the details vary with actual conditions, but in general the solar winds transonic point is at roughly 2 - 5 solar radii, the supersonic asymptotic flow speed is reached within 30 solar radii, and the termination shock has been measured by the Voyager missions between roughly 80 - 100 AU.

The existence and stability of a shocked supersonic solar wind is a very robust result stemming from the lowest order hydrodynamic analysis. At the next level of complexity, as in the case of the solar internal structure, the effects of rotation and a magnetic field are accounted for. On the whole, the solar wind has a plasma $\beta \geq 1$, as opposed to the very low-beta corona. The transition in the energy partition from magnetic to thermal pressure, takes place around 2.5 - 3 solar radii, at which point the expansion of the gas begins to drag the field lines radially outward, defining the so-called, solar wind source surface (Schatten et al. (1969)). The radial expansion combined with the solar differential rotation profile yields an IMF structure with an Archimedes-spiral geometry. The observations of the IMF polarity structure, while highly organized during solar minimum and can be rather complicated near

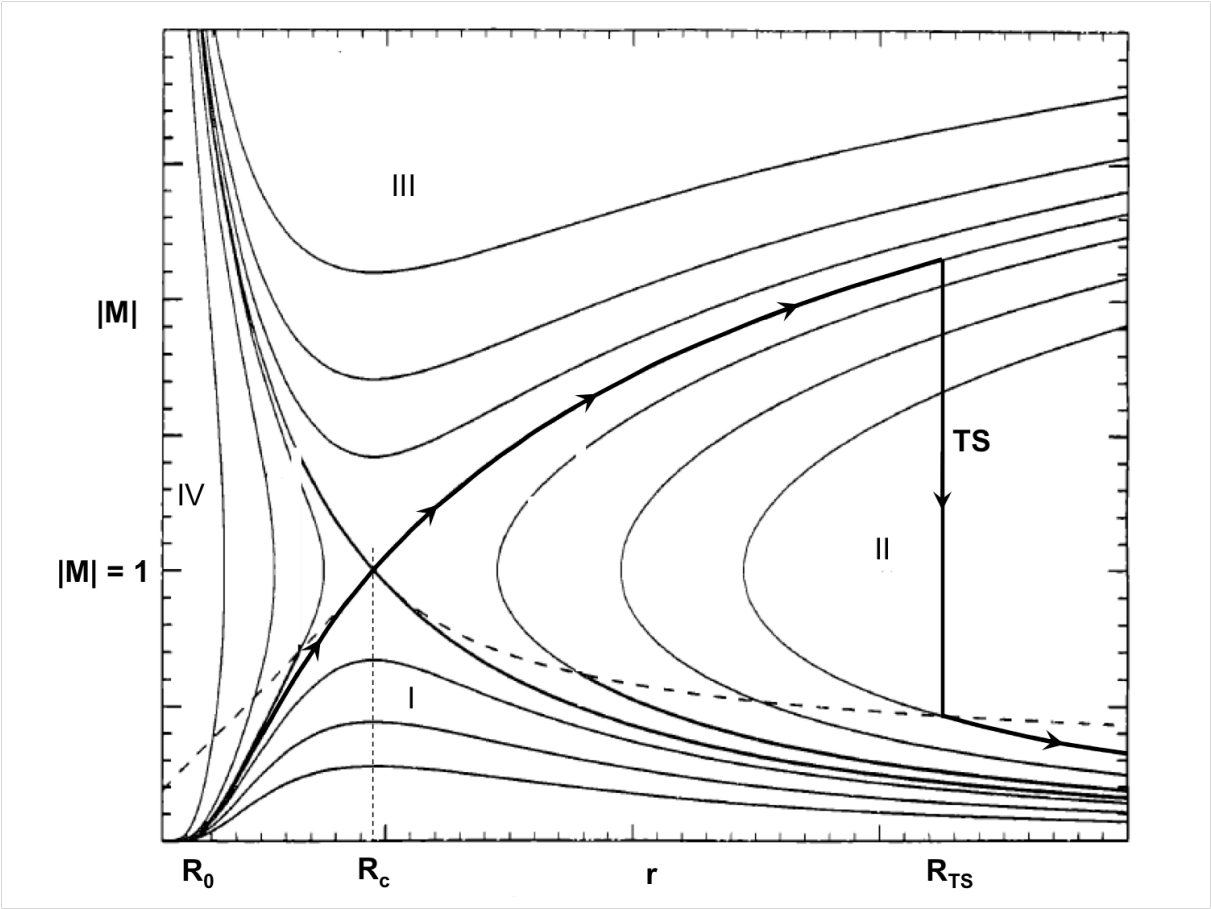

Figure 2.9: The solar wind (M, r) phase plane describing stellar winds, breezes, and accretion. The thick black curve is the physical solution corresponding to solar wind expansion, with a termination shock (TS) connecting the supersonic and subsonic branches of the solution in region II. The dashed line represents the jump condition in flow speed across the shock. (Figure adapted from Velli (1994).)

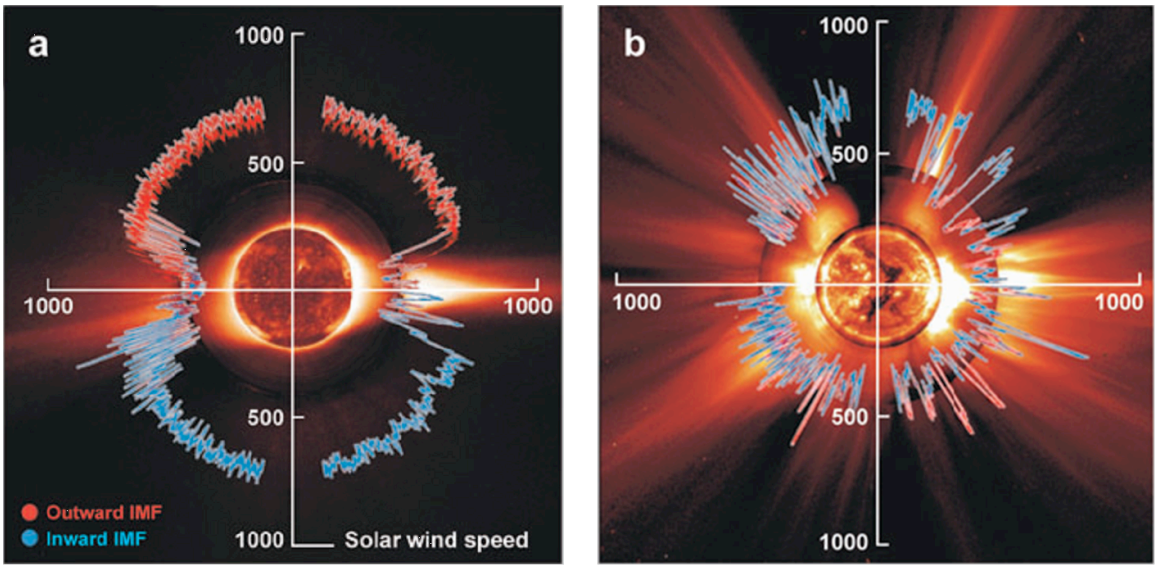

Figure 2.10: Bi-modal solar wind structure and large-scale IMF polarity structure: a) near minimum activity and b) near maximum activity. (McComas et al. (2003))

solar maximum, though are always consistent with a single, global HCS separating the large-scale inward and outward magnetic polarity throughout the entire 11 year sunspot activity cycle (Smith et al. (2001), Jones & Balogh (2003)).

Solar wind plasma observations reveal a fundamentally bi-modal flow profile (Zurbuchen et al. (2000)), the slow and fast wind regimes, which are a direct consequence of the geometric structure of the global solar magnetic field. During the highly organized period near minimum activity, the steady-state slow and fast winds exhibit relatively well ordered, nicely separate profiles (see Figure 2.10a). Observationally, the slow wind consists of transient streams within an approximately 20° envelope about the HCS (Zhao et al. (2009)), and compositionally associated with the topologically closed, streamer-belt regions. The flow speed range is of order 400 - 500 km s^{-1} corresponding to a thermal Mach number greater than 10. The near-Earth kinetic temperature and particle density are of order 10^5 K and typically < 5 particles cm^{-3} respectively (as measured by the Advanced Composition Explorer (ACE) spacecraft orbiting the Lagrangian point L_1). The fast wind is a relatively homogeneous plasma

with composition consistent with coronal holes and therefore associated with topologically open flux. The faster flow speed (600 - 800 km s^{-1}) is a consequence of the plasma's relatively unobstructed coronal escape along open flux lines. Near maximum solar activity the two flow regimes are intermixed across all solar latitudes (see Figure 2.10b).

2.3 Theoretical Global Coronal Magnetic Field Structure

The energy liberation within the thermonuclear core is the source that powers all solar and heliospheric phenomena from the deep interior all the way out to the termination shock. The internal structure of the Sun is characterized by the dominant energy transport mechanisms of radiation and convection. Owing to the highly tenuous nature of the plasma of the solar atmosphere beyond the relatively thin photospheric, chromospheric, and transition region layers, neither radiation nor turbulent convection are efficient means of energy transport. Therefore the magnetic field is the principle conduit that couples the energy of the convective envelope to the solar wind, and is the primary driver of coronal and heliospheric activity. Motivated by the EUV/X-ray observations and by the basic theory of the solar wind given by Parker (1958), a standard model has developed for the large-scale coronal magnetic field, the so-called "quasi-steady" model (e.g., Antiochos et al. (2007)).

The simplest descriptions of the coronal magnetic field that captures the large-scale structures are the so-called potential field source surface (PFSS) models (e.g, Altschuler & Newkirk (1969), Schatten et al. (1969), Hoeksema (1991), Wang & Sheeley (1992)). The PFSS models are based on three underlying assumptions. First, on the largest scales and for specified boundary conditions (typically integrated line-of-sight magnetogram observations of the photospheric normal component, and a purely radial field assumption at the so-called solar wind source surface, around 2.5 - 3 solar radii) the magnetic field energy is a minimum. Second, since the magnetic

field is the dominant physical characteristic throughout the majority of the corona, gas pressure effects can be neglected at the lowest order of approximation. Finally, owing to the fact that the typical Alfvén speed over much of the corona is roughly 10^3 km s^{-1}, orders of magnitude greater than typical driving photospheric flows of 1 km s^{-1}, the coronal field adjusts nearly instantaneously to changes at the photospheric boundary. Thus the evolution may be represented as a time series of stationary, potential field, multipole expansions. The system dynamics are implicitly accounted for by the changes in photospheric flux distribution, and not actually calculated.

Under the minimum energy and instantaneous adjustment assumptions of the PFSS model, no currents develop in the corona. Mathematically, the vector magnetic-field is taken to be everywhere curl-free, and therefore the equations of non-relativistic magnetostatics reduce to a simple elliptic boundary value problem. Combining the curl-free and divergence-free conditions, the magnetic field may be described as the gradient of a potential function satisfying Laplace's Equation (2.2),

$$\nabla^2 \Phi = 0 \tag{2.2}$$

In the corona, the natural representation of this equation is in spherical coordinates $\{ (r, \theta, \phi) \mid r \in [R_\odot, R_{ss}] , \theta \in [0, \pi] , \phi \in [0, 2\pi) \}$. The general solution is given by a spherical harmonic basis expansion,

$$\Phi(r, \theta, \phi) = \sum_{l=0}^{\infty} \sum_{m=-l}^{l} \left[A_{lm} r^l + B_{lm} r^{-(l+1)} \right] Y_l^m (\theta, \phi) \tag{2.3}$$

Since the coordinate domain is a spherical-annulus between the photosphere $R_\odot$ and a solar wind source surface R_{ss}, both radial factors must be included. At the lower boundary, $r = R_\odot$, the field is given by the photospheric normal flux distribution, and at the upper-boundary, $r = R_{ss}$, the field is assumed radial. The angular coordinates $\{\theta, \phi\}$ are respectively the co-latitude and longitude.

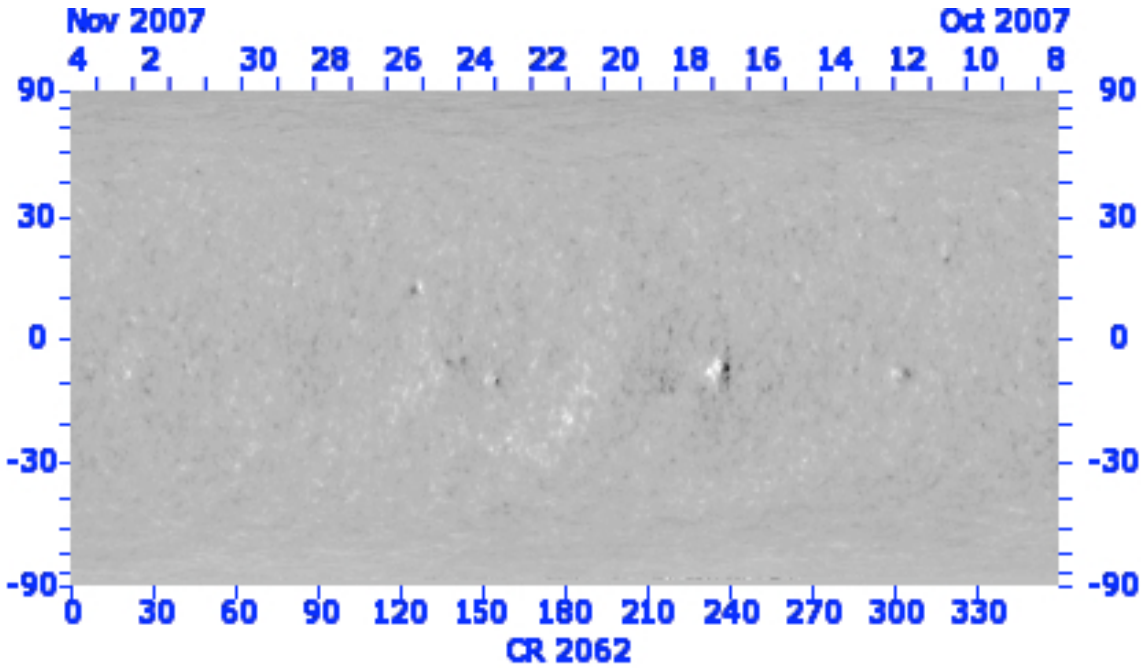

Figure 2.11: Magnetogram synoptic map for Carrington Rotation 2062: Oct - Nov 2007

The normal magnetic field distribution at the $r = R_{\odot}$ boundary is related to the potential by,

$$\left.\frac{\partial \Phi}{\partial r}\right|_{(r=R_{\odot},\theta,\phi)} = g\left(\theta,\phi\right), \tag{2.4}$$

where, the $g\left(\theta,\phi\right)$ distribution is found empirically from photospheric magnetogram observations (e.g., SOHO MDI experiment, see Figure 2.11).

In order to assure a purely radial field at the $r = R_{ss}$ boundary, the potential function along that surface must be a constant. Making use of the gauge freedom to choose the value of the potential field in order to simplify the analysis, the $r = R_{ss}$ boundary condition is,

$$\Phi(r = R_{ss}, \theta, \phi) = 0 \tag{2.5}$$

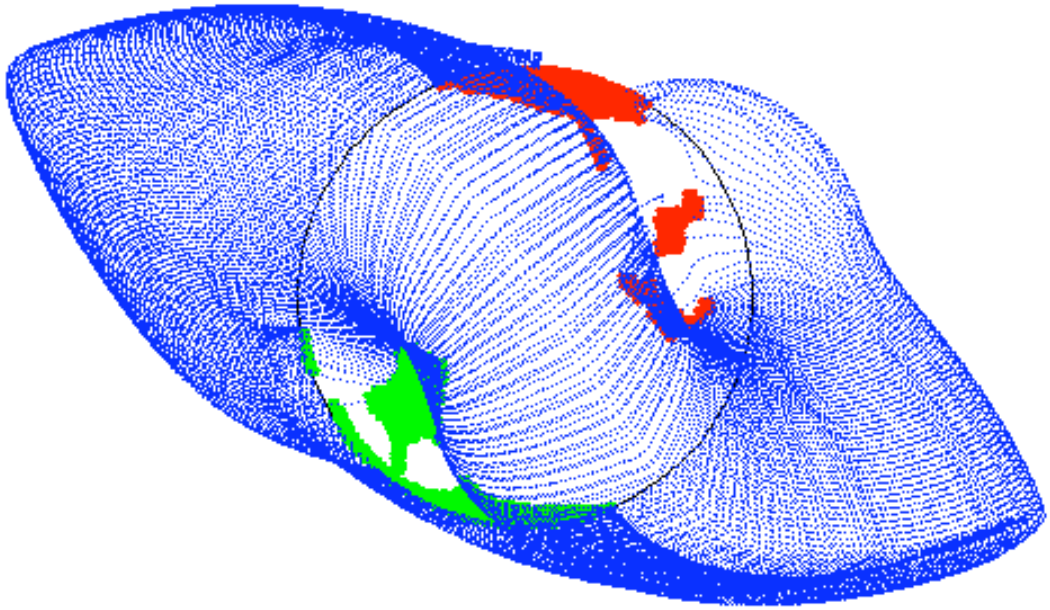

Figure 2.12: PFSS model magnetic field structure corresponding to the magnetogram synoptic map for Carrington Rotation 2062: Oct - Nov 2007. The streamer belt magnetic field is shown in blue. Coronal holes of opposite polarity are shown in red and green. The HCS follows the streamer belt cusp at 2.5 solar radii. (Figure calculated from the PFSS model, Community Coordinated Modeling Center, NASA Goddard Space Flight Center.)

Applying the two boundary conditions (2.4) and (2.5), the general expansion for the magnetic potential can be written as,

$$\Phi(r,\theta,\phi) = R_{\odot} \sum_{l=0}^{\infty} \sum_{m=-l}^{l} A_{lm} \left(\frac{R_{\odot}}{r}\right)^{l+1} \left[\frac{r^{2l+1} - R_{ss}^{2l+1}}{lR_{\odot}^{2l+1} + (l+1)\,R_{ss}^{2l+1}}\right] Y_l^m(\theta,\phi) \quad (2.6)$$

Where the constant factors A_{lm} are given by,

$$A_{lm} = \int_{\Omega} g(\theta,\phi)\; Y_l^m(\theta,\phi)^*\, d\Omega \quad (2.7)$$

Solar researchers typically apply some variation of equation (2.6) to compute the coronal magnetic field. To a first approximation, these models tend to be very robust when predicting and describing the large-scale poperties of the coronal field, capturing the largest-scale structures (i.e., the streamer belt and coronal holes) in its lowest-order moments (see Figure 2.12). As well, PFSS models do very well in predicting the position of the HCS, and polarity of the global field.

Over the last decade, sophisticated MHD codes have been developed to include both the magnetic field stresses and the gas pressure in the steady-state force balance. The MHD codes solve the standard continuity (2.8) and momentum (2.9) equations coupled to Maxwells equations (2.10 - 2.11) and Ohms Law (2.12) (provided in cgs units),

$$\frac{\partial \rho}{\partial t} + \nabla \cdot (\rho \boldsymbol{v}) = 0 \quad (2.8)$$

$$\frac{\partial \rho \boldsymbol{v}}{\partial t} + \nabla \cdot (\rho \boldsymbol{v}\boldsymbol{v}) = \frac{1}{4\pi}\boldsymbol{J} \times \boldsymbol{B} - \nabla P + \rho \boldsymbol{g} + \nabla \cdot (\nu \rho \nabla \boldsymbol{v}) \quad (2.9)$$

$$\nabla \times \boldsymbol{B} = \frac{4\pi}{c}\boldsymbol{J} \quad (2.10)$$

$$\nabla \times \boldsymbol{E} + \frac{1}{c}\frac{\partial \boldsymbol{B}}{\partial t} = 0 \tag{2.11}$$

$$\boldsymbol{E} + \frac{1}{c}\boldsymbol{v} \times \boldsymbol{B} = \frac{1}{\sigma}\boldsymbol{J} \tag{2.12}$$

Where $\boldsymbol{v}$, $\boldsymbol{B}$, $\boldsymbol{E}$, and $\boldsymbol{J}$ are the plasma velocity, magnetic and electric fields, and current density respectively. ρ is plasma mass density, P is the plasma thermal pressure, and $\boldsymbol{g}$ is the acceleration due to gravity. ν and σ are transport coefficients of kinematic viscosity and plasma conductivity, respectively.

To close this set of equations, a specific form of the energy equation must be assumed. Often the equation for internal energy conservation (2.13) is employed,

$$\frac{\partial U}{\partial t} + \nabla \cdot (U\boldsymbol{v}) + P\nabla \cdot \boldsymbol{v} = \frac{1}{(\gamma - 1)}S \tag{2.13}$$

where U = $\frac{P}{(\gamma-1)}$, and γ is the ratio of specific heats. Energy sources (and sinks) such as conduction and radiation can be generically represented by S. Note, if S = 0, this equation reduces to the adiabatic energy equation. Finally, a thermodynamic equation of state is required to close the system, usually taken to be the ideal gas law (2.14) in the solar atmosphere,

$$P = \left(\frac{\rho}{m}\right) kT \tag{2.14}$$

where k is the Boltzmann constant, T is the temperature, and m is the proton mass.

MHD equilibrium codes require a magnetic field structure, and in most cases simply use the PFSS calculation as the initial global magnetic field given by the photospheric boundary conditions at each time step. The field is given at each point in time by the same integrated line-of-sight magnetogram observations for the initial inner boundary condition, but the radial field source surface outer-boundary requirement is

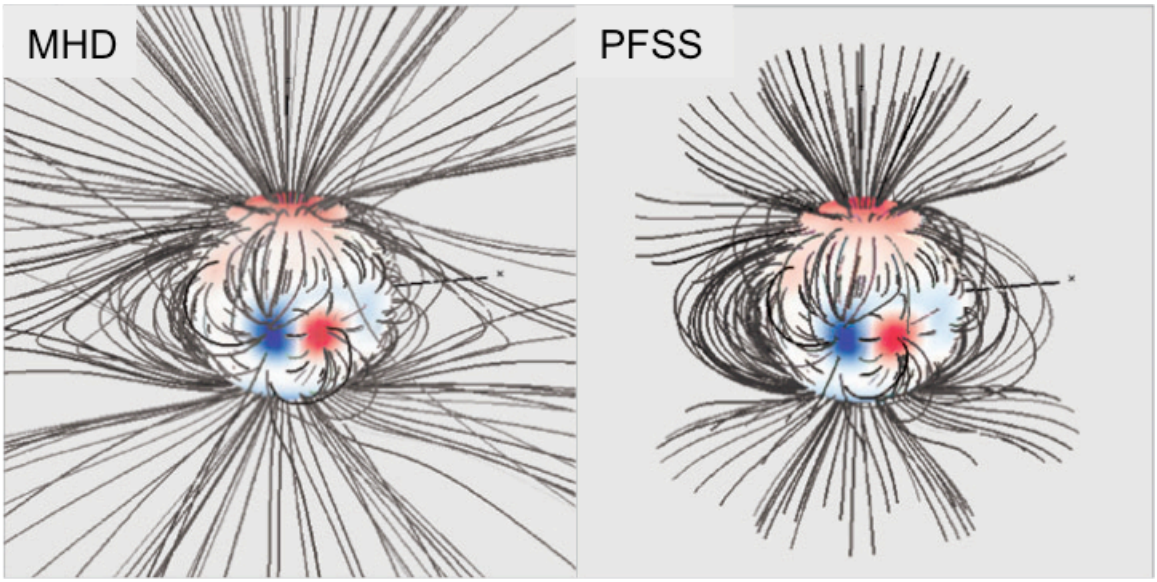

Figure 2.13: MHD-PFSS solution comparison of the global coronal field for Carrington Rotation 1910. Left, MHD equilibrium solution. Right, PFSS solution. (adapted from Zurbuchen (2007))

dropped, and the system is allowed to relax as it would accounting for thermal effects. Relative to the PFSS structure, MHD equilibrium includes inherent thermodynamic effects that tend to become pronounced, such as smoothing of cusp geometries and extending the large-scale structures in the outer corona (see Figure 2.13). In addition, non-dissipative current systems may develop in response to the relaxation, leading to a series of force-free (i.e., the currents are everywhere parallel to the magnetic field) equilibrium states. This MHD equilibrium relaxation process is highly dependent on the details of the magnetic field configuration and the coronal heating mechanism. Still, the force-free MHD equilibrium models are generally a good approximation for stationary state evolutions, again justified by characteristic dynamic time-scales much longer than the average Alfvén travel time.

These sophisticated MHD codes do have the capability to calculate fully-dynamic, time development scenarios that include the effect of driving flow fields. Modern codes such as the Adaptively Refined Magnetohydrodynamic Solver (ARMS) (Welsch et

al. (2005), DeVore & Antiochos (2008), Lynch et al. (2008), Lynch et al. (2009), Pariat et al. (2009)), the Predictive Sciences, Inc. solar corona MHD model (Mikić et al. (1999), Linker et al. (2003), Riley et al. (2003), Lionello et al. (1999)), the Berkeley Space Science Laboratory codes RADMHD (Abbett (2007)) and ANMHD (Abbett et al. (2000), Abbett et al. (2001)), and the University of Michigan code BATSRUS (Powell et al. (1999), Gombosi et al. (2000), Groth et al. (2000), Roussev et al. (2003)), with appropriate initial magnetic field geometry and boundary flows, can simulate full system evolutions within the described MHD framework, including the development of dissipative current sheets. But these codes still require specific and heuristic assumptions regarding the energy transport coefficients and heating function to close the equations. Presently, the major drawback of these fully dynamic calculations is their tremendous computational expense. Furthermore, a rigorous time-dependent coronal environment model would require robust treatment of flux emergence and cancellation, which is not yet available.

The described PFSS and MHD equilibrium time-series of stationary solutions constitute the standard quasi-steady description of the coronal magnetic field. All in all, these quasi-steady models tend to be very robust when describing the large-scale properties (i.e., the polarity and geometric structure) and evolution of the coronal magnetic field. For a given photospheric normal flux distribution, they predict a quiet-sun, large-scale dipolar magnetic field topology with closed field loop regions, clearly separate from the open field coronal hole regions. They capture the largest-scale topological structures of the streamer-belt, active regions, and coronal-hole patterns. As well, they predict a single global HCS at the source surface where the thermal energy of the solar wind exceeds the magnetic energy of the coronal field and proceeds to drag the field lines radially outward. Though the specifics of the dynamic evolution are not calculated, implicit in these models is a continuous field line reconnection process opening-up and closing-down of the magnetic field at the source surface driven

by changes in the photospheric flux distribution (and assumed heating functions). Concisely, the dynamics under the quasi-steady assumption are totally governed by changes in the photospheric flux distribution; no change in the photospheric normal flux distribution implies a static global magnetic field structure.

The force-free evolution of the quasi-steady regime is implicitly justified for a couple of reasons. First, as stated before, the large difference in timescales between the driving flows and the Alfvén speed, allows the field to adjust nearly instantaneously to energy injection. Second, from a phenomenological perspective, the large-scale structures become pronounced with the first few moments in the potential field expansion. More important though, since only a singular current may represent a true discontinuity in the magnetic stress tensor (i.e., current system such that the length scale is small enough for substantial dissipation), the minimum energy force-free field implies an everywhere smooth field condition (Antiochos et al. (2007)):

Smoothness Condition. In the absence of singular currents, magnetic field lines can split only at locations where the field vanishes, such as true null points (Figure 2.14).

In the absence of long-lived singular current dissipation systems and building upon this smoothness condition, Antiochos et al. (2007) identified very powerful restrictions on the allowable geometric and topological structure of the coronal magnetic field, and are listed below:

Uniqueness Conjecture. Every unipolar region on the photosphere can contain at most one coronal hole (Figure 2.15).

Nested Conjecture. Coronal holes of nested polarity region must themselves be nested.

Nested Corollary. Any coronal hole that opens inside a nested polarity must encompass the spine.

PIL Lemma. A coronal hole boundary cannot intersect a polarity inversion line.

Nested Lemma. A nested polarity region must be surrounded by either all open or all closed field (Figure 2.16).

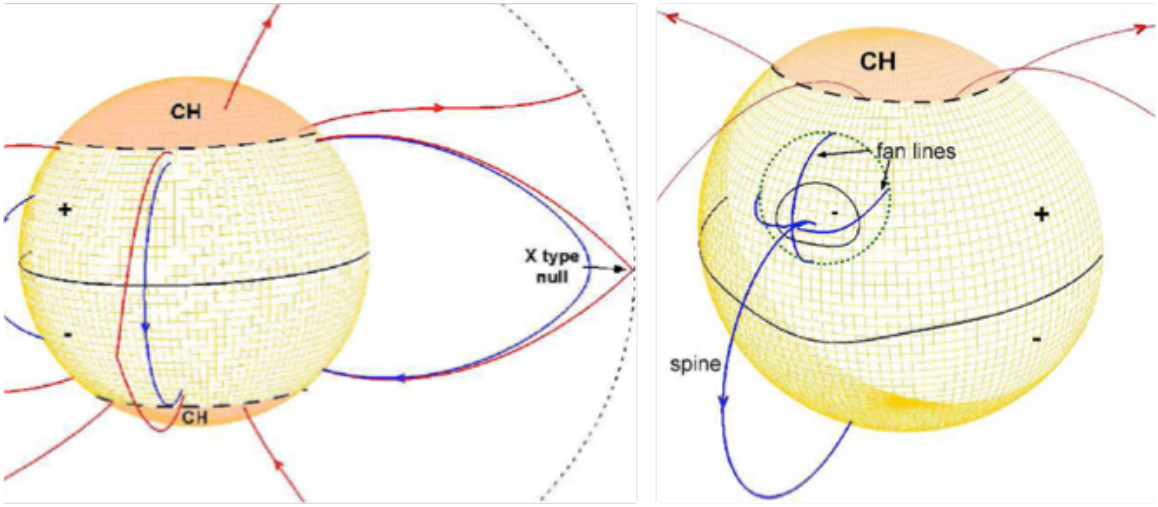

Figure 2.14: Smoothness Condition. Left: Large-scale coronal background field is smooth and continuous. The closed flux region (blue field lines) maps across the equatorial PIL, while the open flux (red field lines) do not map back to the surface. Right: The topological frame (spine and fan field lines) required by the appearance of a 3D null point in the corona that accompanies a PIL on the photosphere. (adapted from Antiochos et al. (2007))

Two points of note are in order here. First, if long-lived current dissipation systems are included, the coronal magnetic field structure is not governed by these theorems, and may sustain any geometric configuration. Second, in the absence of creation and/or annihilation of magnetic null points, fully-dynamic MHD evolutions will preserve initially separate magnetic domains, defined by the topological field line connections. Thus, in the quasi-steady models as well as under dynamic MHD evolution the smoothness condition is preserved even in the presence of transient current sheet discontinuities.

In addition to capturing the observed distribution of coronal holes on the Sun, the quasi-steady models are fairly accurate in reproducing in situ measurements of the steady-state fast solar wind plasma and IMF structure (e.g., Zurbuchen (2007), Lepri et al. (2008)). Furthermore, the dynamics implicit in the model are in qualitative agreement with coronal plasma observations. The observation of plasma inflows and

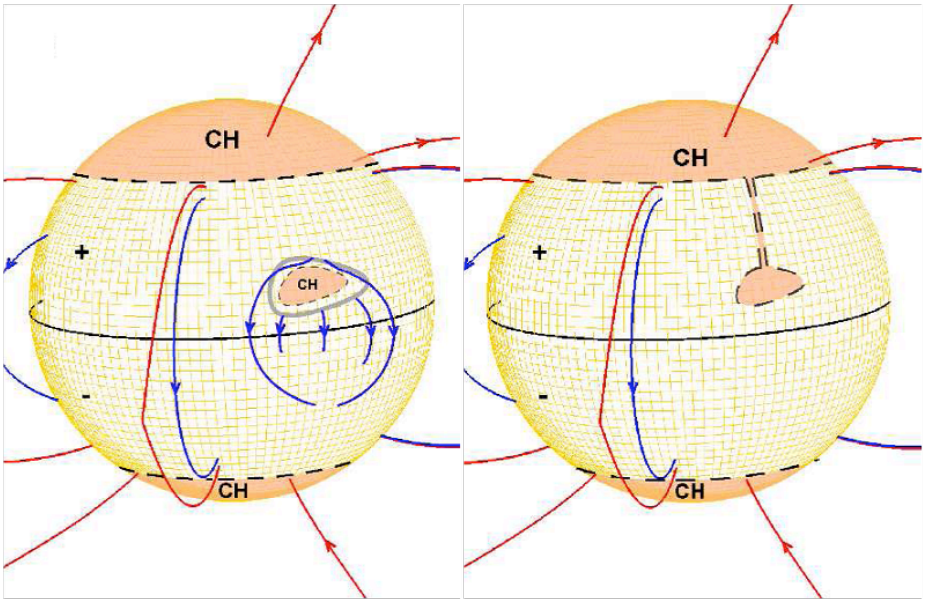

Figure 2.15: Uniqueness Conjecture. Left: Configuration requires the closed flux to the north of the disconnected coronal hole to split, closing across the equatorial polarity inversion line. Such a configuration requires a null-line or a long lived singular current. Right: Open flux corridor connecting the disconnected coronal hole to the main polar coronal hole, satisfying the Smoothness Condition (adapted from Antiochos et al. (2007))

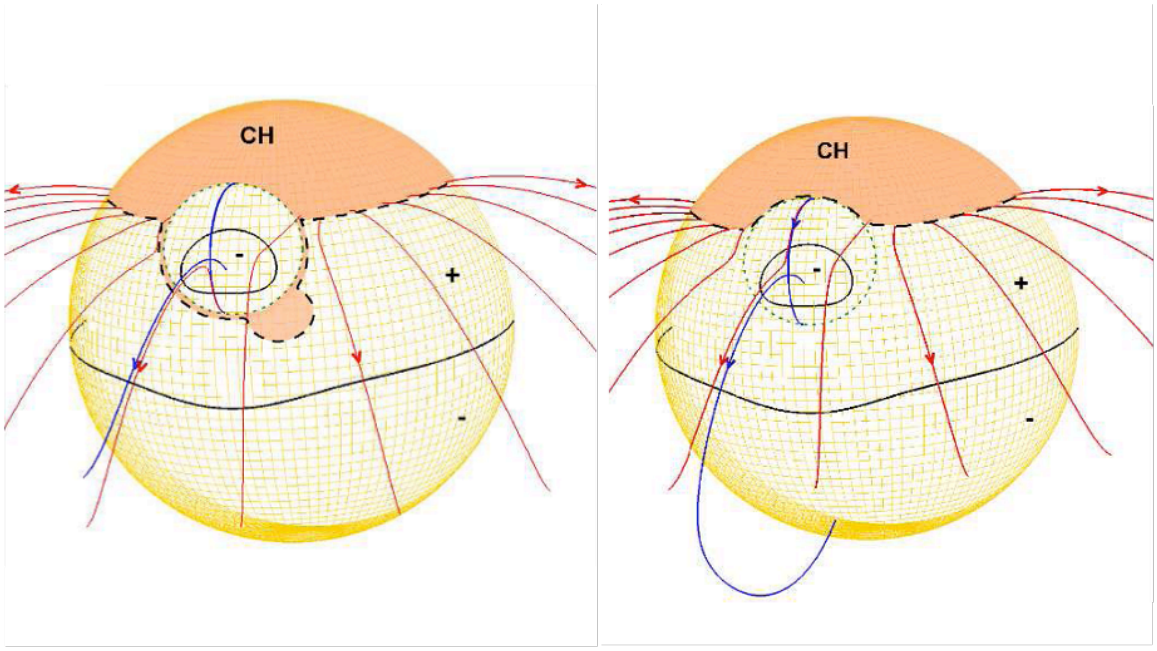

Figure 2.16: Nested Lemma. Left: A polarity region nested within the open field. Right: A polarity region nested within the closed field (adapted from Antiochos et al. (2007))

outflows, (e.g., Hundhausen et al. (1984), Howard et al. (1985), Sheeley & Wang (2002)), the observation of quasi-rigid rotation of coronal holes, and the existence of the highly variable slow wind suggest continuous opening and closing down of flux at the HCS, as predicted by the model.

There are several heliospheric observations, however, that appears to be in direct conflict with the quasi-steady models. One observation in particular is the measurement of electron heat flux in the solar wind. In order to close down heliospheric flux, reconnection between open field lines must occur at an altitude below the Alfvén point, where the magnetic energy still exceeds the thermal energy. Such a reconnection will create two loops: one having both foot points anchored to the solar surface remaining below the Alfvén point, and the other - an inverted-loop - entirely detached from the Sun and dragged away with the solar wind (see Figure 2.17 left). It is exactly this type of reconnection process that is implied by coronal observations of the streamer belt evolution. Conversely, the opening of previously closed flux requires that a loop expand into the heliosphere and be dragged outward by the wind (see Figure 2.17 right).

It has long been recognized that such processes should produce a signature in the field-aligned suprathermal electron beams ($\sim$70 eV to several keV) in the heliosphere (Gosling (1990)). Streaming electrons directed away from the hot corona, indicate open flux attached at a single foot point. Field lines with both foot points anchored in the solar surface and dragged into the heliosphere by the solar wind would exhibit bi-directional, counter-streaming electrons. On the other hand, inverted-loops would be devoid of these suprathermal electron beams altogether, a so-called heat flux dropout. Thus, the suprathermal electrons provide a local measure of the global field-line field topology, and as such, are a predictive indicator of flux opening and closing. The key inconsistency between heliospheric observations and the quasi-steady model is that bi-directional electron beams and heat-flux dropouts in the solar wind are rarely

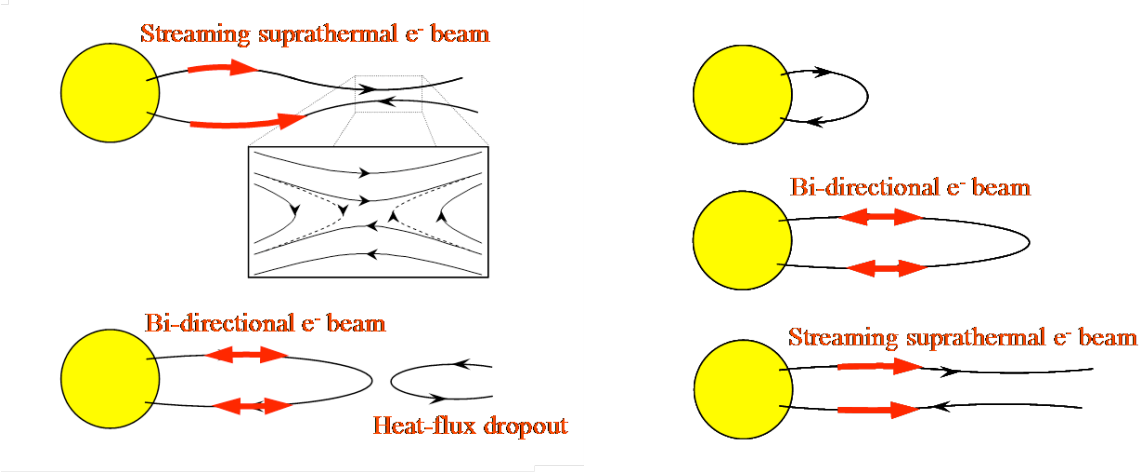

Figure 2.17: Electron heat flux and IMF topology schematic depicting the suprathermal e^- fieldline topology tracers for the reconnection process at the HCS implied by the quasi-steady models. Left: Reconnection below the Alfvén point generating a heat flux dropout in the solar wind. Right: Bi-directional solar wind heat flux generation by fieldline dragging into the solar wind.

observed outside interplanetary CME's (McComas et al. (1989), McComas et al. (1991), Lin & Kahler (1992), Pagel et al. (2005)).

Motivated by these in situ electron observations which imply negligible field line opening or closing, along with energetic particle observations that imply field line wandering across large a latitudinal extent in the heliosphere, and an approximately constant open flux in the heliosphere, Fisk and co-workers have proposed an alternative theory for the solar/heliospheric magnetic field (see Figure 2.18): the interchange model (Fisk et al. (1999), Fisk & Schwadron (2001), Fisk (2005), Fisk & Zurbuchen (2006)). In this model the basic assumption is that the heliospheric open flux is held constant throughout the solar cycle, except for the transient flux of CME's. This assumption appears to be well supported by observations, which show only small variation from cycle to cycle in the total heliospheric flux at solar minimum when the effect of CME's can be accurately removed from the heliospheric data. Note, however, that the observations for the latest minimum, cycle 23, seem to lower the minimum

heliospheric open flux threshold, and may contradict the constant-flux assumption altogether (Fisk & Zhao (2009)).

The basic manner in which the open field evolves in the interchange model is by diffusive transport of the open field component of the coronal magnetic field. The dominant process determining the open-field's evolution is the so-called interchange reconnection between the open and closed flux, which always conserves the amount of each type (e.g., Crooker et al. (2002)). The working mechanism of this model exploits the ubiquitous, rapidly varying, small-scale emergence and subductance of closed magnetic carpet flux, which typically occurs over such short time scales that it is neglected by the quasi-steady models. Effectively, magnetic carpet loops emerge into the corona and come into contact with oppositely directed open field lines. Interchange reconnection exchanges field line identities, swaps foot points, and allows the open flux to execute a random walk, with an average large-scale circulation pattern across the corona (see Figure 2.19).

This diffusive motion leads to a magnetic topology consisting of a complex mixture of open and closed field; in other words, disconnected coronal holes within the loop regions. The important point here lies in the assumption that the continuous emergence of the magnetic carpet flux generates an effective current dissipation layer over the entire closed flux region of the solar surface, and as such allows the diffusing open field lines to thread through this forest of randomly oriented loops.

Mathematically, the interchange model is governed by a diffusion-convection equation (2.15) in which the open magnetic field component is treated as an effective surface density of uniquely defined open field lines that evolve independently of the surrounding field.

$$\frac{\partial B_o}{\partial t} = \nabla^2 \left(\kappa B_o\right) - \nabla \cdot \left(\boldsymbol{u} B_o\right) \tag{2.15}$$

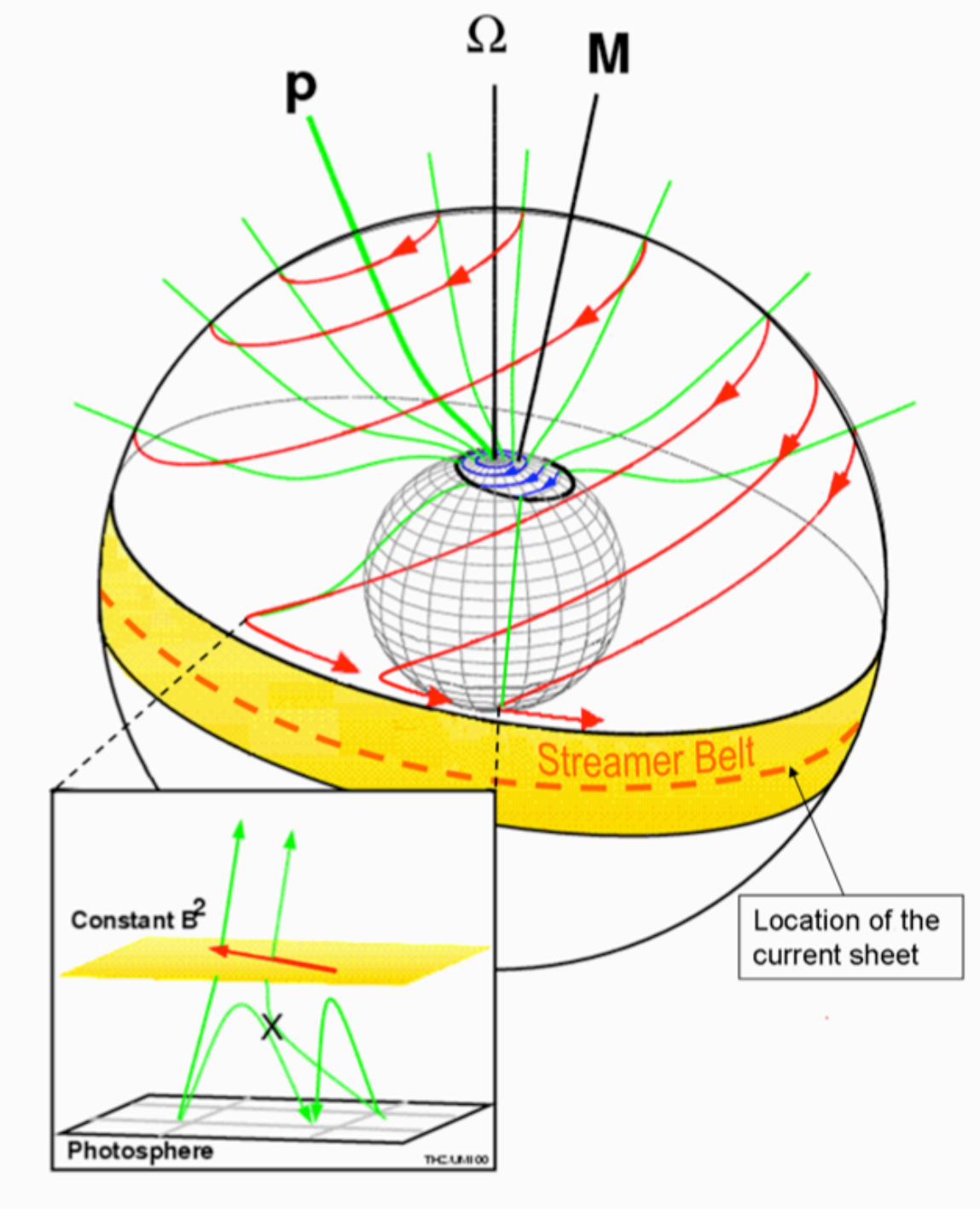

Figure 2.18: The global open flux evolution of the interchange model is by diffusive surface transport. (Note, this figure has been updated from the Fisk et al. (1999) reference, to reflect proper topological interaction of the open and closed flux at the streamer belt boundary.)

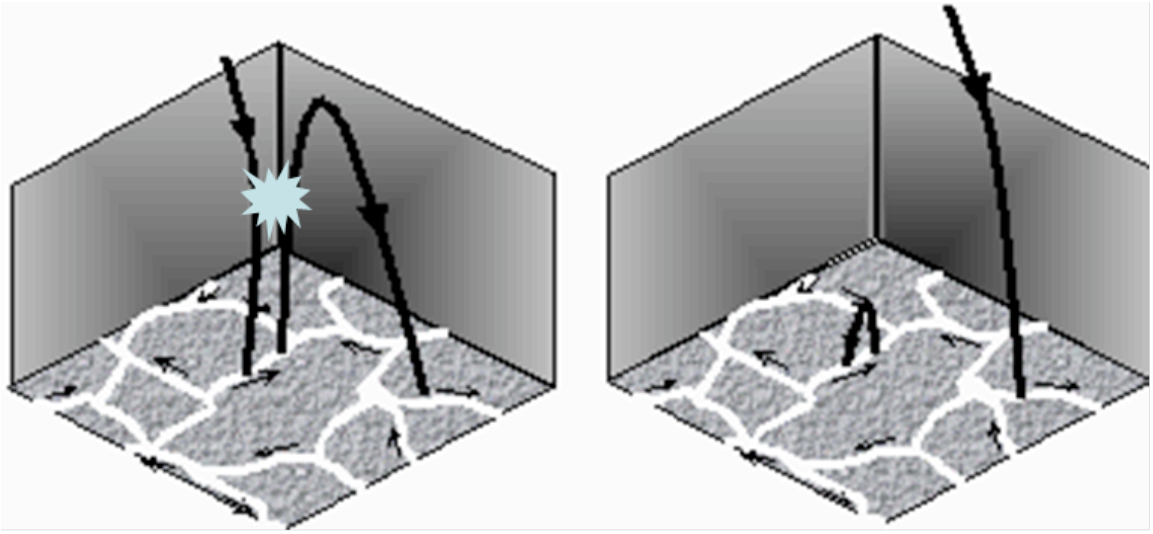

Figure 2.19: Local evolution mechanism for the interchange model schematically depicting the random walk of the open field line as a consequence of interchange reconnection with small carpet loops. (Fisk (2005))

where B_o is the open component of the magnetic field, and $\boldsymbol{u}$ is the horizontal component of the driving velocity field. The interchange reconnection mechanism is captured in the diffusion coefficient $\kappa = \frac{(\delta h)^2}{2\delta t}$, by assuming the field lines exchange identities, and the respective foot point of the open field line jumps a distance δh, the separation of the loop foot points.

This media diffusion equation can be derived from the magnetic induction equation under a quasi-linear approximation (Fisk & Schwadron (2001)), and is appropriate for cases in which systematic convective motions, such as differential rotation, meridional flow, and granular convections of an external medium, are responsible for the diffusion process (Parker (1963)a). The global solution predicts open flux accumulation in regions where the rate of loop emergence is a local minimum, offering an effective self-consistent coronal hole formation theory. Secondarily, this process also offers a route in which small closed loops may coalesce into larger loops. Thus, in some sense, the interchange model on the whole offers a viable explanation regarding the how a given global coronal magnetic field configuration develops; an important aspect

the quasi-steady models are wholly unconcerned with. In addition, the interchange model naturally predicts a slow wind with closed loop plasma properties. The model rationalizes why the heliospheric flux has an approximately constant lower bound throughout the activity cycle.

It should be emphasized that the reconnection postulated by the interchange model is quite different than that in the quasi-steady model. In the latter, reconnection occurs primarily at the HCS, because that is where open field lines close down. Although field line opening does not require reconnection, the opening often involves the ejection of a plasmoid from the top of a streamer, which implies reconnection again at a newly-formed HCS. Reconnection in the interchange model, on the other hand is statistical in nature, and occurs primarily between open flux and the closed flux of coronal loops leading to a diffusive motion of open field in the low corona. The open field is derived to mix indiscriminately with the closed, throughout the corona, so that reconnection between open and coronal-loop field occurs continuously. The interchange model, therefore, postulates a very different magnetic topology than the well-separated open and closed topology of the quasi-steady. For the interchange model to be valid the open-field topology must be discontinuous (i.e., disconnected coronal holes) and inherently dynamic, whereas for the quasi-steady to hold, the topology must remain continuous throughout any coronal-field evolution. We conclude that these topological differences are a strong discriminator between the two models of the open field.

CHAPTER III

Magnetic Field Structure and Dynamics

Within the low-beta solar corona, it is the magnetic field that transmits the forces between fluid regions. These forces can propel CME's, drive solar flares, and are responsible for key aspects of coronal activity. Powered by the convective flows at the photosphere, the storage and transmission of field stresses determine the field geometry across all spatial scales. The evolution of the coronal magnetic field on timescales faster than resistive diffusion depends on the dynamical processes of current sheet formation, stability, and reconnection physics. In this chapter, we review the structure and dynamics of the magnetic field. In section 3.1 we derive the magnetic stress tensor from first principles, and place the structure of the magnetic field in the context of topologically well-separated magnetic domains. Section 3.2 contains a description of the 3D null-point structure associated with the 2-flux, embedded bipole system, likely the simplest and most common magnetic configuration in the solar corona. In section 3.3, we review the theory of current sheet formation, generalizing the 2D formulation of Syrovatskii to 3D. As well, we examine the physics of the resistive instabilities, with a focus on the tearing mode which is the reconnection initiation mechanism. In the last section 3.4, we discuss field relaxation in terms of the Sweet-Parker and Petchek reconnection mechanisms. Finally, we show that helicity constraints require the final configuration of the global magnetic field on

timescales much smaller than the resistive dissipation time to be force-free.

3.1 Structure of the Magnetic Field in 3-Dimensions

Fundamentally, the stress-energy storage and transport within the coronal magnetic field is influenced by field line connectivity. Recall the phenomenological structure of the coronal magnetic field geometry characterized by two fundamentally distinct topologies: the open and the closed flux (see chapter II, section 2.2). The key difference between the separate topologies is that the closed lines can contain long-lived stress (i.e., currents given by relation 2.10) whereas the open lines must be stress-free on time scales long compared to the scale of transients. Closed field lines, by definition, have both ends anchored in the photosphere and thus they maintain the stresses exerted by the gas. Open field lines, on the other hand, have only one end line-tied while the other is at infinity, so that any stress injected by photospheric motions will propagate into the heliosphere. Thus, in general coronal magnetic field evolution is nicely understood when described in terms of multi-polar nested flux domains, which find a natural representation in terms of the magnetic field stress tensor.

The magnetic field stress tensor is directly derivable from the Lorentz force in the frame of the plasma,

$$\boldsymbol{F} = q\boldsymbol{E} + \frac{1}{c}\boldsymbol{J} \times \boldsymbol{B} \tag{3.1}$$

Using Gausss Law and the full Ampere-Maxwell equation to eliminate the charge and current densities, q and $\boldsymbol{J}$, this force equation may be readily derived from the 4-divergence (metric signature = +2) of an electromagnetic field stress-energy tensor,

$$F_i = \frac{\partial}{\partial x_j}\left(M_{ij}\right) - \frac{1}{c}\frac{\partial}{\partial t}\left(\frac{Q_i}{c}\right) \tag{3.2}$$

The stresses transmitted through the electromagnetic field are given by the Maxwell tensor,

$$M_{ij} = \frac{1}{4\pi}\left(E_i E_j + B_i B_j\right) - \frac{1}{8\pi}\left(E^2 + B^2\right)\delta_{ij} \tag{3.3}$$

Physically, the full electromagnetic stress-energy tensor M_{ij} represents the Lorentz force per unit area exerted in the i-th direction, on an area with normal in the j-th direction. In other words, the force exerted ***by*** the field on the positive side of the area, ***on*** the field on the negative side of the area. The orientation sign convention is such that the tension is positive and the pressure is negative. Thus, the first terms on the right hand side (RHS) of equation (3.3) represent the tension along the electric and magnetic field lines, while the second terms can be interpreted as isotropic field pressure forces.

The momentum density contained in the electromagnetic field is $\frac{Q_i}{c^2}$, where $\boldsymbol{Q}$ is the Poynting vector,

$$\boldsymbol{Q} = \frac{c}{4\pi}\boldsymbol{E} \times \boldsymbol{B} \tag{3.4}$$

The electromagnetic momentum density $\frac{Q_i}{c^2}$ term may be neglected with respect to the momentum density of the plasma fluid ρv_i. For non-relativistic fluids the unbalanced dynamical pressures are at best comparable to the magnetic pressure, and the ratio of these two terms is of order $\frac{v_A^2}{c^2}$ where v_A is the Alfvén speed.

For a highly conductive ($\eta << 1$), non-relativistic fluid (v << c), as in the solar corona, comparison of the terms in Ohm's Law $\left|\frac{E_0}{B_0}\right| \sim \left|\frac{v}{c}\right|$, show the electric field terms are everywhere smaller than the magnetic terms by a factor of $\frac{v}{c}$, and therefore the electric field terms may be neglected. Thus the Maxwell tensor (3.3) reduces to,

$$M_{ij} \approx \frac{B_i B_j}{4\pi} - \frac{B^2}{8\pi}\delta_{ij} \tag{3.5}$$

The physical interpretation of the magnetic stress tensor is exactly the same as the Maxwell tensor tension and pressure terms.

Since the magnetic tension acts only along the direction of the field lines, the forces transmitted throughout the field are dependent on the field line connections to various boundary regions. These topological connections divide the total volume into nested magnetic domains, based on the stress distribution within the field. For example, the open and closed field line topology designations define magnetic domains based on the field line boundary conditions. The field line connections that map to different regions of the photosphere (i.e., closed), or from the photosphere to the source surface (i.e., open), distribute and dissipate the stresses differently throughout the domain. In addition, the photospheric flows can generate volumetric stresses (i.e., small field gradients) within a given closed flux domain. On the other hand, the domain boundaries are magnetic surfaces separating regions of different field line boundary conditions. Therefore, sharp stress discontinuities (i.e., large field gradients) tend to form along these surfaces since they divide regions with different Lorentz stress distributions.

The coronal magnetic field and plasma system is energized by the flux emergence from the interior and the boundary flows at the photosphere. In order to determine the relationship between the field stress above the photosphere and the system drivers, consider the rate at which the electromagnetic field does work on a parcel of plasma. Under the same assumptions used in the reduction of the full Maxwell stress tensor (equation refMaxwellStress) to the magnetic stress tensor (equation refMagneticStress), we find the rate of change of magnetic energy to be directly related to the magnetic stress tensor,

$$\frac{\partial}{\partial t}\left(\frac{B^2}{8\pi}\right) = M_{ij}\frac{\partial v_i}{\partial x_j} - \frac{\partial}{\partial x_i}\left(v_i\frac{B^2}{8\pi}\right) \tag{3.6}$$

The first term on the RHS of equation (3.6) represents the energy input due to the stretching of the field lines, and compression against the isotropic magnetic pressure. The second term is the change in energy due to flux passing across the boundary (e.g., flux emergence). In this work we do not consider velocity flows normal to the photosphere, or flux carried away by the solar wind. Thus, we neglect the energy change due to flux passing in/out of the low-beta corona, and the change in magnetic energy is simply the rate at which the fluid velocity does work against the magnetic stresses.

3.2 Structure of 3-Dimensional Magnetic Null Point

The magnetic domains are topological in nature, since they follow directly from the field line connections of the magnetic field structure and remain intact under general physically allowable deformations. If the Smoothness Condition (chapter II, section 2.3) is valid in the solar corona, then the number of nested multi-polar flux domains is correlated with the number of PIL's at the boundary. (n) PIL's at the photosphere implies $(n+2)$ magnetic domains in the corona. To illustrate, the simplest quiet-sun coronal field structure consists of a single equatorial PIL and three global flux domains that are the streamer belt and two polar coronal holes. The addition of a single bipolar flux system embedded within the global coronal background, in general (i.e., excluding the highly-symmetric, nearly-unphysical cases), involves adding one PIL at the photosphere across which low-lying field must connect (e.g., chapter VI, Figure 6.1). Note, the open coronal hole regions do not require a photospheric PIL, and thus in general, the relation must be augmented by adding the number of disconnected coronal holes to the number of flux domains, $(n+2) \rightarrow (n + \text{total number of disconnected coronal holes})$, which for complex topologies can be countably very large.

For a potential field configuration, a boundary PIL implies the existence of a 3D

null-point at an altitude that depends on the strength the opposite polarity spot at the boundary (e.g., Figure 6.1). A 3D magnetic null point is very simply a point in the field in which the magnitude is zero. Note, the global quiet-sun background field structure does in fact include a null point at infinity. The nested flux structure that includes current systems may, depending on the strength of the currents, exhibit deformations in the overall geometry of the domain and null-point. Though, deformed they still retain the basic flux domain structure since volumetric currents reflect smooth gradients in the field geometry, and current sheets are simply stress discontinuities that form along the domain boundaries. In general, multiple magnetic domains within the total volume require multiple boundary PIL's each carrying a (possibly deformed) 3D null-point.

In a potential field, the geometric field structure near the 3D null-point defines the magnetic domain boundaries. By the Smoothness Condition (see chapter II, section 2.3) field lines are degenerate (i.e., the field line mappings through the null point are multi-valued; see Figure 3.1 right) at the null-point, so that the field lines emanating from or converging to the null-point constitute the topological domain boundaries, the so-called "separatricies". The neighboring field lines in its vicinity, on either side of these separatricies map to disconnected boundary regions. The basic field structure of the 3D magnetic null-point, and therefore the domain separatricies, is completely determined by the properties of the first-order Jacobian matrix of the Taylor expansion of the magnetic field about the magnetic null point (Lau & Fin (1990), Parnell et al. (1996)). For a magnetic null-point at position $\boldsymbol{x}_0$, the magnetic field structure in the vicinity $\boldsymbol{x}_0 + \boldsymbol{dx}$ is found from,

$$B_i\left(x_{0j} + dx_j\right) = \left(\frac{\partial B_i}{\partial x_j}\right)\Bigg|_{\boldsymbol{x}_0} dx_j + h.o.t. \tag{3.7}$$

where $\left(\frac{\partial B_i}{\partial x_j}\right)\Big|_{\boldsymbol{x}_0}$ is the Jacobian of the field evaluated at the null point $\boldsymbol{x}_0$, and $h.o.t.$

stands for "higher order terms" in the infinitesimal $\boldsymbol{dx}$.

By the divergence free condition of the magnetic field, the Jacobian $\left(\frac{\partial B_i}{\partial x_j}\right)\Big|_{\boldsymbol{x}_0}$ has a zero trace, which in turn implies the eigenvalues λ_i necessarily sum to zero. For all real eigenvalues, the corresponding magnetic field is potential; for 1 real and 2 complex conjugate eigenvalues, the magnetic field has free energy associated with currents. Regardless of the field energy state, the set of eigenvectors defines the topological frame associated with every first-order magnetic null-point (note, higher-order nulls exhibit highly symmetric properties that are unlikely to be found in nature since they are unstable under general field perturbations). The eigenvalues with the real part of the same sign correspond to eigenvectors that span a 2D plane known as the fan surface, while the other eigenvalue/eigenvector defines the one-dimensional (1D) spine lines (see Figure 3.1 right). The relative magnitudes of the fan-surface eigenvalues represent the relative field line density along the surface. For general properties of the topological spine-fan frame, see Lau & Fin (1990), Parnell et al. (1996), Longcope (2005).

The field line structure in the vicinity of the null-point can be discerned in terms of a position vector $\boldsymbol{r}(s)$ as a function of arc length, s. The field line mapping is defined by,

$$\frac{\partial}{\partial s} r_i(s) \equiv B_i = \left(\frac{\partial B_i}{\partial x_j}\right)\Big|_{\boldsymbol{x}_0} r_j(s) \tag{3.8}$$

Employing the notation of Parnell et al. (1996), under the linear transformation $\boldsymbol{r}(s) = \boldsymbol{P}\,\boldsymbol{u}(s)$, the field lines are the solutions to,

$$\frac{\partial}{\partial s} u_i(s) = \left[P_{ij}^{-1}\left(\frac{\partial B_i}{\partial x_j}\right)\Big|_{\boldsymbol{x_0}} P_{jk}\right] u_k(s) \tag{3.9}$$

where $\boldsymbol{P}$ is the matrix of eigenvectors of $\left(\frac{\partial B_i}{\partial x_j}\right)\Big|_{\boldsymbol{x_0}}$. The field line mappings defined

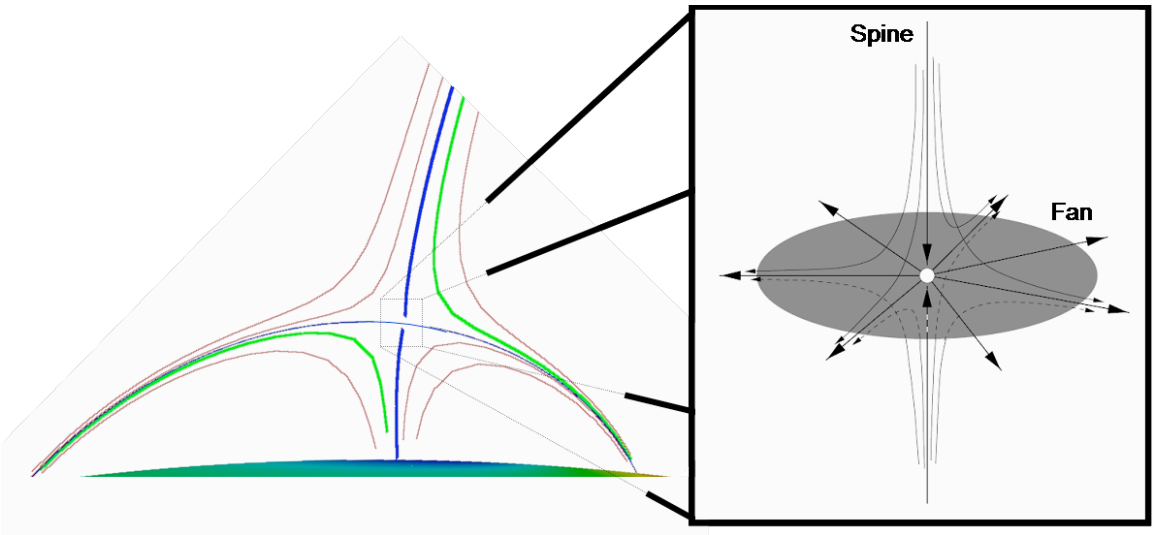

Figure 3.1: 2-Flux embedded bipole system schematic. The separate magnetic domains are defined by the field line connections. The null-point topology adapted from Longcope (2005).

by the solutions to equation (3.9) are degenerate (i.e., multi-valued) at the null point, as can be seen by tracing the solutions (direction depending on the sign of the eigenvalues) through the null point.

The simplest illustration of the 3D null-point and multi-domain geometry is the 2-flux embedded bipole system (see Figure 3.1 left) expected to be found ubiquitously throughout the solar corona. The fan surface, whether emanating from or converging to the 3D null-point, is the magnetic surface separating the various magnetic domains, since the field lines map the overall volume boundary to the null-point. The magnetic domains are themselves topological in that they are preserved under the physically allowed evolutions of both ideal and resistive MHD. Though reconnection alters the topological connections of individual field lines, the process as applied to the magnetic domains serves only to transfer flux across the domain boundaries.

Under certain conditions, the 3D null-point is, in general, a unique invariant of the system topology. This topological invariance implies an additional corollary to the smoothness condition,

Smoothness Corollary. In the absence of flux injection, magnetic null points are preserved.

A qualitative proof follows from very simple physical arguments, though 3D MHD calculations are required for a full rigor. Simply put, for smooth, continuous photospheric flow fields, magnetic null points may only be created by the injection of new field structures, such as bipolar flux emergence at the photosphere without helicity into the background field. The non-equilibrium requires current sheet discontinuities along the magnetic domain boundaries, which in turn dissipate by reconnection. In the absence of helicity, or if the boundary conditions allow the helicity to escape the system (i.e., open field lines act as a helicity sink), the system may relax all the way to a potential field. Thus the final state of the current sheet dissipation is a 3D null-point in order to account for the new magnetic domain topology (see Figure 3.1 left). On the other hand, in MHD evolution existing magnetic null points are not destroyed, only deformed by field stressing and current sheet generation. Presently, the micro-evolution of the magnetic field and reconnection physics in the vicinity of a null-point is not well understood. As a consequence of the smoothness corollary, the fan surfaces associated with each null-point system are also preserved, and therefore the magnetic domains themselves are conserved topological features of the system.

3.3 Dynamics of Current Sheet Formation and Stability

In a high conductivity, low-beta environment, such as the solar corona, the magnetic field is strong enough to dominate the plasma dynamics. Introducing energy and helicity through boundary flows and flux injection generate stresses within the field that significantly affect the geometric structure. Within the framework of MHD, the evolution of the magnetic field is governed by the standard Induction Equation; combining equations 2.10, 2.11, and 2.12, and defining the plasma resistivity transport

coeficient $\eta \equiv \frac{c^2}{4\pi\sigma}$, the standard Induction equation is,

$$\frac{\partial \boldsymbol{B}}{\partial t} = \nabla \times (\boldsymbol{v} \times \boldsymbol{B} - \eta \nabla \times \boldsymbol{B}) \tag{3.10}$$

Equation (3.10) gives a complete MHD description of the magnetic field evolution, which depends on the velocity field, and the plasma resistive transport coefficient. The velocity term governs the ideal evolution (i.e., $\eta = 0$), in which the motions of the magnetic field and the plasma are coincident (i.e., frozen-in). The resistivity term describes the rate at which the magnetic field may slip through the plasma (generating heat in the process). The Lundquist number $R_m \equiv \frac{vL}{\eta}$ (also known as the magnetic Reynolds number), defined by the ratio of the velocity term to the resistivity term, is a measure of the relative importance of these two effects. A high Lundquist number indicates a non-dissipative system in which the ideal, frozen-in description of the plasma is a good approximation across the majority of the medium. Note, dissipative effects may become important even in high-conductivity systems, in places where the characteristic scale lengths are small locally reducing the Lundquist number $R_m \lesssim 1$. Thus, even in the highly-conductive coronal environment, the effective Lundquist number is reduced at places such as pinch sheets where the corresponding characteristic length scale is reduced, and resistive physics becomes very important.

Over the majority of the volume of the corona, the Lundquist number is so high that the system evolution may be described as ideal (i.e., $\eta = 0$). However, in the presence of so-called singular lines, even arbitrarily high conductivity does not ensure ideal evolution. Along these lines the electric current density becomes large enough for dissipation to significantly affect the system evolution. Thus, in these regions the given magnetic field and the frozen-in condition are relegated to initial and boundary conditions, and the problem requires a self-consistent solution of the full system of

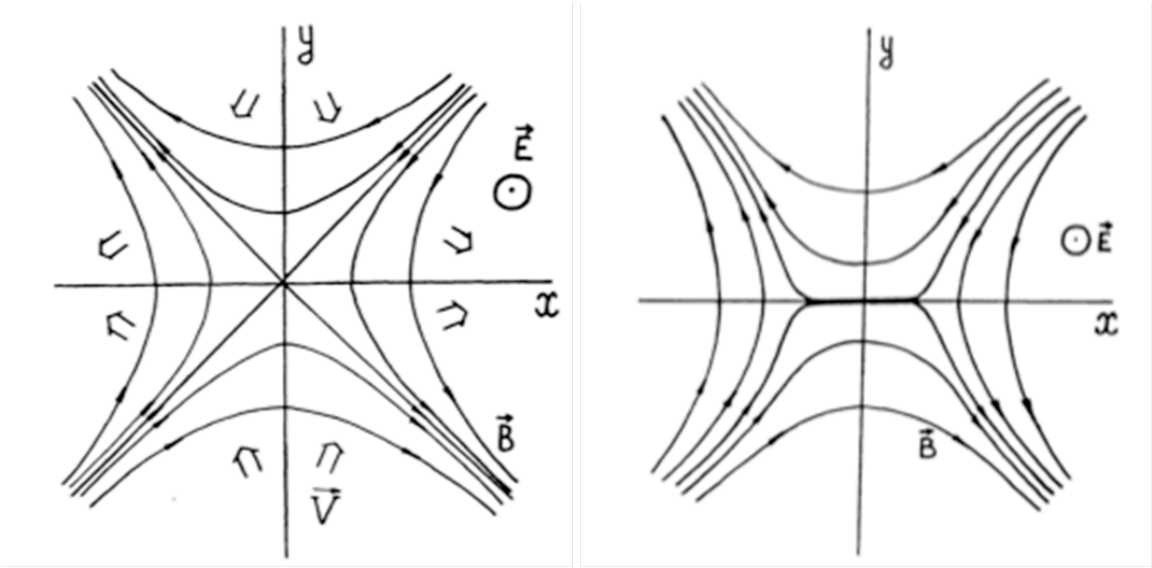

Figure 3.2: 2D X-Point collapse schematic: the non-linear 2D X-point collapse to form a pinch sheet thin enough such that resistive dissipation becomes dominant (adapted from Syrovatskii (1981)).

MHD equations (chapter II, equations 2.8 - 2.12) for both the magnetic field and the velocity field

The simplest case of a singular line is the 2D X-point topology (see Figure 3.2 left). When the system is in relative motion, a non-linear collapse occurs in the vicinity of the singular line, such that a current sheet develops with a thickness small enough to provide the necessary dissipation for arbitrarily high conductivity (see Figure 3.2). Note that near the X-point the thermal pressure dominates, thus the plasma thermodynamic evolution plays an important role in the formation and development of the dissipative current sheet. In fact, only if the conductivity were truly infinite, would the current be confined to an infinitely thin sheet. The research presented in this dissertation generalizes these 2D X-Line results to 3D X-Line (chapter IV) and null-point (chapters V and VI) topologies.

The current sheet discontinuity that forms in the vicinity of the singular line when the magnetic field is stressed is subject to a number of MHD instabilities such

as the resistive-MHD modes of tearing, rippling, and gravitational modes (Furth et al. (1963)), as well as thermal instabilities and various types of current driven micro-instabilities resulting in anomalous resistivity enhancements (ion-acoustic, drift-mode, Buneman, etc.)[1]. The basic idea is that the free magnetic energy available from the sheared field structure drives the instability, in that the energy becomes accessible to the plasma through resistive transport. Furth et al. (1963) showed how diffusion of the field through the plasma drives the three resistive-MHD modes which produce current filaments within the sheet of thickness l on timescales faster than the diffusion time $\tau_\eta = \frac{l^2}{\eta}$ (provided the sheet is wide enough that $\tau_A \gg \tau_\eta$). In each case, the restoring force is always the Lorentz force which acts to straighten the field lines, and if the instability is to take place, the driving force must be of the same magnitude or greater than the restoring force (see Figure 3.3). In the case of the gravitational mode, the driving force arises from a gravitational force transverse to the sheet, such that the density gradient drives the plasma into the current sheet. The driving force for the rippling mode is a positive resistivity gradient into sheet, thus the resistive-slip of the field through the plasma increases for field closer to the center of the sheet. The rippling mode may arise, for example, as a result of a temperature dependence of the resistivity profile.

The tearing mode is the most important of the three resistive-MHD instabilities, since it does not require any external drivers such as the gravitational force, or a resistivity stratification for excitation. This is a long wavelength mode (i.e., for wavelengths longer than the width of the sheet), and occurs in any sheared field geometry regardless of shearing angle. The driving force in this case, is not an actual vector force in the classical sense; rather it is a process that keeps the magnetic pressure in a locally reduced state with respect to the surrounding field. To illustrate, consider if there were no diffusion, a local pinching of field lines would locally increase

[1]We consider only the resistive-MHD modes, in particular the tearing mode, leaving the other instabilities outside the scope of this work.

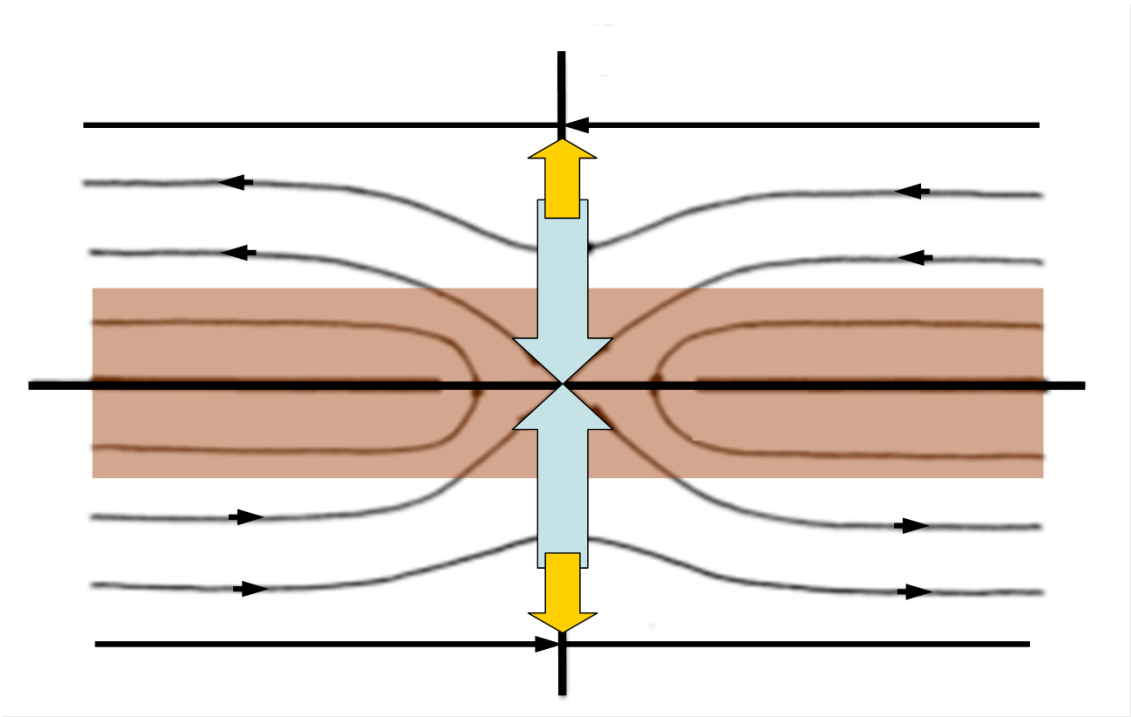

Figure 3.3: Generalized resistive-MHD instability schematic over a single wavelength. The driving force vector F_D is shown in blue, and the restoring Lorentz force vector F_R in yellow.

the magnetic pressure, which would then act to restore the equilibrium. Including the resistivity however, leads to reconnection between neighboring lines. The tension force in the newly reconnected field lines sweeps the flux away from the pinch-off point, lowering the local magnetic pressure clearing the way for new flux to enter and continue the perturbation. Note the pinch wavelength must necessarily be long enough so that the tension-sweep will saturate the tendency for the field lines above and below to straighten out. The process generates an alternating series of X-point and O-point (also known as magnetic islands) topologies within the sheet (see Figure 3.4), each singular point being a place of current density enhancement.

The local dynamics of a 1D current sheet subject to a 2D perturbation has been shown to be unstable to the tearing mode for perturbation wavelengths large relative to the length of the sheet. A rigorous calculation of the linear growth rate for the magnetic islands generated by the tearing mode shows the linear stage of island

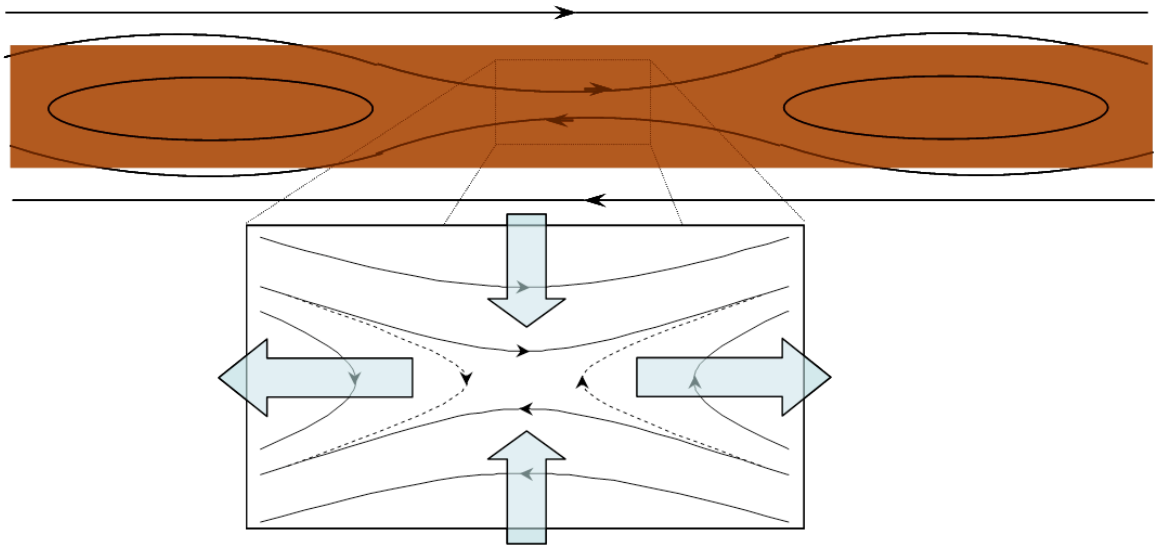

Figure 3.4: Resistive tearing mode instability schematic over a single wavelength. The reconnection process generates an alternating series of X-points and O-points within the sheet.

formation and growth occurs on a timescale intermediate between the relatively short Alfvén time τ_A, and the relatively long resistive timescale $\tau_\eta = R_m \tau_A$ based on the current sheet thickness, and is given by (Furth et al. (1963)),

$$\gamma \approx 0.55 \frac{(\Delta a)^{\frac{4}{5}}}{\tau_A R_m^{\frac{3}{5}}} \tag{3.11}$$

Where a is the sheet half-thickness, and Δ is the normalized jump in perpendicular gradient of the field perturbation normal to the current sheet discontinuity. The product Δa is related to the tearing mode wavelength in the sheared field, and though the exact value varies from place to place along the length of the current sheet, this quantity is roughly of order unity with respect to the global parameters of the system. Non-linear effects tend to saturate the system, limiting the growth of the island sizes to order the current sheet thickness. For pinch sheets of finite length, the overall magnetic reconnection process sweeps the islands out the nearest end on timescales of order the local Alfvén speed.

2D MHD pinch sheet stability theory predicts a thin current discontinuity to be unstable to the tearing mode all the time, even in the presence of a guide field (Furth et al. (1963), Galeev & Zeleny (1976), Bulanov et al. (1979)). We generalize these results to 3D for both a singular X-line (chapter IV), and a null-point (chapters V and VI) as the current systems generated from field stressing relate to the global evolution and dynamics of the coronal environment. We show, in the case of a neutral sheet, the analogues to the 2D magnetic islands are 3D "magnetic plasmoids" with an enhanced density structure. In addition, though such structures are subject to the kink instability, the 3D perturbations limit the correlation length of the quasi-ergotic, slinky-like fieldlines, and allow individual plasmoids to evolve independently of each other as they are ejected from the current sheet. Thus, even though 3D current sheet discontinuities remain unstable to the resistive tearing mode, the current filaments that develop are ejected in such a way that the entire current sheet remains "dynamically stable", regenerating its integrity after each expulsion.

3.4 Magnetic Reconnection Dynamics

Traditionally, the phenomenon of magnetic reconnection is broadly recognized as the rapid dissipation of magnetic stresses by a change in the local field topology structure. Field lines with opposing polarity components squeeze together across the current sheet, and following directly from the local resistive physics the lines of force subsequently reconnect altering the magnetic connections between distant elements of plasma. However, the global domain structure of the magnetic field, defined by the foot point boundary conditions and transmitted stress distributions, is unaffected by the reconnection process. The local topological modification simply relaxes the sheared field by shifting flux between domains, thereby reducing the length of the current sheet. This topological relaxation process conserves the total flux of the system. Therefore, recast in the framework of global magnetic domains, the phenomenon of

magnetic reconnection may be characterized simply as a flux exchange across the domain boundaries, in which the free energy associated with the sheared field geometry is rapidly converted to bulk flow kinetic energy, and particle acceleration[2].

The rate of flux exchange between domains (i.e., rate of reconnection) can be qualitatively estimated from general considerations of the interplay between the magnetic energy and thermal energy of the plasma. Since the reconnection mechanism conserves total flux, the rate of flux exchange between the domains separated by the current sheet boundary, follows from the ratio of merging flow into the sides of the current sheet to the flow out the ends, $\frac{v_{in}}{v_{out}}$ (see Figure 3.5). The Lundquist number is very large away from the resistive region of the current sheet implying ideal, frozen-in evolution of the field and plasma system. Thus, the rate of in-flow is nominally, the relative motions of the plasma due to the system drivers. To determine the rate of out-flow, we note the total pressure $P + \frac{B^2}{8\pi}$ of the system must be balanced across the current sheet. Since the sheared component of the magnetic field changes direction across the current sheet, the magnetic pressure decreases to a local minimum at the center of the sheet (note, the magnetic pressure of a guide component will be a constant across the sheet). To compensate for the constant total pressure, the thermal pressure must increase to a local maximum. Therefore, the amount of increase in thermal pressure at the center of the pinch sheet is simply the magnetic pressure of the sheared component exerted against the sides, $\Delta P = \frac{B^2}{8\pi}$. This increase in thermal pressure at the center of the sheet expels the fluid out the ends of the current sheet. By setting the dynamic pressure equal to the increase of thermal pressure, $\frac{1}{2}\rho v_{out}^2 = \Delta P = \frac{B^2}{8\pi}$, the exit speed of the fluid is simply the Alfvén speed, $v_{out} = \frac{B}{(4\pi\rho)^{\frac{1}{2}}} \equiv V_{Alfvén}$. In effect, it is the magnetic pressure outside the current sheet that is driving the field merging and reconnection.

[2]An MHD description cannot account for particle acceleration, since the only transport coefficients available to connect the macro-continuum physics with the micro-kinetic physics are, at most, the resistivity and viscosity coefficients.

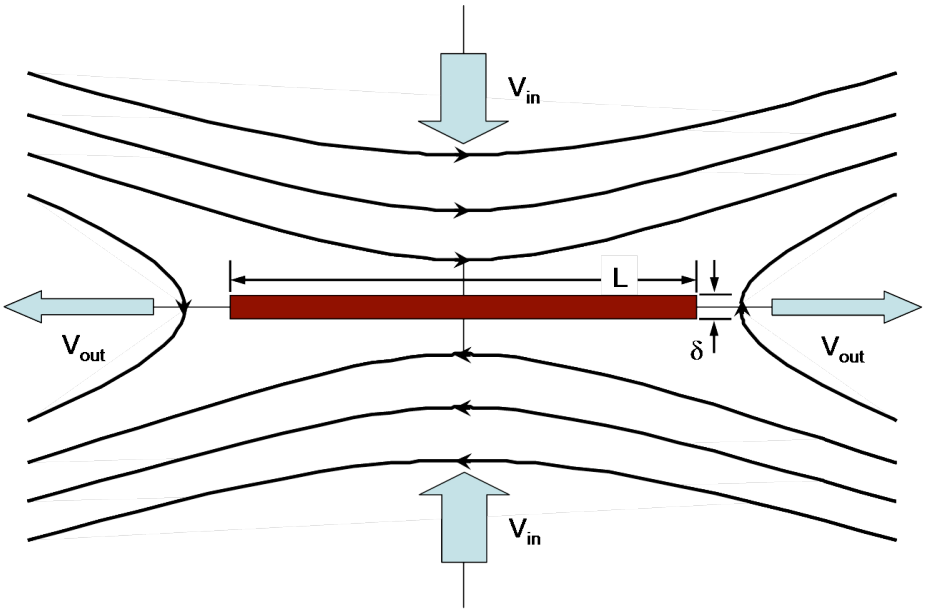

Figure 3.5: Basic reconnection structure illustrating the relationship between the field geometry, current sheet, and in/out flows.

A rigorous derivation of the reconnection rate based on conservation principles (see Appendix A) was first worked out by Parker (1957). For a current sheet of dimensions $L \times \delta$ (as shown in Figure 3.5), Parker showed the reconnection rate is, modulo a constant, inversely proportional to the square root of the Lundquist number,

$$\frac{v_{in}}{V_{Alfvén}} \propto \frac{1}{(R_m)^{1/2}} \tag{3.12}$$

Note, by continuity, the reconnection rate is simply the current sheet aspect ratio, $\frac{v_{in}}{v_{out}} = \frac{\delta}{L}$. Equation (3.12) is effectively an upper-limit on the in-flow speed as a function of the Lundquist number such that the conservation of energy is not violated. For typical coronal Lundquist numbers of 10^4 - 10^6, the corresponding in-flow speed is of order 0.01 $V_{Alfvén}$ - 0.001 $V_{Alfvén}$.

Motivated in part by the fact that the Sweet-Parker reconnection rate (3.12) based on the global Lundquist number is too slow to explain the energy release timescales for solar flares, Petschek (1964) suggested there is no a priori reason that the extent

of the dissipation region should be identified with the overall sheet dimension L. The basic idea is to drive up the merging rate by reducing the size of the dissipation region over which the resistive physics is valid. Recall, the external magnetic pressure drives the field merging, and hence by conservation of energy the sheared component of the magnetic field must either decrease, or at best remain constant, as it is carried toward the current sheet. On the other hand, flow field necessarily includes a stagnation point, and such flows have the geometric property that two neighboring elements separate without bound as the flow passes the stagnation point. Thus, outside the dissipation region, since the field is frozen-in, the sheared field components are stretched without bound. The Sweet-Parker rate is based on the fact that the length of the dissipation region is large enough so there is no appreciable spread in neighboring fluid elements before the merging fields enter the dissipation region. As a consequence, the merging flow velocities remain very low with respect to the Alfvén speed.

The only self-consistent solution to a system with a narrow dissipation length that maintains energy conservation requires a steady-state hydromagnetic shock structure (see Figure 3.6). The shocks in the flow field allow the merging velocities to remain constant all the way down to the dissipation region scales, thereby halting the growth of the sheared field components as they approach the stagnation point. The magnetic field geometry of the standing Alfvén waves associated with the shocks is determined by the system dynamics. The geometry of Figure 3.6 (top), illustrates the standing Alfvén wave initiated on the merging field lines near the local diffusion region, and is the situation first suggested by Petschek (1964). Whereas in Figure 3.6 (bottom), the Alfvén wave is initiated on the merging field lines by some external perturbation[3]. Even though both magnetic field geometries in Figure 3.6 are consistent with the shock structure, it is more likely the disturbance in the magnetic field generating

[3]This configuration permits the most rapid reconnection, though requires an additional standing Alfvén wave in the magnetic field along the out-flow direction (Sonnerup (1970)).

the standing Alfvén wave initiates with the local dissipative region (i.e., the Petschek geometry). The reconnection rate associated with the Petschek geometry is (Petschek (1964)),

$$\frac{v_{in}}{V_{Alfvén}} \propto \frac{1}{ln\,(R_m)} \tag{3.13}$$

For coronal Lundquist numbers of order 10^4 - 10^6, fast reconnection merging rates are a significant fraction of the Alfvén speed, $\sim 0.1 V_{Alfvén}$.

Depending on the driving conditions at the boundary and the stress distribution within the global magnetic field structure, the local reconnection rate can vary continuously from the relatively slow Sweet-Parker (3.12) to fast Petschek (3.13). Reconnection can develop in several ways based on the global stress distribution, the plasma resistivity profile, and the evolution of the boundary conditions away from the current sheet. First, if the merging flux is not replenished, the reconnection rate will reflect the global stress distribution and dissipate enough of the current sheet so that a force-free equilibrium is reached. Second, for steady driving conditions replenishing the merging flux at a fixed rate, the reconnection rate will reflect the driving rate. Third, if the conditions allow, the merging rates may adopt any value, the reconnection rate is likely to take on the fastest possible rate in accordance with the stress distribution, dissipating the current sheet entirely. In the solar corona, current sheet dissipation is likely to be a complicated mixture of each of the three cases depending on the strength and geometry of the driving flows and flux emergence, and the topology of the global field structure (i.e., open flux or closed flux).

Finally, the distribution of helicity in the global magnetic structure plays a major role in the extent of the current sheet dissipation by reconnection in the solar corona[4]. Physically, magnetic helicity is a measure of the overall twist in the magnetic field structure, or equivalently quantifies the links between flux tubes. A gauge-invariant

[4]A full mathematical treatment of helicity and related quantities is given in Appendix B.

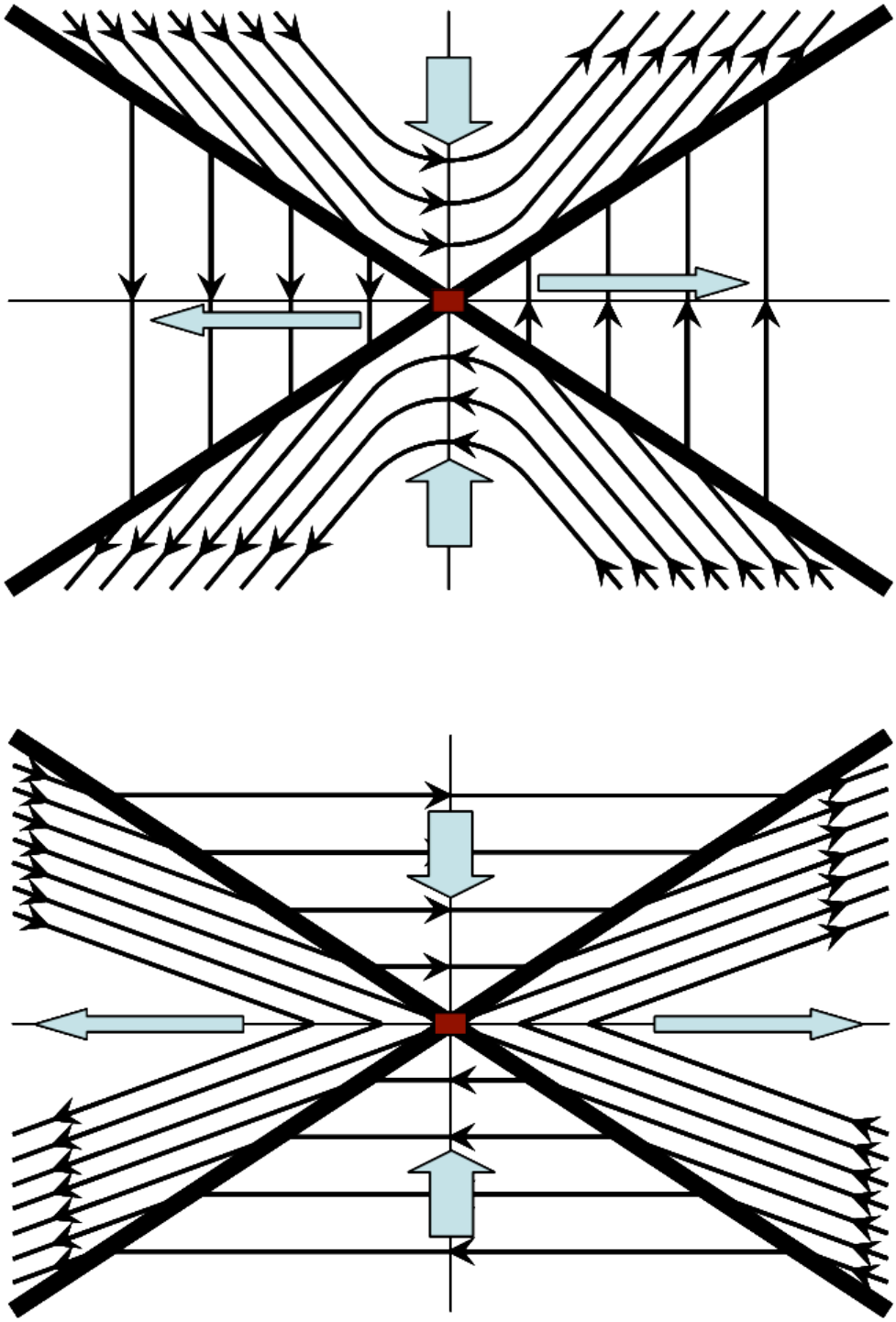

Figure 3.6: The fast reconnection structure requires standing hydromagnetic shocks (thick lines) attached to a small dissipative region. Top: Magnetic field geometry in which standing Alfvén waves initiate with the local dissipation region. Bottom: Magnetic field geometry in which standing Alfvén waves initiate externally to the system.

definition of helicity (see Appendix B.1) in terms of the full magnetic field $\boldsymbol{B}$ and its vector potential $\boldsymbol{A}$, and the corresponding potential fields, $\boldsymbol{B_P}$ and $\boldsymbol{A_P}$, associated with the normal components at the boundary is,

$$\mathcal{K} = \int_{\mathcal{V}} (\boldsymbol{A} + \boldsymbol{A_P}) \cdot (\boldsymbol{B} - \boldsymbol{B_P}) \, \mathrm{d}\mu \tag{3.14}$$

Clearly, a purely potential field structure contains zero helicity. Thus, any equilibrium magnetic field that includes helicity must have global stresses above the minimum energy state distributed throughout the structure.

An ideally evolving global boundary transports helicity (see Appendix B.2) into the volume according to,

$$\frac{\mathrm{d}\mathcal{K}}{\mathrm{dt}} = 2 \, c \int_{\partial\mathcal{V}} [\, (\boldsymbol{A_P} \cdot \boldsymbol{v})\boldsymbol{B} - (\boldsymbol{A_P} \cdot \boldsymbol{B})\boldsymbol{v} \,] \cdot \boldsymbol{n} \, \mathrm{d}S \tag{3.15}$$

where $\boldsymbol{n}$ is the unit normal to the global boundary. Since the potential field $\boldsymbol{B_P}$ is by definition normal to the boundary, its corresponding vector potential $\boldsymbol{A_P}$ is necessarily tangent to the boundary. Thus, the terms on the RHS describe the helicity transport by flow components tangent and normal to the global boundary respectively.

Helicity stress is only dissipated through Ohmic heating (see Appendix B.3) according to,

$$\frac{\mathrm{d}\mathcal{K}}{\mathrm{dt}} = -2 \int_{\mathcal{V}} \eta \boldsymbol{J} \cdot \boldsymbol{B} \, \mathrm{d}\mu \tag{3.16}$$

When compared to the dissipation of magnetic energy at a current sheet discontinuity across which reconnection occurs, we find the helicity is dissipated during the

reconnection process according to,

$$\left|\frac{\Delta\mathcal{K}}{\mathcal{K}}\right| \leq \left(\frac{\Delta t}{\tau_d}\right)^{\frac{1}{2}} \tag{3.17}$$

Therefore, since the reconnection processes are effectively instantaneous ($\Delta t \rightarrow 0$), and occur at internal magnetic domain boundary surface discontinuities (i.e., η is appreciably different from zero over only a small fraction of the total internal volume), magnetic reconnection conserves helicity.

Away from the global boundary, the stresses tend to distribute the helicity as uniformly as possible, encompassing the largest amount of flux within magnetic field structure. In general, the minimum energy state of the global magnetic field geometry, subject to helicity conservation, is a force-free configuration (see Appendix B.4),

$$\nabla \times \boldsymbol{B} = \alpha \boldsymbol{B} \tag{3.18}$$

Globally closed field topologies cannot dissipate the helicity stress on timescales less than the resistive dissipation, which leads to force-free equilibrium configurations that include current sheets maintained by residual stresses regardless of the reconnection mechanism. On the other hand, the globally open field topology acts as a helicity sink, since the stresses may distribute to infinity.

CHAPTER IV

The Formation and Dynamics of 3-Dimensional Current Sheets in the Solar Corona

Magnetic reconnection has long been postulated to be the fundamental process underlying most solar activity (Parker (1972), Parker (1988), Priest (1981)). The basic scenario is that free energy in the form of electric currents is generated in the corona as a result of either the emergence of non-potential flux from below or the stressing of pre-existing coronal field by photospheric motions. Given the high Lunquist numbers for typical coronal parameters $> 10^{10}$, these currents could persist almost indefinitely, but some process (or processes) brings the scale of the currents down to values where the frozen-in-flux condition can be broken. The magnetic free energy is then released to the coronal plasma by reconnection. Depending on the properties of the reconnection the energy release may result primarily in heating, as in models for coronal heating (e.g., Klimchuk (2006), Rappazzo et al. (2008)), or in violent mass motions as in models for chromospheric explosions, coronal jets, and coronal mass ejection (Lynch et al. (2008), Lynch et al. (2009), Pariat et al. (2009)), or even in bursts of particle acceleration as in flare models (e.g., Miller et al. (1997), Drake et al. (2006)).

It is evident from this discussion that the formation of current singularities, which

[0]The material described in this chapter is a modified version of Edmondson et al. (2009)b.

are generically termed "current sheets" is central to reconnection and to solar activity. Various mechanisms have been discussed for current sheet formation, but the one that is most intuitive and most likely to apply to the corona is the null-point deformation process described in Syrovatskii's seminal work (Syrovatskii (1971), Syrovatskii (1978)a, Syrovatskii (1978)b, Syrovatskii (1981)). The fundamental argument is that for a magnetic topology with discontinuous connectivity, in particular, at a classic 2D X-type null point (actually an X-line) with four topologically distinct flux systems, any stress applied to the system is likely to lead to discontinuous stress at the null and separatrices and, hence, to the rapid formation of current sheets there. This picture has been shown to be fully robust by many investigations, both analytic and numerical (Syrovatskii (1981), Antiochos (1990), Karpen et al. (1995), Karpen et al. (1996), Karpen et al. (1998), Birn et al. (1998), Antiochos et al. (2002)). Although Syrovatskii's theory was originally formulated for a 2D null-point configuration, the mechanism appears to be physically valid in 3D as well, with only straightforward modification (Antiochos (1996), as well as chapter V - Edmondson et al. (2009)a, and chapter VI - Edmondson et al. (2009)c).

In addition to the large-scale current sheet formation process, the mechanism that breaks the frozen-in-flux condition locally is critical for magnetic reconnection. In fact, it may well be that this microscale mechanism controls the energy release rate of the reconnection and, thereby, determines its global manifestations. After decades of intense study, a generally-accepted picture has emerged for the simplest possible situation, steady-state reconnection in a 2D X-point topology under the MHD approximation. The studies have shown that if the dissipation mechanism, usually a simple isotropic resistivity, is spatially localized at the X-point (Parker (1973), Biskamp (1993)), then the reconnection takes on the Petschek (1964) form with a pair of slow mode shocks, a current sheet short (in the 2D plane) compared to the global scale, and a reconnection rate of order the Alfven speed (Petschek

(1964), as well as chapter III, section 3.4). On the other hand, if the resistivity is roughly uniform, then the reconnection adopts the Sweet-Parker (Sweet (1958), Parker (1963)b) form, with a current sheet length of order the global scale and a reconnection rate much less than the Alfven speed (see Appendix A). The physical origin for this sensitivity to the spatial localization of the resistivity is well understood; it was originally discussed by Parker (1972) and elaborated on by Kulsrud (2001). It should be emphasized, however, that both the Sweet-Parker and Petschek models are steady state models only and, therefore, do not address the self-consistent problem of current-sheet formation and disruption.

Previous MHD studies of solar activity in a 2.5D[1] null-point coronal topology driven by photospheric motions, found that the resulting evolution was well represented by the combination of the Syrovatskii and Sweet-Parker models (Karpen et al. (1995), Karpen et al. (1996), Karpen et al. (1998), Antiochos et al. (2002)). A smooth horizontal photospheric flow produced discontinuous stress at the null, resulting in its deformation to a current sheet and, hence, to reconnection there. Those studies all used numerical resistivity, which has no pre-defined spatial localization and, consequently, tends to produce a long global-scale current sheet and reconnection resembling the Sweet-Parker model rather than Petschek. A major new feature of these driven models, however, is that if the current sheet becomes sufficiently long, it is subject to tearing mode instabilities (Furth et al. (1963)), which result in the formation of magnetic islands and can enhance the reconnection rate (Karpen et al. (1995), Karpen et al. (1996), Karpen et al. (1998), Antiochos et al. (2002)). The general conclusion, therefore, from the 2.5D MHD studies with numerical or uniform resistivity is that reconnection in the solar corona is well described by the standard Syrovatskii-Sweet-Parker scenario, but with the addition of magnetic island formation and the resulting dynamics.

[1] 2.5 dimensional (2.5D) refers to a fully-3D system that is translationally invariant in one direction.

The key question is whether this conclusion remains valid for a realistic 3D system. Due to the intrinsic complexity of 3D topologies, current-sheet formation and reconnection in such systems have only recently begun to be explored (Lynch et al. (2008), Lynch et al. (2009), Pariat et al. (2009), as well as chapter V - Edmondson et al. (2009)a, and chapter VI - Edmondson et al. (2009)c). For systems that are fully 3D, such as an isolated X-point topology with no special symmetry (e.g., Pariat et al. (2009)), the geometry is so different from the 2D model that it is difficult to relate the knowledge gained from the lower-dimensionality studies to the 3D evolution. One approach to bridging the gap between 2D and 3D is to consider a system that is initially 2D, but allow for a fully 3D evolution. The goal here is to be able to use some of our physical intuition gained from the large body of 2D reconnection in order to understand the more complex 3D system.

Such an approach has been used to investigate the 3D evolution of a pre-existing 1D current sheet (Dahlburg et al. (2003), Dahlburg et al. (2005), Dahlburg et al. (2006)). These studies produced an interesting and potentially important result. As expected, the sheet tears to form 2D magnetic islands, but these are susceptible to a 3D secondary instability, which is much faster than the tearing mode growth rate. The physical interpretation is that a magnetic island in 3D is actually a twisted flux rope, which can be susceptible to kink-type ideal instabilities. It was found that this secondary instability induces a burst of energy release. The results provide a physical mechanism for producing the type of reconnection bursts required by Parker's nanoflare model (Parker (1972)) for coronal heating (Klimchuk (2006)). Although these results are interesting and potentially highly important, they are not fully self-consistent, because the current sheet is assumed a priori rather than generated by photospheric motions. Furthermore, the initial current sheet is 1D, rather than having physical dimensions determined by the global scales in the problem.

In this chapter an investigation of the self-consistent formation and reconnection of

a 3D current sheet driven by photospheric motions is done. The goal is to use as much as possible the insights gained from the 2D studies to understand the 3D evolution. A 2D X-line similar to the previous studies (Karpen et al. (1995), Karpen et al. (1996), Karpen et al. (1998), Antiochos et al. (2002)) is assumed for the initial topology, except that the Parker ansatz of considering the magnetic field in a Cartesian box with the bottom and top of the box representing photospheric regions of different polarity is employed. As will be evident below, this assumption allows us to stress the field with a simple 1D flow at the photosphere, which preserves the photospheric flux distribution there. Although the initial field is 2D and the driving flow is 1D, the evolution is calculated in full 3D from the outset allowing us to investigate 3D current sheet formation and disruption. The numerical details of the model and the results are described below.

4.1 2.5D Magnetic X-Line Model

The magnetic field for our study is given by a rigorous analytic model. Initially, the field is translationally-symmetric and potential. It is constructed from an infinite, continuous-line dipole density (analogous to the electrostatic field due to a continuous line of charge) embedded in a constant background field. The vector potential is given by (see Appendix C),

$$A_z(\boldsymbol{x}) = B_0\left[y - \frac{2\alpha y}{y^2+(z-h)^2}\right] + \alpha B_0 y\left(\frac{2}{d}\right)^2 \sum_{n=1}^{N}\left(\frac{1}{n^2}\right)\frac{\left(1-\frac{1}{n^2}\frac{y^2+(z-h)^2}{d^2}\right)}{\left(1-\frac{1}{n^2}\frac{y^2+(z-h)^2}{d^2}\right)^2+\left(\frac{1}{n^2}\frac{2(z-h)}{d}\right)^2} \tag{4.1}$$

The first terms on the RHS of equation 4.1 represent the constant background field of strength B_0, oriented parallel to the positive z-direction, and the field due to a single line-dipole density of strength αB_0 (where α is a dimensionless scale factor)

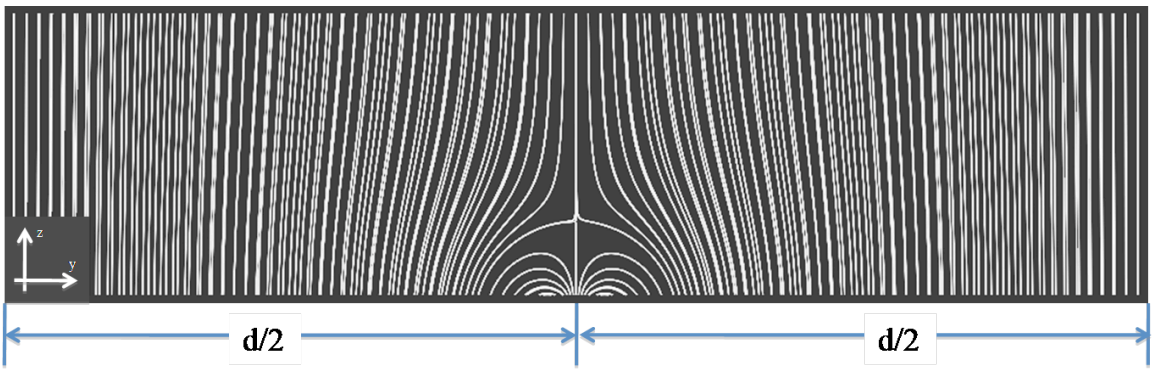

Figure 4.1: Initial magnetic field X-Line topology for self-consistent 3D current sheet formation. 4-flux system topology in the plane perpendicular to the translational symmetry axis derived from an infinite, continuous line dipoles density, oriented anti-parallel to the background field.

positioned at $z = h$, and oriented anti-parallel to the background field. The model is translationally symmetric in the x-direction (i.e., independent of the x coordinate), and the y-direction is determined from the standard right-handed coordinate system. The general topological form is therefore, that of a 4-flux system with an X-type null-point in the y-z plane (see Figure 4.1). The separate flux systems are defined by the field line connections that either close across the dipole polarity inversion lines, or connect the upper and lower z-boundaries.

For simplicity, periodic boundary conditions in the y-direction is assumed; consequently, the magnetic field must be vertical to within the machine error a finite distance, $y = \pm\frac{d}{2}$, from the central system. A purely vertical field entails an infinite series adjustment (i.e., $N \rightarrow \infty$), where the n^{th} term physically represents two continuous line-dipoles separated by a distance $y = nd$, mirrored on either side of the central system. Mathematically, only an infinite series will yield a truly vertical magnetic field at $y = \pm\frac{d}{2}$, since a finite number of terms will result in an asymmetry due to an unbalanced horizontal field component based on the imbalance of dipole systems away from the overall system symmetry plane $y = 0$. Unfortunately, a closed form solution to this infinite series does not exist (the series may be manipulated

into a sum of two associated hypergeometric functions, but these are themselves only a repackaging of infinite series). Even without a closed form solution, we can show convergence with the (numerical) integral test (see Appendix C.2) since successive terms in the series are monotonically decreasing. We find the convergence integral solutions are bounded everywhere within the domain,

$$\left\{ (y, z-h) \;\middle|\; -\frac{d}{2} \leq y \leq \frac{d}{2}\,,\, 0 < (z-h) < \frac{d}{2} \right\} \tag{4.2}$$

For implementation of the model, convergence of the infinite series is not completely necessary though since we are working with a finite grid resolution. A vertical magnetic field at the $y = \pm\frac{d}{2}$ boundaries only requires enough terms in the series such that the magnitude of the horizontal field is less than the machine error. Even for a modest number of terms in the series, the error between the true field and the vertical is far less than necessary. For this simulation we take $N = 25$, which corresponds to 51 total line-dipole systems, each separated by d units in the y-direction. The calculation domain in the y-direction is therefore set to $y \in$ [-1/2 , 1/2] * d inclusive, to satisfy the periodicity. Consequently, only the dynamics of a single line-dipole system about the origin is calculated.

The simulation extent in the z direction is restricted by the $0 < (z-h) \leq \frac{d}{2}$ condition. The lower bound (excluded) follows from keeping any unbounded singularities associated with evaluating the field exactly at the line-dipole out of the calculation domain. The upper boundary (included) keeps successive terms in the series monotonically decreasing to satisfy convergence. Since there are no restrictions on the vector direction of the field at the upper/lower z boundaries, a smaller simulation domain in the z-dimension is employed to cut down on the computational expense. We set the z-domain to $z \in$ [$1/d$, $1/d + 1/4$] * d inclusive, and restrict $h < 1$.

Finally, due to the translational symmetry in the x-direction, there are no restric-

tions on the size of the domain - other than the computational expense of solving the fully-3D set of MHD equations at a very high grid resolution. Therefore we set the x-domain $x \in$ [-1/4 , 1/4] * d, large enough only to insure any 3D structures that develop in the x-direction will in fact be completely covered throughout their evolution.

We calculate the simulation using the ARMS code, solving the standard set of 3D compressible, ideal MHD equations (2.8, 2.9, and 3.10, with $\eta = \nu \equiv 0$) in Cartesian coordinates. In place of the conservative energy equation we solve the adiabatic equation for the temperature,

$$\frac{\partial T}{\partial t} + \nabla \cdot (T\boldsymbol{v}) + (\gamma - 2)\ T \nabla \cdot \boldsymbol{v} = 0 \tag{4.3}$$

with the ratio of specific heats $\gamma = \frac{5}{3}$. We use the ideal gas law (equation 2.14) for the plasma equation of state. Gravity is not included in this calculation, as we are interested in current sheet structure development and evolution in the large scale-height environment of the low-beta corona.

A point of note, the coordinate units are conspicuously missing from the above discussion. The reason for this is scalability, which makes the most important aspect in this calculation is the dimensionless low-beta condition. We calculate the system in cgs units, but the MHD equations above are non-dimensionalized by introducing scale factors for mass density ρ_0, magnetic field strength B_0, characteristic length L, and charicteristic time τ_0. Each of these quantities is of order unity, and adjusted to maintain the low-beta condition as well as keep the global average Alfvén speed of order unity. The background field B_0 and line-dipole density field strength αB_0 were chosen to place the null well inside the calculation domain, such that any boundary effects do not influence the current sheet formation and dynamics. The thermal pressure is chosen to retain the low-beta condition over the majority of the calcu-

lation domain. With these parameters, the plasma beta remains small throughout the majority of the domain. Figure 4.2 illustrates the plasma beta across the magnetic structure, with the white contour showing the $\beta = 1$ surface. Only within a small region in the neighborhood of the singular null-line does the plasma beta rise substantially above unity. We emphasize, however, that although the system as a whole is low-beta, the plasma pressure does play an important role in the evolution. The plasma pressure dominates the region near the null-line, and therefore the formation of the current sheets and the subsequent reconnection dynamics are critically dependent on the plasma evolution.

We calculate this simulation within the ideal MHD framework, thus the current sheet formation, evolution and reconnection dynamics are governed by numerical resistivity. Figure 4.3 shows the initial numerical grid development for the simulation. We start with a base level consisting of $2 \times 2 \times 1$ blocks distributed uniformly in $\{x, y, z\}$ with 8^3 grid points per block. The above block definition is the minimum resolution away from the null-point region. Initially, the grid is refined a maximum of 6 levels over $\{-\frac{1}{4} \leq x \leq \frac{1}{4}, -\frac{1}{d} \leq y \leq \frac{3}{d}, \frac{3}{d} \leq z \leq \frac{6}{d}\} * d$, a volume large enough to encompass the majority of the entire would-be current sheet development volume. We employ adaptive mesh refinement (AMR) to increase the effective Lunquist number R_m near the current sheet. Our mesh refinement criterion tests a normalized field gradient in regions of weak magnetic field strength since we are generating a neutral sheet. The grid refines up to a maximum refinement level of 9 for a normalized gradient greater than 0.5, and de-refines for normalized gradients less than 0.125. The resolution at the maximum refinement level 9 corresponds to a length of approximately $\frac{d}{4096}$ per grid point - far smaller than the scale of the initial magnetic structures. We keep the AMR criterion independent of the current density magnitude in order to avoid computationally expensive grid refinements with the development of magnetic field gradients away from the singular null region of interest.

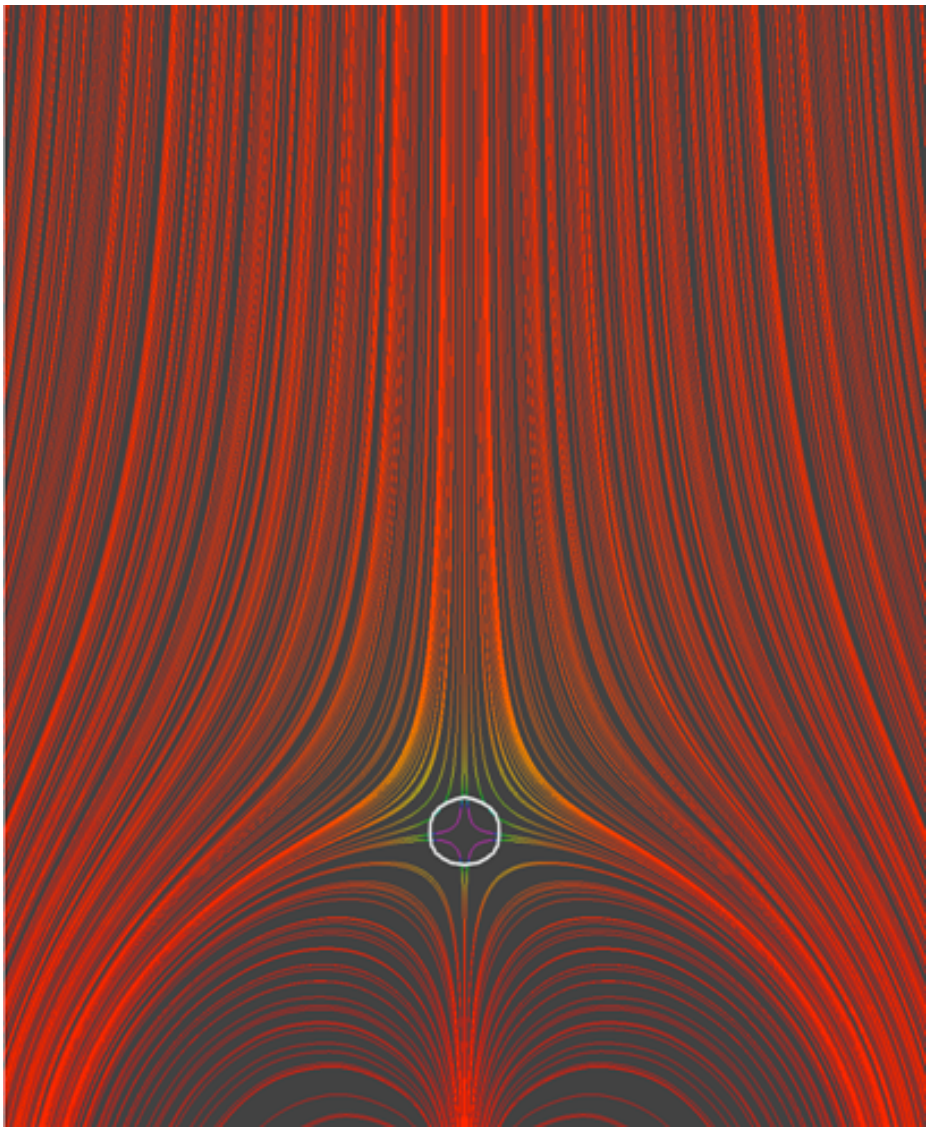

Figure 4.2: Initial X-Line beta profile. The color-scale denotes the beta magnitude: Red is $\beta < 1$, Purple is $\beta > 1$. The white contour marks the $\beta = 1$ boundary.

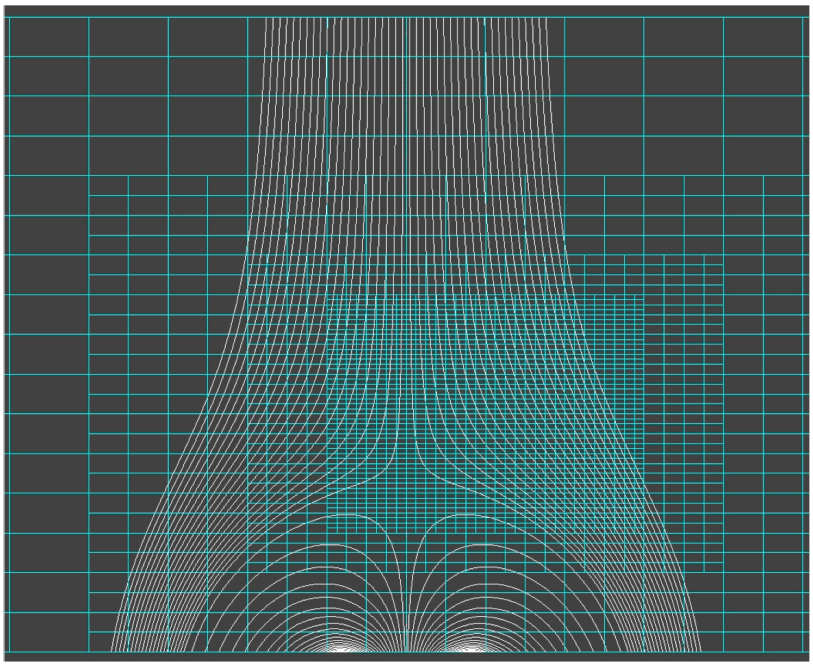

Figure 4.3: Initial X-Line grid definition in the perpendicular plane. This grid definition is uniform in the translationally symmetric (x) direction.

In the strong field (i.e., low-beta) approximation, driving motions slow compared to the Alfvén speed yield a force-free evolution. Similar to the plasma beta, the local Alfvén speed varies considerably over the domain, ranging from nearly zero in the vicinity of the null, to approximately 7 in the very strong field region near the coordinate origin. Thus, we define an average global Alfvén speed based on the total magnetic energy E_M, and total material M_C in the corona,

$$V_A = \sqrt{\frac{2\,E_M}{M_C}} \tag{4.4}$$

where E_M is the total magnetic energy, and M the total mass of the system. The density parameter ρ_0 is initialized to set this global Alfvén speed parameter equal to unity (constant; see Figure 4.4), and the driving flow speed is designed against this reference.

The system is energized by applying a slow, spatially uniform, flow profile at the upper z-boundary. The maximum magnitude reaching only about 4.5% of the global

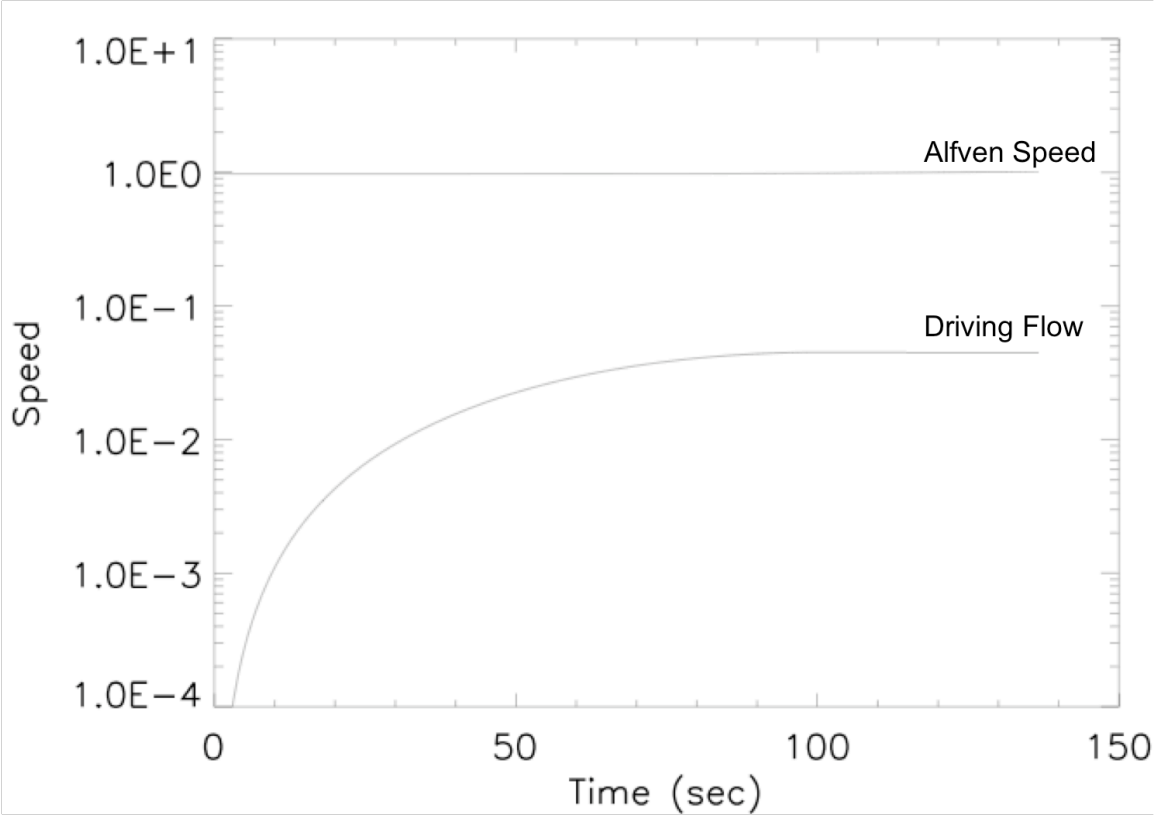

Figure 4.4: X-Line driving flow profile comparison against average global Alfvén speed (arbitrary units). Note, the driving flow profile is remains an order of magnitude less than the global average Alfvén speed.

average Alfvén speed, $V = 0.045\, V_A$. In addition, a time shifted cosine profile is employed in order to minimize transient wave effects as the motions start (see Figure 4.4),

$$\boldsymbol{V} = V_y\,(t)\,\boldsymbol{y} \tag{4.5}$$

$$V_y\,(t) = \begin{cases} \frac{V}{2}\left[1 - cos\left(\pi \frac{t}{100}\right)\right] & 0 \leq t \leq 100 \\ V & t > 100 \end{cases} \tag{4.6}$$

The calculation time partition at $t = 100$ is chosen so that the AMR grid resolution is well established, covering the entire length of the current sheet (see Figure 4.5), by the end of this first phase. After $t = 100$ the driver speed is held constant so that any burstiness in the system must be an intrinsic property of the reconnection rather than a response to a time-variable driver. At the z-coordinate boundaries, we impose line-tied conditions so that the only way for the magnetic field to change topology is through reconnection.

The characteristic length $L = \chi d$ is chosen, where χ varies depending on the particular dynamical process under study. For example, the current sheet thickness is important in analyzing the linear stage of the tearing mode instability, while the fully developed current sheet length is the relevant spatial scale for the non-linear dynamics following the tearing mode. The characteristic length scale defines an Alfvén timescale $\tau_A = \frac{L}{V_A} = \frac{\chi d}{V_A}$. A point of note, since the global average Alfvén speed V_A is unity, the characteristic length L and Alfvénic timescale τ_A are equivalent. Combining the characteristic length L and Alfvén time τ_A scales with the Lunquist number R_m, yields the dissipation timescale $\tau_\eta = R_m\, \tau_A$, and the numerical resistivity $\eta = \frac{V_A L}{R_m}$, for the high-resolution current sheet; parameters important for determining the tearing mode growth rate, as well as plasmoid formation and ejection times.

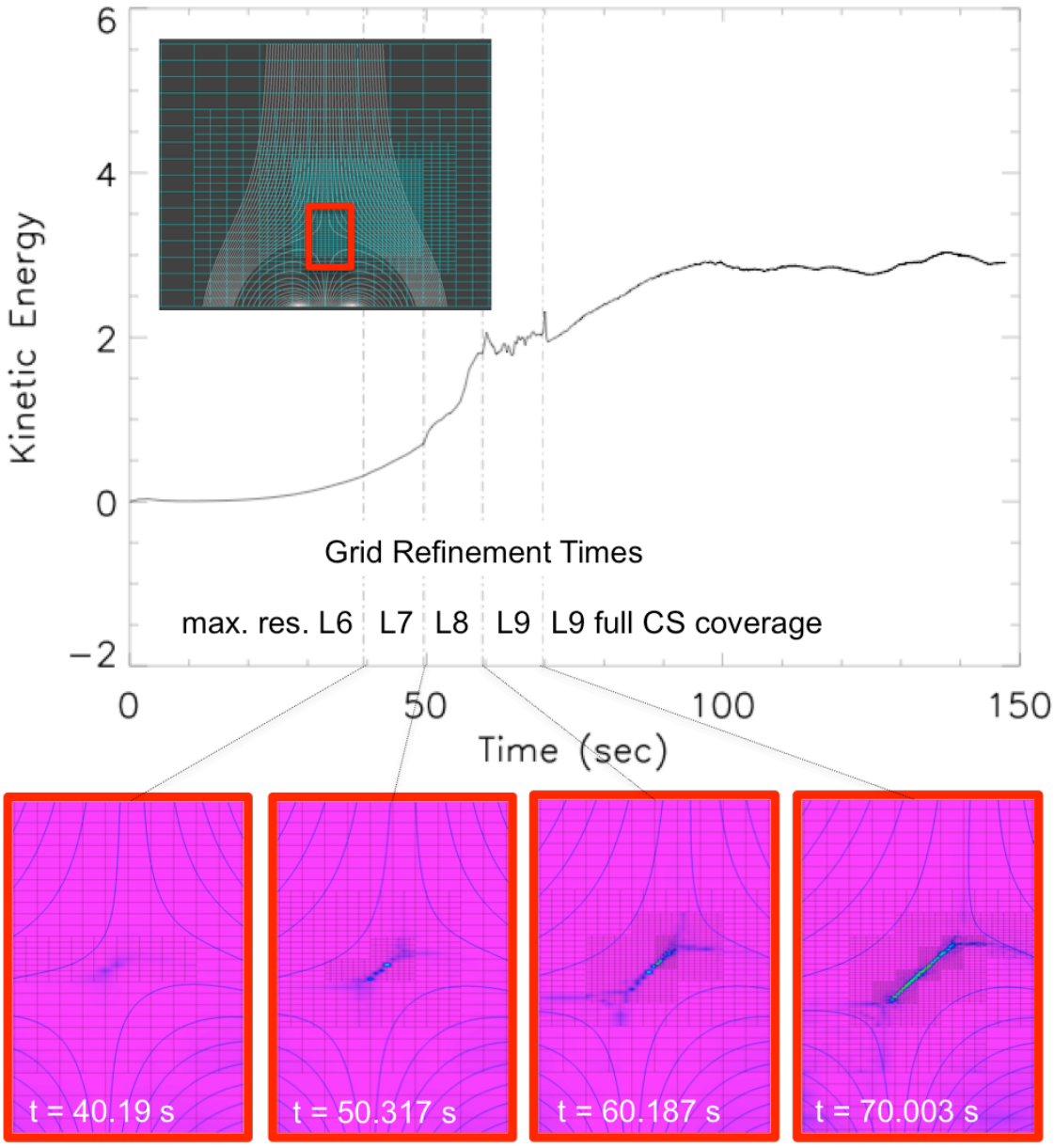

Figure 4.5: X-Line Numerical Grid Refinement. Initial grid definition and refinement times shown against the current density magnitude development. The AMR refines the grid at times $t = 40.19$, 50.317, 60.187, and 70.003, reaching full current sheet coverage at refinement level 9 for $t \geq 70.003$.

4.2 Results: Initial Configuration and Current Sheet Development

The initial state is built with $h = 0$, placing the line-dipole density at the coordinate origin. The global scale length is $d = 40$, which sets the calculation domain to $\{ (x, y, z) \, | x \in [-10, 10] \, , y \in [-20, 20] \, , z \in [1, 11] \}$. The field strengths are set to $B_0 = 3$ and $\alpha B_0 = 20$, respectively, which places the initial null at near mid-altitude in the z-direction (Figure 4.1). The thermal pressure and mass density are $P_0 = 10^{-2}$ and $\rho_0 = 1.0$, maintaining the overall low-beta condition (Figure 4.2). We find that beta reaches a global minimum of approximately 10^{-4} at the lower-z boundary near the high field strength of the line-dipole density. With these numbers, the absolute magnitudes of the total integrated kinetic and thermal energies in this system remain of order unity throughout the evolution (Figure 4.6), in arbitrary units since all quantities may be re-scaled for coronal comparison.

In the early development stage, $t \leq 40.19$, the driving speed and, hence, the footpoint displacements ramp up slowly so that only weak currents appear in the corona. Note that if the central bipole were not present, so that the initial field is purely uniform and vertical, then the field would remain purely potential throughout the evolution, except for transient currents. The photospheric motions would generate a uniform B_y that increases linearly with the total photospheric displacement in the y-direction. In other words, the field lines would simply tilt more and more as their top footpoints undergo increasing displacement. The bipole, however, acts like an obstacle to the background field so that the field must deform around it as it tilts and, hence, currents form near the bipole. Note that inside the bipole, itself, essentially no current appear, because its flux is not distorted directly by the motions of the top boundary.

The current formation process is intuitively obvious from the geometry of our

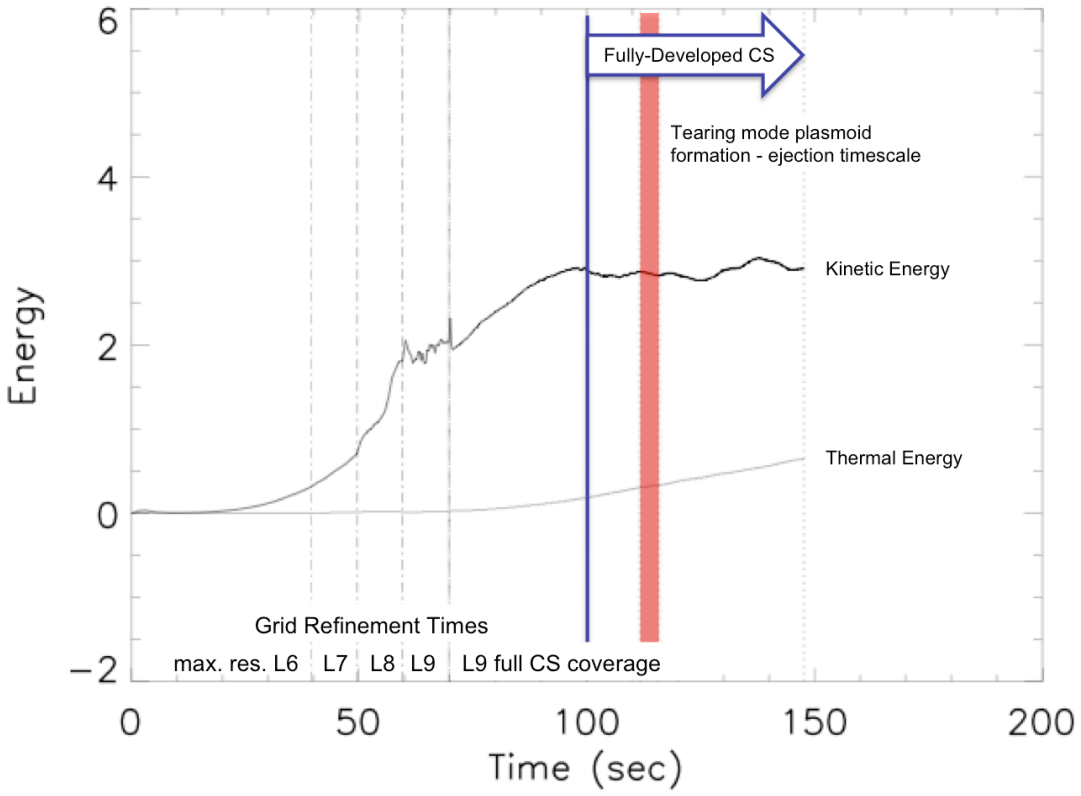

Figure 4.6: Current sheet formation Energy-Time plot. The system kinetic and thermal energy evolution in arbitrary units. The grid refinement times are clearly seen in the kinetic energy profile. The fully-developed current sheet is analyzed after $t = 100$.

system, as can be seen from Figure 4.2, for example. Prior to the boundary driving motion, the inner and outer spine lines (actually planes in 3D) are perfectly vertical and their "ends" meet at the null point. The motion moves the top footpoint of the outer spine to the right, which imparts a stress to the field dragging the end of the outer spine to the right. The inner spine, however, feels no stress and stays more-or-less fixed. Consequently, the spines dislocate, causing the null point to deform into a current sheet. This process begins almost immediately in our system, but the width of the current sheet is limited by the finite gas pressure in the system so that, at first, its width is still larger than the grid scale.

As the driving flows progress, the null-line continues to stress, forming a neutral pinch sheet. The AMR begins at $t = 40.19$ (see Figure 4.5) as the null-region begins to show substantial deformation, and the corresponding width of the current structure generated in the vicinity of the weak field decreases down to the grid scale. At the refinement times $t = 40.19$, 50.317, 60.187, and 70.003, clearly illustrated by the discontinuities in the kinetic energy plot, the neutral current sheet system remains confined to the grid scale. In the final phase of the development stage and throughout the dynamics stage, $t \geq 70.003$, the grid has reached its maximum resolution of 9 times refinement, covering the entire pinch sheet that separates the inner and outer spine lines. At this level of refinement, the current sheet thickness is, on average, of order the grid point spacing, $\delta = 2.44 \times 10^{-4} d = 9.77 \times 10^{-3}$. The effective Lunquist number for the current sheet in the high-resolution region follows directly from the grid refinement, $R_m = 256$.

4.3 Results: Plasmoid Formation and Ejection

Since gravity is not included, the relatively long-wavelength tearing mode is the most important resistive-MHD instability for the current sheet system under study. In 2D, magnetic island formation by the tearing mode generates alternating X-type and

O-type field line topologies along the length of the current sheet (Biskamp (1993)). In 3D, the analogue of the 2D islands are plasmoids characterized by enhanced density twisted flux rope structures. Even without a guide field, as is this case, 3D perturbations generate quasi-ergotic field lines from reconnections with different cross-sectional planes along the current sheet axis. For sheets of finite length, these magnetic plasmoids are ejected in the direction of the closest end of the current sheet. Therefore, we differentiate the tearing mode process into two stages: plasmoid formation and plasmoid ejection. The formation stage can be taken as the initial field line pinching and linear growth of the plasmoid, and its characteristic length is the current sheet thickness (i.e., $\chi = \frac{1}{4096}$). The ejection stage, in contrast, occurs once the plasmoid growth is of order the current sheet thickness and non-linear effects come to dominate the dynamics. In this case, the characteristic length of the system is taken as the length of the current sheet (i.e., $\chi = 0.02$) in the perpendicular plane.

Furth et al. (1963) showed the linear growth rate γ for the resistive tearing mode instability in 2D, is intermediate between the fast Alfvénic timescale τ_A, and the slow dissipation timescale τ_η. The linear growth rate depends on the jump in the properties of the magnetic field across the current sheet, the thickness of the pinch sheet, and (nearly) the geometric mean of the two characteristic timescales, and is given by,

$$\gamma \approx 0.55 \frac{(\Delta a)^{\frac{4}{5}}}{\tau_A R_m^{\frac{3}{5}}}$$

where Δ is the jump in the gradient of the normal-field perturbation component, across the current sheet, and a is the sheets half-thickness. The quantity Δ is dependent completely on the properties of the ideally-evolving field, and therefore in general, the product Δa is of order unity (i.e., ~ 0.1 - 1.0). Recalling the global Alfvén speed $V_A = 1$, the Lunquist number across the maximum grid resolution covering the current sheet is $R_m = 256$ and the current sheet thickness $2a = 9.765 \times 10^{-3}$, the

Alfvén timescale in the formation stage is $\tau_A = 9.765 \times 10^{-3}$. Thus, the linear tearing mode growth rate γ is estimated to be between 0.32 and 2.02. The top panels of Figure 4.7 (t = 111.66, 112.02, and 112.54) illustrate the tearing mode's linear growth stage for a typical time and perpendicular plane. We find the average tearing mode wavelength is nearly 1/3 - 1/2 of the instantaneous current sheet length, and occur on a timescale of order $\tau < 0.88$, which in turn implies a growth rate $\gamma = 1/\tau > 1.14$, in agreement with the predicted theory.

We emphasize this simulation is entirely 3D for all time. The 3D perturbations affect the evolution from the outset in such a way that the plasmoids that form by the tearing mode in a given perpendicular plane do not develop a coherent flux rope structure over any significant length between perpendicular planes. In the case of the truly neutral sheet, the only guide field that emerges is seeded by the numerical perturbations, which limits the correlation length to only a few grid cells.

Non-linear effects begin to saturate the system when the plasmoid width becomes comparable to the current sheet width, limiting the size of the plasmoids in the perpendicular plane, and initiating the ejection stage. For the most part we find plasmoid formation near the center of the sheet. Since the tearing mode wavelength is of order 1/3 - 1/2 of the instantaneous current sheet length, we find on average, there are 3 to 4 plasmoids in any given perpendicular plane. It is unclear from this single high-resolution simulation, how the tearing mode wavelength (i.e., the number of plasmoids that form in a perpendicular plane at fixed time) depends on the Lunquist number.

The plasmoid ejection timescale varies depending on the location of plasmoid formation along the current sheet length, as well as the instantaneous length of the current sheet itself. The ejection speed reflects the local outflow speed, typically about 30% of the Alfvén speed. Any given plasmoid splits the current sheet as it sweeps out the ends - especially the larger plasmoids - temporarily reducing the instantaneous

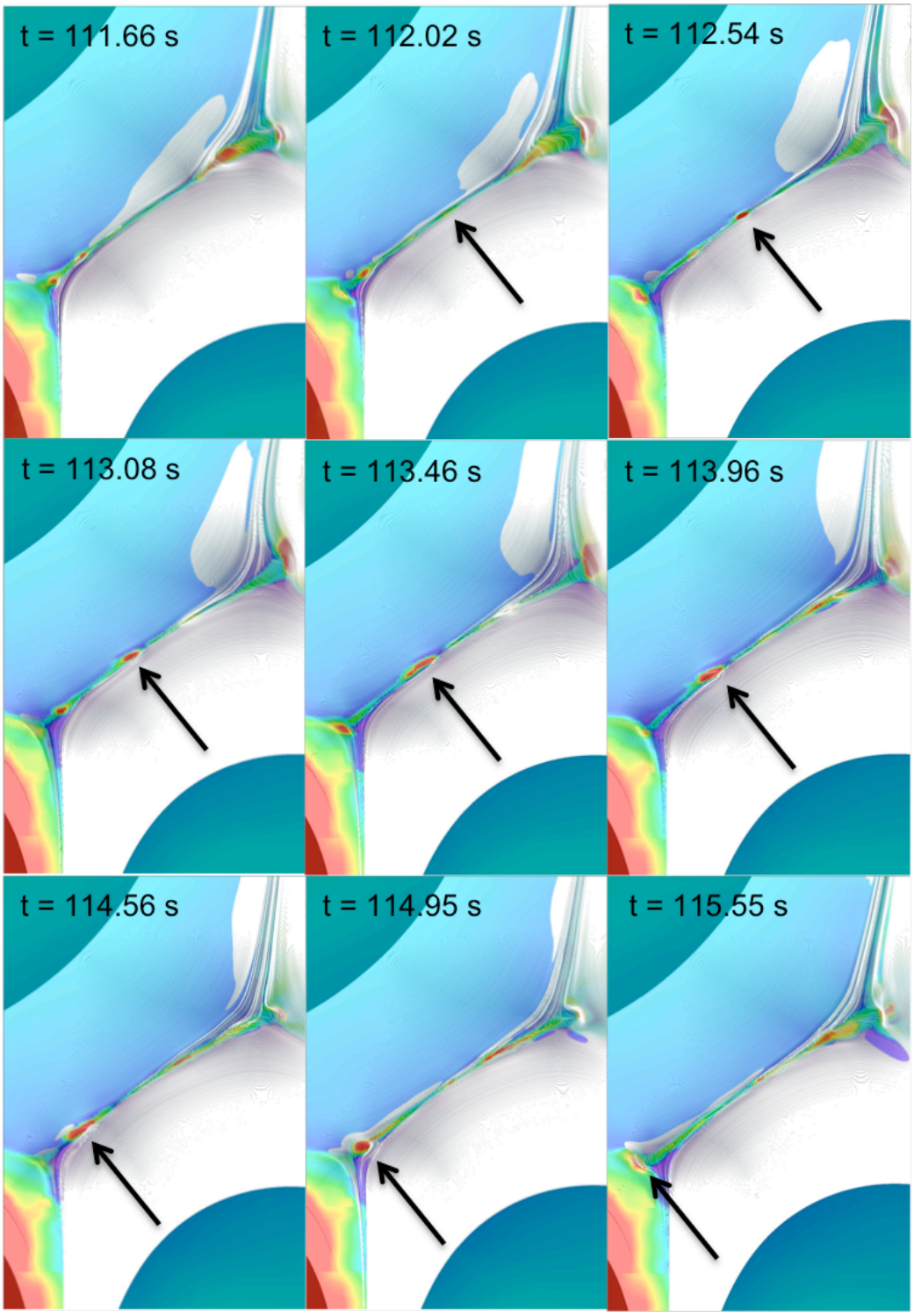

Figure 4.7: 2D Tearing Mode: 2D Island (3D plasmoid cross-section) formation-ejection in the perpendicular plane (x = 0). Linear growth stage within the $t = 111.66$ through $t = 112.54$. Non-linear ejection stage $t = 112.54$ through $t = 115.55$.

global scale length in any given perpendicular plane. We account for this effect, on average by setting the ejection stage characteristic length to 2/3 of the global spine-to-spine distance (i.e., $L = 0.02\,d$). This leads to ejection stage characteristic length scale and Alfvénic timescale of $L = 0.8$ and $\tau_A = 0.8$, respectively. Figure 4.7 illustrates a typical non-linear ejection in the panels $t = 112.54$ through $t = 115.55$, in which the plasmoid forms roughly in the center of the sheet, and ejects on a timescale of approximately 3 - 4 τ_A, a direct result of the tearing mode wavelength.

Since the plasmoid correlation length in the third dimension is limited by the 3D perturbations, the plasmoids are short enough that the ejections evolve effectively independently between the perpendicular planes. Though there is evidence of kinking for these short structures, they never become sufficiently large to affect the overall integrity of the sheet. To illustrate this point, we use the fact that the plasmoids have an associated local density enhancement, clearly seen in the background color map of Figure 4.7 ($\rho \geq 2$ saturate red). Though this is somewhat of an arbitrary threshold, $\rho = 2$ seems to correlate nicely with the width of the quasi-ergotic field lines of the twisted flux rope in the perpendicular plane (a higher threshold would show a smaller plasmoid, and a lower threshold would smear the plasmoid into the background). The point of view covered by Figure 4.8, shows the current sheet from the top down. The white stripe is the same perpendicular plane of Figure 4.7. The purple is the strong current magnitude ($|\boldsymbol{J}| = 5$ iso-surface), and the red structures are the 3D plasmoid density enhancements ($\rho = 2$ iso-surface). The white arrow of Figure 4.8 follows the plasmoid formation, evolution, and ejection, complimenting the black arrow in Figure 4.7. The important features to notice are that the plasmoid structures evolve independently, dividing and coalescing, as they are ejected. Though they do "kink", the length of the plasmoids in the third dimension never becomes long, and they are ejected quickly enough for the sheet to recover its integrity. As evident from Figure 4.8, the structure of the plasmoids is highly irregular and fully

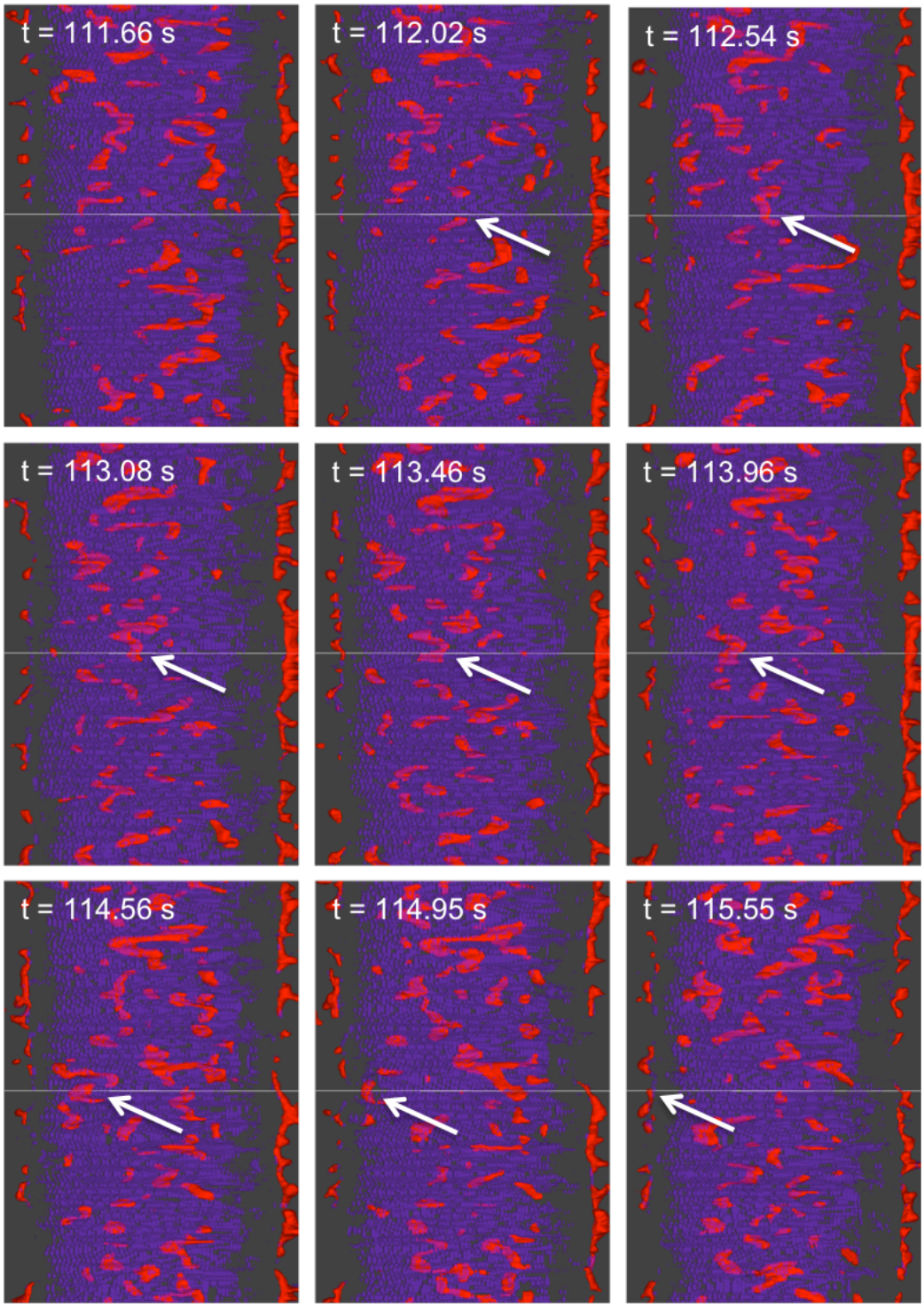

Figure 4.8: 3D Tearing Mode: 3D plasmoid (enhanced density structures) formation-ejection.

3D.

4.4 Results: Steady-State Dynamics

The steady-state stage of this investigation ($t \geq 100$) is characterized by a "dynamically stable", fully-3D neutral current sheet with an aspect ratio of around 40:1. The system dynamics clearly favor a fairly quiet steady-state reconnection, as opposed to explosive, bursty reconnection that leads to large-scale turbulent break-up of the current sheet. The relatively quiet dynamics are likely a direct consequence of the form of the driving flows, which produce magnetic stress that is localized primarily to the separatrices between the flux systems. This stress can be relaxed directly by the reconnection. To that end, the fully developed current sheet maintains a more-or-less constant global length of roughly 0.02 d (i.e., approximately 2/3 of the spine-to-spine separation; see Figure 4.9), implying the reconnection rate and the field stressing rate have converged. We note, however, that the instantaneous length at any given perpendicular plane varies with each plasmoid ejection.

During the steady-state dynamics stage, the average 40:1 aspect ratio of the current sheet is consistent with the Sweet-Parker reconnection rate $\frac{\delta}{L} = \frac{1}{\sqrt{2\pi R_m}} = 0.025$. However, the instantaneous reconnection rate defined by the ratio of in-flow to out-flow value, may increase considerably. For example, Figure 4.10 shows the velocity magnitude at the $x = 0$ mid-plane and $t = 136.48$ (well into the dynamics stage). The black contours are current density magnitude 5, illustrating the extent of the strong current system. The reconnection jets are clearly seen in the purple contours of the figure. The average in-flow speed along the length of the sheet is effectively the driving flow speed, $V_i = 0.045\, V_A$. Averaging the out-flow speed over the reconnection jets, we find $V_o = 0.337\, V_A$. Therefore at $t = 136.48$, the instantaneous reconnection rate in the $x = 0$ mid-plane is $\frac{V_i}{V_o} = 0.134$. The reason for the local increase in the reconnection rate is that the system is not in a pure steady-state, rather it must ac-

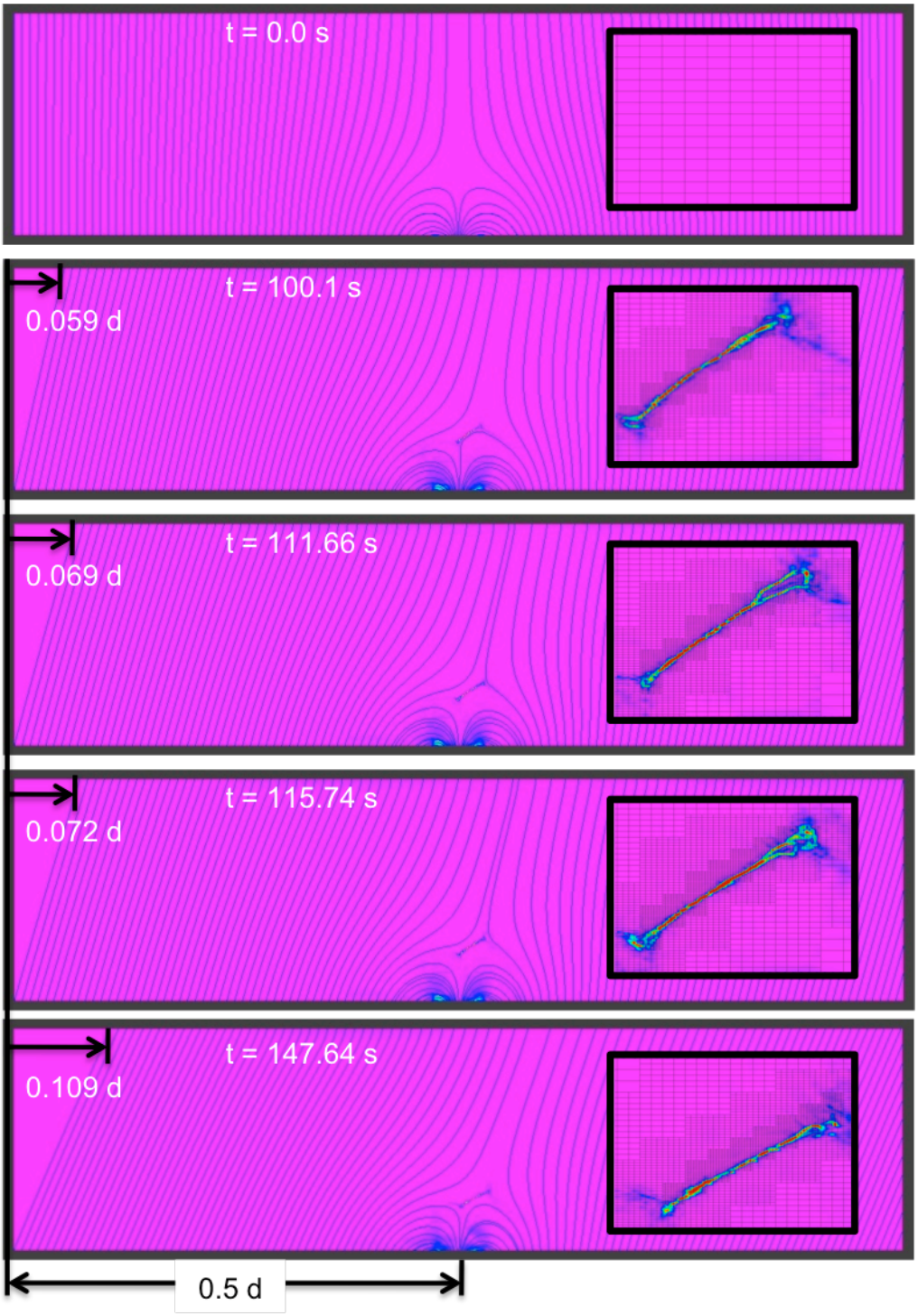

Figure 4.9: Global current sheet development at $t = 0.0$, 100.1, 111.66, 115.74, and 147.64. The fully developed current sheet has little curvature and retains an overall characteristic length L = 0.02 d, roughly $\frac{2}{3}$ spine-to-spine distance.

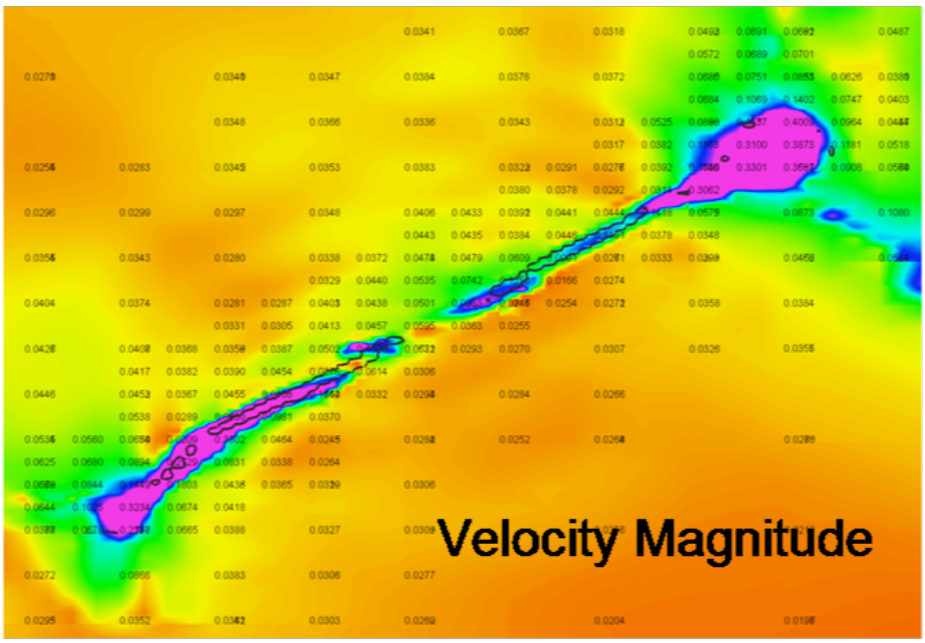

Figure 4.10: Local velocity field magnitude at the mid-plane at time $t = 136.48$. The black contours are current density magnitude 5, showing the approximate extent of the strong current sheet. The reconnection jets are clearly seen as the purple contours in the velocity space.

count for the effects of both driving and local transient plasmoid formation/ejection dynamics. Though, the overall average current sheet length is consistent with the Sweet-Parker rate, the plasmoid ejection dynamics alter both the local Alfvén speed through the density enhancements, as well as the instantaneous current sheet length, both of which adjust the in-flow to out-flow ratio.

As a consequence of the localized reconnection rate enhancement due to plasmoid ejections the system develops localized, transient Petschek geometries at the ends of the current sheet. This effect is seen by comparing the strong current magnitude with the plasma density and overlying field lines (see Figure 4.11). From the lower panel of Figure 4.11, tthe field line (shown in white) structure at the current sheet split clearly shows sharp Alfvénic bends in the field line structures. These Petschek-type Alfvén waves at the ends of the current sheet have very short lengths and are highly transient, forming with the splitting of the current sheet as the plasmoids are ejected,

and dissipating as a single sheet is recovered. In addition, the local reconnection rate enhancement never increases above the predicted fast Petschek rate, $\frac{1}{ln(R_m)} \approx 0.1803$.

Once the current sheet lengthens sufficiently so that the reconnection balances the slow driving velocity, approximately .04 V_A, the sheet stops growing. From this point on the structure around the null region, Figure 4.5, can be characterized as quasi-static with the stretching by the photospheric displacements balanced by the shrinkage from reconnection. Of course, the system is not in a true steady state, because the flux in the right-hand closed arcade of Figure 4.2 decreases continuously due to the reconnection while the flux in the left increases. Eventually the flux imbalance will grow to the point that the reconnection stops, but we see no evidence for this saturation, at least, for the footpoint displacements of our simulation. Although not extreme, the displacements are clearly substantial. Figure 4.9 shows that by the end of the calculation, the footpoints on the upper boundary have moved a distance of order the size of the closed bipole. It is intriguing that at this quasi-steady state, the angle of the uniform background field with respect to its original vertical direction is of order 20°, close to the stress angle required by Parker for his coronal heating model (Parker (1983)). We emphasize, however, that the topology of our system is significantly different than that of Parker's.

The result that the current sheet is so stable is especially surprising, given that the sheet achieves aspect ratios as high as 40:1. The dynamics are very consistent with steady-state Sweet-Parker reconnection except for the addition of magnetic island formation. These islands do not grow to be large in any dimension, primarily because they are ejected from one current sheet end or the other on the same time scale as their growth time. We emphasize, however, that structure in the x-direction does form at both small and global scales, and that this 3D structure is critically important. The small-scale structure is due primarily to the formation of magnetic islands at random locations along the sheet. The large-scale structure is evident as a periodic structure

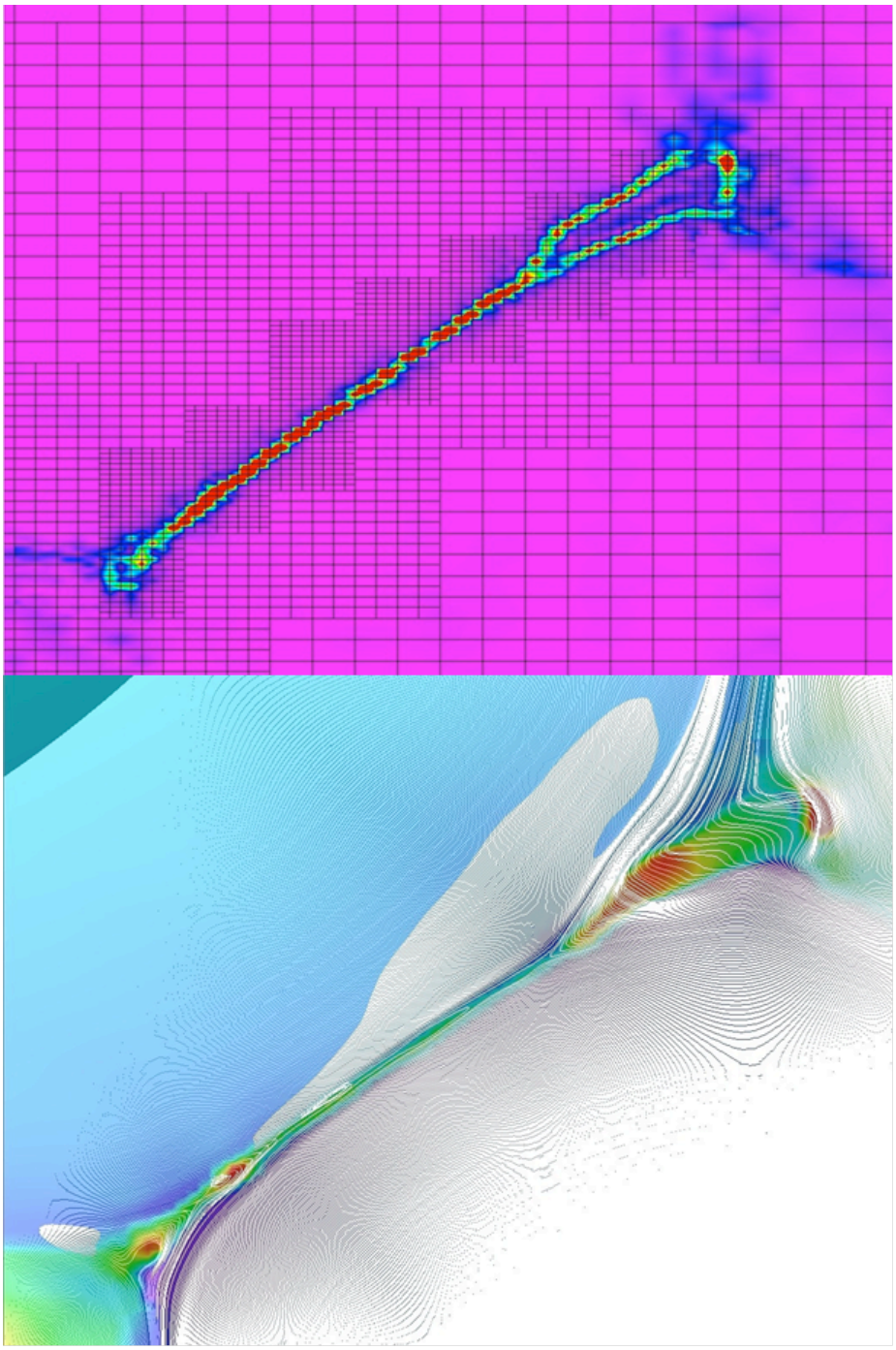

Figure 4.11: Current sheet splitting leads to localized, transient Petschek geometry at $t = 111.66$ by plasmoid ejection. Top: Current density color scale; red signifying strong currents (magnitude greater than 5). Bottom: Plasma density color scale with field lines over layed; red signifying densities greater than 2. Note, the hard bends in the field lines at the right hand reconnection jet are the Alfvén waves associated with plasmoid ejection.

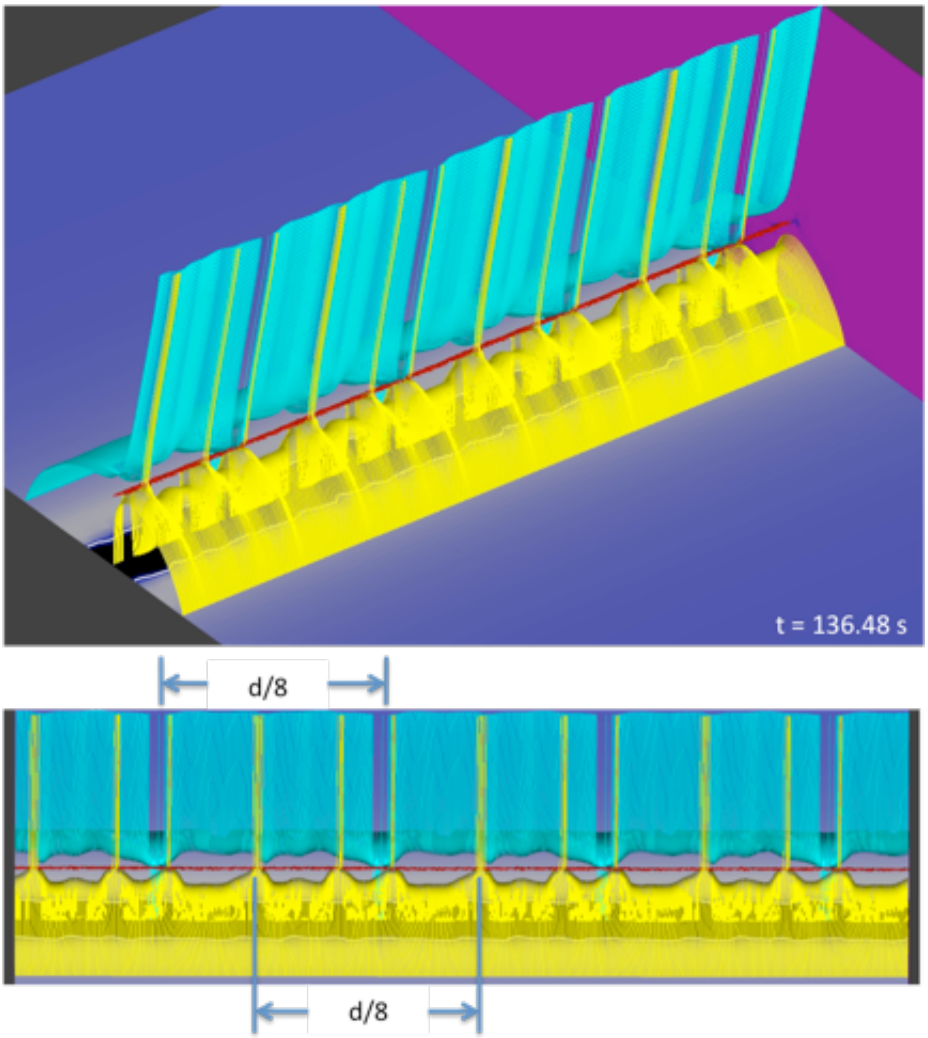

Figure 4.12: Large-scale, periodic structure developing in the field lines along the 3^{rd} dimension with exactly four wavelengths in the domain.

in the field lines with exactly four wavelengths in the domain (see Figure 4.12). This structure is clearly seeded by the finite grid of the calculation, as expected, but only the small-scale structure has any physical importance.

We claim that the small-scale structure in the x direction is directly responsible for the lack of burstiness in the reconnection. Figure 4.8 shows that with regard to the magnetic islands, there is absolutely no symmetry in the x-direction. They are fully 3D and their formation location is random throughout the current sheet. This 3D structure suppresses the secondary instability that generated the bursts of

reconnection seen in previous current sheet studies (Dahlburg et al. (2003), Dahlburg et al. (2005), Dahlburg et al. (2006)). In those studies the system was seeded with 2D perturbations that produced magnetic islands (actually twisted flux tubes) with infinite length in the x-direction. The secondary instability is basically an ideal, kink-like mode of the highly twisted flux tubes. 2D perturbations, however, are somewhat unphysical, because they assume the noise in the system has very long coherence length in a preferred direction. In the present simulations the noise is purely 3D and leads to magnetic islands whose scale is scale in the x-direction is similar to that along the current sheet length. Hence, there is no energy available for a kink mode. Furthermore, the 3D nature of the magnetic islands that we find is likely to limit the effectiveness of the islands in trapping particles, which could have important implications for flare acceleration mechanisms (e.g., Drake et al. (2006)).

One caveat to the conclusions above is that there is no guide field for the reconnection in our simulation. Due to the form of the driving a true neutral sheet is generated. It may well be that if a guide field were present, it would add some coherence along the x-direction so that long flux-tube-like magnetic islands would form. The situation is analogous to the issue of the formation flare ribbons. A strong guide field is necessary in order to provide the reconnection coherence required to produce the distinct ribbon structure. On the other hand, if the guide is too strong, it will suppress any kinking and, hence, the secondary instability (Dahlburg et al. (2003), Dahlburg et al. (2005), Dahlburg et al. (2006)). It is concluded, therefore, that simulations with varying amounts of guide field should be the next step in studying the formation and dynamics of coronal current sheets.

CHAPTER V

Interchange Reconnection and Coronal Hole Boundary Dynamics

In chapter II, section 2.3 we reviewed the topological properties and reiterated the constraints placed on the possible structure of the open field by the quasi-steady models. In particular, the uniqueness conjecture, which states that irrespective of the complexity of the photospheric flux distribution, in the absence of long-lived current dissipation systems, every unipolar region on the photosphere can contain at most one coronal hole (Antiochos et al. (2007)). Note that such a topology in which the open field has well-defined, connected structure is the exact opposite of that of the interchange model. The validity of the uniqueness conjecture and of the quasi-steady model, in general, turns out to depend critically on the properties of interchange reconnection. The key point is that reconnection between open and closed flux is expected to be a generic feature of the solar corona and, therefore, must be incorporated into all coronal models, including the quasi-steady. Due to the magnetic carpet (see Figure **??**; Schrijver et al. (1997)), coronal holes are obviously not magnetically unipolar; they contain numerous small bipoles and, therefore, closed flux. As these bipoles move with the photospheric flows, they will interact with the open field and undergo interchange reconnection. In order for the quasi-steady assumption to remain valid

[0]The material described in this chapter is a modified version of Edmondson et al. (2009)a.

during such open-closed interactions, the magnetic topology must remain smooth, with the open and closed flux topologically well separated. Reconnection, however, requires the formation of current sheets, which are topological discontinuities, and generally give rise to important dynamics, which tend to invalidate the quasi-steady assumption. Consequently, it is not clear that the magnetic topology would remain smooth during actual time-dependent interchange reconnection. Our first objective in this calculation, therefore, is to calculate the rigorous 3D evolution of a closed field bipole as it moves through and interacts with open field, and determine whether the resulting structure and dynamics are compatible with the quasi-steady assumptions or whether the topology becomes discontinuous as in the interchange model.

A related and equally important issue is the interaction of the closed field of a bipole with a coronal hole boundary. Antiochos et al. (2007) analyzed the quasi-steady model, and found that this type of interaction plays a central role in determining the coronal topology, including uniqueness and several other properties. In that work, they argued reconnection would enforce the uniqueness constraint, but this was only a conjecture. The second objective of this calculation is to calculate the time-dependent dynamics of coronal hole boundaries rigorously and test the conjectures. We describe below two numerical simulations that illustrate interchange reconnection in 3D, and discuss the implications for large-scale coronal magnetic field structure and dynamics. It should be emphasized that since the physical systems we calculate are very general and expected to be ubiquitous on the Sun, our results are important for understanding not only the quasi-steady, but any model for the coronal magnetic field, including the interchange.

5.1 The Topology of 3D Interchange Reconnection

In order to perform a rigorous study of interchange reconnection, we first need a physically robust magnetic field. This requires a quantitative description of a com-

plete field topology, not simply a largely two-dimensional sketch of a few open and closed field-lines as used in many previous studies. The simplest and most common magnetic configuration that can describe interchange reconnection is that of a global bipolar field with open and closed regions, and a small-scale closed bipolar region. We can calculate this field exactly with an analytic source-surface model that uses the method of images (Antiochos et al. (2007)). The scalar potential for the source surface field due to a global dipole at sun-center and an arbitrary number of smaller dipoles below the solar surface (see Appendix D) is given by,

$$\Phi(\boldsymbol{x}) = (\boldsymbol{M}_0 \cdot \boldsymbol{x}) \left[\frac{1}{R^3} - \frac{1}{|\boldsymbol{x}|^3} \right] + \sum_i (\boldsymbol{M}_i \cdot \boldsymbol{x}) \left[\left(\frac{R^3}{|\boldsymbol{r}_i|^3} \right) \frac{1}{|\boldsymbol{x} - \frac{R^2}{|\boldsymbol{r}_i|^2} \boldsymbol{r}_i|^3} - \frac{1}{|\boldsymbol{x} - \boldsymbol{r}_i|^3} \right] \tag{5.1}$$

where $\boldsymbol{M}_i$ and $\boldsymbol{r}_i$ are the magnetic dipole and position vectors respectively of dipole source i, and R is the source surface radius. Note that, for simplicity, we have taken the global dipole $\boldsymbol{M}_0$ at Sun center ($\boldsymbol{x} = 0$) to be vertical, parallel to the polar axis, and the smaller dipoles $\boldsymbol{M}_i$ to be horizontal, perpendicular to the radius vector. Their orientation in the horizontal plane, however, can be arbitrary. From this potential, the magnetic field in the volume is obtained directly from $\boldsymbol{B} = \nabla\Phi$, and as can be verified by straightforward calculation, is purely radial at the source surface, $r = R$.

Although the formula above can be used to describe fields of arbitrary complexity, the fundamental topology of interchange reconnection is most clearly seen by focusing on the case of a global dipole and a single near-surface dipole. Such a field is shown in Figure 5.1, for the source surface position at $R = 3\,R_\odot$, a Sun-center dipole of strength $|\boldsymbol{M}_0| = 10$ G oriented toward polar north. The active-region bipole is positioned at $|\boldsymbol{r}_i| = 0.9\,R_\odot$ (below the photosphere) and 49.5° latitude (i.e., north of the equator inside the northern coronal hole), with a magnitude $|\boldsymbol{M}_i| = 50$ G oriented along the surface (i.e., with no radial component) toward the south pole. As expected, the

global dipole produces a large-scale, axi-symmetric coronal magnetic field consisting of polar coronal holes and closed flux at lower latitudes (Figure 5.1). The near-surface dipole produces a small bipolar flux distribution that, for the particular parameters selected, is completely inside the northern, positive-polarity coronal hole. Figure 5.1b shows a close-up of the photospheric flux distribution in the hole. Note the presence of the closed polarity inversion line surrounding the negative-polarity region of the bipole. The field near this polarity inversion line is low-lying and must close across it; consequently, there must be some closed flux inside the coronal hole. This is true irrespective of the size of the negative polarity region. There must be a closed field region associated with ***every*** bipole in a coronal hole.

Figure 5.1b shows the coronal magnetic field above the small bipole. Its structure consists of a hemispherical volume of closed flux surrounded by a background of open coronal-hole flux. The closed-field is topologically separated from the open by a dome-shaped surface. This topology is simply that of the well-known embedded bipole with its fan surface, spine lines, and null point (see chapter III, section 3.2; Greene (1988), Lau & Fin (1990), Antiochos (1990), Priest & Titov (1996)). The intersection of the fan surface with the photosphere forms a closed separatrix curve that defines the boundary between the flux that closes across the polarity inversion line to that connecting to the source surface. In other words, this photospheric separatrix curve is a coronal hole boundary. All the field lines whose photospheric footpoints lie on this curve can be considered to converge onto the null point, where they split into the inner and outer spine lines. It should be emphasized that although the topology is discontinuous at the fan and spines (i.e., the magnetic connectivity is clearly multi-valued there), the magnetic field itself is smooth everywhere. In fact, formula (5.1) yields a potential field that is analytic everywhere in the interior of the volume. Furthermore, there is no mixing of open and closed field. All of the flux inside the fan is closed, whereas all of the flux outside is open. The fan, itself, is a

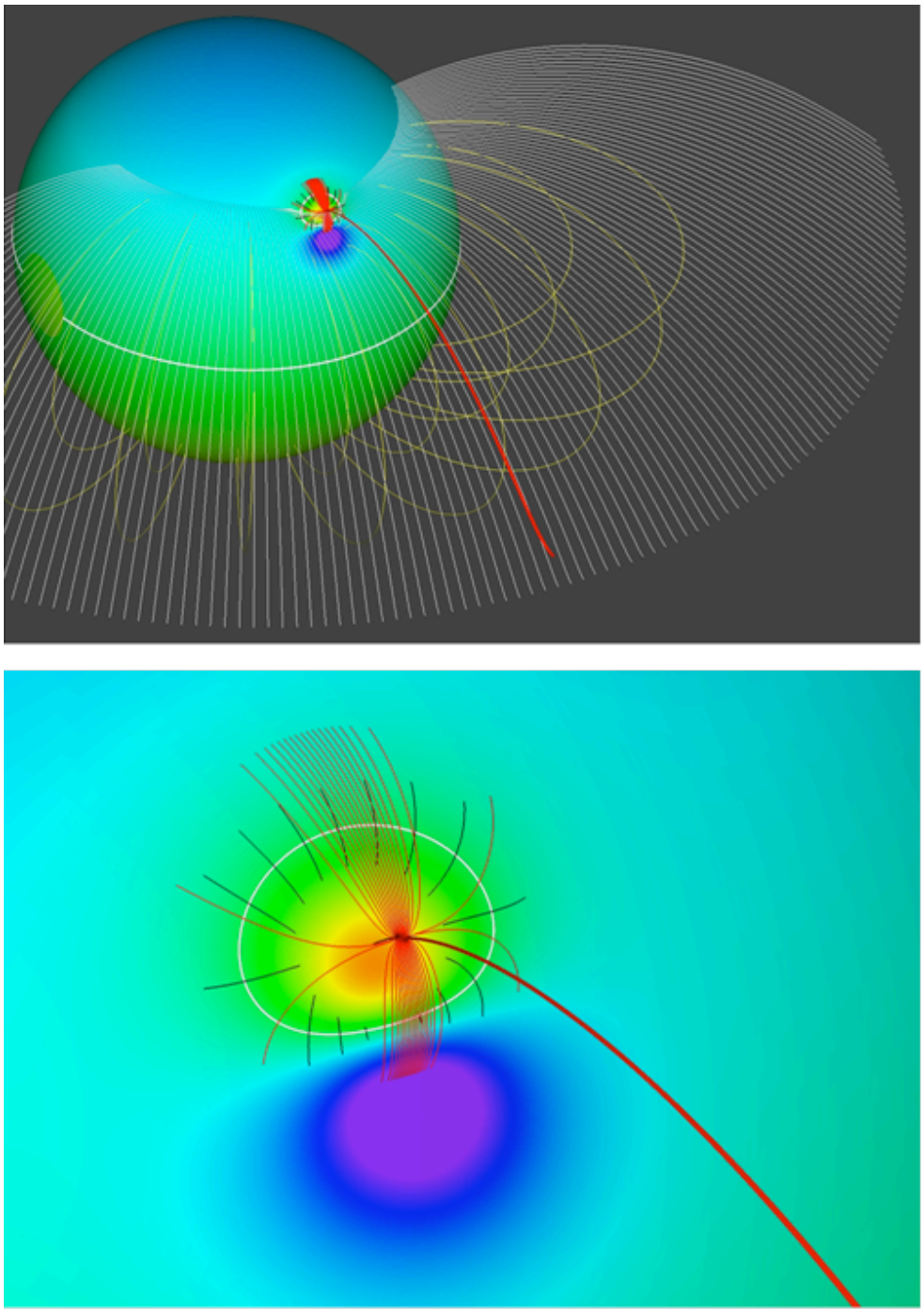

Figure 5.1: 3D Global Potential Field Configuration: Magnetic topology of a small near-surface dipole and global dipole. a) Colored contours show magnitude of radial field at photosphere, the two white curves indicate polarity inversion lines (radial field vanishes). The yellow field lines above the surface correspond to streamer belt closed flux and the white field lines to the open, coronal hole flux that maps to the source surface. b) Close-up of the field near the embedded bipole showing the outer fan field lines and spine.

singular surface as with every coronal hole boundary in that the fan field lines split at the null, so they can be considered to both be open and closed.

The field of Figure 5.1 is the fundamental topology in which interchange reconnection takes place. It is, by far, the most common multi-polar magnetic topology on the Sun, because it is present whenever a parasitic polarity region on the photosphere occurs inside some larger, unipolar flux. This topology is expected for essentially every magnetic carpet, or larger, bipole on the photosphere. Numerous observations show clear evidence for this topology in coronal holes (e.g., Golub et al. (1974)), and both potential and force-free extrapolations of almost every observed photospheric flux distribution find this topology in both open and closed magnetic regions (Aulanier et al. (2007), Fletcher et al. (2001), Luhmann et al. (2003)).

The key question for the coronal models is whether the embedded bipole topology remains smooth, with well-separated regions, once photospheric motions stress the field so that closed and open lines interact via interchange reconnection. A rigorous answer to this question requires solution of the fully-dynamic MHD equations, as presented below, but we claim that considerable insight can be obtained by considering the heuristic model for the stressing and reconnection illustrated by Figure 5.2. There are two basic assumptions underlying this model. First, we can separate the ideal and resistive response of the system so that it evolves, first, purely ideally to some quasi-equilibrium, and then it relaxes by reconnection. This approach is not without justification, because reconnection will not begin until the system has formed substantial current sheets. The second assumption is that the two flux systems on either side of the fan surface move independently of each other, except that they always share a common boundary, the fan surface, which itself is free to deform. Again this assumption has justification; since the photospheric connectivity is discontinuous at the fan, the magnetic stresses due to photospheric driving will be discontinuous there, which will give rise to discontinuous motions in the corona. Note that even if

viscosity were included in the system so that no true discontinuity forms, we would expect the gradients of the motions across the fan to grow exponentially in time and, consequently, the currents there to reach the dissipation scale rapidly.

We can use this model to determine how the embedded-bipole topology would respond to a simple footpoint motion that displaces the closed flux system bodily to the right, while keeping the open flux more-or-less fixed (Figure 5.2b). For such a stressing, we expect that, during the ideal response, the inner spine line connecting to the parasitic polarity dislocates from the outer spine connecting to the source surface. Since each spine line fans out at the null to form its own surface, such a dislocation implies that the fan surface separates into two surfaces that are in contact everywhere, but with field lines that are misaligned. The effect of dislocating the spine lines and fan surfaces, therefore, is to deform the null point into a 3D null patch and to form a 3D current sheet at the fan. If the system were purely ideal then, in principle, it could achieve an equilibrium state containing these discontinuities.

A small resistivity can now be included to consider the subsequent evolution due to reconnection. The system will attempt to relax, as much as possible, back to the potential state to minimize its energy. In particular, reconnection at the null-patch can destroy the current sheets and, as illustrated in Figure 5.2c, deform the null patch back to a point, thereby realigning the spines, and if possible, the fans. Note that the evolution just described is nothing more than the 3D generalization of Syrovatskiis classic current sheet formation and null-point reconnection theory (e.g., Syrovatskii (1981), Antiochos (1996)).

The arguments above suggest that the topology resulting from reconnection will maintain clearly separated open and closed field, as in the initial state. A key point, however, is that since reconnection conserves any helicity injected to the system by the photospheric motions, it cannot undo the photospheric motions and bring the system back to a purely potential field. In the evolution illustrated by Figure 5.2c, the spine

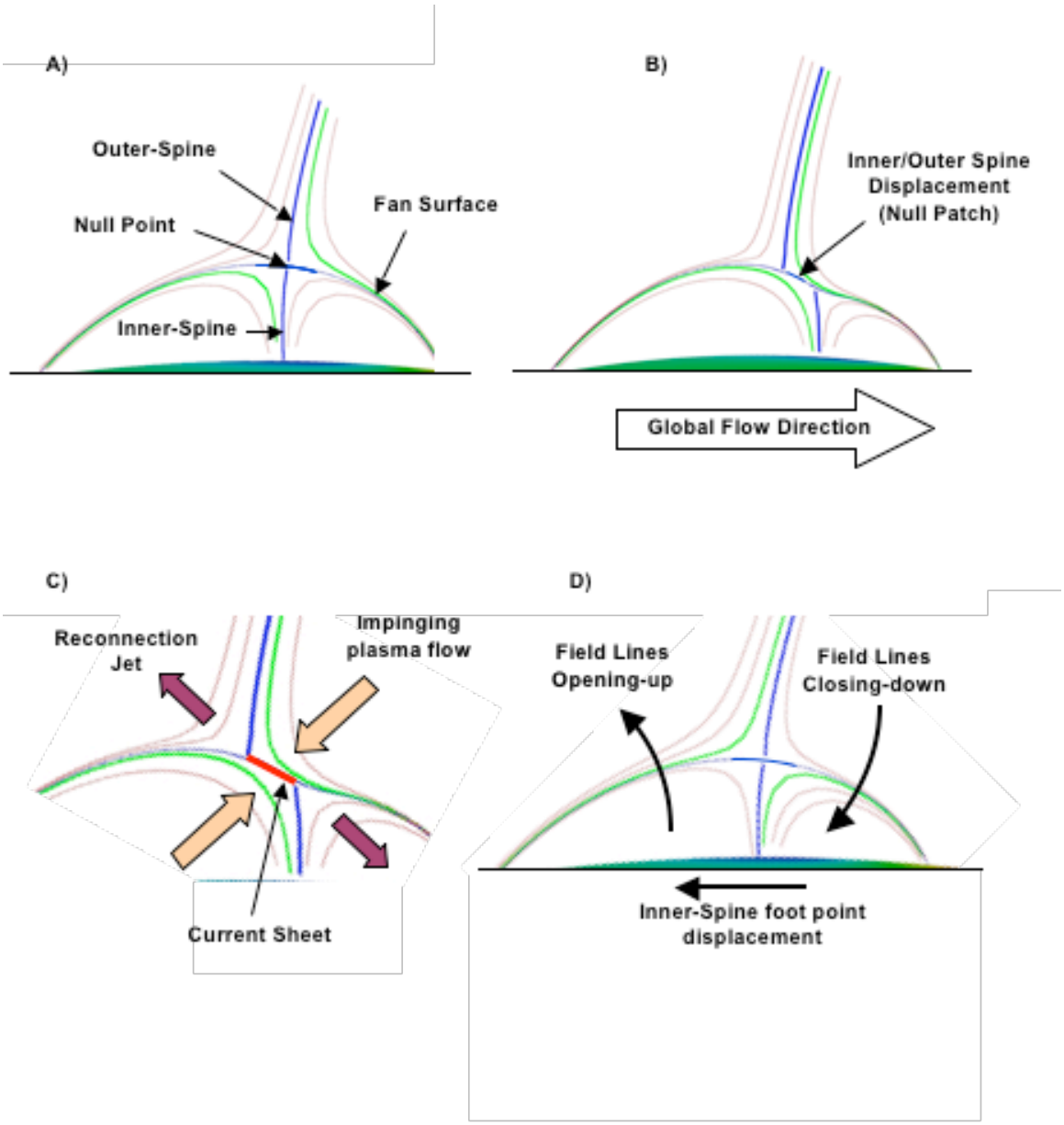

Figure 5.2: Interchange reconnection schematic: A) Initial field configuration. B) Stressed field configuration. C) Current sheet and reconnection jets D) Interchange reconnection flux exchange

lines do not actually move, instead different flux tubes become the spines because of interchange reconnection. It may be, therefore, that the lowest energy state available to the system under the helicity constraints is one with long-lived (up to a dissipation time) current sheets. In fact, such a state seems inevitable if the photospheric motion is large, so that the dislocation of the spines is large. It is evident from Figure 5.2 that reconnection shifts the inner spine to the left by transferring closed flux from overlying the left side of the polarity inversion line to the right. The amount of flux available for such transfer, however, is limited; consequently, if the ideal motions produce too large a dislocation of the spines, reconnection will not be able to realign them.

Furthermore, there is no guarantee that reconnection will even preserve the basic spine-fan topology. 3D reconnection is likely to produce topologically complex structures so that the boundary between open and closed field becomes chaotic and the identification of a 1D spine line or a 2D fan surface is no longer possible. This hypothesis seems even more likely if the closed bipole moves so that it encounters a large-scale coronal hole boundary. In that case the outer spine line would have to change from open to closed (or vice versa) and the fan would interact with the hole boundary. In order to determine the evolutionary topology and dynamics of 3D interchange reconnection, we calculate numerically two simple, but highly illustrative cases. In the first case (open-to-closed) an embedded bipole moves through an open field region and across a coronal hole boundary, into a closed field region. In the second case (closed-to-open), we consider the reverse situation where a bipole moves from the closed field into the open.

We solve the set of 3D compressible, ideal MHD equations (2.8, 2.9, 2.13, and 3.10, with $\eta = \nu = \mathrm{S} \equiv 0$) in spherical coordinates with the ARMS code. The ratio of specific heats γ is taken to be 5/3. The ideal gas law (equation 2.14) is used as the plasma equation of state. Gravity, given by $g = -\frac{GM_{\odot}r}{r^3}$, is included in

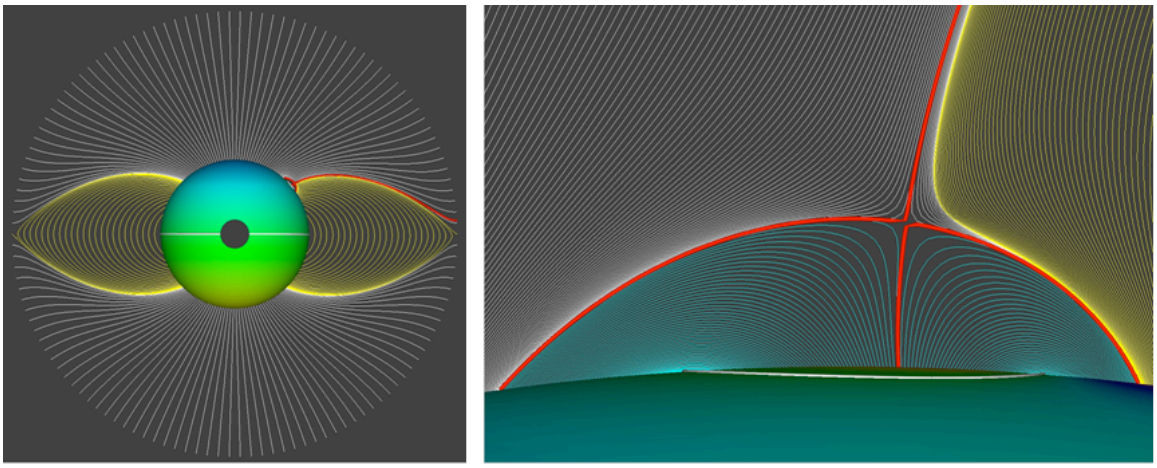

Figure 5.3: Global magnetic field topological structure. Open field coronal hole regions are shown in white. The closed field, streamer belt region is shown in yellow. The spine fan topological characteristics of the embedded bipole are shown in red.

the calculations, but its effects are small with regard to the interchange reconnection dynamics. The primary reason for adding gravity is to keep the coronal plasma beta from becoming too large at large heights.

The simulation domain consists of the spherical volume bounded below by the photosphere at $r = 1\,R_\odot$ and bounded above by the source surface, which is taken to be at $r = 3\,R_\odot$. Within this domain, the initial magnetic field configuration is given by the analytic expression (5.1). The origin-dipole strength is set to $|\boldsymbol{M}_0| = 10$ G, which yields a field strength of approximately 5 G at the photosphere far from the embedded bipole. A single dipole with magnitude $|\boldsymbol{M}_i| = 50$ G, is placed below the surface at $|\boldsymbol{r}_i| = 0.9\,R_\odot$, the angular position of which varies between the two cases, although near the global coronal hole in both cases. Figure 5.3 shows the field for the case of the bipole initially in the coronal hole.

A minor point to note is that we set the global dipole to be aligned with the y-axis ($\theta = \frac{\pi}{2}, \phi = \frac{\pi}{2}$) of the coordinate system rather than the vertical, as is the usual case. This implies that the coronal holes now occur centered about two points on the equator of our spherical coordinate system (at $\phi = \pm\frac{\pi}{2}$) rather than the

coordinate poles (Figure 5.3 left). Furthermore, we select the parameters of the embedded dipole so that it is located at and oriented along the coordinate equator, and impose photospheric flows that move the resulting embedded bipolar region along this equator toward a coronal hole boundary. The reason for this choice of geometry is that the poles have metric singularities in spherical coordinates, making them difficult to treat numerically, especially in 3D. The simplest and most effective procedure for dealing with these singularities is to remove from the computation domain a small conical region centered about each pole, ($\theta < 11.25°$ in the north and $\theta > 168.75°$ in the south), visible in Figure 5.3 (left) as the holes in the Sun. We chose the magnetic and velocity fields so that all the structure and dynamics occurs at the equator, as far from these conical regions as possible. Note that there is no solar rotation in our simulation; hence, our choice of parameters for the magnetic field and flow fields corresponds only to a trivial rotation of coordinate axis and has no physical consequences.

Since the initial magnetic field is potential, we set the initial plasma distribution to be spherically symmetric and in hydrostatic equilibrium:

$$T(r) = T_0 \left(\frac{R_0}{r} \right) \tag{5.2}$$

$$n(r) = n_0 \left(\frac{R_0}{r} \right)^{\mu - 1} \tag{5.3}$$

where the exponent $\mu = \frac{R_0}{H_0} = 11.66$. The pressure scale height $H_0 = \frac{2kT_0}{mg}$. The surface parameters are initialized to: $T_0 = 1$ MK, $P_0 = 1$ dyne cm^{-2}. These plasma profiles and parameters were selected so that the plasma beta would be small throughout the domain. We find that the plasma beta reaches a minimum of approximately 0.0325 inside the strong field of the bipole and an average value ≤ 0.1 near the source

surface; consequently the system is low-beta, as in the true corona. Furthermore, the gravitational energy of the plasma is small compared to the magnetic field energy. We emphasize, however, that although the system as a whole is low beta, the plasma pressure does play an important role in the evolution. Near the coronal null the plasma pressure dominates; therefore, the formation of the current sheets and the subsequent reconnection dynamics are critically dependent on the plasma evolution.

Similar to the plasma beta, the Alfvén speed varies considerably over the domain, but an average global Alfvén speed based on the total magnetic energy E_M, and total material M_C in the corona, can be defined as,

$$V_A = \sqrt{\frac{2\,E_M}{M_C}} \tag{5.4}$$

With this definition, the Alfvén speed in both simulations is approximately 400 $\times 10^5$ cm s^{-1}. An Alfvén time of a little less than 115 minutes ($\tau_A \approx 6900$ s) is similarly defined using a global length scale of 4 R_S about the length of the largest loops).

At the lower boundary, the photosphere, we impose line-tied, no-flow-through ($V_r = 0$) conditions. In both simulations, the embedded bipole is driven toward the coronal hole boundary by an incompressible surface flow applied at the photosphere, Figure 5.4. The flow field is constructed as a 1st-order Fourier trigonometric series in the spherical angular coordinates. The azimuthal component, V_ϕ is assumed to have cosine profiles in both colatitude (θ) and longitude (ϕ) angular coordinates, and corresponding wave numbers that yield adjoining vortices ($k_\theta = 1.0$ and $k_\phi = 0.5$). The polar flow component, V_θ, is then calculated by applying the vanishing divergence condition for this 2D flow field.

$$V_\phi\,(\theta, \phi, t) = V_\phi\, f\,(t)\; cos\left(2\pi k_\theta \frac{\theta - \theta_C}{\theta_H - \theta_L}\right) cos\left(2\pi k_\phi \frac{\phi - \phi_C}{\phi_H - \phi_L}\right) \tag{5.5}$$

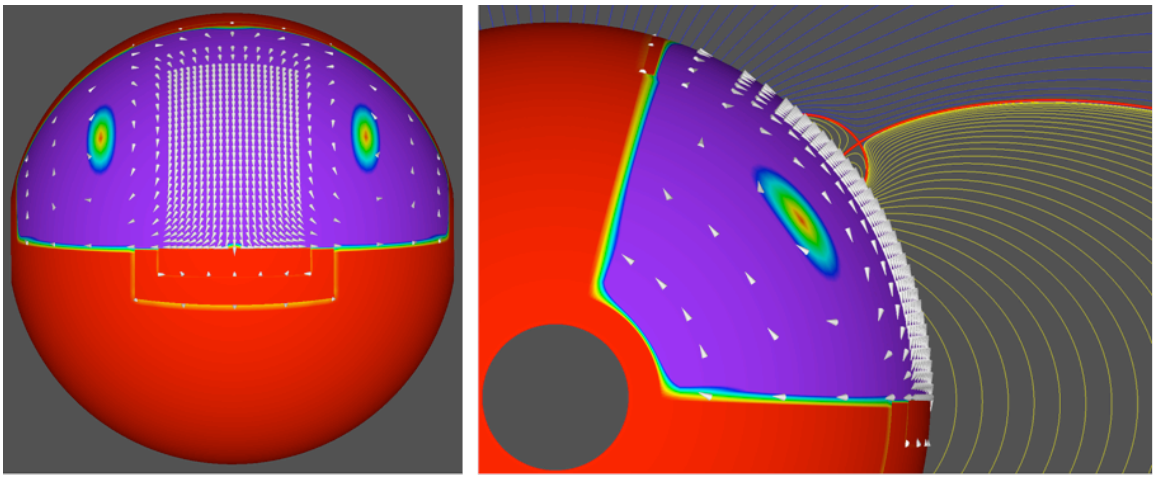

Figure 5.4: Driving flow field vectors. Color scale: red indicates zero velocity magnitude, purple indicates spatial extent of flow field.

$$V_\theta\left(\theta,\phi,t\right) = V_\theta\, f\left(t\right)\left(\frac{k_\phi}{k_\theta}\right)\left(\frac{\theta_H-\theta_L}{\phi_H-\phi_L}\right)\left(\frac{1}{sin\theta}\right) sin\left(2\pi k_\theta\,\frac{\theta-\theta_C}{\theta_H-\theta_L}\right) sin\left(2\pi k_\phi\,\frac{\phi-\phi_C}{\phi_H-\phi_L}\right) \tag{5.6}$$

$$f\left(t\right) = \frac{1}{2}\left[1-cos\left(2\pi k_t\,\frac{t}{t_H}\right)\right] \tag{5.7}$$

where, $k_t = 0.5$, and $t_H = 1.5\times10^4$ s $= 2.17\ \tau_A$. The magnitudes of these angular velocity components are set to be approximately an order of magnitude smaller than the average Alfvén speed defined above; $|V_\theta| = 1.875\times10^6$ cm s^{-1} $= 0.047\,V_A$, and $|V_\phi| = 5\times10^6$ cm s^{-1} $= 0.125\,V_A$. Note, however, that the driving speeds above are much smaller than the local Alfvén speed in the embedded bipole region, which is at least an order of magnitude larger than V_A. In order to minimize transient wave effects as the motions start, the velocity magnitude has a shifted cosine profile in time. The flow is chosen to have a broad latitudinal range ($\theta_H = 0.9\,\pi$, $\theta_C = 0.5\,\pi$, $\theta_L = 0.1\,\pi$) in order to minimize the distortion of the flux distribution within the embedded bipole as it moves across the photosphere (Figure 5.4 left).

We use the velocity expressions above to describe the flows for both the case with the bipole initially in the coronal hole and the case with it initially in the closed field, except for a change in the longitudinal extent of the motions (and the obvious change in sign). In the first case, initially in the coronal hole, we set $\phi_H = 0.4\,\pi$, $\phi_C = 0.2\,\pi$, $\phi_L = 0.0$; whereas for the second case, we set $\phi_H = 0.75\,\pi$, $\phi_C = 0.375\,\pi$, $\phi_L = 0.0$. These values for the flow parameters were selected so that the bipole would definitely cross the coronal hole boundary in both cases.

At the top boundary, the source surface, we impose no-flow-through, free-slip conditions. The free slip conditions allow us to model the physical distinction between open and closed field without having to incorporate in the simulations the added complexity of a solar wind. Field lines that reach the source surface are open, because only one end is line-tied at the photosphere; whereas, those that do not are closed, because both ends are line-tied. The no-flow-through condition allows us to preserve the open or closed property of a field-line under an ideal evolution. In our simulations, a field line can change from being open to closed or vice versa only as a result of reconnection.

Finally, Figure 5.5 shows the numerical grid that is used for the simulations. We start with a base level consisting of $2 \times 3 \times 6$ blocks distributed uniformly in $\{r, \theta, \phi\}$ with 8^3 grid points per block. The initial minimum resolution is 3 levels refined above the $2 \times 3 \times 6$ base, and the grid is then refined a maximum of 6 levels over a volume encompassing the entire photospheric flow field and to a radius above the magnetic null point. The resolution at this highest refinement level corresponds to approximately 2.2×10^9 cm by 1.875° by 1.875°, which is much smaller than the scale of the embedded bipole or the flow field. Note that the grids are nearly identical for the two cases, except for minor adjustments due to the different initial position of the bipole and the latitudinal extent of the flow fields. In order to quantitatively compare the results of the two cases we have kept the grid fixed throughout the two

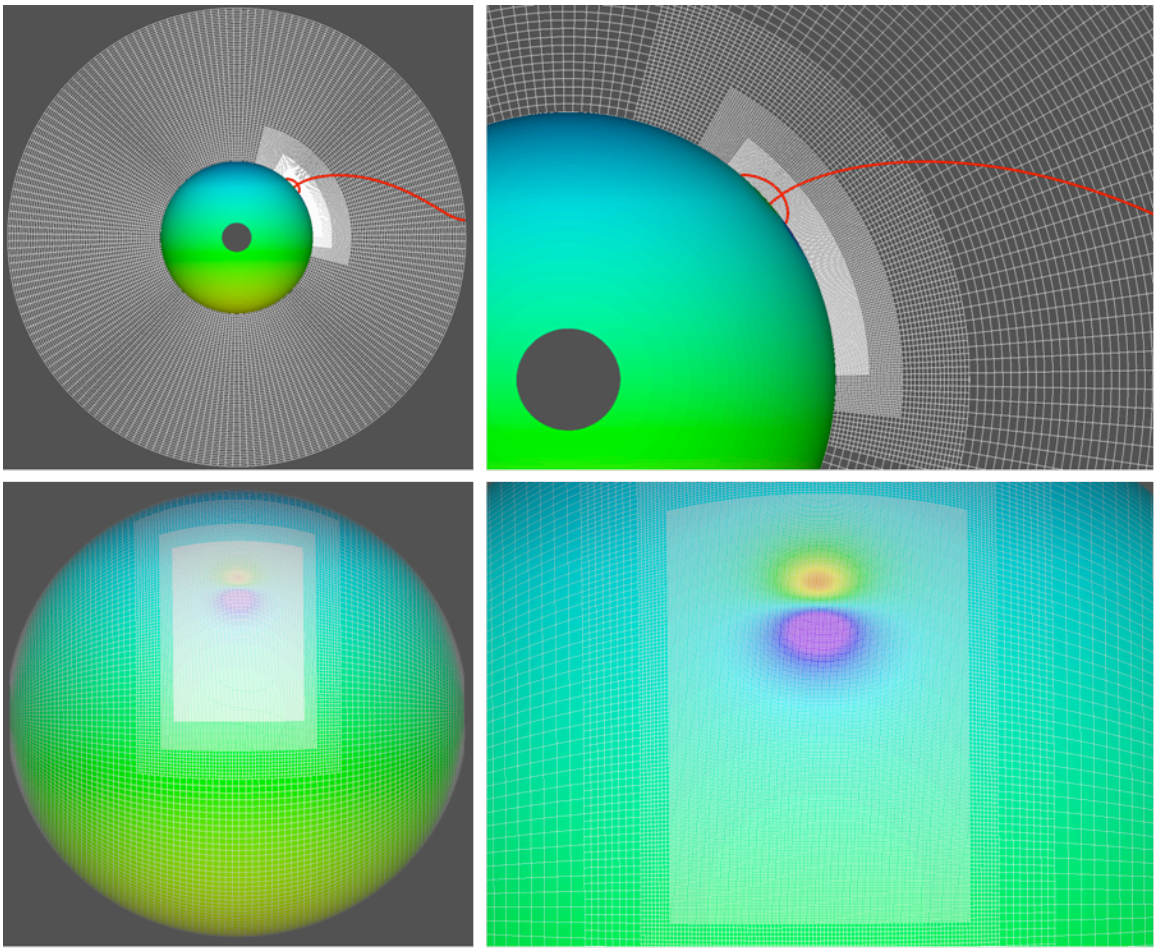

Figure 5.5: Numerical grid structure. Top panels: Grid refinement in the radial direction. Bottom panels: Grid refinement across the surface. Note, the initial minimum refinement is refined to 3 levels above the base $2 \times 3 \times 6$ blocks.

simulations.

5.2 Results: Open-to-Closed Convection-Driven Dynamics

Figure 5.3 shows the initial configuration for this simulation. The near-surface dipole is located at a latitude of 36.4°, which places the outer spine inside the coronal hole, but very near the coronal hole boundary (Figure 5.3 right). We chose this initial location so that the interaction between the embedded bipole field and the coronal hole boundary would occur before extreme distortion of the closed bipole field. The evolution for the convection of the bipole from the open to closed field regions can be considered to consist of 4 phases:

***Phase* 1 :** From $t = 0$ to $t \approx 5900$ s, the bipole moves toward the coronal hole boundary with evidence for only minor reconnection. Due to the finite grid of the simulation, some numerical resistivity is always present; therefore, if one examines field lines on a fine enough scale (less than the grid size), it is always possible to find some systematic flux transfer indicative of reconnection. The null point, however, remains almost undistorted during phase 1, and only weak currents (scale size substantially larger than the grid size) form there, so any reconnection is slow. The distance traveled by the inner spine during this phase is approximately 34 $\times 10^8$ cm, which is a small fraction of the scale of the bipole (the diameter of the polarity inversion line in the direction of the motion is approximately 170 $\times 10^8$ cm, see Figure 5.3 left). As a result of the photospheric motions, the closed field region in front of the bipole is compressed, generating stresses on the open field. These stresses displace the inner and outer spines, exactly as in Figure 5.2, resulting in the eventual formation of a current sheet at the deformed null.

Figure 5.6 presents a close-up of the null region, at $t = 0$, 5,880, 7,480, and 10,000 seconds. The white lines indicate initially open field lines and the yellow

closed. Plotted on the vertical symmetry plane that bisects the bipole are filled contours of current density and 10 black contours of beta with magnitude ranging from 1 to 100. This high-beta region corresponds physically to the null volume where the field is susceptible to strong distortion. It is evident from Figure 5.6 that the deformation of the null region stays small up through $t \approx 5800$, because the beta contours remain approximately circular. The currents clearly build up as the bipoles motion progresses, but at this time they are still small compared to the currents produced by the driving motions.

***Phase* 2 :** From $t \approx 5900$ s to $t \approx 7500$ s the continued motion of the bipole results in sufficient deformation of the null region that the structure of the currents there decreases down to the grid scale, and rapid reconnection occurs. This interchange reconnection exchanges the closed field of the bipole with the open field between it and the coronal hole boundary. It can also be seen in Figure 5.6. Note that the panel corresponding $t = 7480$ has substantially fewer white field lines to the right of the closed fan surface.

We find that once interchange reconnection turns on, it stays on and smoothly moves the outer spine through the open field and closer to the coronal hole boundary. There is little evidence for explosive dynamics such as bursty reconnection or large mass outflows. The dynamics produced by the interchange reconnection in this evolution are dramatically different than those in our simulations of breakout CME's (e.g., Lynch et al. (2008)) or of coronal jets driven by magnetic twist (Pariat et al. (2009)). The reason for this difference is that in the case of the CME and jet calculations, the photospheric motions are chosen so that that the magnetic stress is kept away from any separatrix surface. As a result, substantial free magnetic energy builds up inside the closed field volume until it is released by an explosive burst of reconnection, usually accompanied by some ideal instability or loss-of-equilibrium. In contrast, the

large-scale translational motions of the simulation in this chapter tend to move the bipole bodily, producing little magnetic stress inside its closed field. We find that only weak volumetric currents appear inside the fan and very little free energy is stored there.

The motions do produce significant stress, however, on the large-scale field where the connectivity is discontinuous, the outer fan separatrix and outer spine. This stress leads to the formation of current sheets at the fan and null region, which are quickly dissipated by reconnection without large energy release or strong impulsive behavior, at least, for the Lundquist number of this simulation (approximately 1000). Our result indicates that in order to obtain the large energy release to explain jets or plumes, for example, the closed field inside the fan would have to be stressed by small-scale photospheric motions as in Pariat et al. (2009) or emerge through the photosphere containing large stress. Both effects are almost certain to be true in the Sun due to the presence of subsurface convective flows and the photospheric granule and supergranule motions.

***Phase* 3 :** Interchange reconnection continues until eventually the outer spine reaches the coronal hole boundary. At some instant around $t \approx 7480$ s the null of the closed field bipole lies exactly on the separatrix surface between open and closed field and, hence, the outer spine becomes a separator line that connects the bipole null and the null at the source surface. Of course, this is a singular event. At this time the coronal hole boundary can be taken to jump discontinuously from lying in front of the bipole to behind, so that the fan bipole enters the main closed field region (Figure 5.6). Note that we see no evidence for any special dynamics during this period. The transition from the bipole being surrounded by open field to closed appears smooth. This result is to be expected, because the bipole field has such small scale that its interaction with the large-scale closed field just outside the coronal hole boundary is essentially

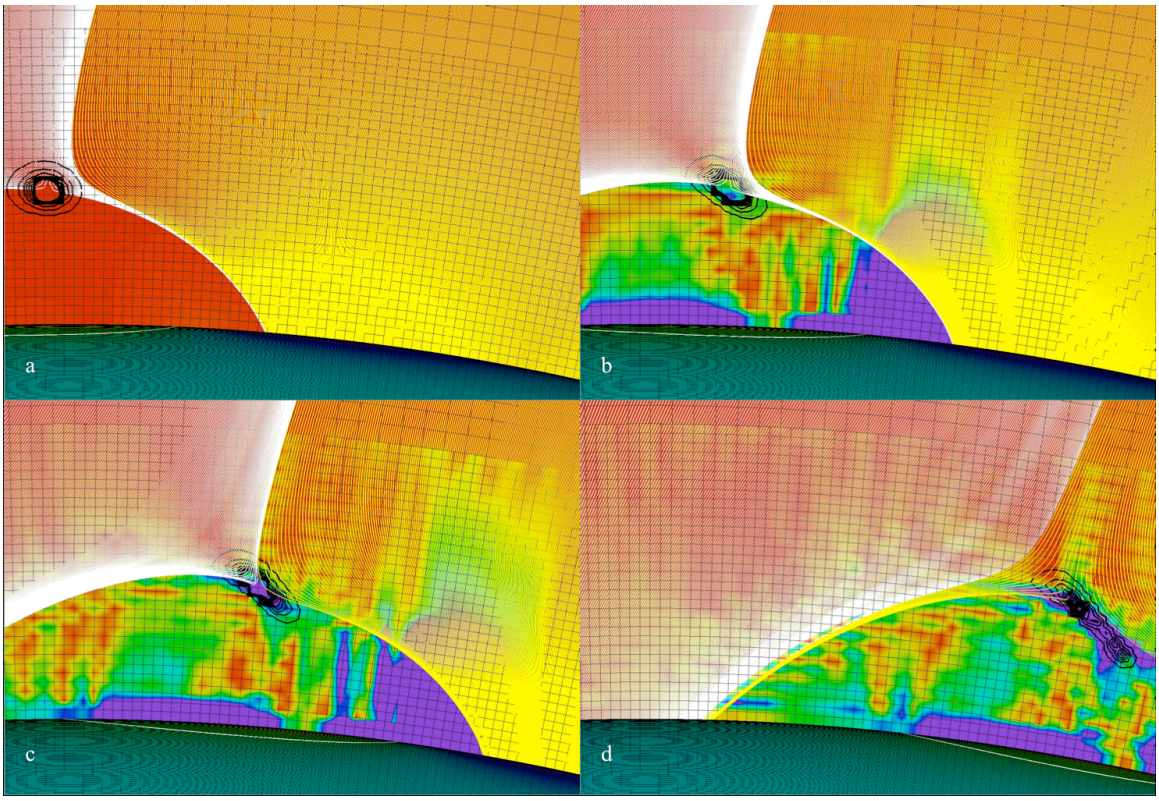

Figure 5.6: Open-to-closed evolution. a) $t = 0$ s, initial configuration. b) $t = 5{,}880$ s, current sheet formation. c) $t = 7{,}480$ s, global topology change of external spine. d) $t = 10{,}000$ s, final configuration.

identical to that of the open field inside that boundary. As far as the magnetic field of the bipole is concerned, there is negligible difference between the open and closed field regions. Furthermore, this result agrees with observations, which indicate that, in general, no special dynamics are seen at coronal hole boundaries (Kahler & Hudson (2002)).

***Phase* 4 :** During the final phase of the evolution, from $t \approx 7500$ s to $t = 10000$ s the bipole field moves steadily through the closed field by reconnecting with this flux. Note that although the total duration of the imposed flows is 15000 s, we end the simulation at $t = 10000$ s; consequently the bipole is still being driven even at the end of the final phase. The reconnection during this phase is no longer of the interchange

type, because it involves two closed field systems, but there appears to be little change in the dynamics. The current sheet at the deformed null region keeps increasing in length while decreasing in width (Figure 5.6), and the reconnection remains smooth with no apparent burstiness. We expect that if the bipole driving were to stop, the current sheet would decrease in length and the reconnection would eventually end, albeit with some residual currents left in the system.

A critical issue is the topology of the open-closed boundary throughout this four-phase evolution. The quasi-steady models require that the reconnection maintains a smooth topology with well-separated open and closed field regions (Antiochos et al. (2007)). In order to determine the topology we have traced a dense sample of field lines from the source surface down to the photosphere and plotted their location there. Figure 5.7 shows the results for the open to closed simulation at three times during the simulation.

The black region in each panel is the area on the photosphere that is magnetically connected to the source surface, in other words, the open field region. Also shown are the polarity inversion lines on the photosphere (thin black lines) and filled contours of B_r at the photosphere, with red indicating strong negative and blue strong positive field. We note that in the first panel, at $t = 5069$ s, the bipole is completely surrounded by open field, so it is still in the coronal hole. The coronal hole forms an open corridor that extends around the negative polarity spot, but this corridor is fully connected at both ends to the main coronal hole open field region. This result shows that the mere observation of open field in strong active region magnetic fields does not constitute evidence for the validity of the interchange model. The quasi-steady models can easily account for such observations.

As the bipole moves toward the closed field region, this open-field arch decreases in width due to interchange reconnection until by $t = 7083$, only a very thin corridor of

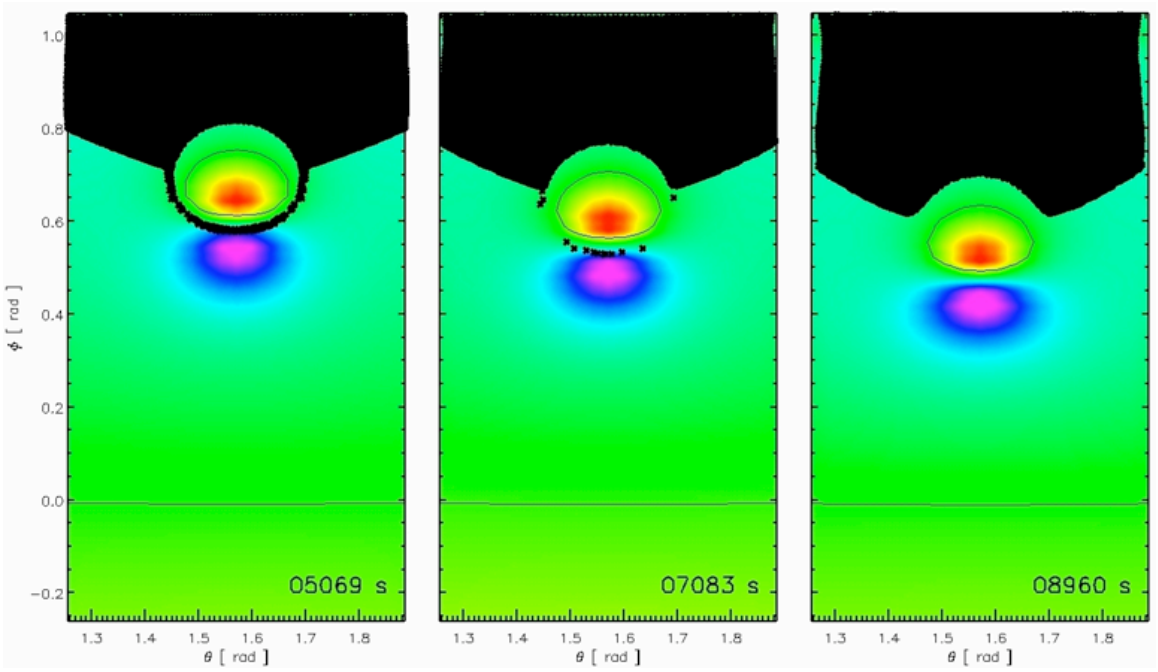

Figure 5.7: Open-to-closed: Photospheric open flux disribution at t = 5,069, 7,083, and 8,960 seconds.

open field remains (Figure 5.7). The key question is whether this corridor continues to be well-connected to the main open field region or whether it breaks up into disconnected segments. It does appear from Figure 5.7 that the corridor has breaks, but this is an artifact produced by the finite resolution of the numerical grid and the geometry of the photospheric flux distribution. Since the negative flux is concentrated into a spot just above the strong positive flux, it is relatively easy to find field lines that connect to this negative spot. This result is also evident in the initial potential field (Figure 5.1). If one draws a line connecting the centers of the positive and negative spots, the fan surface has a high density of field lines in that direction but low density in the perpendicular direction, so that the fan surface appears to have gaps in this perpendicular direction. We know from the analytic expressions, however, that the fan forms a smooth continuous surface. In topological terms, the reason for these apparent gaps is that the eigenvalues of the field Jacobian evaluated at the initial null point are highly asymmetric, so that the one corresponding to the eigenvector

parallel to the center-to-center line is substantially larger than the eigenvalue for the perpendicular direction (e.g., Lau & Fin (1990)). This asymmetry is maintained as the spots move and, hence, the open field corridor that eventually develops also appears to have gaps. However, when we plot field lines from the photosphere upwards with very high resolution, we find that at $t = 7083$ there are always open field lines separating the closed flux that connects to the negative spot from the closed flux that connects across the equatorial inversion line.

As the bipole moves toward the closed field region, the open field corridor continues to thin until eventually the outer spine coincides with the open-closed field boundary boundary, so that the corridor achieves singular width. Since our simulation has finite temporal and spatial resolution, we cannot capture this critical event when the corridor is singular. It is possible that near this time the open field corridor breaks up into discontinuous pieces, because the deformation of the null and the presence of current sheets there cause the outer spine to deform to a sheet-like structure and the fan to some fractal volume. We do not see such topologies in the simulation, the outer spine remains ray-like, but this may be due only to the finite resistivity inherent to our numerical code. Even if such singular topologies do occur, we expect that their structure would be only of order the dissipation scale and, consequently, disappear quickly. Our simulation shows only a smooth topological transition for the bipole as it moves from the open to closed regions, in good agreement with the results of the quasi-steady models (Figure 5.7).

5.3 Results: Closed-to-Open Convection-Driven Dynamics

The closed-to-open case is, for the most part, closely analogous to the open-to-closed evolution. The near-surface dipole is initially located at the latitude of 36.0° placing the outer spine inside the closed field, very near the coronal hole boundary in order to minimize distortion during the interaction (Figure 5.8a). Again, we organize

the evolution of the bipole from the closed to open field regions into 4 phases:

***Phase* 1 :** From $t = 0$ to $t \approx 3758$ s, the bipole moves toward the coronal hole boundary with little reconnection or current sheet formation. The distance traveled by the inner spine during this phase is approximately 80 $\times 10^8$ cm, about half of the dipole polarity inversion line diameter. The photospheric motions expand the entire global closed field region, generating magnetic field stresses behind the dipole. The inner and outer spines separate as a result of these stresses, eventually deforming the null and generating a current sheet. Figure 5.8 shows the evolution similar to the open-to-closed case, at $t = 0$, 3,758, 9,273, and 10,000 seconds. Clearly, from Figure 5.8, the deformation of the null region stays small up through $t \approx 3758$ s as the beta contours are still approximately circular. The currents within the null region build up as the bipole motion progresses, but they are still small compared to the driving motion currents.

***Phase* 2 :** From $t \approx 3758$ s to $t \approx 9273$ s, the continued motion deforms the null region, decreases the current structure to the grid scale, and initiates rapid reconnection. Though not strictly interchange reconnection because the bipole is embedded in a globally closed field region, reconnection exchanges the closed flux inside the bipole fan separatrix with the large-scale closed field. Once again we find that the system evolves by continuous reconnection, smoothly shifting the outer spine through the embedding field, with little evidence of bursty reconnection or large material outflows. As above, only weak volumetric currents appear inside the fan and very little free energy is stored there.

An important difference between this case and the open-to-closed case is that the displacement required for the bipole to cross the coronal hole boundary is much larger than before. The required displacement is approximately 680 $\times 10^8$ cm, nearly

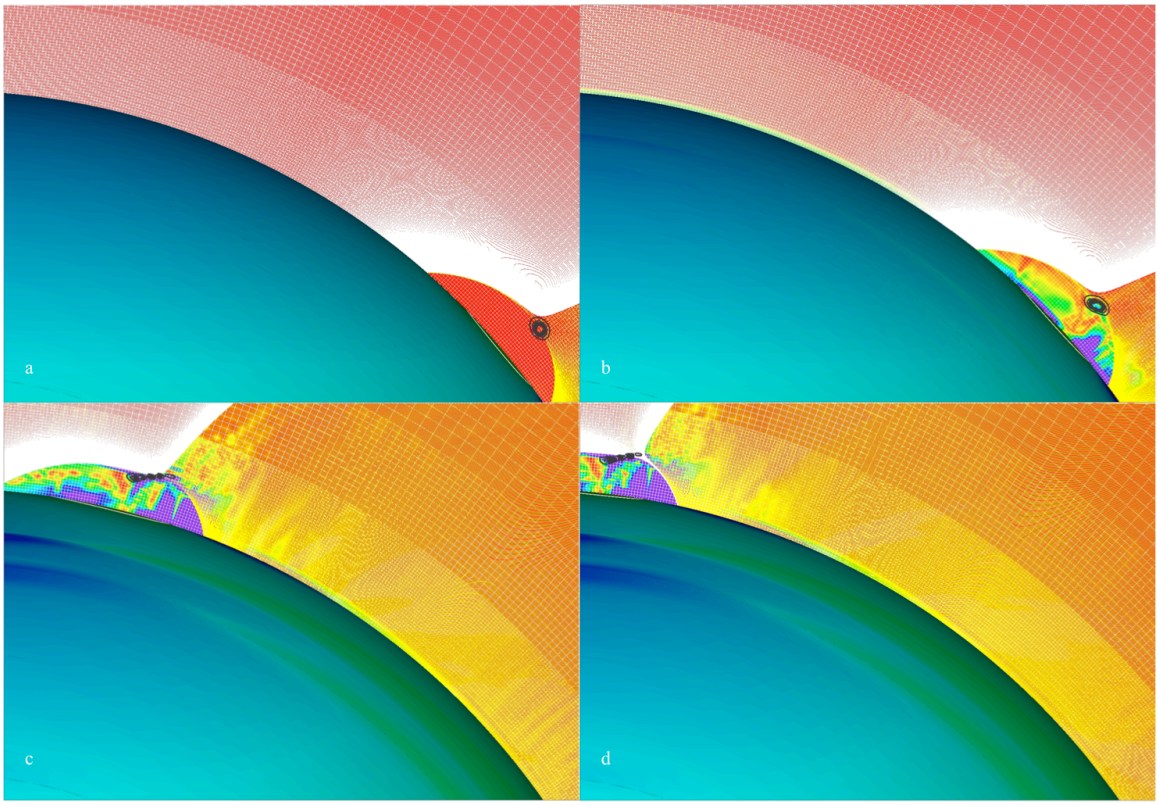

Figure 5.8: Closed-to-open evolution. a) $t = 0$ s, initial configuration. b) $t = 3{,}758$ s, current sheet formation. c) $t = 9{,}273$ s, global topology change of external spine. d) $t = 10{,}000$ s, final configuration.

4 times the bipole polarity inversion line diameter. This result is due to the difference between the response of open field and closed field to photospheric stressing. Since the open field is free to slip at the source surface, significant compression stresses do not build up between the front of the bipole and the coronal hole boundary. For this case, the photospheric motions stress primarily the closed field, which is line-tied at both footpoints. Consequently, the stress at the null and fan surface originates from behind the bipole as a result of the stretching of the closed field there. However, the eventual results of this stress are the same: current sheets form along the fan and deformed null region and dissipate quickly by reconnection without large energy release or strong impulsive behavior.

***Phase* 3 :** At some time around $t \approx 9273$ s, reconnection between the bipole flux inside the fan surface and the external field shifts the outer spine line to the coronal hole boundary, so that the boundary jumps discontinuously across the bipole fan surface (Figure 5.8). Again, this singular topological transition appears smooth, showing no evidence of any special dynamics.

***Phase* 4 :** During the final phase of the evolution, from $t \approx 9273$ s to $t = 10000$ s the bipole field moves steadily through the coronal hole by reconnecting with the open field. The reconnection during this phase is true interchange, because the bipole is now embedded in the open field region. The current sheet aspect ratio continues to increase at the deformed null region (Figure 5.8), and the reconnection remains smooth. We expect that if the bipole driving were to stop, reconnection would eventually dissipate the current sheet. Since the motion is now within the open field, any helicity injected by the photospheric motions may escape the system allowing a realignment of the inner and outer spines. For this case it is possible that the system can achieve a true minimum-energy, potential state, except perhaps for any volumet-

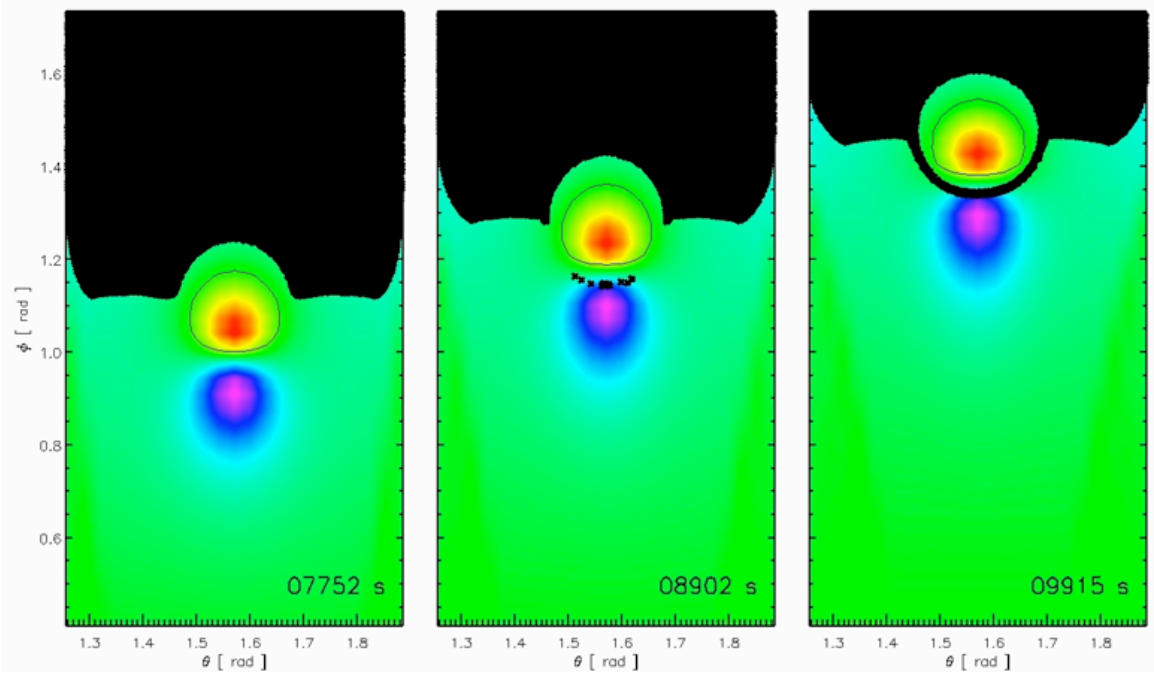

Figure 5.9: Closed-to-open: Photospheric open flux disribution at t = 7,752, 8,902, and 9,915 seconds.

ric currents deep inside the closed bipole field.

Finally, we find that the evolution of the magnetic topology (Figure 5.9), is essentially identical to that above. Initially, the parasitic spot is completely surrounded by closed flux. At some point near $t \approx 8902$ s, the bipole is so close to the coronal hole boundary that the outer spine shifts its global topology, and a very thin open field corridor forms. Using the same arguments as in the open-to-closed case, the open field corridor is expected to be well connected to the main coronal hole even though in the figure it appears to have breaks. Once the motion is completely inside the open field region, the corridor continues to thicken as flux is transferred across the bipole fan surface (Figure 5.9). The sequence shown in Figure 5.9, therefore, is simply the reverse of that in Figure 5.7.

CHAPTER VI

Reconnection-Driven Coronal Hole Boundary Dynamics

Although the quasi-steady models appear to agree with coronal remote-sensing observations, they have great difficulty in accounting for some of the most basic properties of the solar wind. In situ measurements near Earth and throughout the heliosphere have clearly established that there are two types of solar wind, "fast" and "slow", with distinct plasma and magnetic signatures (e.g., Zurbuchen (2007) and references therein). The fast wind has speeds generally > 600 km s^{-1}, is roughly steady except for considerable Alfvénic turbulence, and has elemental abundances that are typical of the solar photosphere. The slow wind, on the other hand, typically has speeds < 500 km s^{-1}, is highly time-varying, and has abundances typical of the closed-field corona (e.g., Feldman et al. (2005), Zurbuchen (2007)). By mapping the solar wind back to its source regions on the Sun, it has now been definitively established, especially by Ulysses data (Gloeckler et al. (1992), Geiss et al. (1995)), that the fast wind originates from those solar regions observed as coronal holes. The fast wind, therefore, is the true quasi-steady wind as in Parkers original theory (Parker (1958)).

The exact source regions and physical mechanisms underlying the generation of

[0]The material described in this chapter is a modified version of Edmondson et al. (2009)c.

the slow wind, however, are still not known, and remain an active area of Heliophysics research. Three general types of models have been proposed, differing primarily by the source location of the slow wind. In one class of models (e.g., Wang & Sheeley (1992), Arge & Pizzo (2000)) the slow wind is hypothesized to originate from open field near the edges of coronal holes, where magnetic flux tubes expand substantially faster than a simple radial expansion. The argument is that a larger expansion factor leads to the slowing of the solar wind flow. The difficulty with these models is that the composition of the slow solar wind is indicative of closed-field plasma and not of plasma originating on open field lines. In another class of models the slow wind is presumed to originate from the base of the heliospheric current sheet, at the tops of streamers (e.g., Suess et al. (1996), Woo & Martin (1997)). The hypothesis is that the open/closed interface at the tips of streamers is unstable and leads to the frequent ejection of plasmoids into the current sheet. Indeed, such a process would release closed-field plasma into the wind, but only over a narrow angular extent. The high-beta plasma sheet surrounding the actual field reversal is observed to be narrow, of order a few degrees, which agrees well with the observed angular extent of the so-called streamer stalks in coronagraph images (Wang et al. (1999)). The slow wind, however, has an observed angular extent of order 20° to 40°, substantially larger than the plasma sheet (Zhao et al. (2009)). In the final class of models the slow wind is presumed to originate from the whole closed-field region as a result of interchange reconnection with open flux that diffuses throughout the corona (e.g., Fisk et al. (1999), Fisk & Schwadron (2001), Fisk (2005), Fisk & Zurbuchen (2006)). This model can naturally account for both the composition and the angular extent of the slow wind. The problem, however, is that the diffusion of open field deep into closed-field regions appears to be in disagreement with the Lorentz forces expected for the low-beta corona (Antiochos et al. (2007)).

In this chapter we demonstrate a process that combines aspects of the second and

third class of models, and that may be critical for understanding both the composition and the angular extent of the slow wind. The underlying idea is that reconnection between the flux of an embedded bipole and the large-scale coronal field can result in the "tunneling" of the bipole flux through the helmet-streamer boundary and into the coronal hole. Interchange reconnection between the bipole field and the open flux of the coronal hole can then inject closed-field plasma into the wind. Note that in this tunneling process the coronal-hole boundary jumps from one side of the bipole field to the other; hence, the whole side of the streamer undergoes "disruption" as opposed to just the Y-point cusp region at the top of the streamer arcade. Consequently, the angular extent of the closed-field plasma injected into the wind may be substantially larger than the instantaneous width of the streamer stalk.

As will be shown, an important aspect of this process is that it is incompatible with the quasi-steady models, which implicitly assume that the evolution of the corona and wind can be calculated as a series of steady states determined by the slowly changing boundary conditions at the photosphere. We describe below the MHD dynamics of the global magnetic field driven by a class of photospheric flows for which the quasi-steady assumption is likely to fail, namely, flow fields that inject helicity with little change to the photospheric normal-flux component. These drivers generate long-lived, large-scale currents within the corona that can have major effects on the global coronal magnetic-field structure (i.e., the coronal-hole pattern and streamer belt), the dynamics of which are completely missed by the steady-state solutions. In fact, we argue that these dynamics may be exactly what is missing from the quasi-steady models, in order to reconcile those models with the existence of the slow solar wind.

In the previous chapter (V) we calculated the 3D MHD evolution of an embedded bipole subject to a translational motion applied at the photosphere. In that case, the dynamics of the coronal magnetic field were determined by the interplay between the change in flux distribution at the photosphere and stress relaxation due to recon-

nection. We found that the coronal bipole topology remained smooth, maintaining well-separated open and closed domains throughout the evolution. In particular, all of the open-field regions remained topologically connected (to the available spatial grid resolution), suggesting that a complex distribution of these bipolar regions impinging on coronal-hole boundaries would lead to an intricate system of open-field corridors extending from the main coronal hole (Antiochos et al. (2007)). These results are in good agreement with the magnetic topology and evolution predicted by the quasi-steady models.

The key feature of our simulations described in chapter V is that magnetic reconnection acts so as to maintain the coronal field close to the quasi-steady solution. As a result of general energy injection (i.e., flux injection, helicity injection, translational motions, or any combination thereof) the null-point topology of the embedded bipole deforms by the inner and outer spine lines separating and forming a current sheet, much like the classic theory of Syrovatskii (1981). Reconnection at this current sheet then leads to the exchange of flux between the bipole and surrounding field, causing the stress to decrease and bringing the spine lines back toward alignment. In chapter V, we energized the system by translational motions, and the resulting reconnection process moved the bipole with the photospheric motion while maintaining a near current-free state as predicted by the quasi-steady models. This result is not universal, however, because as is shown below it is possible to prescribe motions at the photosphere that bring the system far from the potential state. In this alternative scenario, the dynamic MHD evolution is radically different from that predicted by the quasi-steady models, with important implications for our understanding of the slow solar wind.

6.1 Model for Reconnection-Driven Dynamics

To study the reconnection-driven dynamics of the large-scale streamer belt we employ the simplest multipolar model for the solar coronal magnetic field: three polarity regions on the photosphere separated by two distinct polarity inversion lines. The magnetic system consists of a global dipole - which produces the polar coronal holes of open field and a large-scale equatorial streamer belt of closed field - and a strong, bipolar active region, as shown in Figure 6.1. The initial field (equation 5.1) is the same model used in chapter V with the source surface taken at 3 solar radii.

The coronal magnetic field is obtained directly by taking the gradient of equation (5.1), and is given by,

$$\boldsymbol{B} = \sum \boldsymbol{B}_i^S + \sum \boldsymbol{B}_i^*$$

$$\boldsymbol{B}_i^S = \boldsymbol{M}_i \left(\frac{R_i^S}{|\boldsymbol{x} - \boldsymbol{r}_{0,i}|} \right)^3 \left[3 \left(\boldsymbol{m}_i \cdot \boldsymbol{n}_i \right) \boldsymbol{n}_i - \boldsymbol{m}_i \right]$$

$$\boldsymbol{B}_i^* = \boldsymbol{M}_i^* \left(\frac{R_i^S}{|\boldsymbol{x} - \boldsymbol{r}_{0,i}^*|} \right)^3 \left[3 \left(\boldsymbol{m}_i^* \cdot \boldsymbol{n}_i^* \right) \boldsymbol{n}_i^* - \boldsymbol{m}_i^* \right]$$

where the position unit vectors are $\boldsymbol{n}_i \equiv \frac{(\boldsymbol{x} - \boldsymbol{r}_{0,i})}{|\boldsymbol{x} - \boldsymbol{r}_{0,i}|}$, and the dipole orientation unit vectors are $\boldsymbol{m}_i \equiv \frac{\boldsymbol{M}_i}{|\boldsymbol{M}_i|}$ for both source (^{S}) and image (*) dipoles. The image dipoles are geometrically related to their real counterparts with field strengths $\boldsymbol{M}_i^* = -\boldsymbol{M}_i \left(\frac{R}{|\boldsymbol{r}_{0,i}|} \right)^3$, and position vectors $\boldsymbol{r}_i^* = \boldsymbol{r}_i \left(\frac{R}{|\boldsymbol{r}_{0,i}|} \right)^2$, where R is the distance to the source surface. The R_i^S are simple scale factors. The origin dipole (i = 0) is $\boldsymbol{M}_0 = 10\ \boldsymbol{z}$ G, and has a corresponding image at infinity that produces a constant field, $\boldsymbol{B}_0 = 0.1852\ \boldsymbol{z}$ G. This combination yields a field strength of approximately 4 G at the photosphere far from the active region. The active region is modeled with five real dipoles spread

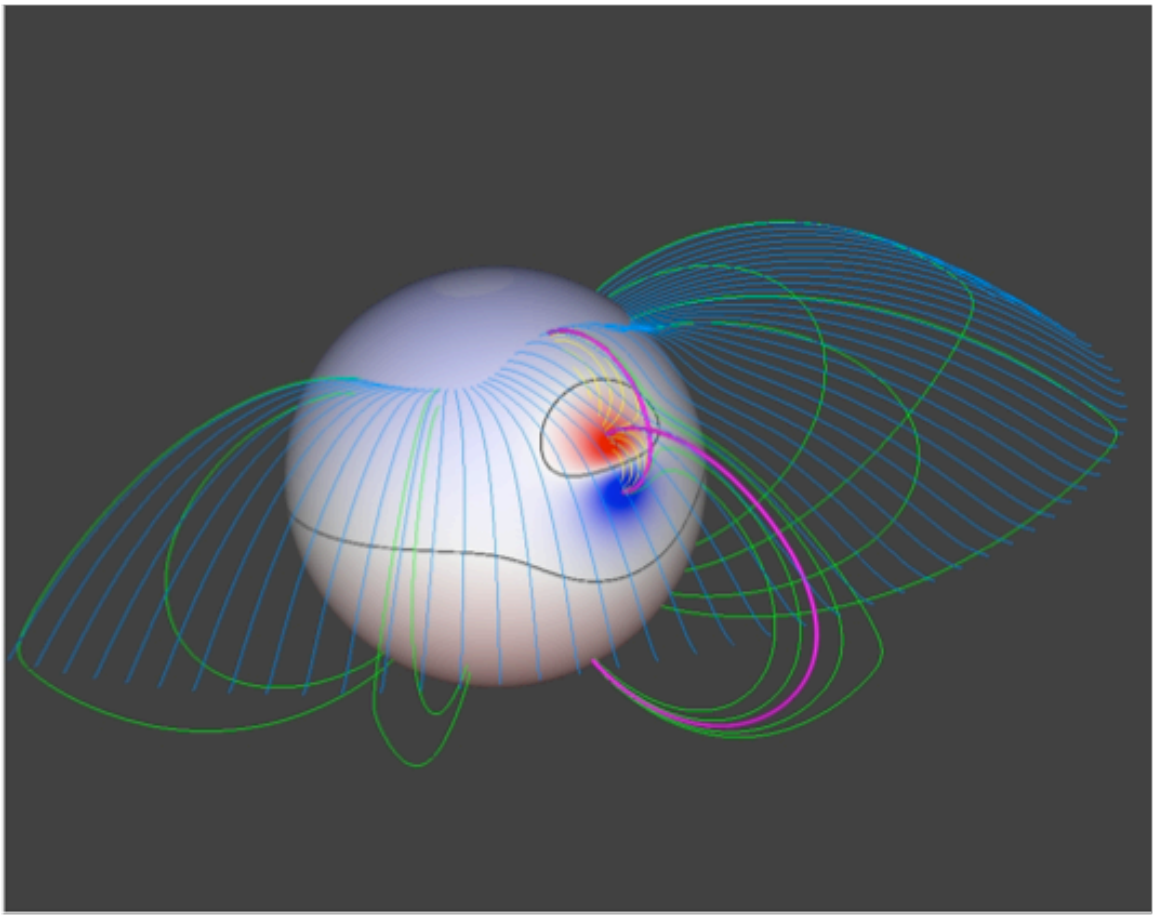

Figure 6.1: 3D Global Potential Field Configuration: Large-scale view of initial coronal magnetic field configuration. Color shading shows the magnitude of the radial field at photosphere; the two thick black curves indicate polarity inversion lines where the radial field vanishes. The green field lines correspond to streamer-belt closed flux, and the blue field lines to the coronal-hole open flux that maps to the source surface. The closed field of the embedded bipole is shown in yellow, the fan and spine field lines in magenta.

uniformly in azimuth, all of equal magnitudes $|\boldsymbol{M}_i| = 150$ G, and scale factors $R_i^S = 0.01\ R_\odot$. The positions are given by $\boldsymbol{r}_{0,i} = 0.8\, R_\odot\, \boldsymbol{r} + 0.01\pi\,(i-3)\,\boldsymbol{\phi}$, where i = $\{1, 2, \ldots 5\}$. For these parameters, the active-region dipole sources produce a large bipolar flux distribution embedded completely within the closed field of the streamer belt, in the vicinity of the coronal-hole boundary.

The basic topological structure of the initial coronal magnetic field above the parasitic spot consists of a roughly hemispherical volume of flux, surrounded by the closed flux of the streamer belt. A single closed PIL surrounds the negative-polarity region of the bipole, across which the near field must close. The topology of this two-flux system is simply that of the well-known embedded bipole with its fan surface, spine lines, and null point (see chapter III, section 3.2; Greene (1988), Lau & Fin (1990), Antiochos (1990), Priest & Titov (1996)). Figure 6.2 illustrates the topologically invariant quantities that are the 3D null-point, the 1D spine lines, and the 2D dome-shaped fan surface. A complete characterization of these topological invariants requires only the magnetic field near the null-point position: the local structure of the spine lines and fan surface are uniquely determined by the eigenvalues and eigenvectors of the fields first-order Jacobian expansion at the null. The intersection of the fan surface field lines at the photosphere forms a 1D, closed, separatrix curve that defines the topological boundary between the local active-region flux and the streamer-belt field. The magnetic connectivity of the field lines whose photospheric footpoints lie on this curve (i.e., that make up the fan surface) converge onto the null point, and thus are multi-valued at the null point. We emphasize that although the topology is discontinuous, the magnetic field is smooth everywhere. All of the bipolar flux inside the fan closes across the local PIL, whereas all of the streamer-belt flux outside the fan closes across the equatorial PIL.

We solve the set of 3D compressible, ideal MHD equations (2.8, 2.9, 2.13, and 3.10, with $\eta = \nu = \mathrm{S} \equiv 0$) in spherical coordinates with the ARMS code. The ratio of

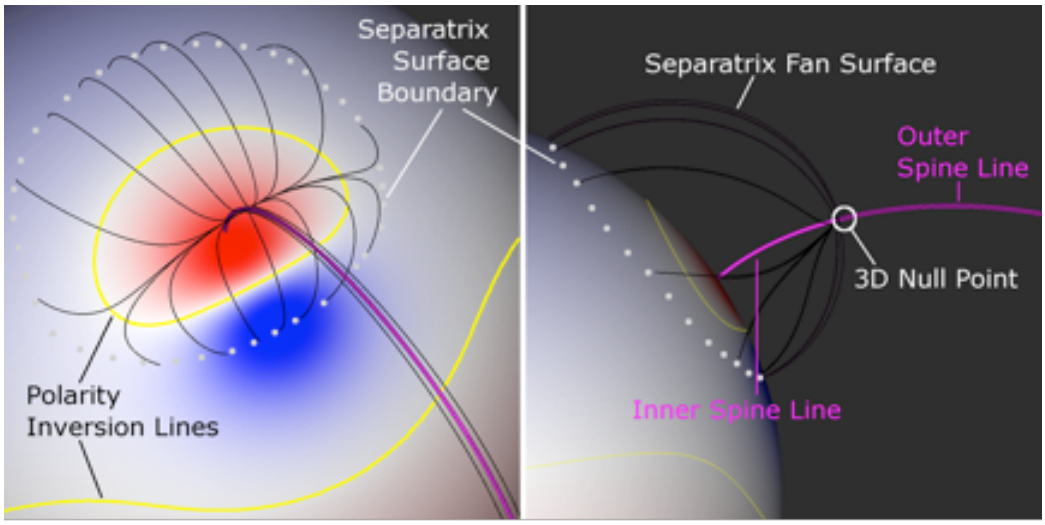

Figure 6.2: Topological structures of the 3D embedded bipole field. The thick inner and outer spine lines are shown in purple. The fan surface, shown with thin black lines, separates the bipole flux volume from the background field. The (continuous) footpoint boundary of the fan surface is represented by the white dots at the photosphere. The polarity inversion lines are shown in yellow.

specific heats γ is taken to be 5/3. For the plasma equation of state the ideal gas law (equation 2.14) is used. The effects of gravity, $g = -\frac{GM_\odot r}{r^3}$, are small, but included in the calculations to keep the plasma beta from becoming too large at large heights.

Our simulation domain consists of the spherical annulus bounded radially by the photosphere and the source surface, $1 \leq \frac{r}{R_\odot} \leq 3$. The longitudinal extent is $-\pi \leq \theta \leq \pi$. We trim the latitude domain to $0.0625 \leq \phi \leq 0.9375\ \pi$, since the poles have coordinate metric singularities that are difficult to treat numerically. Note that the interesting dynamics in this simulation occur near the equator, far away from these excluded latitudes.

The initial magnetic field is potential, thus we set the initial coronal plasma distribution to be spherically symmetric and in hydrostatic equilibrium:

$$T(r) = T_0 \left(\frac{R_0}{r} \right) \tag{6.1}$$

$$n\left(r\right) = n_0 \left(\frac{R_0}{r}\right)^{\mu-1} \tag{6.2}$$

where the exponent $\mu = \frac{R_0}{H_0} = 5.97$ and the pressure scale height $H_0 = \frac{2kT_0}{mg}$. The surface parameters are initialized to $T_0 = 1.94$ MK, $P_0 = 0.25$ dyne cm^{-2}. These plasma profiles and parameters were selected so that the plasma beta would be small throughout the domain. We find that beta reaches a minimum of about 0.004 inside the strong field of the bipole and an average value of less than 0.1 near the source surface, though it does grow higher in the cusp region of the streamer belt. The system is high-beta only in the near vicinity of the null. We emphasize, however, that although the system on average is low beta, the plasma pressure does play an important role in the evolution. The plasma pressure dominates in the vicinity of the null, above the bipole flux domain; therefore, the formation of the current sheets and the subsequent reconnection dynamics there are critically dependent on the plasma.

Much like the plasma beta, the Alfvén speed varies considerably over the domain, but an average global Alfvén speed can be defined in terms of the total magnetic energy E_M and the total coronal mass M_C:

$$V_A = \sqrt{\frac{2\,E_M}{M_C}} \tag{6.3}$$

With this definition, the global average Alfvén speed is approximately 730 km s^{-1}. An Alfvén time of a little less than 2,000 s is similarly defined using a global length scale of 2 $R_\odot$, approximately the half-length of the largest loops.

At the lower boundary, the photosphere, we impose line-tied, no-flow-through ($V_r = 0$) conditions. The velocity profile (Figure 6.3) is a slow, incompressible, asymmetric, rotational motion applied to the negative polarity spot inside the active region PIL, constructed to preserve the normal flux distribution in time. The velocity field

V_t tangent to the surface is similar to that used by DeVore & Antiochos (2008), viz.,

$$V_t(\theta,\phi) = f(t)\, V_0 \left[1 - cos\left(\pi \frac{B_r(\theta,\phi) - B_1}{B_2 - B_1}\right)\right] \boldsymbol{r} \times \nabla_t B_r(\theta,\phi) \tag{6.4}$$

where ∇_t is the gradient operator tangent to the surface. The flow is non-zero only between radial field values of B_1 = -30 G and B_2 = -3 G; consequently, the flow vanishes at both the PIL and the inner spine footpoint. We set the constant factor $V_0 = 9.0 \times 10^{14}$ cm^2 s^{-1} G^{-1} so that the maximum velocity is approximately 45 km s^{-1}, approximately 6% of V_A. The temporal variation factor $f(t)$ is,

$$f(t) = \begin{cases} \frac{1}{2}\left[1 - cos\left(2\pi \frac{t}{4{,}000}\right)\right] & \text{for } 0 \le t \le 2{,}000\, s \\ 1 & \text{for } 2{,}000 \le t \le 20{,}000\, s \\ \frac{1}{2}\left[1 - cos\left(2\pi \frac{t-18{,}000}{4{,}000}\right)\right] & \text{for } 20{,}000 \le t \le 22{,}000\, s \\ 0 & \text{for } 22{,}000 \le t\, \mathrm{s} \end{cases} \tag{6.5}$$

The smooth cosine profiles minimize transient wave effects as the motions start and stop. The temporal extent of the driving rotation is long enough to stress the field so that the external spine line changes its global topology; we then turn off the motions and let the field relax. Although the initial state is symmetric about the meridional plane, the photospheric flows destroy the symmetry so that the evolution is fully 3D and asymmetric.

At the top boundary, the source surface, we impose no-flow-through, free-slip conditions. The free-slip conditions allow us to keep the physical distinction between open and closed field without having to incorporate in the simulations the added complexity of a full solar wind. Field lines that reach the upper boundary are physically open, because only one end is line-tied at the photosphere, and thus any stress imparted by photospheric motions may propagate out to infinity on Alfvénic timescales. Field lines in which both footpoints connect to the line-tied photosphere are closed and can

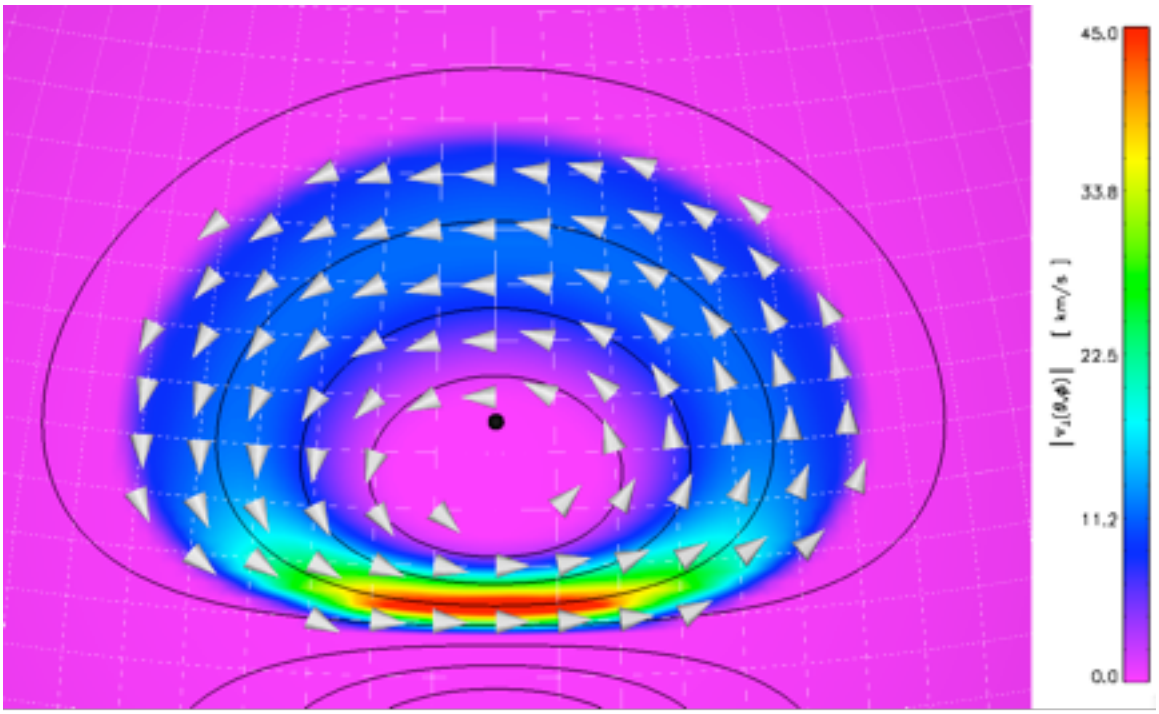

Figure 6.3: Driving flow field vectors of the photospheric velocity field plotted over color shading of the flow speed and black contours of the radial field component B_r.

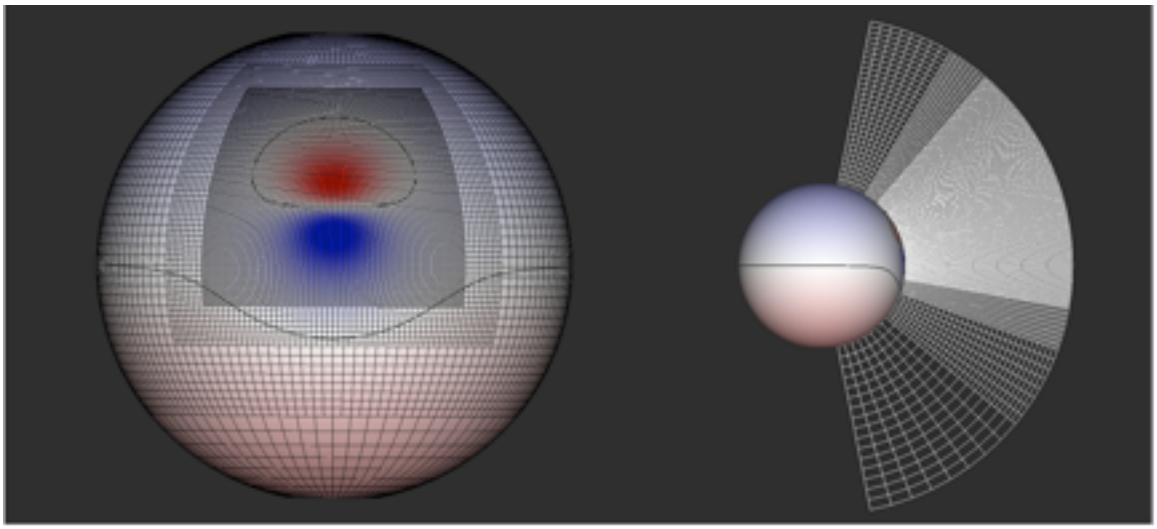

Figure 6.4: Numerical grid structure showing the refinement in the angular and radial directions.

sustain Lorentz stresses for time scales all the way up to the global dissipation time. Under an ideal MHD evolution, the no-flow-through condition forces conservation of the open/closed designation of a field line; thus, the topology of any field line can change only as a result of reconnection.

Finally, Figure 6.4 shows the numerical grid for the simulation. We start with a base level consisting of $2 \times 4 \times 8$ blocks distributed uniformly in $\{ r, \theta, \phi \}$, with 8^3 grid points per block. This sets the minimum resolution far from the bipolar active region. The initial grid is further refined up to a maximum of four levels, over a volume large enough to encompass the entire rotational flow field and extending radially from the photosphere to the source surface. The resolution at this highest refinement level corresponds to approximately 1.1 $\times 10^9$ cm by 0.70° by 0.70°, which is much smaller than the scale of either the embedded bipole or the flow field, sufficient to resolve fields and scalars and their derivatives, so numerical diffusion does not substantially affect the calculation, other than the numerical resistivity responsible for the reconnection dynamics. The grid is held fixed throughout the simulation.

6.2 Results: Reconnection-Driven Dynamics

The overall system evolution is most clearly seen in the time history of the magnetic and kinetic energies (Figure 6.5). An inspection of the kinetic energy profile reveals three stages to the evolution, defined by the location of the outer spine field line. The first stage, $t \in [0, 18,000]$ s, occurs during the initial energy injection and is characterized by a topologically closed outer spine. The second stage occurs for $t \in [18,000, 36,000]$ s, and is characterized by a topologically open spine line. During this phase, any helicity injected by the boundary flow field and conserved by interchange reconnection can escape the system along open field lines. Recalling that the system drivers are turned off at t = 22,000 s, the field relaxes by ejecting enough helicity and energy to close the outer spine line around $t \approx$ 36,000 s. This re-closing of the outer spine line characterizes the third and final stage, $t >$ 36,000 s, during which the dynamics effectively cease for time scales less than the global dissipation time.

The dynamics are illustrated from two complementary points of view in Figures 6.6 and 6.7 at times t = 0, 9,000, 19,000, 23,000, 30,000, and 37,500 seconds. Figure 6.6 illustrates the geometric expansion of the bipole flux volume as a result of the magnetic stresses imparted by the photospheric flow field, as well as the spatial structure of the resulting currents. We show field lines and current-density magnitude in the initial symmetry plane bisecting the bipole flux volume. The rotation immediately destroys this symmetry, however, as we noted above. The field-line color map identifies the different flux systems: yellow field lines indicate the closed bipole flux, green the closed flux of the global streamer belt, and blue the open coronal holes. All closed-flux footpoints are traced from fixed photospheric positions away from the driving flows, while the open field lines are traced from footpoints on the source surface. Consequently, the movie shows the true evolution of the selected field lines. Plotted on the vertical background (in the plane of the sky) are filled contours of current-

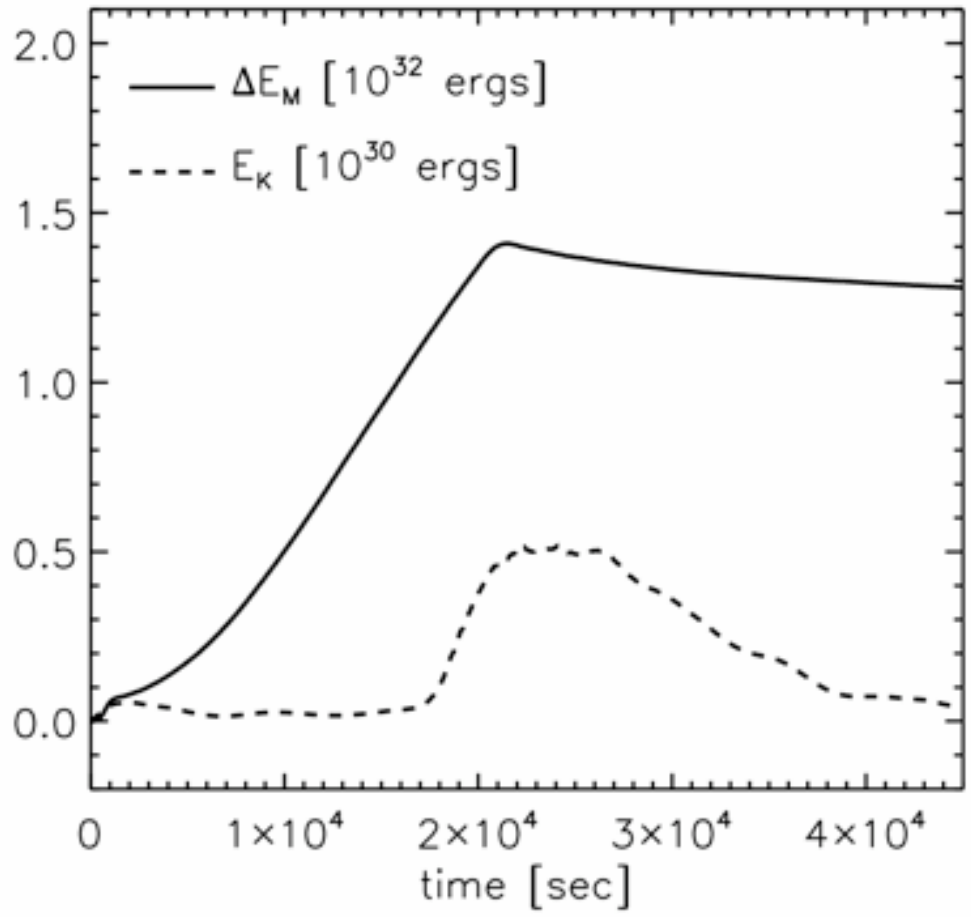

Figure 6.5: Energy-Time Plot: Solid line shows the change of the global magnetic energy from its initial value; dashed line shows the global kinetic energy.

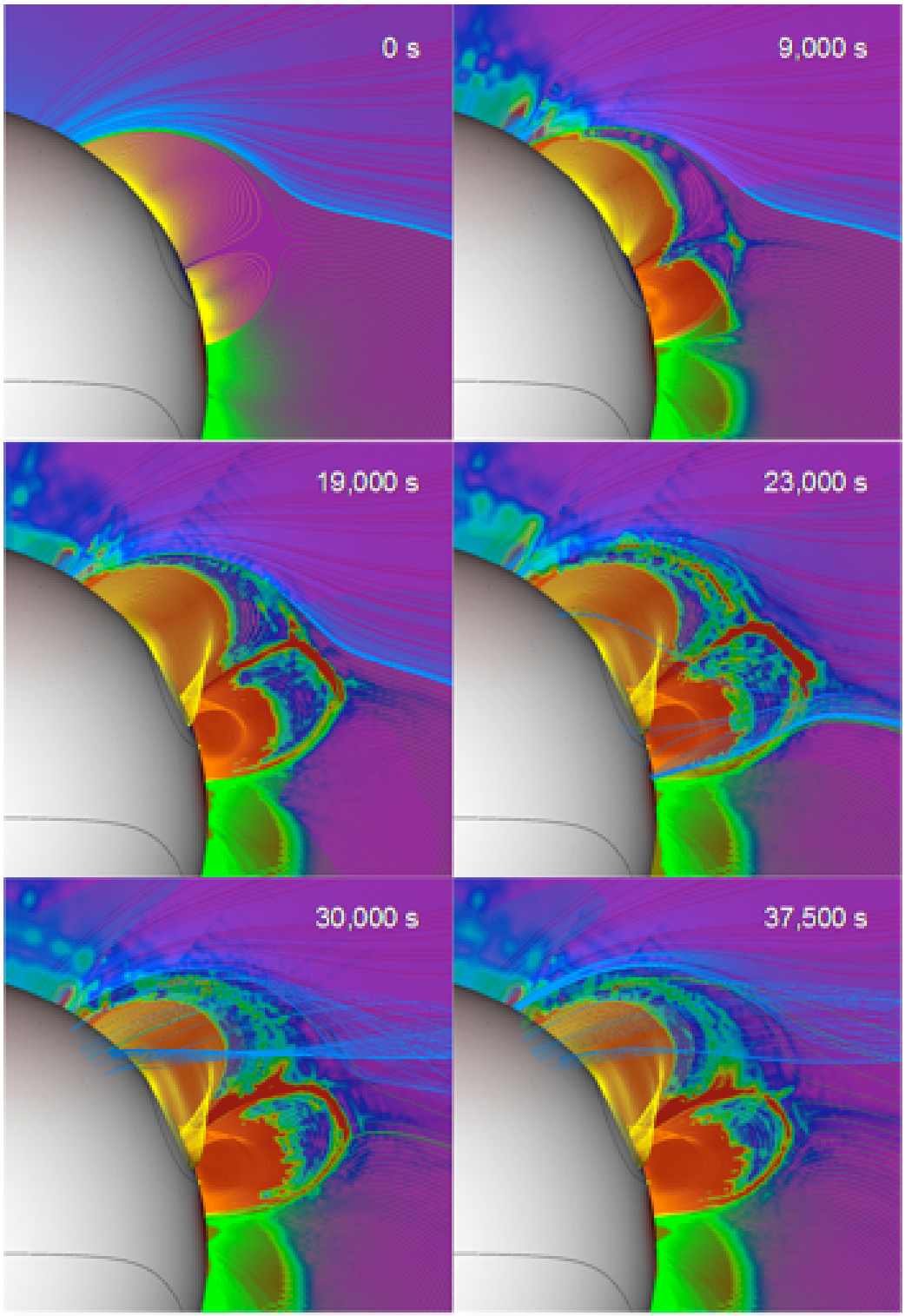

Figure 6.6: Bipole field geometry evolution. t = 0 s, initial configuration; t = 9,000 s, strong current sheet formation; t = 19,000 s, global topology change of external spine (closed to open); t = 23,000 s, external spine open topology; t = 30,000 s; global topology change of external spine (open to closed); t = 37,500 s, relaxation phase.

density magnitude. The color scale saturates for current-density magnitudes greater than 1.0 A m^{-2}, in order to show the spatial extent of the strong currents.

A critical issue is the topology of the open/closed boundary throughout the systems evolution. From consideration of a sequence of potential states, Antiochos et al. (2007) argued that reconnection can maintain a smooth topology with well-separated open- and closed-field regions in agreement with the quasi-steady models. Our previous MHD simulations (Chapter V, sections 5.2 and 5.3) support this assertion for a fully dynamic system, at least down to the numerical grid resolution and time cadence. Figure 6.7 shows the evolution of the open field in the present simulation by tracing a dense sample of field lines from the source surface down to the photosphere, and plotting their footpoint locations there. The black region in each panel is the area on the photosphere that is magnetically connected to the source surface, i.e., is the open-field region. Also shown are the polarity inversion lines on the photosphere (thin black lines) and filled contours of B_r at the photosphere, with red indicating strong negative and blue strong positive field.

Let us now consider the detailed evolution of the system as determined by our simulation. From $t = 0$ to $t \approx 9{,}000$ s, the rotational flow twists the bipole, stressing the field with evidence for only negligible reconnection. The null point remains relatively undistorted, and only weak currents with a scale size substantially larger than the grid size form there. As a result of the photospheric motions, the closed-field bipole expands and shears, transmitting the stresses to the separatrix and into the global streamer belt. These stresses tend to displace the inner and outer spines, in both a radial direction due to the volumetric expansion and a longitudinal direction due to the rotational shearing, resulting in the eventual formation of a current sheet at the deformed null. It is evident from Figure 6.6 that the deformation of the null region stays small up through $t \approx 9{,}000$ s, because the spatial extent of the large current contours in the vicinity of the null point remain small. The currents clearly build up

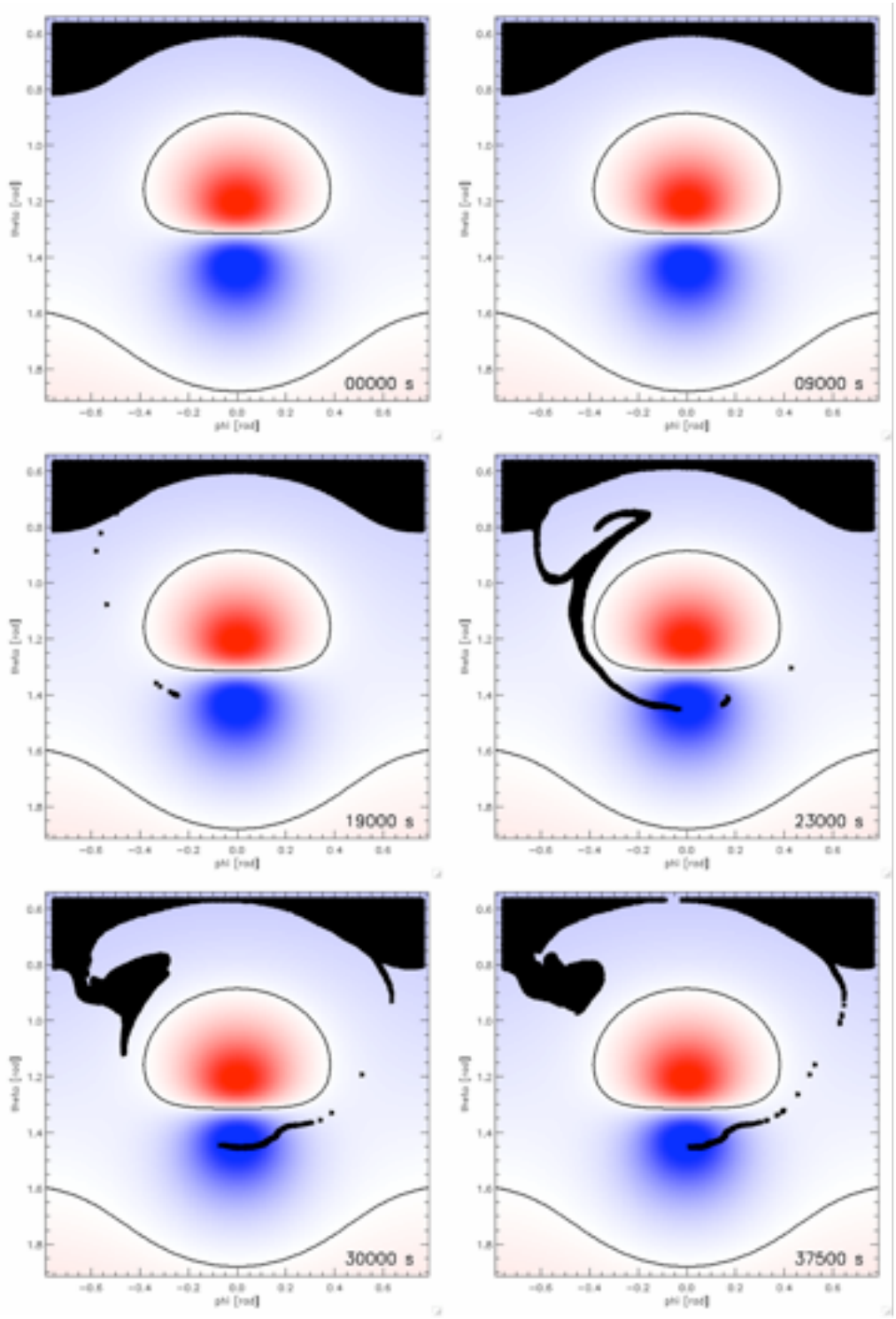

Figure 6.7: Photospheric open flux distribution evolution showing the formation of the open-field corridor. Times are the same as in Figure 6.6.

as the driving motions progress, but during this phase they are small compared to the body currents within the bipole flux volume and are much larger than the grid scale. Furthermore, the bipole remains well within the closed field of the streamer belt, and thus no changes are seen in the top panels of Figure 6.7.

From $t \approx 9{,}000$ s to $t \approx 18{,}000$ s the continued rotation of the bipole flux sufficiently deforms the null region that the current structure there decreases down to the grid scale and rapid reconnection ensues. This reconnection is technically not yet interchange reconnection, because the bipole flux is still embedded within the streamer belt, but the closed field of the bipole does exchange with the globally closed flux. Since the initial symmetry is broken by the rotational flow, the reconnection during this phase is not easily seen. However, we can infer that rapid reconnection has initiated at this time by the greatly increased rate of expansion of the bipole field volume, especially on the southern end overlying the fastest flow speeds. We find that once reconnection turns on, it stays on, and the null patch tunnels its way toward the coronal-hole boundary, smoothly transferring the outer spine through the streamer-belt flux.

Between $t \approx 18{,}000$ s and $t \approx 19{,}000$ s, the stress of the twisting motions and the amount of reconnection are enough to transfer the external spine line to the coronal-hole boundary. At some instant, the null of the closed-field bipole lies exactly on the separatrix surface between open and closed field, hence the outer spine becomes a separator line that connects the bipole null to the null at the source surface. We expect from the coronal hole uniqueness theorem (Antiochos et al. (2007)) that the outer spine line opens during this time. Numerically, it is extremely challenging to capture this singular topological transition. Unlike in the real Sun where field lines can open and close simply in response to changing gas pressure, our no-flow-through boundary conditions at the source surface imply that the only way for a field line to change from open to closed or vice versa is via reconnection at the null patch. Therefore,

the appearance of the thin open-flux extension connected to the northern coronal hole on the western side of the bipole (Figure 6.7) implies that the null patch has tunneled its way through the closed field and crossed into the coronal hole. Although the corridor may appear discontinuous, this is only an artifact of the finite numerical grid resolution and of the extreme deformation of the null. Except possibly over a short grid-dissipation time scale, we expect that the open-field corridor is actually well connected and encircles the entire bipole flux domain, as it does in chapter V.

Prior to the creation of the open-field corridor, there is little evidence for explosive dynamics such as bursty reconnection or large mass outflows. As the null patch eats its way through the streamer belt, removing more and more flux from between the bipole and the coronal-hole boundary, we find that the kinetic energy increases rapidly just before the appearance of the open-field corridor (Figure 6.5).

In the next phase of the evolution, from $t \approx 19{,}000$ s to $t \approx 36{,}000$ s, the closed bipole field is embedded completely within the open field of the coronal hole. Recall that between $t = 20{,}000$ s and $t = 22{,}000$ s, we steadily decrease the driving flows to zero, so that beyond $t = 22{,}000$ s the system undergoes pure relaxation. The reconnection during this phase is truly interchange, occurring between open and closed field. There is a gradual decrease in kinetic energy over time (Figure 6.5), but we see no dramatic change in the system dynamics. The reconnection remains fairly smooth with no impulsive burstiness and no evidence of any ideal instability such as the kinking that drove impulsive reconnection in our model for coronal hole jets (Pariat et al. (2009)).

Throughout this phase, the helicity that was injected at the photosphere and conserved by the reconnection process is ejected from the computational domain along open field lines. Since the photospheric driving has ceased by this time, this ejection of magnetic helicity is the main process by which the system relaxes. The relaxation of the stress inside the bipole field can be seen from a slight volumetric contraction of

the closed bipole flux. Along with magnetic energy and helicity, closed-field plasma is ejected from the system; but since we use an adiabatic energy equation, the plasma cools rapidly as it expands outward. Furthermore, our no-flow-through condition at the base does not allow for chromospheric evaporation, so the amount of plasma released into the wind is clearly underestimated by this simulation. The time scale of the relaxation phase is determined almost exclusively by the rate of reconnection, because the propagation of helicity out of the system occurs on the global Alfvén time scale, which is of order 2,000 s.

After sufficient stress has been ejected from the system along the open field, the external spine closes down sometime between $t \approx 35{,}500$ s and $t \approx 36{,}500$ s (Figure 6.8). The interchange reconnection and helicity ejection within the open field impart a kind of "dynamic inertia" to the relaxing system so that the spine overshoots the coronal-hole boundary into the closed-field region. The amount of overshoot and the final location of the external spine are expected to depend upon the details of the reconnection process, which in turn depend upon the dissipation mechanism. For $t > 36{,}000$ s, we find that the system achieves a quasi-steady force balance with the closed outer spine in the vicinity of the coronal-hole boundary (Figure 6.9). During this phase helicity is conserved, so that the only true relaxation process available to the system is a de-twisting of the photospheric shear by resistive dissipation.

Figure 6.10 shows two separate viewpoints at four typical times, $t = 0$, 19,000, 23,000, and 45,500 seconds, in the evolution of the global streamer-belt/bipole system. It is evident from the figure that the rotational flow field does not change the photospheric normal flux distribution, yet we find a major reconfiguration of the global streamer belt as the bipole flux volume passes across the dynamically shifting coronal-hole boundary. Note that when the bipole has shifted into the coronal hole, the streamer-belt envelope has dipped below the parasitic spot (see Figure 6.10, $t = 23{,}000$ s). The opening of the bipolar flux low down in the corona, far from

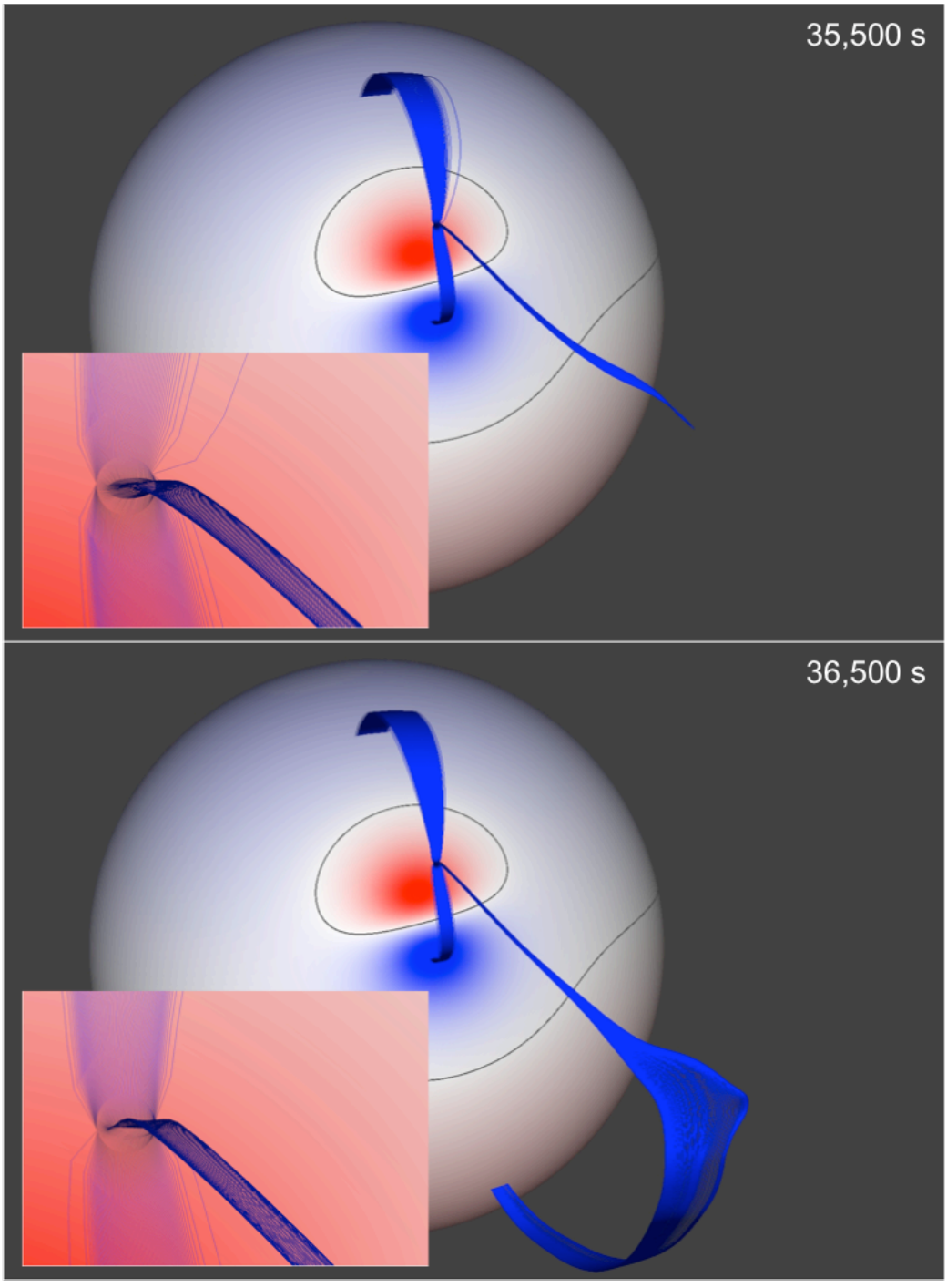

Figure 6.8: Late-stage external spine topology change. Between $t = 35{,}500$ and 36,500 s, enough stress is ejected from the system to close the fan and external spine field lines (blue).

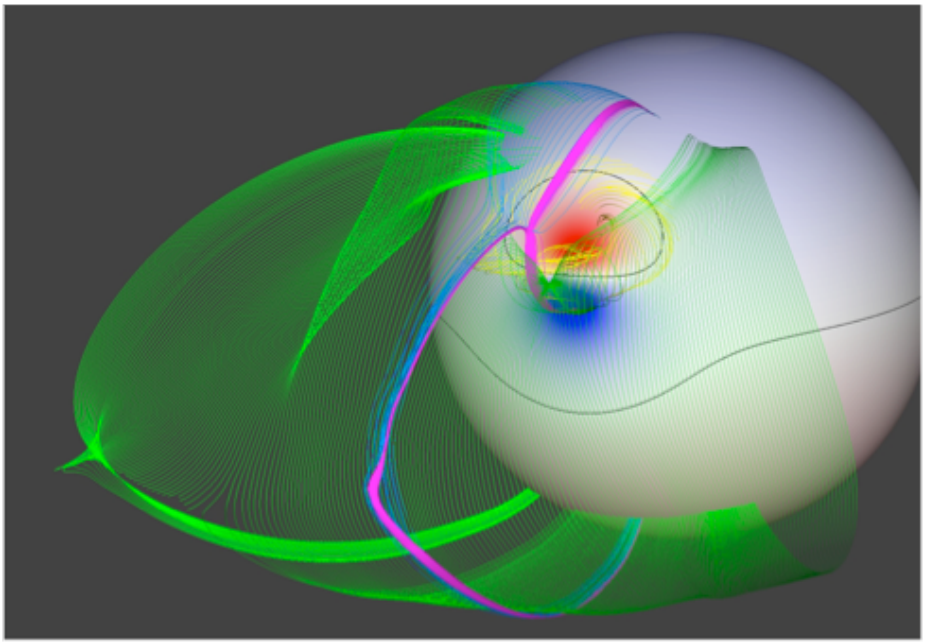

Figure 6.9: Final global field configuration at $t = 45{,}500$ s, showing the closed external spine (purple), neighboring closed flux that was initially open (blue), and the large-scale streamer field (green).

the dynamically evolving streamer-stalk cusp, implies closed-field plasma release and, therefore, a widening of the angular extent of the slow-wind source region.

We find that embedded bipole regions near coronal-hole boundaries can tunnel through the boundaries via reconnection, thereby releasing their plasma onto open field lines. The reconnection while inside the helmet streamer causes the null point and spine to tunnel into the coronal-hole, whereas the interchange reconnection while inside the coronal-hole causes enough stress release for the null and spine to drop back inside the helmet streamer. Consequently, the coronal-hole boundary jumps back and forth to include or exclude the embedded bipole region throughout the evolution. Depending on the size of the bipole, the jump could be substantial. This type of evolution is exactly what is needed in order to explain the observations that the slow wind has both a closed-corona composition and a large angular extent. Note that if we were to maintain the photospheric flows in our simulation, we expect that the system would undergo a continuous sequence of reconnection-driven openings

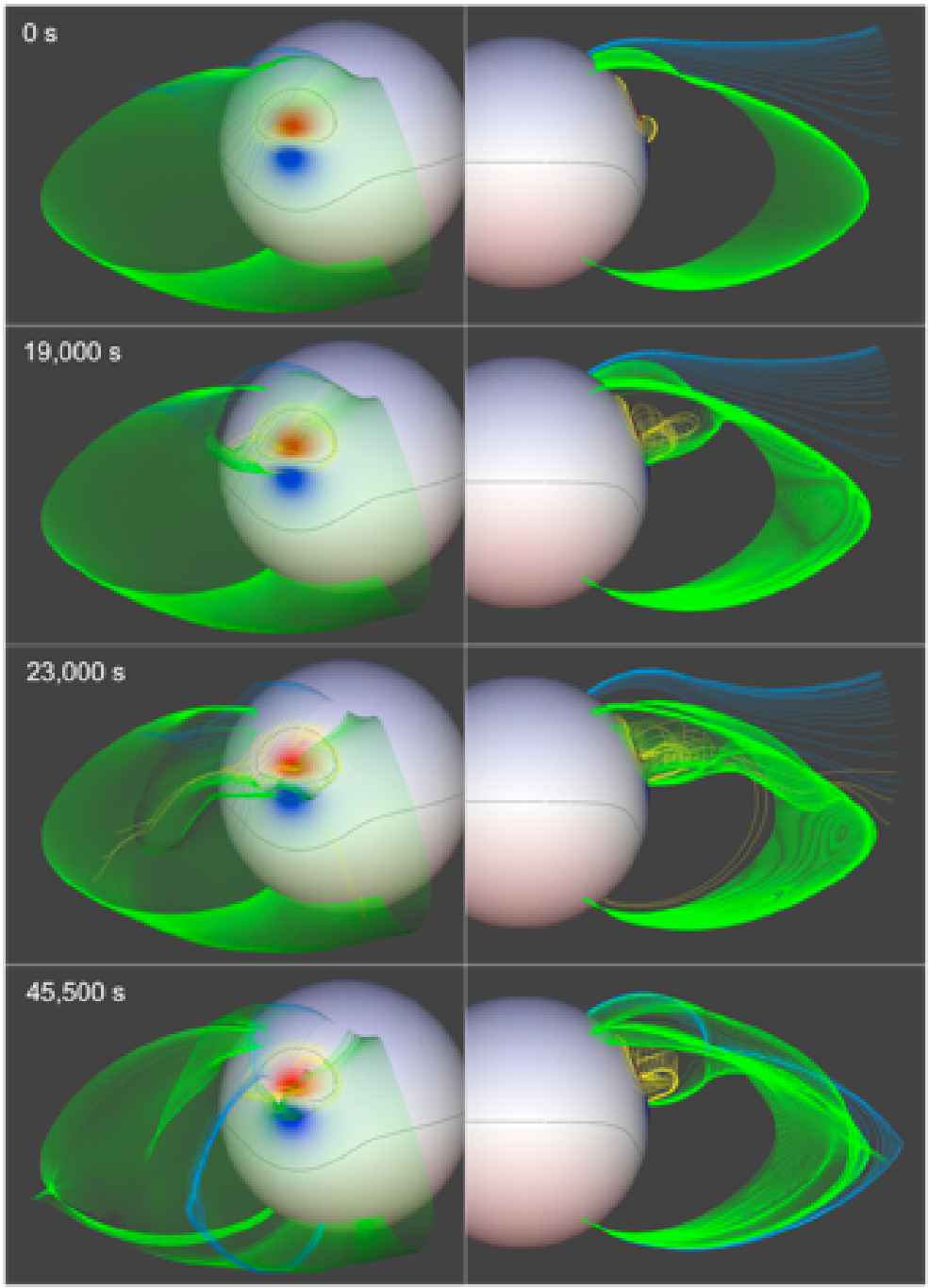

Figure 6.10: Streamer belt re-configuration at times t = 0, 19,000, 23,000, 45,500 s. The green and blue field lines respectively illustrate the initial closed field lines of the streamer belt and a patch of initially open flux in the coronal hole. The yellow field is the low-lying bipole flux that closes across the parasitic spot polarity inversion line. The left and right columns respectively present isometric and profile views.

and closings, which would result in a sequence of closed-field plasma releases into the wind. Furthermore, the temporal evolution of this plasma release appears to be compatible with observations that coronal-hole boundaries do not exhibit strong dynamics in coronal images. We note from Figure 6.5 that although there is clearly an increased energy release rate when the bipole enters the coronal hole, this release is quite gradual with a long time scale, of order hours. From the viewpoint of comparison with observations, a key result is that the reconnection does not produce bursty dynamics. Energy is released during the reconnection, primarily as mass flows, but the release does not show impulsive behavior. The reason for this difference is that there is no sign of any ideal instability in our simulation; everything is driven by the slow photospheric driving and by the fairly gentle coronal reconnection.

CHAPTER VII

Conclusions

The results of this dissertation research have a number of important implications for both theories and interpreting observations of the corona, and the heliosphere. The calculations demonstrate that local current sheet formation, dissipation mechanism, and subsequent reconnection dynamics are as important to the global dynamics as the velocity drivers at the photospheric boundary. We demonstrate that, though there are differences between the X-Line (chapter IV) and 3D null point (chapters V and VI) evolutions depending on the specifics of the energy injection, the general result of a Syrovatskii-type current sheet formation along topological separatricies seems very robust. The corresponding reconnection dynamics across the current sheet proceeds in a smooth manner, maintaining a clear topological separation between the nested magnetic domains. In effect, under MHD evolution, the general topological complexity always reflects the initial topological complexity. Of course, this work was done within the framework of MHD and the reconnection was calculated using numerical resistivity, and thus cannot account for physical affects, such as particle acceleration and direct plasma heating. With these caveats in mind, we enumerate the major conclusions of the simulations below. We begin with the local current sheet development and reconnection dynamics, and discuss the differences between the X-Line and the 3D null point formulations. From there we analyze the consequences of

the fully-dynamic 3D MHD calculations in terms of the limitations of the fundamental assumptions of both the quasi-steady and interchange models. Finally, we offer that, depending on the complexity of the coronal magnetic field structure, the predictions of both theoretical paradigms seems to converge, with interchange reconnections as a viable mechanism for the generation of the slow solar wind.

The calculation discussed in chapter IV constitutes, in a sense, a minimalist extension of 2D current sheet formation and reconnection to the fully 3D regime. The advantage of our approach is that it lends for straightforward comparison to previous 2D and 3D work and allows for very high numerical resolution applied at the current sheet. The results have a number of important implications for solar activity and for reconnection, in general. First, it is clear that a current sheet does form due to the photospheric motions, even though the motions are the smoothest possible uniform flow. This result demonstrates convincingly that a multipolar topology, even the extremely simple one of our model, will inevitably lead to current sheets in the corona. The formation process is physically identical to the Syrovatskii model: an initial X-type null deforms as a result of applied stress to a current sheet (technically a neutral sheet) bounded by two Y-type nulls. For our particular magnetic configuration and photospheric driving, the currents are confined to the deformed null point region and are small at the separatrix surfaces. But, if we were to apply a flow at the upper surface that drove the field in the initial-symmetry direction, parallel to the current sheet axis, current singularities would form along the separatrices, as well.

The current sheet formation process is rapid and efficient. It is evident from Figure 4.5 that the structure at the deformed null thins down to the highest resolution for fairly small displacement of the outer spine, less than 20°. The thinning of the current structure is expected to occur exponentially (e.g., Antiochos et al. (1999)), so that even for the very large Lunquist numbers of the real corona, current structures down to the dissipation scale form on essentially ideal time scales. An important implication of

this result is that current sheets are likely to be present in the corona even though the magnetic field there is generally observed to be near the potential state. As illustrated in Figure 4.9, even a modest distortion from the potential state is sufficient to generate structure at the dissipation scale. Note, however, that these current singularities occur at very specific locations, the topological boundaries between different flux systems. It is still an open question as to whether current sheets form ubiquitously in the corona (Parker (1972), van Ballegooijen (1985), Antiochos (1987)).

A striking result of the simulation in chapter IV, is the extreme stability of the current sheet and reconnection dynamics, Figure 4.6. The dynamics are much less explosive than simulations of reconnection with isolated 3D null-point topologies (Pariat et al. (2009), chapter V - Edmondson et al. (2009)a, and chapter VI - Edmondson et al. (2009)c), and even less impulsive than 2.5D simulations with null-lines (Karpen et al. (1995), Karpen et al. (1996), Karpen et al. (1998)). We believe that the origins of the differences between the results of chapter IV and previous simulations of coronal reconnection lie in the form of the driving field. First, the photospheric motions in this calculation deform only the large-scale external flux system, not the small-scale embedded bipole; consequently, there is no need for free energy to spread outward. Second, the motions inject no helicity into the corona; the field lines are not twisted or sheared. Therefore, the reconnection, by itself, can lower the magnetic energy to the minimum-energy potential state without the need for propagating helicity over global scales. The implications for the corona are that slow photospheric driving of the large-scale coronal field can result in the quasi-steady energy release by reconnection, without dramatic dynamics. Such a process is exactly what is required to account for the near-steady heating of solar quiet regions.

From a global theory point of view, it is clear that the quasi-steady models are limited in their ability to reproduce coronal dynamics and, in certain cases, can fail completely. In chapter V, we assumed a form for the photospheric flows that was most

compatible with the quasi-steady models: a translation that changed the normal flux distribution at the photosphere by moving the bipole flux system without introducing significant internal structure (see chapter V, section 5.1). In chapter VI, we assumed the opposite situation of a flow that preserves exactly the photospheric flux distribution but produces a substantial internal twist in the bipole. Unlike the quasi-steady PFSS and equilbruim MHD models which assume a time series of current-free coronal fields given uniquely by the photospheric normal flux distribution, the field in these calculations does not remain current-free during the evolution. Large currents do form in the corona in response to the photospheric motions, and these currents are long-lived. Consequently, the position and geometry of the open-closed boundary will be different than that calculated from the quasi-steady model, which is important for comparison with observations. Given the proper boundary conditions, the MHD models can, in principle, calculate the field and currents precisely, but determining such boundary conditions from available observations may not be possible.

A key conclusion is that the velocity field at the photosphere is not a sufficient boundary condition to determine the structure of the corona, even the large-scale structure such as the geometry of the open-field regions. It is evident from Figures 5.7, 5.9, and 6.7, that the coronal-hole structure is determined by both the flows imposed at the photosphere and the reconnection that results in the corona. In our simulations, reconnection plays the decisive role in determining the location and topology of the open-field regions. All of the open-field evolution seen in these figures is due solely to reconnection. This implies that the coronal dissipation mechanism is critical to predicting coronal structure. In the calculations, we use numerical diffusion, which is adequate for obtaining the qualitative features of the evolution, but is unlikely to be valid for quantitative comparison with data. Unfortunately, the true coronal dissipation mechanism is largely unknown and, hence, no model at present can be expected to calculate coronal structure robustly. This is especially true in situations

such as those considered above in which an embedded bipole region is located near a coronal-hole boundary, so that even a small amount of reconnection can have a large effect on that boundary. An intriguing point is that given observations with sufficient resolution and sensitivity we may be able to use the observed geometry and evolution of the coronal-hole boundary to place constraints on the reconnection and, consequently, infer the properties of the dissipation mechanism.

One aspect of this general result is that the uniqueness conjecture (Chapter II, section 2.3; Antiochos et al. (2007)) appears to hold even during interchange reconnection. We see no evidence for disconnected coronal holes as the bipole evolves, which argues against the basic assumptions of the interchange model. The basic topology of the interchange process is that of the closed field of a bipole interacting with surrounding open field, as in Figure 5.2. The reconnection occurs along the fan surface, primarily at the null. Note that the topology is continuous and, hence, it is not valid physically to assume a picture in which reconnection takes place between an isolated open and closed field line. The difference between the continuous topology of Figure 5.2 and the often-used discontinuous picture of Figure 2.19 may seem minor, because in both models the open field undergoes a jump in footpoint position as a result of reconnection. The key point, however, is that in the continuous model the reconnection releases energy only after a large current sheet forms. If the reconnection at the null is highly efficient, the open field will smoothly transfer from one side of the bipole to the other with no heating or mass acceleration. It should be pointed out, however, that we have calculated the evolution of only a single bipole moving in a simple trajectory. The interchange model of Fisk et al. (1999) inherently assumes that the evolution of the open field is dominated by its reconnections with a dynamic complex of random bipoles, as in the magnetic carpet. It may well be that if a sufficiently complex distribution of bipoles is present, then key features of the interchange model, such as large-scale open-flux diffusion patterns, start to become

valid. It remains unclear though, if a differential rotation surface pattern, and full solar wind solution were also included in the model, that a global circulation pattern in the open flux may develop, as suggested by Fisk and co-workers.

From our simulations, the magnetic topology appears to remain fairly smooth throughout the interchange reconnection process, even when a bipole crosses the helmet streamer boundary. To the resolution of the simulations, the open-field topology remains smooth with a well-connected corridor satisfying uniqueness (Antiochos et al. (2007)). Our numerical resolution is quite high for 3D MHD simulations, but of course, the simulation is still very far from resolving the true range of scales in the corona. Within this limitation, we do not see the type of disconnected open flux postulated by the Fisk-type interchange models (e.g., Fisk et al. (1999), Fisk & Zurbuchen (2006)). Our results, therefore, constitute strong support for the topologically smooth quasi-steady models as far as the photospheric-normal distribution changes. This result, however, is sensitive to the details of the reconnection process, especially the effective resistivity. It may be that for sufficiently high Lundquist numbers and true coronal dissipation, the fan/spine topology breaks up into a turbulent-like structure so that open- and closed-flux regions become intermixed. We expect that such a topology would survive only for short time scales, but if the system were continuously driven, then an intermixed topology might be maintained in a limited region surrounding the coronal-hole boundary. The net effect would be to turn the 2D coronal-hole boundary of the quasi-steady models into a 3D dynamic structure with small but finite thickness, which could have major implications for understanding the origin of the slow wind.

The reconnection-driven dynamics calculated in this dissertation have all the essential features to explain the origin of the slow wind. The fact that slow wind is seen only near the heliospheric current sheet, within 20° - 40°, implies that the origin of the slow wind must be associated with coronal hole boundaries. It is tempting to

conjecture that this process of releasing the closed-field plasma of embedded bipoles onto open field is the origin of the slow wind. The key question, however, is whether the process is sufficiently frequent. The results shown in Figures 5.7, 5.8, and 6.7, indicate that if there are many bipoles moving randomly in response to photospheric motions, the coronal hole boundary is likely to consist of a complex dynamic web of open-field corridors. Such a dynamic topology would blur the distinction between the interchange and quasi-steady models, at least in the vicinity of coronal hole boundaries. We conjecture that a mixing of the two types of models is, in fact, the key to understanding the origins of the slow wind. Further studies using observed photospheric flux distributions and more accurate plasma energetics (including thermal conduction and chromospheric evaporation) will be needed in order to determine the importance of our results for the actual corona and wind.

There are a number of follow-up investigation that will be done. First, the study of self-consistent generation and stability of a high resolution current sheet in 3D MHD (chapter IV) is concerned with only the neutral sheet case (i.e., no magnetic field component oriented along the current direction). In this case, plasmoid formation due to the tearing mode instability was shown to be of very short correlation length in the third dimension - only of order the grid scale. The obvious next step is to include a guide field in the plane of the current sheet, and characterize the plasmoid structure and overall current sheet stability. This can be done in two ways: one, by including a guide field component in the initial magnetization state, or two, by adding a driving velocity component in the translationally symmetric direction. This situation will better reflect the solar coronal structure which is likely to have a variety of magnetic field shearing angles across the current sheet singularities. Second, the two-flux system dynamics calculations of chapters V and VI were concerned with the basic magnetic interaction (i.e., the 3D null point reconnection process) that is the simplest, non-trivial configuration of the solar coronal environment. The next step will

be to increase the complexity of the system. Most importantly, we will include a full solar wind solution, which will allow an estimate and characterization of the material being released onto open field lines by the interchange reconnection interaction. In addition, the structural complexity of the system will be increased by introducing multiple bipolar flux systems and complex photospheric driving flow fields, consistent with observed photospheric magnetogram and velocity fields. These proposed tasks, as well as properly treated flux emergence calculations, can strengthen the important structural theorems provided in chapter II, section 2.3. The generalization of such strong theoretical constraints will play a very important roll in our understanding of the magnetic field structure and heating of the solar corona, and thus the generation of the solar wind.

APPENDICES

APPENDIX A

Derivation of the Sweet-Parker Reconnection Rate

In this appendix, the Sweet-Parker reconnection rate is derived from basic conservation principles.

A.1 Derivation of Sweet Parker Reconnection Rate

Assume the current sheet has dimensions: Length = L and Width = δ. Conservation mass requires the material flowing into the current sheet at speed V_{in} along the top and bottom, must balance the material flowing out of the current sheet along the sides at speed V_{out}.

$$V_{in}\, L = V_{out}\, \delta \tag{A.1}$$

Assuming all the magnetic flux that enters the current sheet along the top and bottom reconnects, conservation of energy implies the magnetic energy density powers the fluid out-flow kinetic energy density,

$$\frac{B^2}{8\pi} = \frac{1}{2}\rho V_{out}^2 \tag{A.2}$$

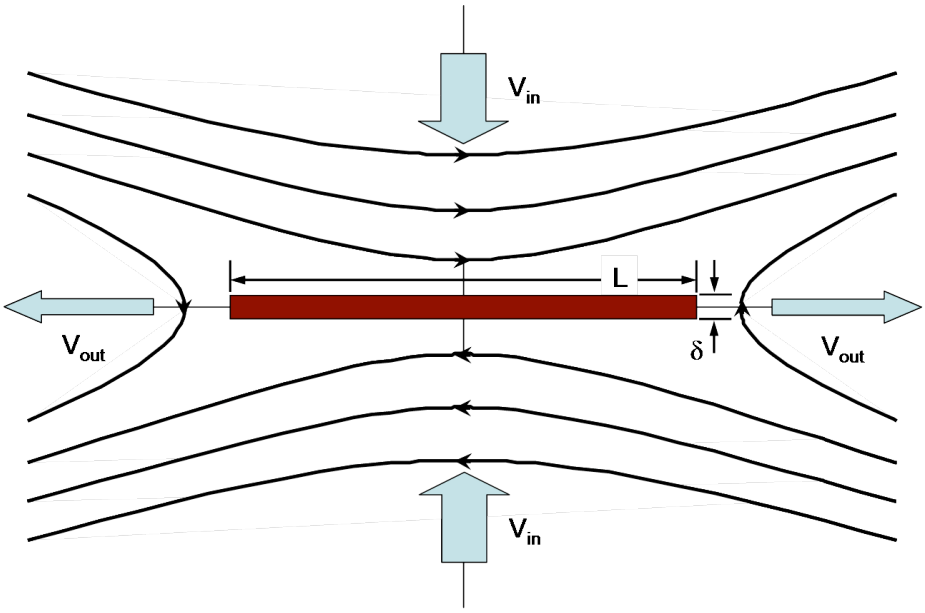

Figure A.1: Steady-state Sweet-Parker reconnection configuration.

Solving for V_{out}, and noting the definition of the Alfven speed,

$$V_{out} = \frac{B}{(4\pi\rho)^{1/2}} = V_{Alfven} \tag{A.3}$$

Equation (A.3) states that, physically, the fastest possible out-flow velocity is the characteristic Alfven speed.

From Ampere's Law we find,

$$\int \boldsymbol{B} \cdot d\boldsymbol{l} = \int \boldsymbol{J} \cdot d\boldsymbol{S} \tag{A.4}$$

$$B_x \left(2L\right) = 4\pi J_z \left(L\delta\right) \tag{A.5}$$

Solving for δ,

$$\delta = \frac{B_x}{2\pi J_z} \tag{A.6}$$

Combining equations (A.1), (A.3), and (A.6),

$$V_{in}\, L = V_{Alfven}\, \frac{B_x}{2\pi J_z} \tag{A.7}$$

The reconnection rate is defined as the unsigned ratio of the in-flow to the out-flow speeds,

$$\frac{V_{in}}{V_{Alfven}} = \frac{B_x}{2\pi L J_z} \tag{A.8}$$

In order to determine the relationship between the magnetic field component B_x, and the current density J_z, we examine the electric field. Outside the current sheet, ideal (i.e., frozen-in) MHD applies. Thus, Ohms Law reduces to,

$$\boldsymbol{E} + \boldsymbol{V}_{in} \times \boldsymbol{B} = 0 \tag{A.9}$$

Thus, the out of plane component of the electric field external to the current sheet is, in terms of the in-flow speed and magnetic field component along top (bottom) of the current sheet,

$$(E_z)_{external} = -V_{in} B_x \tag{A.10}$$

On the other hand, the electric field inside the current sheet is found from dissipative physics,

$$\boldsymbol{E} = \eta \boldsymbol{J} \tag{A.11}$$

In terms of components, all are out-of-plane,

$$(E_z)_{internal} = \eta J_z \tag{A.12}$$

For steady-state flow, the internal and external electric field components are equal,

$$(E_z)_{internal} = (E_z)_{external} \tag{A.13}$$

$$\eta J_z = -V_{in} B_x \tag{A.14}$$

Thus,

$$\frac{B_x}{J_z} = -\frac{\eta}{V_{in}} \tag{A.15}$$

Substituting equation (A.15) into equation (A.8),

$$\frac{V_{in}}{V_{Alfven}} = \frac{\eta}{2\pi L V_{in}} \tag{A.16}$$

$$\frac{V_{in}^2}{V_{Alfven}^2} = \left(\frac{\eta}{2\pi L}\right)\left(\frac{1}{V_{Alfven}}\right) \tag{A.17}$$

Noting the definition of the Lundquist number,

$$R_m \equiv \frac{L V_{in}}{\eta} \tag{A.18}$$

Thus, the Sweet-Parker reconnection rate is, modulo a constant, inversely proportional to the square root of the Lundquist number,

$$\frac{V_{in}}{V_{Alfven}} = \frac{1}{(2\pi R_m)^{1/2}} \tag{A.19}$$

APPENDIX B

Magnetic Helicity: Definition, Transport, Dissipation, and the Force-Free Condition

In this appendix, the force-free condition over the low-beta corona is derived for magnetic helicity injection.

B.1 Magnetic Helicity for General Boundary Conditions

Magnetic helicity, in a physical sense is a measure of the linking between two field lines, or equivalently the amount of twist of a given flux tube. Mathematically, the helicity is a volume dependent quantity defined as,

$$\mathcal{K} = \int_{\mathcal{V}} \boldsymbol{A} \cdot \boldsymbol{B} \, \mathrm{d}\mu \tag{B.1}$$

where the vector potential $\boldsymbol{A}$ satisfies,

$$\nabla \times \boldsymbol{A} = \boldsymbol{B}$$

$$\boldsymbol{A}(\boldsymbol{x}) = -\frac{1}{4\pi} \int_{\mathcal{V}} \frac{(\boldsymbol{x} - \boldsymbol{x'}) \times \boldsymbol{B}(\boldsymbol{x'})}{|\boldsymbol{x} - \boldsymbol{x'}|^3} \, \mathrm{d}\mu' \tag{B.2}$$

The helicity integral (B.1) is invariant under the gauge transformation $\boldsymbol{A}' \rightarrow \boldsymbol{A} + \nabla\phi$, provided: i) the volume $\mathcal{V}$ is simply connected (i.e., ϕ is single valued), and ii) bounded by a magnetic surface (i.e., $\boldsymbol{B} \cdot \boldsymbol{n}|_{\partial\mathcal{V}} = 0$).

$$\mathcal{K} = \int_{\mathcal{V}} (\boldsymbol{A} + \nabla\phi) \cdot (\nabla \times \boldsymbol{A} + \nabla \times \nabla\phi) \, \mathrm{d}\mu$$

$$\mathcal{K}' = \int_{\mathcal{V}} \boldsymbol{A} \cdot \nabla\times \ \boldsymbol{A} + \nabla\phi \cdot \nabla\times \ \boldsymbol{A} \, \mathrm{d}\mu$$

$$\mathcal{K}' = \int_{\mathcal{V}} \boldsymbol{A} \cdot \boldsymbol{B} + \nabla \cdot (\phi \boldsymbol{B}) \, \mathrm{d}\mu$$

$$\mathcal{K}' = \mathcal{K} + \int_{\partial\mathcal{V}} \phi \boldsymbol{B} \cdot \boldsymbol{n} \, \mathrm{d}S \tag{B.3}$$

Gauge invariance ($\mathcal{K}' = \mathcal{K}$) follows if assumptions (i) and (ii) above are satisfied.

In addition, a helicity integral measuring the mutual linking of two different, divergence free, vector fields ($\boldsymbol{V}$ and $\boldsymbol{W}$) may be defined,

$$\mathcal{H}(\boldsymbol{V}, \boldsymbol{W}) = \int_{\mathcal{V}} \boldsymbol{A}_{\boldsymbol{V}} \cdot \boldsymbol{W} \, \mathrm{d}\mu \tag{B.4}$$

If the argument vector fields are closed (i.e., tangent to the boundary, $\boldsymbol{V} \cdot \boldsymbol{n}|_{\partial\mathcal{V}} = 0$ and $\boldsymbol{W} \cdot \boldsymbol{n}|_{\partial\mathcal{V}} = 0$), then equation (B.4) is symmetric in it arguments.

$$\mathcal{H}(\boldsymbol{V}, \boldsymbol{W}) = \mathcal{H}(\boldsymbol{W}, \boldsymbol{V})$$

On the other hand, if the vector magnetic field $\boldsymbol{B}$ is open (i.e., $\boldsymbol{B} \cdot \boldsymbol{n}|_{\partial\mathcal{V}} \neq 0$, at least over some section of the boundary), then equation (B.4) is not unique since the field linking geometry is, in general, not unique for a given boundary normal distribution. However, the current-free, potential field $\boldsymbol{B}_{\boldsymbol{P}}$ solution consistent with the boundary condition $\boldsymbol{B} \cdot \boldsymbol{n}|_{\partial\mathcal{V}} = g$, is a unique configuration. In fact, the potential

field $\boldsymbol{B_P}$ is the minimum energy state of the magnetic field geometry for the given normal-field distribution at the boundary. Therefore, in order to construct a unique mutual helicity integral (B.4) for a general magnetic field $\boldsymbol{B}$ with a given normal boundary distribution $\boldsymbol{B} \cdot \boldsymbol{n}|_{\partial\mathcal{V}} = g$, decompose into the sum of open and closed components which respectively satisfy,

$$\nabla \times \boldsymbol{B_P} = \boldsymbol{0} \qquad \boldsymbol{B_P} \cdot \boldsymbol{n}|_{\partial\mathcal{V}} = g$$

$$\boldsymbol{B_{cl}} = \boldsymbol{B} - \boldsymbol{B_P} \qquad \boldsymbol{B_{cl}} \cdot \boldsymbol{n}|_{\partial\mathcal{V}} = 0$$

Equation (B.4) becomes,

$$\mathcal{H}(\boldsymbol{B}, \boldsymbol{B}) = \mathcal{H}(\boldsymbol{B_{cl}} + \boldsymbol{B_P}, \boldsymbol{B_{cl}} + \boldsymbol{B_P})$$

$$\mathcal{H}(\boldsymbol{B}, \boldsymbol{B}) = \mathcal{H}(\boldsymbol{B_{cl}}, \boldsymbol{B_{cl}}) \ + \ 2\,\mathcal{H}(\boldsymbol{B_P}, \boldsymbol{B_{cl}}) \ + \ \mathcal{H}(\boldsymbol{B_P}, \boldsymbol{B_P}) \tag{B.5}$$

The first two terms on the RHS of equation (B.5) measure the self-linking of the closed component, and the mutual linking of the closed component with the open component. The last term is ill defined by equation (B.5) since the closed field assumption is not satisfied. Physically, the potential field is the unique minimum energy state of all possible magnetic field geometries for a given normal-component distribution at the boundary, so it is natural to reset the zero helicity datum to this level (i.e., $\mathcal{H}(\boldsymbol{B_P}, \boldsymbol{B_P}) \equiv 0$). With this definition, the mutual helicity integral (B.4) reduces to,

$$\mathcal{H}(\boldsymbol{B}, \boldsymbol{B}) = \mathcal{H}(\boldsymbol{B_{cl}}, \boldsymbol{B_{cl}}) \ + \ 2\,\mathcal{H}(\boldsymbol{B_P}, \boldsymbol{B_{cl}}) \tag{B.6}$$

Since equation (B.6) represents the helicity of a single magnetic field configuration,

$$\mathcal{K} = \mathcal{H}(\boldsymbol{B}, \boldsymbol{B})$$

$$\mathcal{K} = \mathcal{H}(\boldsymbol{B} - \boldsymbol{B_P}, \boldsymbol{B} - \boldsymbol{B_P}) \; + \; 2\,\mathcal{H}(\boldsymbol{B_P}, \boldsymbol{B} - \boldsymbol{B_P})$$

$$\mathcal{K} = \int_{\mathcal{V}} (\boldsymbol{A} + \boldsymbol{A_P}) \cdot (\boldsymbol{B} - \boldsymbol{B_P}) \; \mathrm{d}\mu \tag{B.7}$$

Equation (B.7) is a gauge invariant ($\boldsymbol{A}' \rightarrow \boldsymbol{A} + \nabla\phi$, for both vector potentials describing the full field and potential field) measure of the relative helicity for a general magnetic field configuration with a normal component at the domain boundary.

B.2 Ideal Transport of Magnetic Helicity

In this section, the transport of magnetic helicity in the framework of ideal MHD is derived. Starting by taking the total time derivative of equation (B.7), assuming a fixed volume $\mathcal{V}$,

$$\frac{\mathrm{d}\mathcal{K}}{\mathrm{dt}} = \frac{\mathrm{d}}{\mathrm{dt}} \int_{\mathcal{V}} (\boldsymbol{A} + \boldsymbol{A_P}) \cdot (\boldsymbol{B} - \boldsymbol{B_P}) \; \mathrm{d}\mu$$

$$\frac{\mathrm{d}\mathcal{K}}{\mathrm{dt}} = \int_{\mathcal{V}} \frac{\partial}{\partial \mathrm{t}} (\boldsymbol{A} + \boldsymbol{A_P}) \cdot (\boldsymbol{B} - \boldsymbol{B_P}) + (\boldsymbol{A} + \boldsymbol{A_P}) \cdot \frac{\partial}{\partial \mathrm{t}} (\boldsymbol{B} - \boldsymbol{B_P}) \; \mathrm{d}\mu$$

It can be shown,

$$\frac{\partial \boldsymbol{A}}{\partial \mathrm{t}} \cdot \boldsymbol{B} = \nabla \cdot \left(\boldsymbol{A} \times \frac{\partial \boldsymbol{A}}{\partial \mathrm{t}} \right) + \boldsymbol{A} \cdot \frac{\partial \boldsymbol{B}}{\partial \mathrm{t}}$$

Substituting the above vector identity and combining relevant terms,

$$\frac{\mathrm{d}\mathcal{K}}{\mathrm{dt}} = \int_{\mathcal{V}} \nabla \cdot \left[(\boldsymbol{A} - \boldsymbol{A_P}) \times \left(\frac{\partial \boldsymbol{A}}{\partial \mathrm{t}} + \frac{\partial \boldsymbol{A_P}}{\partial \mathrm{t}} \right) \right] + 2 \left(\boldsymbol{A} \cdot \frac{\partial \boldsymbol{B}}{\partial \mathrm{t}} - \boldsymbol{A_P} \cdot \frac{\partial \boldsymbol{B_P}}{\partial \mathrm{t}} \right) \; \mathrm{d}\mu$$

$$\frac{\mathrm{d}\mathcal{K}}{\mathrm{dt}} = \int_{\mathcal{V}} 2 \left(\boldsymbol{A} \cdot \frac{\partial \boldsymbol{B}}{\partial \mathrm{t}} - \boldsymbol{A_P} \cdot \frac{\partial \boldsymbol{B_P}}{\partial \mathrm{t}} \right) \; \mathrm{d}\mu + \int_{\partial \mathcal{V}} (\boldsymbol{A} - \boldsymbol{A_P}) \times \left(\frac{\partial \boldsymbol{A}}{\partial \mathrm{t}} + \frac{\partial \boldsymbol{A_P}}{\partial \mathrm{t}} \right) \cdot \boldsymbol{n} \; \mathrm{d}S \tag{B.8}$$

Noting the vector identity,

$$(\boldsymbol{A} - \boldsymbol{A_P}) \times \left(\frac{\partial \boldsymbol{A}}{\partial \mathrm{t}} + \frac{\partial \boldsymbol{A_P}}{\partial \mathrm{t}} \right) \cdot \boldsymbol{n} = \frac{\partial}{\partial \mathrm{t}} (\boldsymbol{A} + \boldsymbol{A_P}) \cdot [(\boldsymbol{A} - \boldsymbol{A_P}) \times \boldsymbol{n}]$$

Recall, by definition, the open field boundary condition,

$$\boldsymbol{B}\cdot\boldsymbol{n}|_{\partial\mathcal{V}} = \boldsymbol{B_P}\cdot\boldsymbol{n}|_{\partial\mathcal{V}} \qquad \Rightarrow \qquad \boldsymbol{A}\times\boldsymbol{n}|_{\partial\mathcal{V}} = \boldsymbol{A_P}\times\boldsymbol{n}|_{\partial\mathcal{V}}$$

Thus, the surface integral in equation (B.8) vanishes leaving only the volume integral.

$$\frac{\mathrm{d}\mathcal{K}}{\mathrm{dt}} = \int_{\mathcal{V}} 2\left(\boldsymbol{A}\cdot\frac{\partial\boldsymbol{B}}{\partial\mathrm{t}} - \boldsymbol{A_P}\cdot\frac{\partial\boldsymbol{B_P}}{\partial\mathrm{t}}\right)\,\mathrm{d}\mu \tag{B.9}$$

Making use of Faraday's Law and the definition of the potential field,

$$\frac{\partial\boldsymbol{B}}{\partial\mathrm{t}} + c\,\nabla\times\boldsymbol{E} = \boldsymbol{0} \qquad\qquad \boldsymbol{B_P}\equiv\nabla\Phi$$

Equation (B.9) becomes,

$$\frac{\mathrm{d}\mathcal{K}}{\mathrm{dt}} = -2\int_{\mathcal{V}} \boldsymbol{A}\cdot(c\,\nabla\times\boldsymbol{E}) + \boldsymbol{A_P}\cdot\frac{\partial}{\partial\mathrm{t}}(\nabla\Phi)\,\mathrm{d}\mu \tag{B.10}$$

It can be shown,

$$\boldsymbol{A}\cdot(\nabla\times\boldsymbol{E}) = \boldsymbol{E}\cdot\boldsymbol{B} - \nabla\cdot(\boldsymbol{A}\times\boldsymbol{E})$$

$$\boldsymbol{A_P}\cdot\frac{\partial}{\partial\mathrm{t}}(\nabla\Phi) = \nabla\cdot\left(\boldsymbol{A_P}\,\frac{\partial\Phi}{\partial\mathrm{t}}\right) - \frac{\partial\Phi}{\partial\mathrm{t}}(\nabla\cdot\boldsymbol{A_P})$$

Substituting into equation (B.10),

$$\frac{\mathrm{d}\mathcal{K}}{\mathrm{dt}} = 2\,c\int_{\mathcal{V}} \nabla\cdot\left(\boldsymbol{A}\times\boldsymbol{E} + \boldsymbol{A_P}\,\frac{1}{c}\frac{\partial\Phi}{\partial\mathrm{t}}\right) - \left(\boldsymbol{E}\cdot\boldsymbol{B} + \frac{1}{c}\frac{\partial\Phi}{\partial\mathrm{t}}(\nabla\cdot\boldsymbol{A_P})\right)\,\mathrm{d}\mu \tag{B.11}$$

At this point, it is useful to choose the Coulomb gauge for both vector potentials $\boldsymbol{A}$ and $\boldsymbol{A_P}$,

$$\nabla\cdot\boldsymbol{A} = 0 \qquad \Rightarrow \qquad \boldsymbol{A}\cdot\boldsymbol{n}|_{\partial\mathcal{V}} = 0$$

By fixing the Coulomb gauge, equation (B.11) reduces to,

$$\frac{\mathrm{d}\mathcal{K}}{\mathrm{dt}} = 2\ c \int_{\partial\mathcal{V}} (\boldsymbol{A} \times \boldsymbol{E}) \cdot \boldsymbol{n}\ \mathrm{d}S - 2\ c \int_{\mathcal{V}} \boldsymbol{E} \cdot \boldsymbol{B}\ \mathrm{d}\mu \tag{B.12}$$

Again recalling the definition of the open field boundary condition,

$$\boldsymbol{A} \times \boldsymbol{n}|_{\partial\mathcal{V}} = \boldsymbol{A_P} \times \boldsymbol{n}|_{\partial\mathcal{V}}$$

And assuming ideal MHD evolution,

$$\boldsymbol{E} = -\ \boldsymbol{v} \times \boldsymbol{B}$$

Equation (B.12) becomes,

$$\frac{\mathrm{d}\mathcal{K}}{\mathrm{dt}} = 2\ c \int_{\partial\mathcal{V}} [\ (\boldsymbol{v} \times \boldsymbol{B}) \times \boldsymbol{A_P}\ ] \cdot \boldsymbol{n}\ \mathrm{d}S$$

Expanding the triple vector product,

$$\frac{\mathrm{d}\mathcal{K}}{\mathrm{dt}} = 2\ c \int_{\partial\mathcal{V}} [\ (\boldsymbol{A_P} \cdot \boldsymbol{v})\boldsymbol{B} - (\boldsymbol{A_P} \cdot \boldsymbol{B})\boldsymbol{v}\ ] \cdot \boldsymbol{n}\ \mathrm{d}S \tag{B.13}$$

Equation (B.13) is the equation for ideal transport of magnetic helicity. The terms on the RHS describe the helicity transport due to motions respectively parallel and perpendicular to the boundary. $\boldsymbol{A_P}$ is the unique vector potential for the potential field $\boldsymbol{B_P}$ (given by the boundary normal distribution $\boldsymbol{B} \cdot \boldsymbol{n}|_{\partial\mathcal{V}} = g$), and satisfies,

$$\boldsymbol{B_P} = \nabla \times \boldsymbol{A_P}$$

$$\nabla \cdot \boldsymbol{A_P} = 0 \qquad\qquad \boldsymbol{A_P} \cdot \boldsymbol{n}|_{\partial\mathcal{V}} = 0$$

B.3 Helicity Dissipation

The dissipation of magnetic helicity follows from resistive slippage of the field through the plasma. Starting with equation B.12,

$$\frac{\mathrm{d}\mathcal{K}}{\mathrm{dt}} = 2\ c \int\limits_{\partial\mathcal{V}} (\boldsymbol{A} \times \boldsymbol{E}) \cdot \boldsymbol{n}\ \mathrm{d}S - 2\ c \int\limits_{\mathcal{V}} \boldsymbol{E} \cdot \boldsymbol{B}\ \mathrm{d}\mu$$

Assuming a fixed boundary flux $\boldsymbol{B} \cdot \boldsymbol{n}|_{\partial\mathcal{V}} =$ constant, such that no helicity may transported across the boundary. And using Ohm's Law $\boldsymbol{E} = \eta \boldsymbol{J}$ to express the electric field in terms of the current density. Equation B.12 reduces to,

$$\frac{\mathrm{d}\mathcal{K}}{\mathrm{dt}} = -2 \int\limits_{\mathcal{V}} \eta \boldsymbol{J} \cdot \boldsymbol{B}\ \mathrm{d}\mu \tag{B.14}$$

On the other hand, the magnetic energy is defined as,

$$\mathcal{W} = \frac{1}{8\pi} \int\limits_{\mathcal{V}} \boldsymbol{B} \cdot \boldsymbol{B}\ \mathrm{d}\mu \tag{B.15}$$

The rate of dissipation of the magnetic energy is therefore,

$$\frac{\mathrm{d}\mathcal{W}}{\mathrm{dt}} = \frac{1}{4\pi} \int\limits_{\mathcal{V}} \boldsymbol{B} \cdot \frac{\partial \boldsymbol{B}}{\partial t}\ \mathrm{d}\mu \tag{B.16}$$

Substituting Faraday's Law for $\frac{\partial \boldsymbol{B}}{\partial t} + c\nabla \times \boldsymbol{E} = 0$, equation B.16 becomes,

$$\frac{\mathrm{d}\mathcal{W}}{\mathrm{dt}} = \frac{-c}{4\pi} \int\limits_{\mathcal{V}} \boldsymbol{E} \cdot \nabla \times\ \boldsymbol{B}\ \mathrm{d}\mu \tag{B.17}$$

Where the vector identity $\boldsymbol{B} \cdot (\nabla \times \boldsymbol{E}) - \boldsymbol{E} \cdot (\nabla \times \boldsymbol{B}) = \nabla \cdot (\boldsymbol{E} \times \boldsymbol{B})$, and the fixed boundary flux condition have been used. Finally, substituting Ampere's Law $\nabla \times \boldsymbol{B} = \frac{4\pi}{c} \boldsymbol{J}$, and Ohm's Law $\boldsymbol{E} = \eta \boldsymbol{J}$, the dissipation of magnetic energy, expressed

in terms of the current density, is,

$$\frac{\mathrm{d}\mathcal{W}}{\mathrm{dt}} = -\int_{\mathcal{V}} \eta J^2 \, \mathrm{d}\mu \tag{B.18}$$

Note, the negative sign simply says the magnetic energy decreases by resistive dissipation. The helicity and magnetic energy dissipation rates may be compared using the Cauchy-Schwartz Inequality for the volume integrals of $\boldsymbol{B} \cdot \boldsymbol{B}$ (B.15) and $\boldsymbol{J} \cdot \boldsymbol{J}$ (B.18),

$$\left|\frac{\mathrm{d}\mathcal{K}}{\mathrm{dt}}\right| \leq \left(2\,\eta\,\mathcal{W}\left|\frac{\mathrm{d}\mathcal{W}}{\mathrm{dt}}\right|\right)^{\frac{1}{2}} \tag{B.19}$$

To apply condition (B.19) to reconnection events, define a length scale $L \equiv \frac{\mathcal{K}}{\mathcal{W}}$. This length scale, in turn, may be used to define a dissipation time $\tau_d \equiv \frac{L^2}{f\eta}$, where $f \ll 1$ is the fraction of the total volume over which the resistivity is appreciable enough for current sheet generation and reconnection. Thus, any reconnection process that occurs over a time Δt, will dissipate an amount of magnetic helicity according to the integral of (B.19),

$$\left|\frac{\Delta\mathcal{K}}{\mathcal{K}}\right| \leq \left(\frac{\Delta t}{\tau_d}\right)^{\frac{1}{2}} \tag{B.20}$$

Noting that reconnection events take place effectively instantaneously ($\Delta t \to 0$), over a very small fraction of the volume, equation (B.20) shows helicity is preserved under reconnection.

B.4 Force Free Condition

The force-free condition on a general magnetic field configuration follows directly from energy minimization subject to a volumetric helicity conservation.

$$\delta \int_{\mathcal{V}} \left[\frac{1}{2}(\boldsymbol{B} \cdot \boldsymbol{B}) - \lambda(\boldsymbol{A} \cdot \boldsymbol{B}) \right] \mathrm{d}\mu = 0 \tag{B.21}$$

Modulo a constant on the energy term depending on the choice of units, and the vector potential $\boldsymbol{A}$ satisfies,

$$\boldsymbol{B} = \nabla \times \boldsymbol{A}$$

At this point, indicial notation better illustrates the derivation. Rewriting equation (B.21),

$$\delta \int_{\mathcal{V}} \left[\frac{1}{2} \, (\varepsilon_{ijk}\partial_j A_k)(\varepsilon_{ilm}\partial_l A_m) - \lambda \, A_i(\varepsilon_{ijk}\partial_j A_k) \right] \mathrm{d}\mu = 0 \tag{B.22}$$

Where ε_{ijk} is the alternating tensor. The Lagrangian density here is,

$$\mathcal{L}(A_i, \partial_j A_k) \equiv \frac{1}{2} \, (\varepsilon_{ijk}\partial_j A_k)(\varepsilon_{ilm}\partial_l A_m) - \lambda \, A_i(\varepsilon_{ijk}\partial_j A_k) \tag{B.23}$$

The Euler-Lagrange equations satisfy,

$$\partial_j \left(\frac{\partial \mathcal{L}}{\partial(\partial_j A_k)} \right) - \frac{\partial \mathcal{L}}{\partial A_i} = 0$$

Which for this system become,

$$\partial_j \left(\frac{1}{2} \, \varepsilon_{ijk}(\varepsilon_{ilm}\partial_l A_m) - \lambda \, A_i \varepsilon_{ijk} \right) + \lambda \, (\varepsilon_{ijk}\partial_j A_k) = 0 \tag{B.24}$$

Noting the antisymmetric properties of the alternating tensor,

$$\varepsilon_{ijk} = -\varepsilon_{kji}$$

Collecting like terms and relabeling dummy indices equation (B.24) becomes,

$$\varepsilon_{kji}\partial_j(\varepsilon_{ilm}\partial_l A_m) - 2 \, \lambda \, (\varepsilon_{kji}\partial_j A_i) = 0$$

Returning to vector notation,

$$\nabla \times (\nabla \times \boldsymbol{A}) = \alpha \, (\nabla \times \boldsymbol{A})$$

Finally,

$$\nabla \times \boldsymbol{B} = \alpha \boldsymbol{B} \tag{B.25}$$

APPENDIX C

X-Line Potential Field Model

In this appendix, the analytic vector potential field model used in Chapter IV is derived in section C.1, and the infinite series is shown to converge in section C.2.

C.1 Derivation of the Vector Potential Field due to a Linear Dipole Density Distribution

The differential potential due to a differential charge distribution dq, at position $\boldsymbol{r}$, is (Jackson (1975)):

$$d\Phi\left(\boldsymbol{x}\right) = \frac{dq}{|\boldsymbol{x} - \boldsymbol{r}|} \tag{C.1}$$

Given a linear charge density $|\lambda| = \frac{|Q|}{2L}$, where Q is the total charge and $2L$ is the total length. The total differential potential due to a positive linear charge distribution $+dq = +\lambda dl$ at position $\boldsymbol{r}$, and a negative linear charge distribution $-dq = -\lambda dl$ at position $\boldsymbol{r} + \boldsymbol{\epsilon}$ (see Figure C.1), is given by,

$$d\Phi\left(\boldsymbol{x}\right) = \frac{+\lambda}{|\boldsymbol{x} - \boldsymbol{r}|} + \frac{-\lambda}{|\boldsymbol{x} - (\boldsymbol{r} + \boldsymbol{\epsilon})|} \tag{C.2}$$

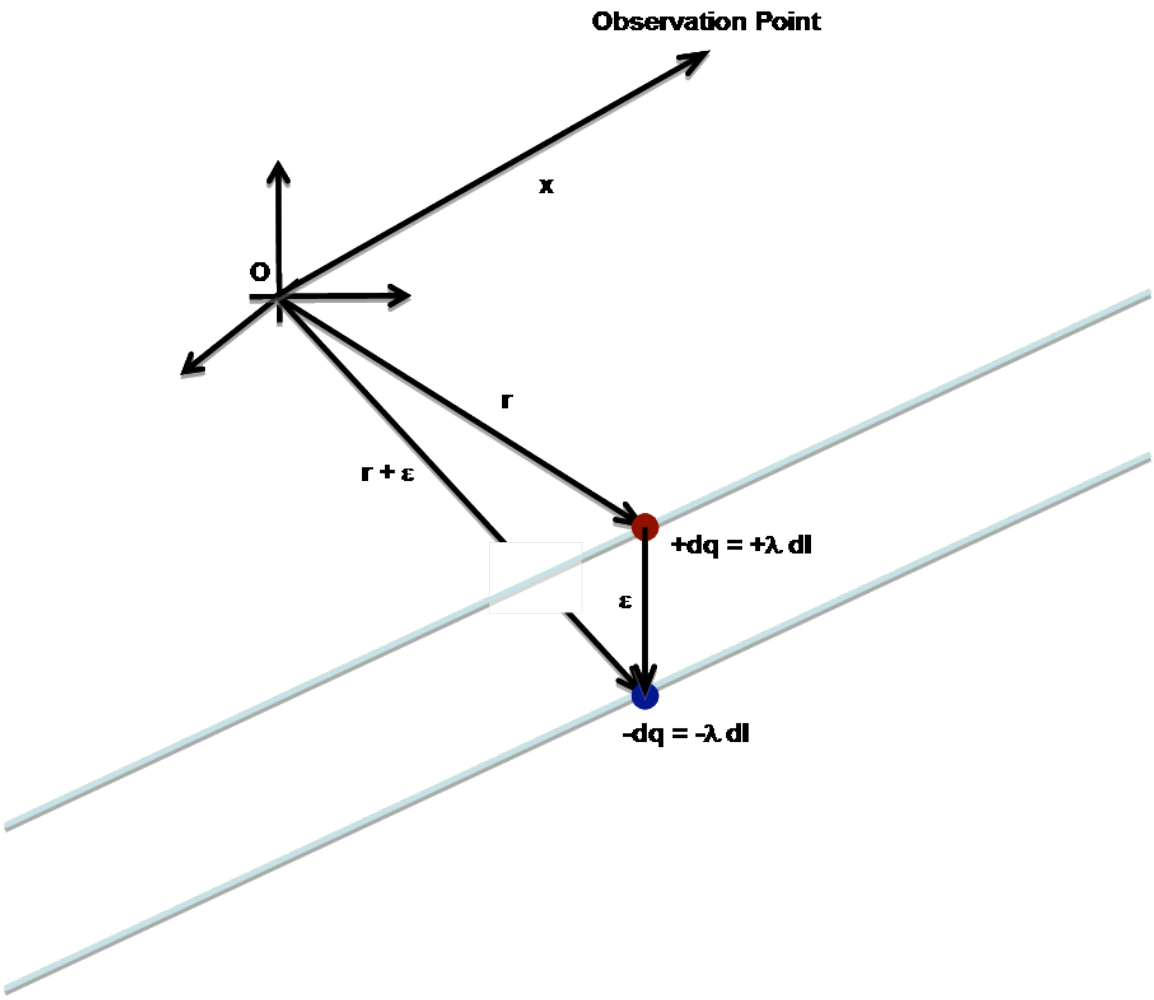

Figure C.1: Linear dipole density distribution general set-up

To 1st order in $\boldsymbol{\epsilon}$,

$$\left[\frac{1}{|\boldsymbol{x}-\boldsymbol{r}|}+\frac{1}{|\boldsymbol{x}-(\boldsymbol{r}+\boldsymbol{\epsilon})|}\right]\lambda dl \approx -\frac{(\boldsymbol{x}-\boldsymbol{r})\cdot(\boldsymbol{\epsilon}\lambda dl)}{|\boldsymbol{x}-\boldsymbol{r}|^3} \tag{C.3}$$

Define the dipole density distribution as $\boldsymbol{M} \equiv \lambda\boldsymbol{\epsilon}$, such that,

$$d\Phi(\boldsymbol{x}) = -\boldsymbol{M}\cdot\frac{(\boldsymbol{x}-\boldsymbol{r})}{|\boldsymbol{x}-\boldsymbol{r}|^3}dl \tag{C.4}$$

Thus, the generalized total potential field is,

$$\Phi(\boldsymbol{x}) = -\boldsymbol{M}\cdot\int_C \frac{(\boldsymbol{x}-\boldsymbol{r})}{|\boldsymbol{x}-\boldsymbol{r}|^3}dl \tag{C.5}$$

where the dipole density distribution $\boldsymbol{M}$ follows the path C in space.

At this point, choose a coordinate system such that the linear charge densities are given by, $|dq| = |\lambda|dx$ (see Figure C.2).

The position vector $\boldsymbol{r}$ and the differential dl may now be written as, $\boldsymbol{r} = x\boldsymbol{e}_x - h\boldsymbol{e}_z$ and $dl = dx$, respectively. Fixing the dipole orientation along the negative z-axis, $\boldsymbol{M} = -M\boldsymbol{e}_z$. (And for notational purposes, designate the observation point $\boldsymbol{x}_0$.) The total potential field is now expanded,

$$\Phi(\boldsymbol{x}_0) = -M\int_{-L}^{+L}\frac{(z_0+h)}{\left[(x_0-x)^2+y_0^2+(z_0+h)^2\right]^{\frac{3}{2}}}dx \tag{C.6}$$

This is easily integrated to yield,

$$\begin{aligned}\Phi(\boldsymbol{x}_0) = &\frac{M(z_0+h)(x_0+L)}{\left[y_0^2+(z_0+h)^2\right]\left[(x_0+L)^2+y_0^2+(z_0+h)^2\right]^{\frac{1}{2}}}\\ &-\frac{M(z_0+h)(x_0-L)}{\left[y_0^2+(z_0+h)^2\right]\left[(x_0-L)^2+y_0^2+(z_0+h)^2\right]^{\frac{1}{2}}}\end{aligned} \tag{C.7}$$

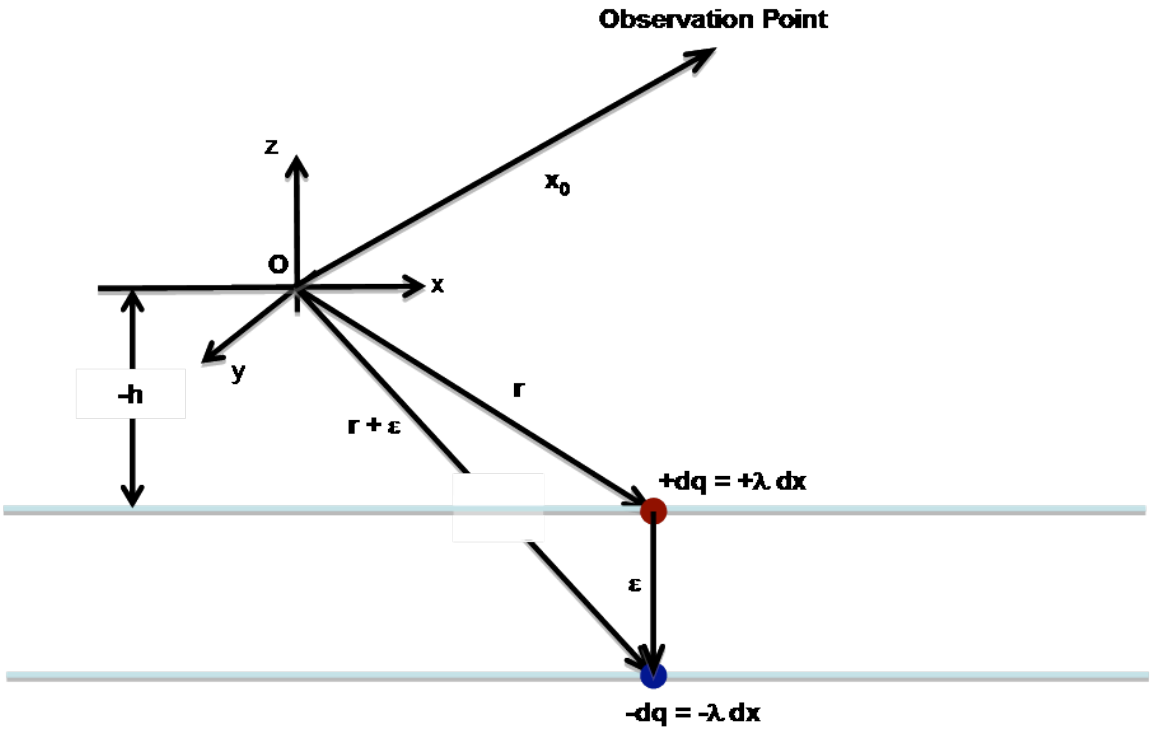

Figure C.2: Linear dipole density distribution in fixed coordinate system such the the integration path C may be easily defined.

Which for $L \gg 1$, looks like,

$$\Phi(\boldsymbol{x}_0) = -\frac{M(z_0+h)}{y_0^2+(z_0+h)^2}\left(1+\frac{x_0}{L}\right)\left[1-\frac{x_0}{L}+O\left(L^{-2}\right)\right] - \frac{M(z_0+h)}{y_0^2+(z_0+h)^2}\left(1-\frac{x_0}{L}\right)\left[1+\frac{x_0}{L}+O\left(L^{-2}\right)\right] \tag{C.8}$$

In the limit as $L \to \infty$, the potential field observed at position $\boldsymbol{x}_0$, due to a single linear dipole moment density distribution $\boldsymbol{M}$, oriented in the negative z-direction, placed a distance h below the x-y plane is,

$$\Phi(\boldsymbol{x}_0) = -\frac{2M(z_0+h)}{y_0^2+(z_0+h)^2} \tag{C.9}$$

To include a null-point in the magnetic field geometry, we simply add a constant vertical field in the z-direction, of magnitude B_0, oriented anti-parallel to the dipole density direction.

$$\Phi(\boldsymbol{x}_0) = B_0 z - \frac{2M(z_0+h)}{y_0^2+(z_0+h)^2} \tag{C.10}$$

In accordance with the periodic numerical boundary conditions requiring a vertical magnetic field at the boundaries of the y-domain, we must generalize this distribution. Since equation (C.10) is linear in the dipole moment density distribution, we may easily generalize this distribution to an infinite series of linear dipole density distributions, at positions $y = nd$, mirrored about the origin. Thus,

$$\Phi(\boldsymbol{x}_0) = B_0 z - \sum_{n=-\infty}^{+\infty} \frac{2M(z_0+h)}{(y_0-nd)^2+(z_0+h)^2} \tag{C.11}$$

Note, oppositely directed horizontal field components are balanced at the y positions $y = \left|\left(n+\frac{1}{2}\right)d\right|$. Since this model for the total potential due to a periodic set of linear dipole density distributions, separated by a distance d in the y-direction, is

translationally symmetric (i.e., independent of one of the coordinate variables), we may solve for the corresponding vector potential $\boldsymbol{A}(\boldsymbol{x}_0) = A(\boldsymbol{x}_0)\,\boldsymbol{e}_x$ by setting,

$$\nabla\Phi(\boldsymbol{x}_0) = \nabla A(\boldsymbol{x}_0) \times \boldsymbol{e}_x \tag{C.12}$$

Which in this coordinate system reduces to,

$$\frac{\partial}{\partial z}\Phi(\boldsymbol{x}_0) = -\frac{\partial}{\partial y}A(\boldsymbol{x}_0) \tag{C.13}$$

$$A(\boldsymbol{x}_0) = -\frac{\partial}{\partial z}\int\left[B_0 z - \sum_{n=-\infty}^{+\infty}\frac{2M(z_0+h)}{(y_0-nd)^2+(z_0+h)^2}\right]dy \tag{C.14}$$

$$A(\boldsymbol{x}_0) = -\frac{\partial}{\partial z}\left[B_0 zy - \sum_{n=-\infty}^{+\infty} 2M\,Arctan\left(\frac{y_0-nd}{z_0+h}\right) + g(x,z)\right] \tag{C.15}$$

Making use of the gauge freedom for the magnetic vector potential, we set $g(x,z) = 0$,

$$A(\boldsymbol{x}_0) = -B_0 y + \sum_{n=-\infty}^{+\infty}\frac{2M(y_0-nd)}{(y_0-nd)^2+(z_0+h)^2} \tag{C.16}$$

Rearranging the series, we find the final form of the magnetic field model vector potential $\boldsymbol{A}(\boldsymbol{x}) = A(\boldsymbol{x})\,\boldsymbol{e}_x$,

$$\begin{aligned} A(\boldsymbol{x}) = B_0 y &- \frac{My}{2}\left(\frac{2}{d}\right)^2\left(\frac{d^2}{y^2+(z-h)^2}\right) \\ &+ My\left(\frac{2}{d}\right)^2\sum_{n=1}^{+\infty}\left(\frac{1}{n^2}\right)\frac{\left(1-\frac{1}{n^2}\frac{y^2+(z-h)^2}{d^2}\right)}{\left(1-\frac{1}{n^2}\frac{y^2+(z-h)^2}{d^2}\right)^2+\left(\frac{1}{n^2}\frac{2(z-h)}{d}\right)^2} \end{aligned} \tag{C.17}$$

Over the domain, $\{(y,z)\,\big|\,-\frac{d}{2}\le y\le\frac{d}{2}, 0<(z-h)<\frac{d}{2}\}$.

C.2 Proof of Convergence for the Infinite Series Vector Potential Model

Now that the model (equation C.17) has been derived, it is a simple matter to show convergence. Proof of convergence for the infinite series,

$$\sum_{n=1}^{+\infty} a_n = \sum_{n=1}^{+\infty} \left(\frac{1}{n^2}\right) \frac{\left(1 - \frac{1}{n^2}\frac{y^2+(z-h)^2}{d^2}\right)}{\left(1 - \frac{1}{n^2}\frac{y^2+(z-h)^2}{d^2}\right)^2 + \left(\frac{1}{n^2}\frac{2(z-h)}{d}\right)^2} \tag{C.18}$$

is done by the integral test, since the function is monotonically decreasing in its successive terms (i.e., $a_{n+1} > a_n$). Convergence follows from the (numerical) integral test. It suffices to show,

$$CT\left(y, z-h\right) = \int_1^{\infty} \left(\frac{1}{n^2}\right) \frac{\left(1 - \frac{1}{n^2}\frac{y^2+(z-h)^2}{d^2}\right)}{\left(1 - \frac{1}{n^2}\frac{y^2+(z-h)^2}{d^2}\right)^2 + \left(\frac{1}{n^2}\frac{2(z-h)}{d}\right)^2} dn \tag{C.19}$$

is everywhere bounded over the domain $\{(y,z)\,\big|\, -\frac{d}{2} \leq y \leq \frac{d}{2}, 0 < (z-h) < \frac{d}{2}\}$. Plotting the $CT\left(y, z-h\right)$ surface over the domain, where the parameter $d = 40$ (coinciding with the value taken in chapter IV), we find the solution is bounded everywhere (see Figure C.3) and thus the series converges.

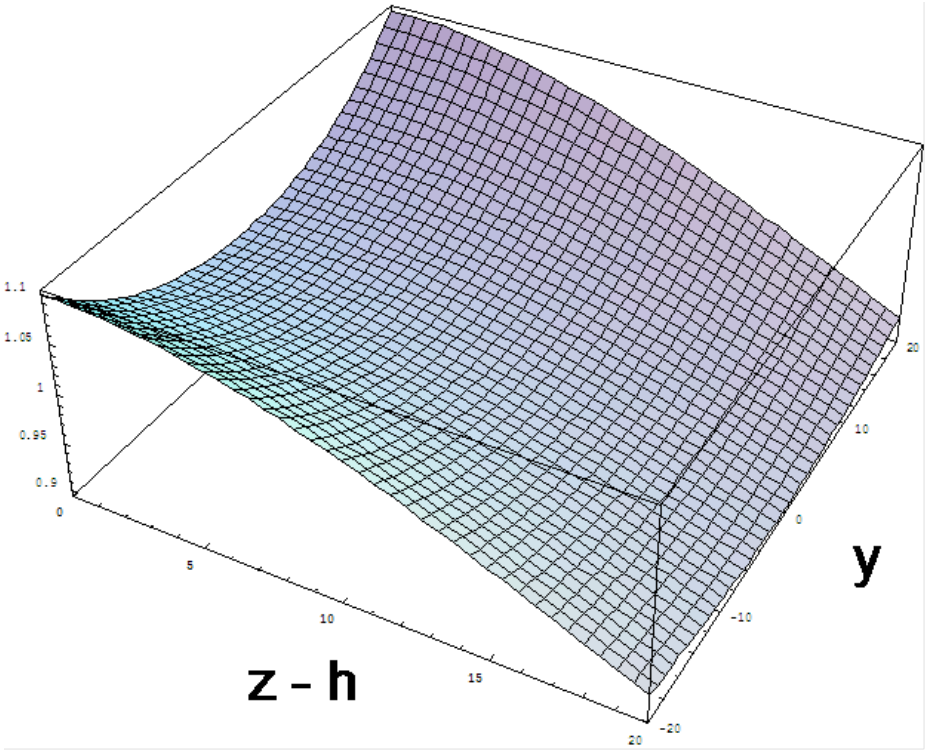

Figure C.3: Convergence of the Linear Dipole Density Distribution: Surface plot of $CT\,(y, z-h)$ surface over the domain is everywhere finite, therefore the infinite series in the model (equation C.17) converges.

APPENDIX D

Coronal Potential Field Source Surface Model

In this appendix, the analytic potential field model used in Chapters V and VI is derived from the method of images.

D.1 Derivation of Dipole Distribution Potential Field with a Source Surface at Radius R

The potential field due to a single positive point charge +q, at position $\boldsymbol{r}$, in the presence of a grounded, conducting sphere (Jackson (1975)):

$$\Phi(\boldsymbol{x}) = \frac{q}{|\boldsymbol{x}-\boldsymbol{r}|} - \left(\frac{R}{|\boldsymbol{r}|}\right)\frac{q}{|\boldsymbol{x}-\left(\frac{R}{|\boldsymbol{r}|}\right)^2\boldsymbol{r}|} \tag{D.1}$$

The potential field due to a positive point charge $+q$, at position $\boldsymbol{r}$, a negative point charge q, at position $\boldsymbol{r}+\boldsymbol{\epsilon}$, and a spherical source surface at radius R (Figure

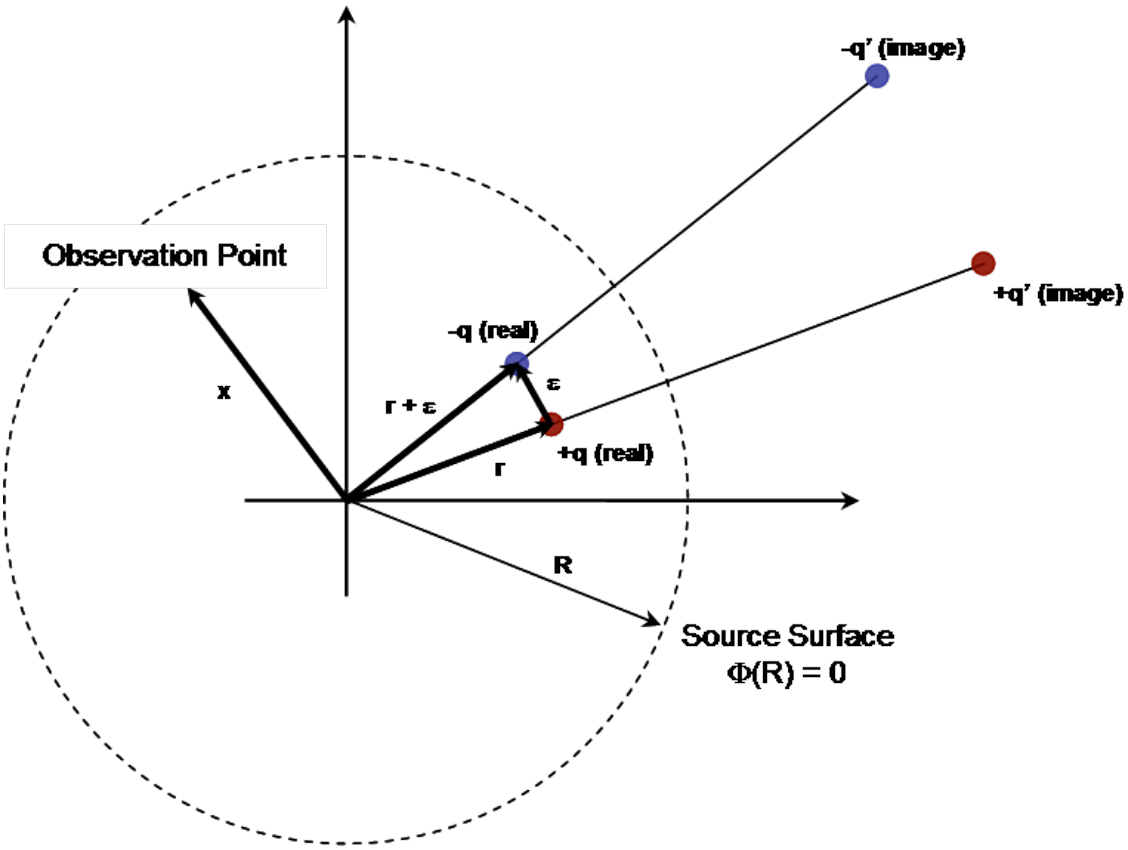

Figure D.1: Potential field model method of images set-up.

D.1):

$$\Phi(\boldsymbol{x}) = \left[\frac{(+q)}{|\boldsymbol{x}-\boldsymbol{r}|} - \left(\frac{R}{|\boldsymbol{r}|}\right)\frac{(+q)}{\left|\boldsymbol{x}-\left(\frac{R}{|\boldsymbol{r}|}\right)^2\boldsymbol{r}\right|}\right] + \left[\frac{(-q)}{|\boldsymbol{x}-(\boldsymbol{r}+\boldsymbol{\epsilon})|} - \left(\frac{R}{|\boldsymbol{r}+\boldsymbol{\epsilon}|}\right)\frac{(-q)}{\left|\boldsymbol{x}-\left(\frac{R}{|\boldsymbol{r}+\boldsymbol{\epsilon}|}\right)^2(\boldsymbol{r}+\boldsymbol{\epsilon})\right|}\right] \tag{D.2}$$

Rearranging terms,

$$\Phi(\boldsymbol{x}) = q\left[\frac{1}{|\boldsymbol{x}-\boldsymbol{r}|} - \frac{1}{|\boldsymbol{x}-\boldsymbol{r}-\boldsymbol{\epsilon}|}\right] + qR\left[\left(\frac{1}{|\boldsymbol{r}+\boldsymbol{\epsilon}|}\right)\frac{1}{|\boldsymbol{x}-\left(\frac{R}{|\boldsymbol{r}+\boldsymbol{\epsilon}|}\right)^2(\boldsymbol{r}+\boldsymbol{\epsilon})|} - \left(\frac{1}{|\boldsymbol{r}|}\right)\frac{1}{|\boldsymbol{x}-\left(\frac{R}{|\boldsymbol{r}|}\right)^2\boldsymbol{r}|}\right] \tag{D.3}$$

To first order in $\boldsymbol{\epsilon}$ the first term becomes,

$$q\left[\frac{1}{|\boldsymbol{x}-\boldsymbol{r}|} - \frac{1}{|\boldsymbol{x}-\boldsymbol{r}-\boldsymbol{\epsilon}|}\right] \approx -\frac{(q\boldsymbol{\epsilon})\cdot(\boldsymbol{x}-\boldsymbol{r})}{|\boldsymbol{x}-\boldsymbol{r}|^3} \tag{D.4}$$

And the second term becomes,

$$qR\left[\left(\frac{1}{|\boldsymbol{r}+\boldsymbol{\epsilon}|}\right)\frac{1}{|\boldsymbol{x}-\left(\frac{R}{|\boldsymbol{r}+\boldsymbol{\epsilon}|}\right)^2(\boldsymbol{r}+\boldsymbol{\epsilon})|} - \left(\frac{1}{|\boldsymbol{r}|}\right)\frac{1}{|\boldsymbol{x}-\left(\frac{R}{|\boldsymbol{r}|}\right)^2\boldsymbol{r}|}\right] \approx \left(\frac{R}{|\boldsymbol{r}|}\right)^3\frac{(q\boldsymbol{\epsilon})\cdot\left(\boldsymbol{x}-\left(\frac{|\boldsymbol{x}|}{R}\right)^2\boldsymbol{r}\right)}{|\boldsymbol{x}-\left(\frac{R}{|\boldsymbol{r}|}\right)^2\boldsymbol{r}|^3} \tag{D.5}$$

Define the dipole vector $\boldsymbol{M} \equiv q\boldsymbol{\epsilon}$, and assuming all charges $|q|$ have equivalent magnitudes, the potential field reduces to,

$$\Phi(\boldsymbol{x}) = \left(\frac{R}{|\boldsymbol{r}|}\right)^3\frac{\boldsymbol{M}\cdot\left(\boldsymbol{x}-\left(\frac{|\boldsymbol{x}|}{R}\right)^2\boldsymbol{r}\right)}{|\boldsymbol{x}-\left(\frac{R}{|\boldsymbol{r}|}\right)^2\boldsymbol{r}|^3} - \frac{\boldsymbol{M}\cdot(\boldsymbol{x}-\boldsymbol{r})}{|\boldsymbol{x}-\boldsymbol{r}|^3} \tag{D.6}$$

Note the first term on the RHS is nonlinear in the observation distance $|\boldsymbol{x}|$, therefore this field in general, is not that of a dipole distribution. To produce the special case of a dipole distribution potential field, require $\boldsymbol{M}\cdot\boldsymbol{r} = 0$ (i.e., force the set of point dipoles parallel to the surface). Thus, the potential field due to a point dipole $\boldsymbol{M}$, at position $\boldsymbol{r}$, and a spherical source surface at radius R, requires an image dipole

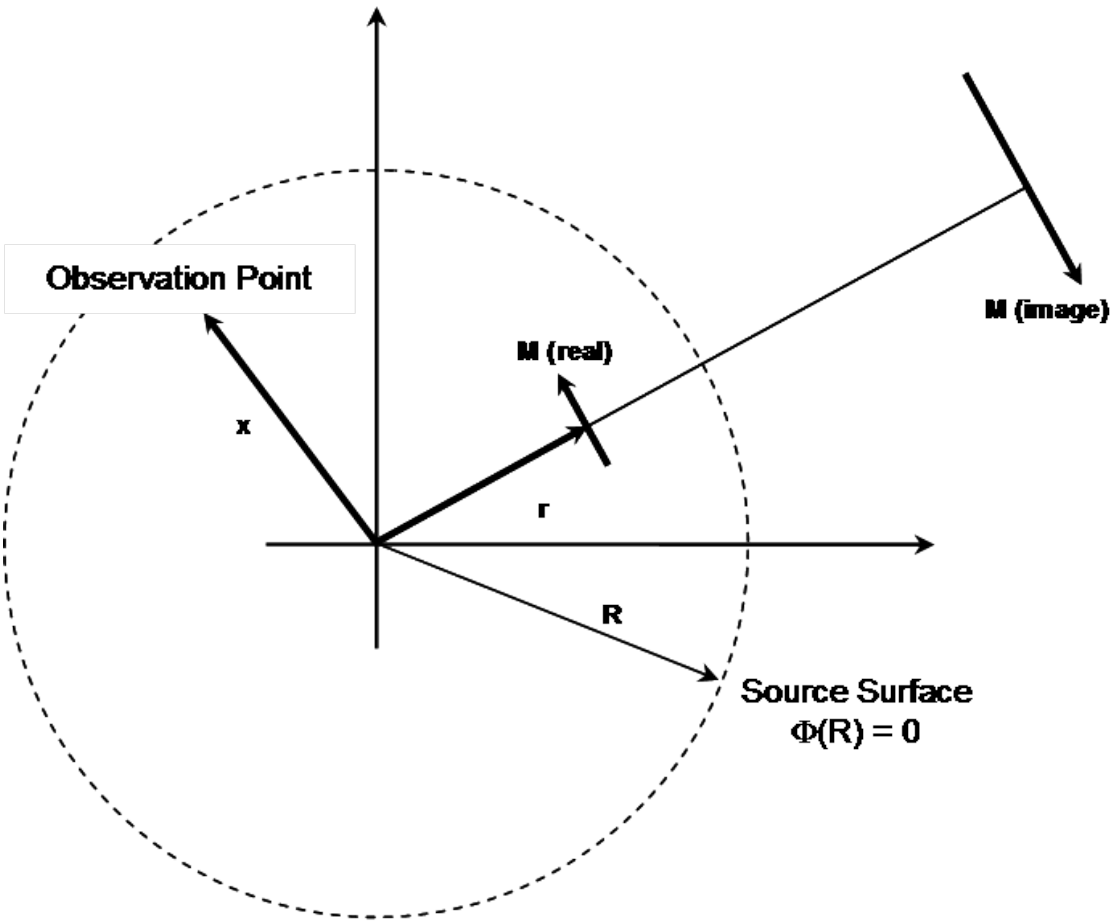

Figure D.2: Single real-image dipole pair potential field model.

vector $\left(\frac{R}{|\boldsymbol{r}|}\right)^3 \boldsymbol{M}$, at position $\left(\frac{R}{|\boldsymbol{r}|}\right)^2 \boldsymbol{r}$. Collecting terms,

$$\Phi(\boldsymbol{x}) = (\boldsymbol{M} \cdot \boldsymbol{x}) \left[\left(\frac{R}{|\boldsymbol{r}|}\right)^3 \frac{1}{|\boldsymbol{x} - \left(\frac{R}{|\boldsymbol{r}|}\right)^2 \boldsymbol{r}|^3} - \frac{1}{|\boldsymbol{x} - \boldsymbol{r}|^3} \right] \tag{D.7}$$

Equation D.7 describes the potential field due to a single real and geometrically related image dipole pair (see FigureD.2).

To include the potential field due to a dipole $\boldsymbol{M}_0$ at the origin with a spherical

source surface at radius R, take the limit that the position $|\boldsymbol{r}| \to 0$,

$$\Phi(\boldsymbol{x}) = \lim_{|\boldsymbol{r}|\to 0} (\boldsymbol{M}_0 \cdot \boldsymbol{x}) \left[\left(\frac{R}{|\boldsymbol{r}|} \right)^3 \frac{1}{|\boldsymbol{x} - \left(\frac{R}{|\boldsymbol{r}|} \right)^2 \boldsymbol{r}|^3} - \frac{1}{|\boldsymbol{x} - \boldsymbol{r}|^3} \right] \tag{D.8}$$

$$\Phi(\boldsymbol{x}) = (\boldsymbol{M} \cdot \boldsymbol{x}) \left[\frac{1}{R^3} - \frac{1}{|\boldsymbol{r}|^3} \right] \tag{D.9}$$

Therefore, the total potential field with a spherical source surface at radius R is the sum of the dipole positioned at the origin $\boldsymbol{M}_0$, along with a single real and geometrically related image dipole pair,

$$\begin{aligned} \Phi(\boldsymbol{x}) = {} & (\boldsymbol{M}_0 \cdot \boldsymbol{x}) \left[\frac{1}{R^3} - \frac{1}{|\boldsymbol{r}|^3} \right] \\ & + (\boldsymbol{M} \cdot \boldsymbol{x}) \left[\left(\frac{R}{|\boldsymbol{r}|} \right)^3 \frac{1}{|\boldsymbol{x} - \left(\frac{R}{|\boldsymbol{r}|} \right)^2 \boldsymbol{r}|^3} - \frac{1}{|\boldsymbol{x} - \boldsymbol{r}|^3} \right] \end{aligned} \tag{D.10}$$

Since this potential field is linear in the real-image dipole pairs, this model can therefore be extended to the superposition of a set of discrete real-image dipoles,

$$\begin{aligned} \Phi(\boldsymbol{x}) = {} & (\boldsymbol{M}_0 \cdot \boldsymbol{x}) \left[\frac{1}{R^3} - \frac{1}{|\boldsymbol{r}|^3} \right] \\ & + \sum_i (\boldsymbol{M}_i \cdot \boldsymbol{x}) \left[\left(\frac{R}{|\boldsymbol{r}_i|} \right)^3 \frac{1}{|\boldsymbol{x} - \left(\frac{R}{|\boldsymbol{r}_i|} \right)^2 \boldsymbol{r}_i|^3} - \frac{1}{|\boldsymbol{x} - \boldsymbol{r}_i|^3} \right] \end{aligned} \tag{D.11}$$

To generalize, this potential field model can be extended to a continuous distribution dipole density distribution $\boldsymbol{M}(\boldsymbol{x})$, and a point dipole at the origin $\boldsymbol{M}_0$ (see

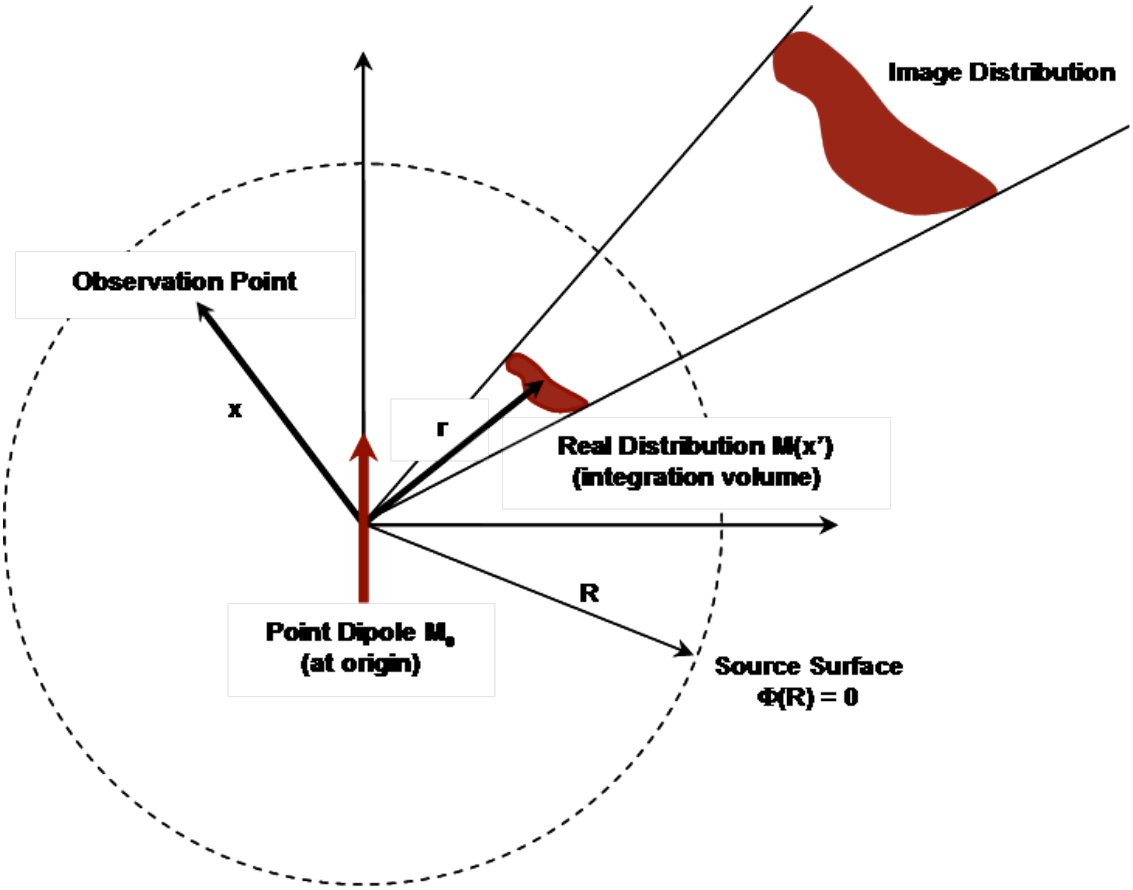

Figure D.3: Dipole density distribution potential field model.

FigureD.3),

$$\Phi(\boldsymbol{x}) = (\boldsymbol{M}_0 \cdot \boldsymbol{x}) \left[\frac{1}{R^3} - \frac{1}{|\boldsymbol{r}|^3} \right] + \iiint (\boldsymbol{M}(\boldsymbol{x}') \cdot \boldsymbol{x}) \left[\left(\frac{R}{|\boldsymbol{x}'|} \right)^3 \frac{1}{|\boldsymbol{x} - \left(\frac{R}{|\boldsymbol{x}'|} \right)^2 \boldsymbol{x}'|^3} - \frac{1}{|\boldsymbol{x} - \boldsymbol{x}'|^3} \right] d^3x' \quad \text{(D.12)}$$

To recover the discrete set of dipoles $\boldsymbol{M}_i$, at positions $\boldsymbol{r}_i$,

$$\boldsymbol{M}(\boldsymbol{x}') = \sum_i \boldsymbol{M}_i \, \delta^3(\boldsymbol{x}' - \boldsymbol{r}_i) \quad \text{(D.13)}$$

where $\delta^3(\boldsymbol{x}' - \boldsymbol{r}_i)$ is the 3-dimesnional delta function.

BIBLIOGRAPHY

BIBLIOGRAPHY

Abbett, W. P., Fisher, G. H., & Fan, Y. 2000, ApJ, 540, 548

Abbett, W. P., Fisher, G. H., & Fan, Y. 2001, ApJ, 546, 1194

Abbett, W. P. 2007, ApJ, 665, 1469

Antiochos, S. K., 1987, ApJ, 312, 886

Antiochos, S. K., 1990, Mem. Soc. Astron. Italiana, 61, 369

Antiochos, S. K., 1996, Astron. Soc. Pac. Conf. Series, 95, 1

Antiochos, S. K., & Dahlburg, R. B., 1997, Sol. Phys., 174, 5

Antiochos, S. K., DeVore, C. R., & Klimchuk, J. A. 1999, ApJ, 510, 485

Antiochos, S. K., Karpen, J. T., & DeVore, C. R. 2002, ApJ, 575, 578

Antiochos, S. K., DeVore, C. R., Karpen, J. T., & Mikić, Z. 2007, ApJ, 671, 936

Altschuler, M. D., & Newkirk, G. 1969, Sol. Phys., 9, 131

Arge, C. N., & Pizzo, V. J. 2000, J. Geophys. Res., 107, A10, 1319

Aulanier, G., DeLuca, E. E., Antiochos, S. K., McMullen, R. A., & Golub, L. 2007, ApJ, 540, 1126

Bahcall, J. N., Basu, S., & Pinsonneault, M. H., in Dynamic Sun, ed. B. N. Dwivedi, Cambridge University Press, 2003

Birn, J., Hesse, M., & Schindler, K. 1998, J. Geophys. Res., 103, A4, 6843

Biskamp, D., Nonlinear Magnetohydrodynamics, Cambridge University Press, 1993

Bulanov, S. V., Sakai, J., & Syrovatskii, S. I. 1979, Fiz. Plasmy USSR, 5, 280

Carroll, B. W., & Ostlie, D. A., An Introduction To Modern Astrophysics, Addison-Wesley Publishing Co. Inc., 1996

Christensen-Dalsgaard, J., & Thompson, M. J., in Dynamic Sun, ed. B. N. Dwivedi, Cambridge University Press, 2003

Crooker, N. U., Gosling, J. T., & Kahler, S. W. 2002, J. Geophys. Res., 107(A2), SSH 2, DOI: 10.1029/2001JA000236

Dahlburg, R. B., Klimchuk, J. A., & Antiochos, S. K. 2003, Adv. Space Res., 32, 1029

Dahlburg, R. B., Klimchuk, J. A., & Antiochos, S. K. 2005, ApJ, 622, 1191

Dahlburg, R. B., Klimchuk, J. A., & Antiochos, S. K. 2006, Adv. Space Res., 37, 1342

DeVore, C. R. 1991, J. Comput. Phys., 92, 142

DeVore, C. R., & Antiochos, S. K., 2008, ApJ, 680, 740

Drake, J. F., Swisdak, M., Che, H., & Shay, M. A., 2006, Nature, 443, 553

Edmondson, J. K., Antiochos, S. K., DeVore, C. R., Lynch, B. L., & Zurbuchen, T. H. 2009, ApJ, (submitted)

Edmondson, J. K., Antiochos, S. K., DeVore, C. R., & Zurbuchen, T. H. 2009, ApJ, (in prep)

Edmondson, J. K., Lynch, B. L., Antiochos, S. K., DeVore, C. R., & Zurbuchen, T. H. 2009, ApJ, (submitted)

Feldman, U., Landi, E., & Schwadron, N. A. 2005, J. Geophys. Res., 110, A07109, DOI: 10.1029/2004JA010918

Fisk, L. A., Zurbuchen, T. H., & Schwadron, N. A. 1999, ApJ, 521, 868

Fisk, L. A., & Schwadron, N. A. 2001, ApJ, 560, 425

Fisk, L. A. 2005, ApJ, 626, 563

Fisk, L. A., & Zurbuchen, T. H. 2006, J. Geophys. Res., 111, A09115, DOI: 10.1029/2005JA011575

Fisk, L. A., & Zhao, L., 2009, Universal Heliophysical Processes, Proceedings of the International Astronomical Union, IAU Symposium, 257, 109

Fletcher, L., Lpez Fuentes, M. C., Mandrini, C. H., Schmieder, B., Dmoulin, P., Mason, H. E., Young, P. R., & Nitta, N., 2001, Sol. Phys., 203, 255

Furth, H. P., Killen, I., & Rosenbluth, M. N. 1963, Phys. Fluids, 6, 459

Galeev, A. A., & Zeleny, L. M. 1976, Zh. Eksp. Teor. Fiz. 70, 2133

Gary, G. A. 2001, Sol. Phys., 203, 71

Geiss, J., et al. 1995, Science, 268, 1033

Gloeckler, G., et al. 1992, Astron. Astrophys. Suppl. Ser., 92, 267

Golub, L., Krieger, A. S., Silk, J. K., Timothy, A. F., & Vaiana, G. S. 1974, ApJ, 189, L93+

Gombosi, T. I., De Zeeuw, D. L., Groth, C. P. T., Powell, K. G., & Stout, Q. F. 2000, J. Atmos. Sol. Terr. Phys., 62, 1515

Gosling, J. T. 1990, in Physics of Magnetic Flux Ropes, ed. C. T. Russell, E. R. Priest, & L. C. Lee (AGU Geophys. Monogr. 58; Washington: AGU), 343

Greene, J. M. 1988, J. Geophys. Res., 93, 8583

Groth, C. P. T., De Zeeuw, D. L., Gombosi, T. I., & Powell, K. G. 2000, Adv. Space Res.,26, 793

Hoeksema, J. T. 1991, Adv. Space Res., 11, 15

Howard, R. A., Sheeley, N. R., Jr., Michels, D. J., & Koomen, M. J. 1985, J. Geophys. Res., 90, 8173

Hundhausen, A. J., Sawyer, C. B., House, L., Illing, R. M. E., & Wagner, W. J. 1984, J. Geophys. Res., 90, 8173

Jackson, J. D., Classical Electrodynamics 3rd Edition, John Wiley & Sons, New York, 1975

Jones, G. H., & Balogh, A. 2003, Ann. Geophys. 21, 1377

Kallenrode, M. B., Space Physics, An Introduction to Plasma and Particles in the Heliosphere and Magnetospheres, Springer-Verlag, Berlin Heidelberg, 2004

Kahler, S. W., & Hudson, H. S., 2002, ApJ, 574, 476

Karpen, J. T., Antiochos, S. K., & DeVore, C. R. 1995, ApJ, 450, 422

Karpen, J. T., Antiochos, S. K., & DeVore, C. R. 1996, ApJ, 460, L73

Karpen, J. T., Antiochos, S. K., Devore, C. R., & Golub, L., 1998, Apj, 495, 491

Klimchuk, J. A. 2006, Sol. Phys., 234, 41

Kulsrud, R. M. 2001, Earth Planets Space, 53, 417

Lau, Y.-T., & Fin, J. M. 1990, ApJ, 350, 672

Lepri, S. T., Antiochos, S. K., Riley, P., Zhao, L., & Zurbuchen, T. H., 2008, ApJ, 674, 1158

Lin, R. P., & Kahler, S. W. 1992, J. Geophys. Res., 97, 8203

Linker, J. A., Mikić, Z., Biesecker, D. A., Forsyth, R. J., Gibson, S. E., Lazarus, A. J., Lecinski, A., Riley, P., Szabo, A., & Thompson, B. J., 1999, J. Geophys. Res., 94, 6907

Linker, J. A., Mikić, Z., Lionello, R., Riley, P., Amari, T., & Odstrcil, D. 2003, Phys. Plas. 10, 1971

Lionello, R., Linker, J. A., & Mikić, Z. 2009, ApJ, 690, 902

Longcope, D. W., Topological Methods for the Analysis of Solar Magnetic Fields, Living Rev. Solar Phys., 2, (2005), 7, http://www.livingreviews.org/lrsp-2005-7

Luhmann, J. G., Li, Y., Zhao, X., & Yashiro, S., 2003, Sol. Phys., 213, 367

Lynch, B. J., Antiochos, S. K., DeVore, C. R., Luhmann, J. G., & Zurbuchen, T. H., 2008, ApJ, 683, 1192

Lynch, B. J., Antiochos, S. K., Li, Y., Luhmann, J. G., & DeVore, C. R., 2009, ApJ, 697, 1918

McComas, D. J., Gosling, J. T., Phillips, J. L., Bame, S. J., Luhmann, J. G., & Smith, E. J. 1989, J. Geophys. Res., 104, A5, 9809

McComas, D. J., Phillips, J. L., Hundhausen, A. J., & Burkpile, J. T. 1991, Geophys. Res. Lett., 18, 73

McComas, D. J., Elliot, H. A., Schwadron, N. A., Gosling, J. T., Skoug, R. M., & Goldstein, B. E. 2002, J. Geophys. Res. Lett., 30, 1517, DOI: 10.1029/2003GL017136

Mikić, Z., Linker, J. A., Schnack, D. D., Lionello, R., & Tarditi, A. 1999, Phys. Plas., 6, 2217

Miller, J. A., Cargill, P. J., Emslie, A. G., Holman, G. D., Dennis, B. R., La Rosa, T. N., Winglee, R. M., Benka, S. G., & Tsuneta, S. 1997, J. Geophys. Res., 102, A7, 14631

Odstrcil, D. 2003, Adv. Space Res., 32, 497

Pagel, C., Crooker, C. U., & Larson, D. E. 2005, Geophys. Res. Lett., 32, L14105, DOI: 10.1029/2005GL023043

Pariat, E., Antiochos, S. K., & DeVore, C. R., 2009, ApJ, 691, 61

Parker, E. N. 1957, J. Geophys. Res., 62, 509

Parker, E. N. 1958, ApJ, 128, 664

Parker, E. N., Interplanetary Dynamical Processes, New York: Interscience, 1963

Parker, E. N. 1963, ApJS, 8, 177

Parker, E. N. 1964, ApJ, 139, 72

Parker, E. N. 1964, ApJ, 139, 93

Parker, E. N. 1965, ApJ, 141, 146

Parker, E. N. 1966, ApJ, 143, 32

Parker, E. N. 1972, ApJ, 174, 499

Parker, E. N. 1973, ApJ, 180, 247

Parker, E. N. 1983, ApJ, 264, 642

Parker, E. N. 1984, ApJ, 283, 343

Parker, E. N. 1988, ApJ, 330, 474

Parnell, C. E., Smith, J. M., Neukirch, T., & Priest, E. R. 1996, Phys. Plasmas, 3, 759

Petschek, H. E., 1964, The physics of solar flares, AAS-NASA Symposium, NASA SP-50 (ed. W. N. Hess), p. 425

Priest, E. R., Solar Flare Magnetohydrodynamics, edited by E. R. Priest, Vol. 1, Gordon and Breach, Newark, NJ, 1981

Priest, E. R., & Titov, V. S. 1996, Phil. Trans. R. Soc., 354, 2951

Priest, E. R., & Forbes, T., Magnetic Reconnection, Cambridge University Press, 2000

Powell, K. G., Roe, P L., Linde, T. J., Gombosi, T. I., & De Zeeuw, D. L. 1999, J. Comp. Phys., 153, 284

Rappazzo, A. F., Velli, M., Einaudi, G., & Dahlburg, R. B. 2008, ApJ, 677, 1348

Riley, P., Linker, J. A., Mikić, Z., Odstrcil, D., Zurbuchen, T. H., Lario, D., & Lepping, R. P. 2006, JGR, 108, 1272

Riley, P., Linker, J. A., Mikić, Z., Lionello, R., Ledvina, S. A., & Luhmann, J. G., 2006, ApJ, 653, 1510

Rose, W. K., Advanced Stellar Astrophysics, Cambridge University Press, 1998

Roussev, I. I., Gombosi, T. I., Sokolov, I. V., Velli, M., Manchester, W., IV, DeZeeuw, D. L., Liewer, P., Tth, G., & Luhmann, J., 2003, ApJ, 595, L57

Schatten, K., Wilcox, J. W., & Ness, N. F. 1969, Sol. Phys., 9, 442

Schrijver, C. J., Title, A. M., van Ballegooijen, A. A., Hagenaar, H. J., & Shine, R. A. 1997, ApJ, 487, 424

Sheeley, N. R., Jr., & Wang, Y.-M. 2002, ApJ, 579, 874

Smith, E. J., Balogh, A., Forsyth, R. J., & McComas, D. J. 2001, Geophys. Res. Lett., 28, 4159

Sonnerup, B. U. O. 1970, J. Plasma Phys., 4, 161.

Suess, S. T., Smith, E. J., Phillips, J., Goldstein, B. E., & Nerney, S. 1996, Astron. Astrophys., 316, 304

Sweet, P. A. 1958, in Electromagnetic Phenomena in Cosmic Physics, ed. B. Lehnert (New York: Cambridge Univ. Press), 123

Syrovatskii, S. I. 1971, Sov. Phys. JETP, 33, 933

Syrovatskii, S. I. 1978, Sol. Phys., 58, 89

Syrovatskii, S. I. 1978, Astrophys. & Sp. Sci., 56, 3

Syrovatskii, S. I. 1981, Annu. Rev. Aston. & Astrophysics, 19, 163

Thompson, M. J. 2003, Annu. Rev. Aston. & Astrophysics, 41, 599

Title, A. M., & Schrijver, C. J. 1998, in Cool Stars, Stellar Systems and the Sun, ed. R. A. Donahue & J. A. Bookbinder (ASP Conference Series, Vol 154)

van Ballegooijen, A. A. 1985, ApJ 298, 421

Velli, M. 1994, ApJ, 432, L55

Wang, Y.-M., & Sheeley, N. R. 1992, ApJ, 392, 310

Wang, Y. M., Sheeley, N. R., Howard, R. A., & Rich, N. B. 1999, Geophys. Res. Lett., 26, 10, 1349

Wang, Y.-M., & Sheeley, N. R. 2007, ApJ, 449, L157

Wang, Y.-M., Sheeley, N. R., & Rich, N. B. 2007, ApJ, 658, 1340

Wang, Y.-M., & Muglach, K., 2008, Sol. Phys., 249, 17

Welsch, B. T., DeVore, C. R., & Antiochos, S. K. 2005, ApJ, 634, 1395

Woo, R., & Martin, J. M. 1997, Geophys. Res. Lett., 24, 2535

Zhao, L., Zurbuchen, T. H., & Fisk, L. A. 2009, Geophys. Res. Lett., 36, L14104

Zirker, J. B. 1977, Rev. Geophys. Space Phys., 15, 257

Zurbuchen, et. al., JGR, 105, A8, 18327 (2000)

Zurbuchen, T. H. 2007, Annu. Rev. Aston. & Astrophysics, 45, 297